



Defence Research and
Development Canada

Recherche et développement
pour la défense Canada



Soil Electromagnetic Properties and Metal Detector Performance

Theory and Measurement

G. Cross, Terrascan Geophysics

Contract Scientific Authority: Y. Das, DRDC Suffield

The scientific or technical validity of this Contract Report is entirely the responsibility of the contractor and the contents do not necessarily have the approval or endorsement of Defence R&D Canada.

Defence R&D Canada

Contract Report

DRDC Suffield CR 2009-062

November 2008

Canada

Soil Electromagnetic Properties and Metal Detector Performance

Theory and Measurement

G. Cross
Terrascan Geophysics
4506 West 4th Avenue
Vancouver BC V6R 1R3

Contract Number: W7702-03R941

Contract Scientific Authority: Y. Das (403-544-4738)

The scientific or technical validity of this Contract Report is entirely the responsibility of the contractor and the contents do not necessarily have the approval or endorsement of Defence R&D Canada.

Defence R&D Canada – Suffield

Contract Report

DRDC Suffield CR 2009-062

November 2008

© Her Majesty the Queen as represented by the Minister of National Defence, 2008

© Sa majesté la reine, représentée par le ministre de la Défense nationale, 2008

Soil Electromagnetic Properties and Metal Detector Performance: Theory and Measurement



Submitted to:

Canadian Centre for Mine Action Technologies
Defence Research & Development Canada
Suffield, Alberta

17 November, 2008

Terrascan Geophysics
4506 West 4th Avenue
Vancouver, British Columbia, Canada V6R 1R3
Tel/Fax: (604) 221-2400
www.terrascan.ca



DISCLAIMER

The following report was prepared by Terrascan Geophysics (Terrascan) as an account of research conducted under Defence Research and Development Canada (DRDC) Contract W7702-03R941/001/EDM. Funding was provided by the Canadian Centre for Mine Action Technologies (CCMAT). Terrascan makes no warranty, express or implied, or assumes any legal liability or responsibility for the accuracy, completeness, or application of any information, apparatus, or methodology cited or reported. Reference herein to any specific commercial product, trademark, manufacturer, or otherwise does not constitute or imply its endorsement, recommendation, or favouring by Terrascan.

TABLE OF CONTENTS

<u>SECTION</u>	<u>PAGE</u>
ABSTRACT.....	1
1.0 BACKGROUND.....	2
2.0 ELECTROMAGNETIC THEORY - ROLE OF SOIL EM PROPERTIES	3
3.0 METAL DETECTORS - INFLUENCE OF SOIL EM PROPERTIES	6
3.1 Frequency Domain (FDEM) Response	7
3.2 Time Domain (TDEM) Response	15
3.3 Dispersive Soil EM Properties and TDEM Response	19
3.3.1 <i>General Formulation</i>	19
3.3.2 <i>Non-Magnetic, Non-Dispersive Conductive Soil</i>	20
3.3.3 <i>Non-Conductive, Non-Dispersive Magnetic Soil</i>	21
3.3.4 <i>Non-Conductive, Dispersive Magnetic Soil</i>	22
3.3.5 <i>Non-Dispersive Conductive-Magnetic Soil</i>	24
3.3.6 <i>Conductive, Dispersive Magnetic Soil</i>	25
3.3.7 <i>Non-Magnetic, Dispersive Conductive Soil</i>	28
3.4 Summary	32
4.0 MEASUREMENT OF SOIL EM PROPERTIES.....	34
4.1 Complex Impedance - Admittance.....	35
4.2 Electrical Parameters - Theory	36
4.3 Magnetic Parameters - Theory	39
4.4 Electrical Parameters - Measurement.....	41
4.4.1 <i>Laboratory Methods and Procedures</i>	41
4.4.2 <i>Laboratory Instrumentation</i>	47
4.4.3 <i>Field Methods and Procedures</i>	49
4.4.4 <i>Field Instrumentation</i>	56
4.5 Magnetic Parameters - Measurement	58
4.5.1 <i>Laboratory Methods and Procedures</i>	58
4.5.2 <i>Laboratory Instrumentation</i>	67
4.5.3 <i>Field Methods, Procedures and Instrumentation</i>	76
5.0 SOIL NOISE - SUMMARY AND CONCLUSIONS	80
6.0 REFERENCES CITED.....	84

SOIL EM PROPERTIES AND METAL DETECTOR PERFORMANCE: THEORY AND MEASUREMENT

Guy Cross

Terrascan Geophysics, Vancouver, Canada

Abstract:

Metal detectors are unquestionably the workhorses of humanitarian demining. Although hybrid dual-sensor systems incorporating a ground penetrating radar (GPR) have recently been introduced and are gaining acceptance, a standard electromagnetic induction (EMI) sensor remains the primary mode of detection. Despite ongoing evolution and refinement of metal detector technology, however, the practical performance of both continuous wave (FDEM) and pulse induction (TDEM) systems continues to be restricted by so-called “soil noise” effects. Generally, “problem” or “difficult” soils reduce signal to noise ratio and increase the false-detection rate. At certain locations, the soil effect is so severe as to render a given metal detector practically inoperable.

Although soil interference is well established and widely appreciated, the precise origin(s) of related noise has remained elusive as evidenced by the range of common descriptions for problem soils, including “lateritic soil”, “mineralized soil”, “conducting soil” and “magnetic soil”. The absence of clarity and definitive understanding has impeded specification of appropriate methods and procedures for related assessment of soil conditions and for predicting the nature and extent of corresponding influence on a given metal detector technology.

To address the foregoing situation, the study reported herein has been part of a broader international effort to define and quantify the effects of soil electromagnetic properties on the operation and performance of metal detectors and allied (GPR) sensors. In particular, the present study is restricted to EMI metal detectors and our aim has been to characterize the nature and extent of influence due to specific soil electromagnetic properties and related frequency dispersion.

Our report begins with a brief review of relevant electromagnetic theory and subsequently explores the basic physics of EMI metal detectors and associated implications for the relative significance of specific soil EM parameters. Particular attention is focused on TDEM sensors and related influence of dispersive soil electromagnetic properties. The balance of the report is devoted to the theory and practice of measuring low-frequency (100 Hz - 100 kHz) soil electromagnetic properties. A range of practical instrumentation and procedures are investigated with reference to three DRDC reference soils.

1.0 BACKGROUND

Previous and ongoing conflicts have left approximately 100 million unexploded landmines within the soils of more than fifty countries worldwide. Unfortunately, developing nations that are least prepared to cope with the problem are disproportionately affected. Vast tracts of land have been effectively removed from agriculture or other productive utilization, and the human cost is intolerable. The United Nations estimates that approximately 25,000 civilians are killed or maimed by landmines each year.

Growing awareness of the landmine problem over the past decade has fostered a substantial international response, with governments and non-governmental organizations currently sponsoring active humanitarian demining programs in virtually every mine-affected nation. However, demining is a costly and time-consuming process and it is currently estimated that for every mine that is removed or neutralized, approximately 20 more are laid. Clearly there is an urgent requirement for new and effective mine detection technologies and, concurrently, for the refinement of well-established and proven methodologies.

In particular, despite ongoing development of novel and alternative sensor technologies, metal detectors remain the workhorses of humanitarian demining. Crucially, however, the performance of both continuous wave and pulse induction metal detectors can be severely restricted by so-called “soil-noise” effects. Generally, “problem soils” reduce detector sensitivity and increase the false-detection rate. In certain locations, the soil-effect is so strong as to render a given detector practically inoperable.

Although the adverse influence of certain soils are widely recognized and acknowledged by the demining community, there has only recently been a concerted effort to understand and establish the responsible soil properties and underlying physical mechanisms (Das, et al., 2002, 2003; ITEP, 2002). The current study is a part this ongoing effort to define and quantify the influence of soil electromagnetic properties on the operation of metal detectors. Specifically, our focus has been to identify key soil parameters and to investigate appropriate technologies and procedures for related soils characterization.

We begin with a brief review of relevant electromagnetic theory and subsequently explore the basic physics of metal detectors and related implications for the relative significance of specific soil EM parameters. The remainder of the report is devoted to the theory and practice of measuring low-frequency (100 Hz - 100 kHz) soil electromagnetic properties. The connection between measured soil electromagnetic properties and related physical, chemical and mineralogical characteristics of soils is not addressed here (see Cross, 2000).

2.0 ELECTROMAGNETIC THEORY — ROLE OF SOIL EM PROPERTIES

In connection with a previous project (DRES CR 2000-091), Cross (2000) reviewed the nature and description of soil electromagnetic properties as relevant to the performance of ground penetrating radar (GPR) sensors. Analysis emphasized the frequency-dependent, complex nature of electromagnetic parameters and associated effective soil properties.

Beginning with Maxwell's equations

$$\nabla \times \mathbf{E} = -\frac{\partial \mathbf{B}}{\partial t} \quad (1)$$

$$\nabla \times \mathbf{H} = \mathbf{J} + \frac{\partial \mathbf{D}}{\partial t}, \quad (2)$$

and assuming constitutive relations

$$\mathbf{B} = \mu \mathbf{H}, \quad (3)$$

$$\mathbf{D} = \epsilon \mathbf{E}, \quad (4)$$

$$\mathbf{J} = \sigma \mathbf{E}, \quad (5)$$

relating electric \mathbf{E} and magnetic \mathbf{H} fields, associated electric displacement \mathbf{D} , magnetic induction \mathbf{B} and the electric current density \mathbf{J} , the governing relations

$$\nabla^2 \mathbf{E} = \gamma^2 \mathbf{E} \quad (6)$$

$$\nabla^2 \mathbf{H} = \gamma^2 \mathbf{H}, \quad (7)$$

were derived for harmonically-varying electromagnetic fields within a uniform, linear isotropic soil. The associated propagation constant

$$\begin{aligned} \gamma &= [i 2\pi f \mu (\sigma + i 2\pi f \epsilon)]^{1/2} \\ &= 2\pi f \left[\mu \epsilon \left(i \frac{\sigma}{2\pi f \epsilon} - 1 \right) \right]^{1/2} \end{aligned} \quad (8)$$

encompasses the influence of soil electromagnetic properties, including the magnetic permeability μ , electrical permittivity ϵ and electrical conductivity σ . In addition, it was observed that these parameters are ordinarily frequency dependent and, consequently, complex valued. Moreover, because observed dispersion is in each case associated with some form of polarization and alternating relaxation, it was shown

that the frequency dependence of soil electromagnetic parameters can be usefully modelled by appropriate generalizations of the well-known Debye spectrum as depicted in Figure 1.

It was also emphasized that in the practical process of measuring soil electromagnetic parameters, and to the extent that soil properties influence the response of a ground radar (or metal detector), it is impossible to separate the combined influence of multiple properties contributing in-phase. In particular, defining complex parameters

$$\sigma = \sigma' + i\sigma'' \quad (9)$$

$$\epsilon = \epsilon' - i\epsilon'' \quad (10)$$

$$\mu = \mu' - i\mu'', \quad (11)$$

it was demonstrated that the propagation constant can be rewritten as

$$\gamma = 2\pi f \left[\mu \tilde{\epsilon} \left(i \frac{\tilde{\sigma}}{2\pi f \tilde{\epsilon}} - 1 \right) \right]^{1/2} \quad (12)$$

in terms of a real-valued effective conductivity

$$\tilde{\sigma} = \sigma' + 2\pi f \epsilon'' \quad (13)$$

and real-valued effective permittivity

$$\tilde{\epsilon} = \epsilon' + \frac{\sigma''}{2\pi f}, \quad (14)$$

each comprising the combined influence of separate processes that are unresolved by measurement. The composite nature of effective electromagnetic properties is illustrated in Figure 2, where measured high-frequency electrical parameters are compared with effective properties predicted by Equations (13) and (14). Theoretically predicted spectra are based on Debye models for complex electrical conductivity and permittivity as depicted in Figure 1.

The propagation constant also incorporates the complex magnetic permeability

$$\mu = \mu' - i\mu'' \quad (6)$$

and in connection with the analysis of the ground radar measurements, it is commonly assumed that $\mu'' = 0$, yielding an effective real-valued permeability $\tilde{\mu} = \mu'$. While there are established and significant exceptions to this assumption for GPR, it is not an unreasonable simplification at radar frequencies. In contrast, however, it is certainly not valid at the lower operational frequencies of metal detectors, particularly in electrically resistive soils. On the contrary, it is now widely accepted that anomalous

magnetic susceptibility and related viscosity are in large part responsible for observed soil-noise and associated degradation of metal detector performance.

Finally, in the previous report (Cross, 2000), approximate forms of the propagation constant for non-conductive ($\sigma/2\pi f\epsilon \ll 1$) and conductive ($\sigma/2\pi f\epsilon \gg 1$) media were considered in connection with representative soils property data. As displayed in Figure 3a, corresponding governing relations from Equations (6) and (7) describe unattenuated wave propagation for non-conductive media while for conductive media the mode is diffusion. As suggested by Figure 3b, modelling of the GPR response with representative soil parameters demonstrated that even at radar frequencies appropriate for mine detection (~ 1.0 GHz), the non-conductive or dielectric approximation $\gamma \approx i2\pi f(\mu\epsilon)^{1/2}$ is not generally appropriate. Now, in connection with metal detectors, we find ourselves at the opposite end of the spectrum and we consider the low-frequency or conductive approximation $\gamma \approx (i2\pi f\mu\sigma)^{1/2}$. Although theoretical analyses of the electromagnetic induction problem are nearly uniform in this so-called quasi-static assumption, and while it is certainly more viable than a dielectric assumption for GPR, data in Figure 3b suggest that limitations could be significant at higher operational frequencies as well as for time-domain measurements ¹. However, assuming in general that displacement currents are negligible at typical metal detector frequencies, Equations (6) and (7) yield corresponding governing relations

$$\nabla^2 \mathbf{E} = \gamma^2 \mathbf{E} = i2\pi f\tilde{\mu}\sigma \mathbf{E} \quad (15)$$

$$\nabla^2 \mathbf{H} = \gamma^2 \mathbf{H} = i2\pi f\tilde{\mu}\sigma \mathbf{H} \quad (16)$$

or, equivalently,

$$\nabla^2 \mathbf{E} = \mu\sigma \frac{\partial \mathbf{E}}{\partial t} \quad (17)$$

$$\nabla^2 \mathbf{H} = \mu\sigma \frac{\partial \mathbf{H}}{\partial t}. \quad (18)$$

In general, solutions of foregoing diffusion equations describe a strongly damped oscillatory electromagnetic field advancing at a diffusion rate of $v_d = 2(\pi f/\mu\sigma)^{1/2}$ and with attenuation rate $\alpha = 1/d_s = (\pi f\mu\sigma)^{1/2}$, where d_s is the associated skin depth. This is, in essence, the nature of the metal detector field within the host soil. The actual field depends on the specific geometry, orientation and height of the source coil, time-dependence of the applied current waveform and, of course, soil electromagnetic properties.

¹ Note Stewart et al. (1994) observed that in practice, displacement currents become significant as their relative magnitude exceeds approximately 5 percent of corresponding conduction currents and that this condition is commonly satisfied at frequencies between 50 and 100 kHz. Clearly, the transition frequency could be lower for dry surface soils.

3.0 METAL DETECTORS — INFLUENCE OF SOIL EM PROPERTIES

Metal detectors operate on the basis of electromagnetic induction (EMI) as illustrated in Figure 4². In general, transmitter circuitry impresses a time-varying current waveform I_0 upon the transmit coil to generate a primary magnetic field \mathbf{H}_p . Associated magnetic flux $\mathbf{B}_p = \tilde{\mu}\mathbf{H}_p$ passing through the receiver or search coil generates a related primary signal current I_p . The primary field also penetrates the subsurface, inducing a combination of magnetization \mathcal{M} and electrical eddy currents I_E within the host soil, proportional to bulk magnetic permeability μ_1 and electrical conductivity σ_1 , respectively. On average, resulting secondary magnetic fields associated with time-varying magnetization and eddy currents within the soil, combine to induce a secondary background current I_b in the receive coil. Greater or lesser magnetization and eddy current induction within localized heterogeneities, having anomalous permeability/conductivity, yield corresponding anomalous secondary fields and a related anomalous current I_a in the receive coil. Consequently, net current in the receiver coil is $I_s = I_p + I_b + I_a$, reflecting the contribution of primary, background and anomalous magnetic fields. As depicted in Figure 4, the anomalous field can be due to the target, where I_a is considered "signal" or due to localized heterogeneity of the host soil, with I_a considered "noise". Of course, in practice the anomalous component is generally some combination of signal and noise.

There are two principal classes of metal detectors: continuous wave (CW) and pulse induction (PI). The essential difference is the nature of the time-variable source current waveform as illustrated in Figure 5. The transmit coil of a continuous wave or frequency-domain (FDEM) metal detector is driven by a continuous sinusoidal current waveform. Through appropriate null adjustment and receiver circuitry, amplitude and phase of secondary signal voltage $v_s = v_b + v_a$, due to background and anomalous fields, are measured relative to the primary signal voltage v_p . Alternatively, the response may be quantified by measuring the amplitudes of secondary signal components in-phase and quadrature (90 degrees phase-shifted) with respect to the primary signal. In contrast, the pulse induction or time-domain (TDEM) metal detector employs a transient source current waveform and following termination of current in the transmit coil at time t_0 , measures the amplitude of the decaying secondary signal voltage in the receiver coil. The secondary voltage waveform is sampled at one or more specified time-offsets ($t_{s1}, t_{s2}, t_{s3}, \dots$) to define the signal decay rate.

² For informative reviews of metal detector design operation and application see Bruschini (2002) and Guelle et al. (2004).

As per standard treatment (Grant and West, 1965; Keller and Frischknecht, 1966; Telford, et al., 1990), basic physical insight into metal detector response and related dependence on material electromagnetic properties can be obtained by investigating the response of an equivalent lumped element circuit, including a series combination of resistance and inductance. The influence of material parameters and frequency are investigated by quantifying the mutual inductive coupling between the model circuit, and the metal detector's transmitter and receiver coils. In particular, the model comprises a shorted turn, having effective resistance \tilde{R} and effective inductance \tilde{L} . The model is illustrated in Figure 6. For now, we shall neglect any influence of the non-conductive, magnetically permeable core.

3.1 Frequency Domain (FDEM) Response:

A time-varying current

$$I = I_0 e^{i2\pi ft}, \quad (19)$$

in the transmit coil generates a primary time-varying magnetic field \mathbf{H}_0 that couples with both target and receiver coils. Associated time-varying magnetic flux through the receiver induces an electromotive force or voltage

$$v_{02} = -M_{02} \frac{dI}{dt} = -M_{02} \frac{dI}{dt} = -M_{02} i2\pi f I_0 e^{i2\pi ft} \quad (20)$$

in the receiver coil where M_{02} denotes the related mutual inductance³ between the

³ The mutual inductance between two closed loops is a scalar constant defined by

$$M_{12} = \frac{\Phi_{12}}{I},$$

where

$$\Phi_{12} = \int_{A_2} \mathbf{B}_2 \cdot d\mathbf{a}_2 = \mu_2 \int_{A_2} \mathbf{H}_0 \cdot d\mathbf{a}_2$$

is the magnetic flux generated by time-varying current I in loop 1 and threading loop 2. The vector magnetic flux density \mathbf{B}_2 is, of course, related to the magnetic field \mathbf{H}_1 , produced by time varying current I in loop 1 by the constitutive relation $\mathbf{B}_2 = \mu_2 \mathbf{H}_1$, where μ_2 denotes the magnetic permeability of the (isotropic) medium surrounding loop 2 and $d\mathbf{a}_2$ is a local unit vector normal to the cross-sectional area A_2 of loop 2. The reciprocity theorem yields $M_{21} = M_{12}$.

Note that Equation (2) is a form of Faraday's induction law

$$v = \int_{C_2} \mathbf{E}_2 \cdot d\mathbf{s}_2 = -\frac{d}{dt} \int_{A_2} \mathbf{B}_2 \cdot d\mathbf{a}_2 = -\frac{d\Phi_{12}}{dt},$$

that is, the electromotive force v around loop 2, given by the curl or line integral of the related electric field vector \mathbf{E}_2 around the circuit C_2 of loop 2, is equal to the negative time rate of change of magnetic flux \mathbf{B}_2 threading the loop. In accordance with Lenz's law, the negative sign implies that the induced voltage yields a current in loop 2 that opposes the source current in loop 1.

transmit coil (0) and the model circuit (1).

Simultaneously, primary magnetic flux through the target coil induces a voltage

$$v_{01} = -M_{01} \frac{dI}{dt} = -M_{01} i2\pi f I_0 e^{i2\pi ft} \quad (21)$$

where M_{01} denotes the corresponding mutual inductance between transmitter and target coils. An associated current I_1 is developed in accordance with a generalized Ohm's law

$$I_1 = \frac{v_{01}}{Z} = \frac{v_{01}}{\tilde{R} + i2\pi f \mu_1 \tilde{L}} = -M_{01} \frac{i2\pi f}{\tilde{R} + i2\pi f \tilde{L}} I_0 e^{i2\pi ft}, \quad (22)$$

where $Z = \tilde{R} + i2\pi f \tilde{L}$ denotes the effective complex impedance of the model circuit. Note that $I_1 = I_E$ is the model eddy current. The eddy current, in turn, produces a secondary magnetic field at the receiver coil, inducing a related voltage

$$v_{12} = -M_{12} \frac{dI_1}{dt} = -M_{01} M_{12} \frac{(2\pi f)^2}{\tilde{R} + i2\pi f \tilde{L}} I_0 e^{i2\pi ft} \quad (23)$$

where M_{12} is the mutual inductance between the model circuit and the receiver coil.

Finally, assume that by appropriate electronics and nulling, the metal detector measures the voltage ratio

$$\begin{aligned} \frac{v_{12}}{v_{02}} &= \frac{-M_{01} M_{12} (2\pi f)^2 I_0 e^{i2\pi ft}}{-M_{02} i2\pi f (\tilde{R} + i2\pi f \tilde{L}) I_0 e^{i2\pi ft}} \\ &= -\frac{M_{01} M_{12}}{M_{02} \tilde{L}} \frac{i(2\pi f \tilde{L}/\tilde{R})(1 - i2\pi f \tilde{L}/\tilde{R})}{1 + (2\pi f \tilde{L}/\tilde{R})^2}, \\ &= -\frac{M_{01} M_{12}}{M_{02} \tilde{L}} \frac{(2\pi f \tilde{L}/\tilde{R})^2 + i(2\pi f \tilde{L}/\tilde{R})}{1 + (2\pi f \tilde{L}/\tilde{R})^2}, \end{aligned} \quad (24)$$

which is commonly expressed as

$$\frac{v_{12}}{v_{02}} = -\frac{M_{01} M_{12}}{M_{02} \tilde{L}} \left(\frac{\alpha^2 + i\alpha}{1 + \alpha^2} \right) = K_\sigma F_\sigma(\alpha), \quad (25)$$

where $K_\sigma = M_{01} M_{12} / M_{02} \tilde{L}$ is the so-called coupling coefficient and

$$F_\sigma(\alpha) = -\left(\frac{\alpha^2 + i\alpha}{1 + \alpha^2} \right) = -\frac{\alpha^2}{1 + \alpha^2} - \frac{i\alpha}{1 + \alpha^2} \quad (26)$$

is the associated response function in terms of response parameter $\alpha = 2\pi f \tilde{L} / \tilde{R}$.

Note that while the coupling coefficient is a purely geometrical relation dependent on transmitter receiver configuration and model geometry, the complex inductive response function is obviously dependent upon frequency and the electromagnetic properties of the model circuit or equivalent soil as characterized by the response parameter (effective induction number) α . Although the negative polarity indicated in Equations (24) and (25) is more commonly incorporated in the coupling coefficient, it is instructive and perhaps more appropriate to retain it as an integral part of the response function.

Real and imaginary parts of the resulting induction response function are depicted in Figure 7a, together with corresponding amplitude and phase spectra

$$|F_\sigma| = \frac{\alpha}{(1 + \alpha^2)^{1/2}} \quad \theta_\sigma = \tan^{-1} \left(\frac{1}{\alpha} \right). \quad (27)$$

Note that for $\alpha \rightarrow 0$, the so-called resistive limit, the negative-valued quadrature component dominates as the overall response diminishes toward zero for either a static source field ($f = 0$) or a resistive ($R = \infty$ or $\sigma = 0$) ground. Equivalently, as the response amplitude trends toward zero, the secondary signal voltage (v_{12}) is phase-shifted or lagged by 90 degrees relative to the primary signal voltage (v_{02}). In contrast, as frequency increases and/or the anomalous ground becomes more conductive, both in-phase (real) and quadrature (imaginary) components increase, initially the quadrature more rapidly and, subsequently, the in-phase until the two contributions are equivalent ($\text{Re}\{F_\sigma\} = \text{Im}\{F_\sigma\} = -0.5$) for $\alpha = 1$. Notice that this condition is associated with a relative phase-shift of 45 (-135) degrees between primary and secondary coil voltages, or what is effectively the transition between resistive and inductive response regimes.

With further increase in frequency or conductivity $\alpha \rightarrow \infty$, the response function becomes purely real-valued, reaching an absolute maximum ($|F_\sigma| = 1.0$) referred to as the inductive limit. The secondary signal voltage (v_{12}) becomes saturated and 180 degrees out of phase ($\text{Re}\{F_\sigma\} = -1.0$) with the primary (v_{02}). Practically speaking, in the inductive limit, eddy currents are restricted to the surface of the conductive medium (soil) and the associated secondary field effectively cancels the primary field within the conductor. In contrast, for a resistive ground and/or at lower frequencies, the eddy currents penetrate more deeply.

Now, beyond the standard treatment of an anomalously conductive ground, we extend the model to consider the added influence of anomalous magnetic permeability. Again, neglecting any interaction between the shorted turn and permeable core, the core is magnetized parallel to the primary magnetic field, yielding a net magnetic moment that reinforces the primary field at the receiver coil ⁴. In particular, assuming real-valued (lossless) permeability, magnetization of the permeable core produces

⁴ Note that within a magnetically polarizable medium (e.g. a magnetically susceptible soil), the

a secondary magnetic field that is purely in-phase with the primary field and independent of frequency. Thus, adding a corresponding real-valued magnetization component $F_\mu = K_\mu(\mu_r - 1)$ to the inductive response F_σ in Equation (9), we obtain the net non-interacting response function

$$F_{\sigma+\mu} = F_\sigma + F_\mu = \left[K_\mu(\mu_r - 1) - \frac{\alpha^2}{1 + \alpha^2} \right] + \frac{i\alpha}{1 + \alpha^2}, \quad (28)$$

where K_μ is a geometry-dependent factor that appropriately scales the inductive coupling coefficient K_σ and $\mu_r = \mu/\mu_0$ denotes the relative magnetic permeability⁵. Corresponding response parameters are displayed in Figure 7b, assuming an arbitrary relative permeability such that $F_\mu = 0.333\text{Re}\{F_\sigma(\infty)\}$.

In contrast with the purely inductive case in Figure 7a, the net low-frequency or resistive ($\alpha \rightarrow 0$) response $|F_{\sigma+\mu}|$ is now dominated by the magnetization response, with zero phase-shift between (v_{12}) and (v_{02}) . Again, with increasing frequency or conductivity, the absolute response amplitude increases, albeit more gradually, and there is a polarity reversal of the in-phase component consistent with transition from magnetization to induction dominated response. Equivalently, the phase-shift between secondary and primary signal voltages transitions from zero to -180 degrees, approaching the inductive limit for $\alpha \rightarrow \infty$.

vector magnetization \mathbf{M} is defined as the difference between the observed magnetic flux density $\mathbf{B} = \mu\mathbf{H}$ and the corresponding free-space magnetic flux density $\mathbf{B}_0 = \mu_0\mathbf{H}$, normalized by free-space permeability μ_0 . Thus we have

$$\begin{aligned} \mathbf{M} &= \frac{\mathbf{B} - \mu_0\mathbf{H}}{\mu_0} = \frac{\mu_r\mu_0\mathbf{H} - \mu_0\mathbf{H}}{\mu_0} \\ &= (\mu_r - 1)\mathbf{H} \\ &= \chi_v\mathbf{H} \end{aligned}$$

where $\mu_r = \mu/\mu_0$ is the relative permeability and $\chi_v = (\mu_r - 1)$ is the related volume magnetic susceptibility. Now for a volume limited distribution of magnetized material, the net vector magnetic moment \mathcal{M} is just the integrated magnetization

$$\mathcal{M} = \int_V \mathbf{M} dv.$$

Conversely, the magnetization is simply the magnetic moment per unit volume. Of course, at sufficient distance from the magnetized source material, the resulting field is indistinguishable from that of a infinitesimal magnetic dipole with equivalent moment and direction, or for that matter an equivalent current loop like that of our model.

⁵ Note that a constant magnetization response F_μ implies that related secondary signal voltage generated in the receiver coil is directly proportional to frequency as for the primary signal.

The non-interacting model, however, predicts this induction limited response remains diminished by the offsetting influence of frequency-independent magnetization. In fact, however, on accounting for interaction between core and coil, the inductive response is also enhanced by magnetization within the core and vice versa. Related effects are modelled in Figure 8a, where polarity of the response function is reversed to be consistent with common convention. Note that while transition to the inductive limit is substantially more gradual, the limiting high-frequency response ($\alpha \rightarrow \infty$) for an anomalous conductive-magnetic ground remains purely inductive, consistent with a -180 degree phase-shift. In effect, the secondary magnetic field associated with saturation eddy currents virtually cancels the primary field within the medium (permeable core) and, consequently, nullifies related influence of magnetization. In practice, magnetization associated with increased permeability enhances both primary and induced fields with equivalent net effect. Moreover, because effective model inductance \tilde{L} increases with core permeability, the entire response is correspondingly displaced as a function of induction number α . In particular, transition from resistive to inductive response regimes occurs for an induction number $\alpha > 1$, increasing with increasing permeability (susceptibility).

Comparison with Figure 8b indicates that the modelled response is consistent with that expected for a horizontal coplanar coil system over a homogeneous conductive-permeable soil (Huang and Won, 2000)⁶. In particular, response curves are displayed in Figure 8b for an effective induction number $\sigma\mu f$. Depicted response characteristics assume a coil separation $s = 1.66$ m and are similar for more closely spaced or coaxial coils. In general, as coil separation decreases, peak quadrature response and related in-phase inflection occur for a lower effective induction number. Corresponding magnitude and phase spectra are depicted in Figure 8.5.

In effect, the response parameter α (modelled as $\alpha = 2\pi f\tilde{L}/\tilde{R}$) is equivalent to the attenuation rate as defined in Chapter 2.0. Although we have referred to α rather loosely as the “induction number”, the actual induction number is more generally

$$\eta = \alpha s = \frac{s}{d_s} = (\pi f \mu \sigma)^{1/2} s, \quad (29)$$

where, $d_s = 1/\alpha = (\pi f \mu \sigma)^{-1/2}$ is the corresponding skin depth as introduced in Section 2.0 and s represents an appropriate dimensional parameter. For the case of a bistatic dual-coil system considered in Figure 8/8.5, s denotes the separation between coplanar coil axes. Assuming $s = 1.0$ to facilitate scaling, Figure 9 provides some indication of the connection between soil electromagnetic parameters and induction number as related to associated FDEM response characteristics modelled in Figure

⁶ It is emphasized that the range of modelled permeabilities in Figures 7 and 8/8.5 greatly exceeds that of natural soils and other geological materials. Model permeability is exaggerated for purpose of illustration.

8. In particular, Figure 9 charts electrical conductivity σ as a function of magnetic susceptibility $\chi = (\mu/\mu_0 - 1)$ for $\eta = \alpha = 1.0, 0.1$ and 0.01 and with operating frequency ($f < 100$ kHz) as a parameter.

First, it is generally observed that the induction number is comparatively insensitive to magnetic susceptibility within the nominal range of electromagnetic parameters for natural soils. In fact, this is to be expected given the equal weight of magnetic permeability and electrical conductivity and the relatively minimal deviation of permeability $\mu = \mu_0(1 + \chi)$ on the scale of natural soil susceptibility variation. However, this is not to say that instrument response is insensitive to magnetic susceptibility fluctuation. In fact, as suggested by Figure 8 and for soils possessing a significant magnetic susceptibility, related magnetization yields the bulk of measured signal for resistive soils and at lower frequencies, where $\alpha \ll 1$. Although the induction number depends primarily on the frequency-conductivity $f\sigma$ product, it is clear that for typical operating frequencies the vast majority of soils satisfy $\alpha < 1$. In fact, the chart for $\alpha = 1$ indicates that the entire range of nominal soil electromagnetic properties satisfies the condition $\alpha < 1.0$ for frequencies less than $f=100$ kHz. Similarly, while $\alpha=0.1$ and 0.01 are clearly more limiting conditions, even soils with significant electrical conductivity approaching 1.0 mS/m satisfy the condition $\alpha < 0.01$ for an operating frequency of $f=30$ kHz.

Of course, the actual induction number η , related response characteristics and associated soil influence for a given FDEM device are dependent on the specific coil configuration and operating frequency. Consequently, beyond foregoing general development, it is useful to consider specific theory-predicted results for a horizontal coaxial coil arrangement as representative of common metal detectors.

In general, for source current I impressed on a horizontal, single-turn circular coil of radius a positioned height $z = -h$ above a homogeneous, linear and isotropic soil, the resulting electromagnetic field comprises the following orthogonal electric and magnetic field components as developed in Section 4 (Equations 4.86-4.88) of Ward and Hohmann (1987)

$$E_\phi = -i\pi f\mu_0 a I \int_0^\infty \left[e^{-u_0(z+h)} + r_{TE} e^{u_0(z-h)} \right] \frac{\lambda}{u_0} J_1(\lambda a) J_1(\lambda \rho) d\lambda, \quad (30)$$

$$H_\rho = \frac{aI}{2} \int_0^\infty \left[e^{-u_0(z+h)} + r_{TE} e^{u_0(z-h)} \right] \lambda J_1(\lambda a) J_1(\lambda \rho) d\lambda \quad (31)$$

and

$$H_z = \frac{aI}{2} \int_0^\infty \left[e^{-u_0(z+h)} + r_{TE} e^{u_0(z-h)} \right] \frac{\lambda^2}{u_0} J_1(\lambda a) J_0(\lambda \rho) d\lambda. \quad (32)$$

Here, E_ϕ , H_ρ and H_z denote the azimuthal electric field, the radial magnetic field and the vertical magnetic field, respectively. $J_0()$ and $J_1()$ denote Bessel functions

of first kind and integer orders 0 and 1, respectively, and λ is the Hankel transform variable. The consistent portion of the integrand in brackets comprises an initial term associated with the primary field and a second term due to the soil-related field, where

$$r_{\text{TE}} = \frac{\mu_1 u_0 - \mu_0 u_1}{\mu_1 u_0 + \mu_0 u_1} \quad (33)$$

denotes the effective reflection coefficient, $u_k^2 = \lambda^2 - \gamma_k^2$, and

$$\gamma_k = 2\pi f \left[\mu_k \epsilon_k \left(i \frac{\sigma_k}{2\pi f \epsilon_k} - 1 \right) \right]^{1/2} \approx [-i2\pi f \mu_k \sigma_k]^{1/2} \quad (34)$$

is the quasi-static (see Section 2.0) propagation constant for air ($k = 0$) and for soil ($k = 1$), respectively.⁷ For air, we have $\sigma_0 = 0$, $\mu_0 = 4\pi \times 10^{-7}$ H/m and, thus $u_0 = \lambda$, yielding

$$r_{\text{TE}} = \frac{\mu_1 \lambda - \mu_0 u_1}{\mu_1 \lambda + \mu_0 u_1} \quad (35)$$

For the specific case of a coincident horizontal (coaxial) coil system, Equation (32) yields the following relation for the ratio of secondary H_s to primary H_p magnetic fields threading the receiver coil (Won and Huang, 2004).⁸

$$\frac{H_s}{H_p} = a^2 \int_0^\infty r_{\text{TE}} e^{-2\lambda h} \lambda J_1(\lambda a) d\lambda. \quad (37)$$

Associated in-phase and quadrature response characteristics are displayed as functions of induction number $\eta = (\pi f \mu \sigma)^{1/2} a$ in Figure 10a. Note that in this case, the dimensional parameter $s = a$ is the coil radius.

Equivalent results are described by Bruschini (2004) for the corresponding secondary signal voltage

$$v(f) = -i2\pi f \mu_0 \pi a^2 I \int_0^\infty r_{\text{TE}} e^{-2\lambda h} [J_1(\lambda a)]^2 d\lambda, \quad (38)$$

that follows from Equation 30 or 32 with $z = -h$ and $\rho = a$.⁹ Related (absolute) response curves are displayed in the right-hand panel of Figure 10 for both non-magnetic

⁷ Note the corresponding induction number η is the product of the real part of the quasi-static propagation constant $Re\{\gamma\} = \alpha = 1/d_s = (\pi f \mu \sigma)^{1/2}$ and the dimensional parameter s .

⁸ The corresponding field ratio for horizontal coplanar coils (Figure 8b) is

$$\frac{H_s}{H_p} = s^3 \int_0^\infty r_{\text{TE}} e^{-2\lambda h} \lambda^2 J_0(\lambda a) d\lambda \quad (37.5).$$

⁹ See Section 3.3.1 for details. In general, integral expressions (37) and (38) are evaluated numerically. See for example Anderson (1979, 1982); Johansen and Sorensen (1979).

and magnetic soils with finite electrical conductivity. Note that the corresponding response parameter $\alpha = 2\pi f\mu\sigma a^2$ is related to the induction number η by the relation $\alpha = 2\eta^2$.

In general, complex response characteristics in Figure 10 are consistent with those predicted by the heuristic model (Figures 7-8) and illustrate the very significant influence of soil magnetic susceptibility. More specifically, results indicate that the resistive limit is extended to higher induction numbers with increasing magnetic susceptibility and that, within the resistive limit ¹⁰, the in-phase component of the response is predominant and proportional to magnetic susceptibility.

In particular, for single-turn coincident coils located height h above a non-conducting and non-dispersive magnetic soil, Equation 38 yields (Das, 2004; 2006) the corresponding secondary signal voltage

$$v_{12} = -i2\pi f\mu_0\pi a^2 I \left[\frac{\chi}{2 + \chi} \right] m(h) \approx -i\pi f\mu_0\pi a^2 I \chi m(h), \quad (39)$$

where $\chi = (\mu_r - 1)$ denotes the volume magnetic susceptibility and $m(h)$ is a stand-off dependent coupling factor analogous to K_μ in foregoing development (see details in Section 3.3.3). For natural soils ($\chi \ll 2$), we obtain the indicated approximation with v_{12} proportional to χ and in phase with the corresponding primary signal voltage $v_{02} = -i2\pi f\mu_0\pi a^2 I \int_0^\infty [J_1(\lambda a)]^2 d\lambda$.

As regards practical constraints on the resistive limit, the lower left diagram in Figure 10 (Won and Huang, 2004) displays the accuracy of a resistive-limit assumption as a function of soil magnetic susceptibility χ and frequency-conductivity product $f\sigma$. It is clear that even for modest magnetic susceptibility $\chi = 1.0 \times 10^{-4}$ SI, related error is only marginally in excess of 30% for $f\sigma=1000$ (for example, $\sigma=100$ mS/m for $f=10$ kHz).

Response characteristics are also substantially dependent on sensor height or stand-off above grade as illustrated in Figure 11 from Bruschini (2004). In particular, it is observed that the resistive limit for given magnetic permeability is effectively shifted to a significantly lower response parameter value as normalized sensor height $h_N = h/a$ increases. In addition, it is noted that (within the resistive limit) the absolute value of the in-phase response decreases by more than two orders of magnitude on increasing the sensor roughly from surface ($h_N = 0.01$ as per Figure 10) to height above grade equal to coil radius ($h_N = 1.0$). In comparison, corresponding reduction in quadrature-phase response is relatively limited. Relative influence reverses, however, as the response parameter approaches the inductive limit.

¹⁰ As a common rule of thumb, the resistive limit for a non-magnetic ground is $\eta \leq 0.02$ (e.g. Frischknecht, 1987).

A final consideration for frequency domain devices is the influence of dispersive soil electromagnetic properties. In theory, associated effect could be investigated by appropriate generalization of the foregoing heuristic model (i.e. substituting a complex coil impedance $\tilde{R} - i/2\pi f\tilde{C}$ for \tilde{R} and allowing a complex core permeability $\mu_r = \mu'_r - i\mu''_r$). However, to first order, related quadrature influence is predictable in a qualitative sense. Compared with an equivalent non-dispersive soil, electrical polarization produces a relative increase in the in-phase response (for common $f\sigma$) while magnetic viscosity yields an effective increase in the quadrature response.

For example, generalizing the previous result in Equation (39) for a non-conductive soil with frequency dependent complex magnetic susceptibility $\chi(f) = \chi' - i\chi''$, Equation (38) yields a complex-valued secondary voltage $v_{12}(t) = v'_{12} + iv''_{12}$ with in-phase and quadrature signal components

$$v'_{12}(f) = -i2\pi f\mu_0\pi a^2 I \left[\frac{-i2\chi''}{(\chi' + 2)^2 + \chi''^2} \right] m(h) \approx -\pi f\mu_0\pi a^2 I \chi'' m(h) \quad (40)$$

and

$$v''_{12}(f) = -i2\pi f\mu_0\pi a^2 I \left[\frac{\chi'^2 + 2\chi' + \chi''^2}{(\chi' + 2)^2 + \chi''^2} \right] m(h) \approx -i\pi f\mu_0\pi a^2 I \chi' m(h), \quad (41)$$

respectively (see Das 2004; 2006). Note, as indicated, the real part of the secondary signal voltage v'_{12} is approximately proportional to the quadrature susceptibility χ'' and lags the primary signal voltage v_{02} by 90 degrees.

In general, quadrature parameters are small compared with corresponding real parts and, consequently, soil electromagnetic dispersion is anticipated to have relatively limited influence on frequency domain (FDEM) devices at a given operating frequency. For multi-frequency sensors and/or in connection with compensation adjustments, however, influence can be significant. More significant, however, is the pivotal influence of soil electromagnetic dispersion and related viscosity on the response and performance of time domain metal detectors. Related response characteristics and implications are discussed in the following Section and in greater detail in Section 3.3.

3.2 Time Domain (TDEM) Response:

As demonstrated by Grant and West (1965), the same heuristic model employed to investigate the FDEM response can be extended to provide useful insight on the nature of the time-domain response and related influence of soil electromagnetic properties. Neglecting the charging portion of the applied transmit current waveform, we assume a step termination of constant current and take the termination as zero time reference. Thus, we write the drive current waveform as

$$I = I_0 [1 - u(t)], \quad (42)$$

where

$$u(t) = \begin{cases} 0; & t < 0 \\ t/\Delta t; & 0 \geq t < \Delta t \\ 1; & t \geq \Delta t \end{cases} \quad (43)$$

defines a step function $u(t)$ with finite rise-time Δt . Again, we begin by ignoring the influence of the permeable core. As per Equation (21), the induced voltage in the model circuit is given by

$$v_{01} = -M_{01} \frac{dI}{dt} = -M_{01} I_0 \frac{d}{dt}[1 - u(t)] = M_{01} I_0 \frac{du(t)}{dt}. \quad (44)$$

Now, as per Kirchoff's circuit conventions, we must have that the induced emf is balanced by related potential drops across effective resistance \tilde{R} and inductance \tilde{L} , yielding

$$M_{01} I_0 \frac{du(t)}{dt} = \tilde{R} I_1 + \tilde{L} \frac{dI_1}{dt}, \quad (45)$$

where $I_1 = I_E$ denotes the model eddy current induced in the shorted turn (compare with the equivalent frequency domain expression in Equation (22)). Of course, prior to constant current termination $dI/dt = v_{01} = I_1 = 0$. Subsequently, the source current is terminated and falls to zero as $I_0(t/\Delta t)$. Thus, during the finite termination interval Δt , we have $du(t)/dt = 1/\Delta t$ and the previous equation yields

$$\frac{M_{01} I_0}{\Delta t} = \tilde{R} I_1 + \tilde{L} \frac{dI_1}{dt} \quad (46)$$

or, equivalently the differential equation

$$(\tilde{L}/\tilde{R}) \frac{dI_1}{dt} + I_1 = \frac{M_{01} I_0}{\tilde{R} \Delta t}, \quad (47)$$

yielding solution

$$\frac{M_{01} I_0}{\tilde{R} \Delta t} \left[1 - e^{-(\tilde{R}/\tilde{L})t} \right] \quad (48)$$

under condition $I_1 = 0$ for $t = 0$. However, given $t \ll \tilde{L}/\tilde{R}$ for $t < \Delta t$ the approximation $e^x \approx 1 + x$ leads to the following linear relation for initial ‘‘eddy current’’ build-up in the model circuit

$$I_1 = \frac{M_{01} I_0}{\tilde{L}} \frac{t}{\Delta t}. \quad (49)$$

Subsequently, for $t > \Delta t$, when there is no longer current flowing in the transmit coil, we are left with the homogeneous (no source term) equivalent of Equation (47)

$$(\tilde{L}/\tilde{R}) \frac{dI_1}{dt} + I_1 = 0, \quad (50)$$

with purely exponential solution

$$I_1 = \frac{M_{01} I_0}{\tilde{L}} e^{-(\tilde{R}/\tilde{L})t}, \quad (51)$$

where initial amplitude is determined by the condition $I_1 = M_{01} I_0 / \tilde{L}$, for $t = \Delta t$ from Equation (49). Thus, we find that upon terminating a constant source current in the transmit coil, there is initially a linear build-up of the “eddy current” within the model circuit that parallels the linear decay of the source current. Subsequently, this eddy current decays exponentially with time constant $\tau = \tilde{L}/\tilde{R}$ depending upon the equivalent lumped circuit parameters of the model. Finally, of course, the induced time-varying current within the model circuit generates a secondary magnetic field that, in turn, produces a secondary signal voltage (from Equations 49 and 51)

$$v_{12} = -M_{12} \frac{dI_1}{dt} = -\frac{M_{01} M_{12}}{\tilde{L}} I_0 \left[\delta(t) - (\tilde{R}/\tilde{L}) e^{-(\tilde{R}/\tilde{L})t} \right], \quad (52)$$

where

$$\delta(t) = \begin{cases} 0; & t < 0 \\ 1/\Delta t; & 0 \leq t \leq \Delta t \\ 0; & t > \Delta t \end{cases} \quad (53)$$

represents an impulse having amplitude $1/\Delta t$ and duration Δt . The corresponding primary signal voltage is

$$v_{02} = -M_{02} \frac{d}{dt} I_0 [1 - u(t)] = M_{02} I_0 \delta(t). \quad (54)$$

The predicted time-dependent response is illustrated in Figure 12a. It is useful to consider the connection between these results and corresponding frequency domain response spectra displayed in Figure 7a. In particular, it is noted that the time-domain decay constant $\tau = \tilde{L}/\tilde{R}$ is closely related to the transition between resistive and inductive response regimes. Specifically, we have $\tau = 1/2\pi f$ for $\alpha = 1$. Comparing the secondary time-domain signal voltage $v_{12}(t)$ in Equation (52) with the equivalent frequency domain signal $v_{12}(f)$ given by Equation (23), it is emphasized that the two signals do not constitute a time-frequency pair. Rather, $v_{12}(f)$ is the Fourier transform of the impulse response of the soil model, while $v_{12}(t)$ is the corresponding step response (neglecting finite rise time Δt). Consequently, ignoring polarity, $v_{12}(f)$ is equivalently the Fourier transform of the time derivative of $v_{12}(t)$. That is

$$v_{12}(f) = \int_{-\infty}^{\infty} \frac{d}{dt} [v_{12}(t)] e^{-i2\pi f t} dt, \quad (55)$$

or, via the derivative property of the Fourier transform,

$$\begin{aligned} v_{12}(f) &= i2\pi f \int_{-\infty}^{\infty} v_{12}(t) e^{-i2\pi f t} dt, \\ &= i2\pi f \mathcal{F}\{v_{12}(t)\} \end{aligned} \quad (56)$$

where $\mathcal{F}\{g(t)\}$ denotes the forward Fourier transform of an arbitrary time-dependent functional argument $g(t)$. Inversely, it follows that the time-domain step response is obtained via the inverse transform

$$\begin{aligned} v_{12}(t) &= \int_{-\infty}^{\infty} \frac{v_{12}(f)}{i2\pi f} e^{i2\pi ft} df \\ &= \mathcal{F}^{-1} \left\{ \frac{v_{12}(f)}{i2\pi f} \right\}, \end{aligned} \quad (57)$$

where $\mathcal{F}^{-1}\{g(f)\}$ denotes the inverse Fourier transform of an arbitrary frequency-dependent functional argument $g(f)$.

Now, as for previous analysis of the frequency domain response, let's consider the qualitative influence of magnetization within the permeable core. Again, we ignore interaction between the core and the shorted turn. Prior to terminating the source current ($t < 0$), there is constant magnetization $\mathbf{M} = \chi_v \mathbf{H}_0$ of the core proportional to the primary field \mathbf{H}_0 . Moreover, it follows that related magnetic flux threading the receiver coil is also in static state and, consequently, produces no related signal voltage in the receiver coil. However, on termination of source current at $t = 0$, this flux decreases as inductive flux associated with increasing "eddy current" in the model coil increases for $0 \leq t \leq \Delta t$. In general, these fluxes are 180 degrees out of phase, so that the time rate of change of magnetization flux supports that due to increasing inductive flux. The result, as suggested in Figure 12b, is that the initial impulsive signal voltage induced in the receiver coil during finite termination time Δt is enhanced by declining magnetization in the permeable core. Thus, for $0 \geq t \leq \Delta t$, the total signal voltage is

$$v_{12} = - \left[\frac{M_{01}M_{12}}{\tilde{L}} I_0 + \hat{K}_\mu (\mu_r - 1) \right] \delta(t), \quad (58)$$

where \hat{K}_μ denotes an appropriate coupling coefficient and $\delta(t)$ is given by Equation (53). Assuming real-valued (nondispersive) permeability, however, magnetization is zero for $t > \Delta t$ with no further influence on the time domain response that is subsequently due only to decaying "eddy-current" within the model circuit.

Although the foregoing conclusion is consistent with the non-interacting frequency-domain response depicted in Figure 7b, it is evident that on allowing interaction between coil and core, magnetization within the core will continue to exert a second order influence as long as decaying eddy current yields a finite magnetic field within the core. Consequently, as per prior frequency-domain analysis, related influence is largely restricted to the induction-dominated response regime for $\alpha > 1.0$. In view of relations described by Equations (55-57), the relatively gradual decay of eddy currents and limited deviation from $\mu_r = 1.0$, however, foregoing analysis suggests that second-order effects within a conductive-permeable soil are relatively minor. In practice, for

common soils, the result is equivalent to a marginal increase in effective conductivity (see Section 3.3.5).

Finally, it is emphasized that foregoing analysis of the TDEM response has been restricted to constant, real-valued soil electromagnetic parameters. However, as discussed in the previous Section, soil properties are generally frequency-dependent, dispersive quantities. In particular, for soils with significant magnetic viscosity (quadrature permeability), magnetization does not fall to zero in termination time Δt as indicated in Figure 12b but, rather, decays more gradually as for the eddy current. Consequently, soils having significant quadrature permeability can have a substantial and, in fact, dominant influence on the decay rate of the time-domain response.

Recent research and investigations (Guelle, 2002; Pasion, et al., 2002, Billings, et al., 2003a, 2003b; Borry, et al, 2003; Das 2004, 2006) have confirmed the significance of soil magnetic viscosity and identified related influence as the primary factor restricting the performance of time-domain PI metal detectors. For example, Das (2006) demonstrated that even for an extreme soil electrical conductivity of $\sigma = 5.0$ S/m, a viscous magnetic soil with only moderate static susceptibility $\chi = 0.0005$ SI yields a substantially greater response at times exceeding $10 \mu s$ as illustrated in Figure 13. Thus, in light of growing consensus on the singular significance of magnetic viscosity, the following section is devoted specifically to characterizing the nature of the viscous magnetic response and, concurrently, to investigating the analogous and potentially significant influence of electrical conductivity dispersion on TDEM sensors.

3.3 Dispersive Soil EM Properties and TDEM Response:

3.3.1 General Formulation:

We begin by returning to Equations (30-32) for the electromagnetic field due to source current I impressed on a horizontal single-turn circular coil of radius a at height $z = -h$ above a homogeneous, linear and isotropic soil. The frequency-dependent voltage induced in a coaxial, coplanar single-turn receiver coil of radius b follows as the integral of the azimuthal electric field (Equation 30) around the circular coil

$$v(f) = \oint \mathbf{E} \cdot d\mathbf{l} = b \int_0^{2\pi} E_\phi d\phi \quad (59)$$

or, equivalently via Faraday's law, as the time rate of change of integrated magnetic flux density (Equation 32) through the coil

$$v(f) = - \int_S \frac{\partial \mathbf{B}}{\partial t} \cdot d\mathbf{s} = -i2\pi f \mu_0 \int_0^b \int_0^{2\pi} H_z \rho d\phi d\rho. \quad (60)$$

The result is

$$v(f) = -i2\pi f \mu_0 \pi a b I \int_0^\infty \left[e^{-u_0(z+h)} + r_{\text{TE}} e^{u_0(z-h)} \right] J_1(\lambda a) J_1(\lambda b) d\lambda \quad (61)$$

and, on setting $b = a$, $z = h = 0$, we have for coincident, surface deployed coils

$$v(f) = -i2\pi f \mu_0 \pi a^2 I \int_0^\infty [1 + r_{\text{TE}}] [J_1(\lambda a)]^2 d\lambda, \quad (62)$$

where, again,

$$r_{\text{TE}} = \frac{\mu_1 \lambda - \mu_0 u_1}{\mu_1 \lambda + \mu_0 u_1} \quad (35)$$

denotes the effective reflection coefficient at the boundary between air and soil.

Finally, the corresponding time-domain step response is obtained by dividing the previous equation by $i2\pi f$ (equivalent to integrating the associated impulse response) and evaluating the Fourier transform with respect to frequency

$$v(t) = -\mu_0 \pi a^2 I \int_0^\infty \int_{-\infty}^\infty [1 + r_{\text{TE}}] e^{i2\pi f t} df [J_1(\lambda a)]^2 d\lambda \quad (63)$$

or, equivalently, by Laplace transformation with substitution $s = i2\pi f$.

In what follows, we review a range of solutions for specified soil property models, and provide a comparative assessment of related influence on the TDEM response for a small-scale, horizontal coincident-coil configuration at the surface of a uniform half-space.

3.3.2 Non-Magnetic, Non-Dispersive Conductive Soil:

For reference, we begin with a uniform non-magnetic, non-dispersive conductive soil. Assuming $\sigma_1 = \sigma_{dc}$ and $\mu_1 = \mu_0$, we have

$$1 + r_{\text{TE}} = 1 + \frac{\lambda - u_1}{\lambda + u_1} = \frac{2\lambda}{\lambda + u_1} \quad (64)$$

and, consequently, from Equation (63)

$$v(t) = -\mu_0 \pi a^2 I \int_0^\infty \int_{-\infty}^\infty \frac{2\lambda}{\lambda + u_1} e^{i2\pi f t} df [J_1(\lambda a)]^2 d\lambda \quad (65)$$

with $u_1 = [\lambda^2 + i2\pi f \mu_0 \sigma_{dc}]$. The problem was initially treated by Lee and Lewis (1973) and, subsequently, by Raiche and Spies (1981). On evaluating the Laplace transform of $1/(\lambda + u_1)$ and redefining the integration variable $\lambda' = a\lambda$, the resulting solution is

$$v(t) = v_1(t) = \frac{-2\mu_0 \sqrt{\pi} a I}{t} S(\tau), \quad (66)$$

where

$$S(\tau) = \int_0^\infty \left[e^{-\tau\lambda'^2} - \sqrt{\pi\tau} \lambda' \operatorname{erfc}(\sqrt{\tau} \lambda') \right] \sqrt{\tau} \lambda' [J_1(\lambda')]^2 d\lambda' \quad (67)$$

is an integral function of normalized time $\tau = t/\sigma\mu_0 a^2$, with $\operatorname{erfc}()$ denoting the complementary error function. With substitution $r = \tau\lambda'^2$, $S(\tau)$ is readily evaluated numerically using a Gauss-Laguerre quadrature rule. The result is depicted in Figure 14. It is observed that for $\tau < 0.005$, $S(\tau)$ becomes constant leaving $v_1(t) \propto t^{-1}$ and independent of conductivity. In particular, the early-time asymptote is $v(t) = \mu_0 a I / 2t$ ($\lim_{\tau \rightarrow 0} S(\tau) = 1/4\sqrt{\pi}$).

More significantly, for $\tau > 10$, $S(\tau) \propto t^{-3/2}$, yielding $v(t) \propto t^{-5/2}$. The computed response is depicted in Figure 15 for three values of σ_{dc} . Absolute signal voltage is normalized for arbitrary source current I (and by displaying the absolute value of the response, we effectively chart the response for the typical case of a step-off source current). As predicted, transition from t^{-1} to $t^{-5/2}$ dependence occurs at later time with increasing soil conductivity. Note for $\sigma_{dc} = 0.1$ mS/m asymptotic early time t^{-1} dependence is particularly evident with transition to $t^{-5/2}$ dependence at approximately $t = 10^{-10} - 10^{-9}$ ns.

Employing a power series expansion for the Bessel function in Equation (67) and integrating term by term, Raiche and Spies (1981) obtained the following late-time approximation for $S(\tau)$

$$S(\tau) = \left(\frac{1}{4\tau} \right)^{3/2} \sum_{k=0}^{\infty} \frac{(-1)^k}{k!} \frac{(2k+2)!}{(k+1)!(k+2)!(2k+5)} \left(\frac{1}{4\tau} \right)^k. \quad (68)$$

Retaining only the initial term for $k = 0$, one obtains the common late-time ($\tau > 10$) approximation

$$v(t) \approx v_2(t) = -\frac{\mu_0 \sqrt{\pi} a I}{20 t} \left(\frac{\sigma \mu_0 a^2}{t} \right)^{3/2} = -\frac{\sqrt{\pi} \mu_0^{5/2} \sigma^{3/2} a^4 I}{20} t^{-5/2}. \quad (69)$$

The foregoing approximation $v_2(t)$ is compared with the previous result $v_1(t)$ in Figure 16 for $t \geq 10^{-10}$ s. Clearly, for the majority of metal detectors with measurement windows in the range of ten to several hundred microseconds, this late-time approximation is perfectly adequate.

3.3.3 Non-Conductive, Non-Dispersive Magnetic Soil:

For a non-conductive soil $\sigma_1 = 0$, we have $\gamma_1 = 0$, $u_1 = \lambda$ and, consequently,

$$1 + r_{TE} = 1 + \frac{\mu_0 \lambda (\mu_r - 1)}{\mu_0 \lambda (\mu_r + 1)} = 1 + \frac{\chi}{\chi + 2} \quad (70)$$

where, $\mu_r = \mu_1/\mu_0 = \mu_{dc}/\mu_0$ represents the relative magnetic permeability and $\chi = \mu_r - 1$ is the volume-specific magnetic susceptibility. In particular, for a non-dispersive magnetic soil, $\chi = \mu_{dc}/\mu_0 - 1 = \chi_{dc}$ and Equation (63) yields

$$v(t) = -\mu_0\pi a^2 I \left(1 + \frac{\chi_{dc}}{\chi_{dc} + 2}\right) \delta(t) \int_0^\infty [J_1(\lambda a)]^2 d\lambda, \quad (71)$$

where the Dirac delta function $\delta(t)$ is defined as follows

$$\delta(t) = 0; \quad t \neq 0$$

$$\int_{-\infty}^\infty \delta(t) dt = 1.$$

As anticipated, the response for a non-conductive, non-dispersive magnetic soil is limited to an impulse at the instant of source current termination ($t=0$). There is no sustained transient response. In practice, because detection circuitry is designed to avoid the primary switching transient, no signal is registered.

Das (2004, 2006) treated the more general case of coaxial, coplanar coils at height h above the air-soil interface. In general, the stand-off dependent coupling coefficient is

$$\begin{aligned} \mathcal{M}(h) &= \int_0^\infty J_1(\lambda a) J_1(\lambda b) e^{-2\lambda h} d\lambda \\ &= \frac{2}{\pi k \sqrt{ab}} \left[\left(1 - \frac{k^2}{2}\right) K - E \right], \end{aligned} \quad (72)$$

where $k^2 = 4ab/[(a+b)^2 - 4h^2]$ and K and E represent complete elliptic integrals of the first and second kind respectively. For the specific case of surface-deployed ($h = 0$) coincident ($b = a$) coils, we have

$$\mathcal{M}(0) = \int_0^\infty [J_1(\lambda a)]^2 d\lambda = \infty. \quad (73)$$

Again, for instantaneous source current termination, the impulsive response is infinite. In practice, of course, the response is finite for finite termination time. The main finding, however, is that a non-conductive and non-dispersive magnetic soil yields no sustained transient response. The same cannot be said for a dispersive or viscous magnetic soil.

3.3.4 Non-Conductive, Dispersive Magnetic Soil:

As Das (2004) has demonstrated, a useful approximation for the response over a non-conductive, dispersive magnetic soil is obtained by generalizing the previous result for a frequency-dependent magnetic susceptibility. In particular, a well established model

for susceptibility dispersion of a viscous magnetic soil (Richter, 1937; Chikazumi, 1965; Lee, 1984) assumes a log-uniform distribution of grain-volume related relaxation constants. The corresponding magnetic susceptibility is given by

$$\chi(f) = \chi_{dc} \left[1 - \frac{1}{\ln(\tau_2/\tau_1)} \ln \left(\frac{1 + i2\pi f\tau_2}{1 + i2\pi f\tau_1} \right) \right], \quad (74)$$

where τ_1 and τ_2 denote, respectively, lower and upper band-limits on the time-constant distribution. For $\tau_1 = \tau_\chi - \Delta\tau$, $\tau_2 = \tau_\chi + \Delta\tau$ and in the limit $\Delta\tau \rightarrow 0$, Equation (74) reduces to the standard Debye dispersion relation (Debye, 1929)

$$\chi(f) = \frac{\chi_{dc}}{1 + i2\pi f\tau_\chi} \quad (75)$$

and the accompanying transient decay of magnetization is purely exponential. In general, for an arbitrary time-constant distribution $\mathcal{T}_\chi(\tau)$, with $\int_0^\infty \mathcal{T}_\chi(\tau) d\tau = 1$, we have

$$\chi(f) = \chi_{dc} \int_0^\infty \frac{\mathcal{T}_\chi(\tau)}{1 + i2\pi f\tau} d\tau, \quad (76)$$

which yields Equation (74) for the specific $1/\tau$ -scaled logarithmic time-constant distribution

$$\mathcal{T}_\chi(\tau) = \mathcal{T}_\chi(\ln \tau)/\tau = \begin{cases} 0, & \tau < \tau_1; \\ 1/\tau \ln(\tau_2/\tau_1), & \tau_1 \leq \tau \leq \tau_2; \\ 0, & \tau > \tau_2. \end{cases} \quad (77)$$

The nature of related frequency dependence is displayed in Figure 17 for $\log(\tau_2/\tau_1)$ ranging between 0.0 ($\chi_{FD} \sim 90\%$) and 100.0 ($\chi_{FD} \sim 2\%$).¹¹ In general, together with available empirical evidence (e.g. Dearing, et al., 1996), the foregoing model suggests that a relatively broad time-constant bandwidth $\log(\tau_2/\tau_1) > 10$ ($\chi_{FD} < 15 - 20\%$) is the practical reality. Indeed, it is well recognized (Nagata, 1961; Dunlop and Özdemir, 1997) that relatively minute variation in the grain volume of magnetic particles (in proximity of the stable single-domain/superparamagnetic transition) is associated with a comparatively enormous swing in related viscous time-constants.

Now, noting that for the vast majority of soils $\chi \ll 2$, we have from Equation (70)

$$1 + r_{TE} \approx 1 + \frac{\chi(f)}{2} \quad (78)$$

¹¹ A commonly referenced measure of frequency dependence of magnetic susceptibility is defined as $\chi_{FD} = [(\chi_{LF} - \chi_{HF})/\chi_{LF}] \times 100$, where χ_{LF} and χ_{HF} denote low-frequency and high-frequency susceptibility measured at frequencies f_L and f_H , spanning a decade. See Figure 17.5 for connection between χ_{FD} and common dispersion models, including log-uniform (Richter, 1937 - Equation 74), Cole-Cole (Cole and Cole, 1941) and log-normal (Wagner, 1913; Yager, 1936) models.

and, therefore,

$$v(t) \approx -\mu_0 \pi a^2 I \mathcal{M}(0) \int_{-\infty}^{\infty} \left(1 + \frac{\chi_{dc}}{2} \left[1 - \frac{1}{\ln(\tau_2/\tau_1)} \ln \left(\frac{1 + i2\pi f \tau_2}{1 + i2\pi f \tau_1} \right) \right] \right) e^{i2\pi f t} df \quad (79)$$

from Equation (63). Finally, substituting $s = i2\pi f$ and applying standard Laplace transforms yields

$$v(t) \approx -\mu_0 \pi a^2 I \mathcal{M}(0) \left[\delta(t) - \frac{\chi_{dc}}{2 \ln(\tau_2/\tau_1)} \frac{1}{t} \left(e^{-t/\tau_1} - e^{-t/\tau_2} \right) \right] \quad (80)$$

and assuming $\tau_1 \ll t \ll \tau_2$,

$$v(t) \approx -\mu_0 \pi a^2 I \mathcal{M}(0) \frac{\chi_{dc}}{2 \ln(\tau_2/\tau_1)} \frac{1}{t}. \quad (81)$$

Note that in addition to an instantaneous primary impulse associated with source current termination, magnetic viscosity leads to a sustained transient response having t^{-1} dependence. Thus, in comparison with $t^{-5/2}$ late-time dependence due to eddy currents in a non-magnetic and non-dispersive conductive soil (Equation 69), signal decay is far more gradual for a viscous magnetic soil, resulting in a substantially enhanced and potentially anomalous response.

Although $\mathcal{M}(0) = \infty$ for coincident coils, a finite approximation is obtained for $b \approx a$. In particular, Das (2006) compared the late-time response predicted by Equation (81) with that for a purely conductive soil as per Equation (69). As previously noted, it was observed that even for an extreme soil conductivity, a viscous magnetic soil with only moderate static susceptibility yields a substantially greater response over the typical measurement time range. We shall return to the case of a viscous magnetic soil but, first, we consider the more general case of a magnetic and conductive soil.

3.3.5 Non-Dispersive Conductive-Magnetic Soil:

Lee (1984) treated the common case of a soil having both finite electrical conductivity and magnetic susceptibility. Beginning with Equation (30) and considering a single-turn coil of finite cross-sectional radius ϱ , a corresponding field relation was obtained for step source current with

$$1 + r_{TE} = \frac{2\mu_1 \lambda}{\mu_1 \lambda + \mu_0 u_1}. \quad (82)$$

The corresponding time-domain response is

$$v(t) = -2\mu_0 \pi a^2 I \int_0^{\infty} \int_A \int_{-\infty}^{\infty} \frac{2\mu_1 \lambda}{\mu_1 \lambda + \mu_0 u_1} \frac{e^{i2\pi f t}}{\pi \varrho^2} df [J_1(\lambda a)]^2 dA d\lambda, \quad (83)$$

where A represents the cross-sectional area of a coincident receiver loop (conductor). Assuming a non-dispersive soil with $\mu_1 = 1 + \chi_{dc}$, the integral with respect to f is evaluated by appropriate contour integration and the integral over the cross-section of the coil is approximated by $\pi \rho^2$. Finally, the integral with respect to λ is evaluated by expanding the Bessel functions as a power series and integrating term by term. For small χ_{dc} Lee obtained the following late-time ($\tau = t/\sigma\mu_0 a^2 \gg 1$) response by Taylor series approximation about $\chi_{dc} = 0$ (see also Ignatik, et al., 1985)

$$v(t) = v_3(t) \approx -\frac{\mu_0 \sqrt{\pi} a I}{20 t} \left(\frac{\sigma \mu_0 a^2}{t} \right)^{3/2} - \frac{19 \mu_0 \chi_{dc} \sqrt{\pi} a I}{280 t} \left(\frac{\sigma \mu_0 a^2}{t} \right)^{3/2}. \quad (84)$$

Comparing this result with Equation (69), it is observed that the first term is identical to the late-time response for a non-magnetic soil. Moreover, the second term associated with frequency-independent susceptibility χ_{dc} is characterized by an equivalent $t^{-5/2}$ time dependence. Thus, as Lee suggested, the response can be rewritten as

$$v(t) \approx -\frac{\mu_0 \sqrt{\pi} a I}{20 t} \left(\frac{\sigma_a \mu_0 a^2}{t} \right)^{3/2} = -\frac{\sqrt{\pi} \mu_0^{5/2} \sigma_a^{3/2} a^4 I}{20} t^{-5/2}, \quad (85)$$

where

$$\sigma_a = \sigma \left(1 + \frac{19 \chi_{dc}}{14} \right)^{2/3}. \quad (86)$$

denotes a correspondingly enhanced apparent conductivity. In effect, the influence of non-dispersive susceptibility on the late-time response is indistinguishable from a marginal increase in electrical conductivity. Induced magnetization enhances the decaying inductive field by a factor $\mu_r = \mu_1/\mu_0 = 1 + \chi_{dc}$. As indicated by Equation (86), however, the effect is minor for typical soil susceptibilities and the resulting late-time response does not deviate appreciably from that predicted by Equation (69). Related influence is illustrated in Figure 18 and in Figure 19 for a representative range of χ_{dc} . As demonstrated in previous sections, the principal signature of non-dispersive magnetic susceptibility is an impulsive signal accompanying source current termination at $t = 0$.

3.3.6 Conductive, Dispersive Magnetic Soil:

More generally, Lee (1984) considered a frequency-dependent magnetic permeability. In particular, assuming the susceptibility dispersion model in Equation (74) and Figure 17, we have the related soil magnetic permeability

$$\mu_1 = \mu_0 \left(1 + \chi_{dc} \left[1 - \frac{1}{\ln(\tau_2/\tau_1)} \ln \left(\frac{1 + i2\pi f \tau_2}{1 + i2\pi f \tau_1} \right) \right] \right), \quad (87)$$

in Equation (82). More specifically, Lee (1984) expands Equation (82) via Taylor series about $(\mu_1 - \mu_0)/\mu_0$ and evaluates the resulting field equation via methods

similar to those employed for a non-viscous permeability. The resulting late-time ($\tau = t/\sigma\mu_0a^2 \gg 1$) response is

$$\begin{aligned}
v(t) = v_4(t) \approx & -\frac{\mu_0\sqrt{\pi}aI}{20t} \left(\frac{\sigma_a\mu_0a^2}{t}\right)^{3/2} \\
& + \frac{19\mu_0\chi_{dc}\sqrt{\pi}aI}{280t} \left(\frac{\sigma\mu_0a^2}{t}\right)^{3/2} \left[\frac{\psi(5/2)}{\ln(\tau_2/\tau_1)} - \frac{\ln(t/\tau_2)}{\ln(\tau_2/\tau_1)}\right], \quad (88) \\
& - \frac{2\mu_0\chi_{dc}\pi aI}{3t\ln(\tau_2/\tau_1)} \left(\frac{\sigma\mu_0a^2}{t}\right) - \frac{\mu_0\chi_{dc}aI}{2t} \frac{\ln(2a/\varrho)}{\ln(\tau_2/\tau_1)}
\end{aligned}$$

where the digamma function $\psi(5/2) \approx 0.703157$. Note that the initial term is consistent with Equations (85-86), comprising the late-time response for a soil having apparent conductivity σ_a , including the influence of non-viscous magnetic susceptibility (for $\tau_2/\tau_1 \rightarrow \infty$, Equation (88) reduces to Equation (85))¹². Remaining terms reflect the influence of magnetic viscosity and related frequency-dependent permeability as described by Equation (87). In general, for practical coil geometries, the coil radius a is large compared with its cross-sectional radius ϱ and the late-time response is ultimately dominated by the final term with t^{-1} dependence, compared with $t^{-5/2}$ dependence for nondispersive soils. Thus, as previously discussed, magnetic viscosity yields a substantially enhanced and potentially anomalous response. The value of a/ϱ , combined with the electrical conductivity σ_{dc} , magnetic susceptibility χ_{dc} and the viscous magnetic time-constants τ_1, τ_2 , determine the precise transition from $t^{-5/2}$ to t^{-1} dependence.

The predicted response is displayed in Figure 20 for $\chi_{dc} = 0.001$, $\log(\tau_2/\tau_1) = 20$ ($\chi_{FD} \approx 10\%$), $a/\varrho=100$ and the same three conductivity values in Figure 18 and previous figures. Decreasing the ratio a/ϱ by a factor of 10 only marginally reduces the predicted response. In general, with increasing electrical conductivity, predicted transition from $t^{-5/2}$ to t^{-1} dependence is effectively delayed as per Equation (88). However, assuming typical coil dimensions for hand-held systems and practical limits on soil electrical conductivity, the viscous magnetic response is generally predominant within the practical measurement range ($t > 10 \mu s$). We shall return to this issue in following discussion. First, we consider the relative influence of specific magnetic parameters.

While magnetic dispersion is an essential condition for sustained t^{-1} decay, Figure 21 suggests that the predicted response is not as sensitive to the degree of underlying

¹² Related expressions (31) and (35) in Lee (1984) are not entirely consistent, with (35) (in the limit $\tau_1 \rightarrow 0$) implying a marginally higher apparent conductivity $\sigma_a = \sigma(1 + 19\sqrt{\pi}\chi_{dc}/14)^{2/3}$ than (31) and current Equations (86) and (88). The effect is indistinguishable on the scale of current diagrams and insignificant in the present context.

dispersion as it is to the absolute level of magnetic susceptibility. In particular, Figure 21a displays the influence of increasing time-constant bandwidth from $\log(\tau_2/\tau_1) = 10$ ($\chi_{FD} > 15\%$) to $\log(\tau_2/\tau_1) = 100$ ($\chi_{FD} \approx 2\%$), a representative range for the majority of magnetic soils that are nominally viscous. It is observed that the corresponding order of magnitude reduction in related response is relatively minor compared with the effect of varying the static (low-frequency) susceptibility χ_{dc} over a representative range spanning several orders of magnitude for a nominal time-constant bandwidth (Figure 21b). Thus, although magnetic dispersion is a prerequisite condition for the critical transition from $t^{-5/2}$ to t^{-1} decay rate, the onset and level of viscosity dominated response is more strongly influenced by absolute magnetic susceptibility. In effect, absolute susceptibility scales underlying viscosity to yield net frequency dependence that can be considerable despite a relatively modest χ_{FD} . Indeed, this would appear to confirm the direct influence of both absolute susceptibility and related frequency dependence ($\Delta\chi = \chi_{LF} - \chi_{HF}$) on ground reference height (GRH) for a standard calibrated metal detector as reported by Guelle, et al. (2006).

Returning to Equation (81), it is useful to compare the foregoing result with the late-time approximation

$$v(t) = v_5(t) \approx -\mu_0\pi a^2 I \mathcal{M}(0) \frac{\chi_{dc}}{2 \ln(\tau_2/\tau_1)} \frac{1}{t}. \quad (89)$$

Note that in place of $\mathcal{M}(0) = \infty$ as predicted by Equation (72) for $b = a$, $h = 0$, Equation (88) implies $\mathcal{M}(0) = \ln(2a/\varrho)/\pi a$. The resulting approximation is illustrated in Figure 22. As expected, there is excellent agreement with predicted t^{-1} response over the practical measurement range ($10 \mu s - 1000 \mu s$). Again, although Equation (89) hinges on a dispersive magnetic susceptibility, the expression also emphasizes the modulating and potentially predominant influence of absolute susceptibility χ_{dc} (largely reflecting composition and concentration of the viscous soil magnetic fraction).

Equating expressions (89) and (85), we obtain the following approximate relation

$$t_V \approx \mu_0 \sigma_a a^2 \left[\frac{\sqrt{\pi}}{10 \chi_{dc}} \frac{\ln(\tau_2/\tau_1)}{\ln(2a/\varrho)} \right]^{2/3} \quad (90)$$

for the transition time from $t^{-5/2}$ to t^{-1} dependence for a conductive and viscous magnetic soil. Although the resulting expression inevitably overestimates the actual transition time, it is an adequate approximation and provides additional insight on related influence of specific soil electromagnetic parameters. In particular, Figure 23 illustrates the offsetting influence of time-constant bandwidth $\log(\tau_2/\tau_1)$ and absolute low-frequency susceptibility χ_{dc} .

Given well established bounds on χ_{dc} and accepting $\log(\tau_2/\tau_1) > 10$ ($\chi_{FD} < 15 - 20\%$) as an empirical lower limit, it remains of interest to consider a practical upper limit on time-constant bandwidth and related implications. In theory, so long as τ_2/τ_1 remains finite, the corresponding response (Equation 88) continues to be viscosity dominated and display t^{-1} dependence for $t \geq t_V$. However, as practical matter, increasing $\log(\tau_2/\tau_1)$ requires a proportional rise in χ_{dc} to maintain a given t_V or related signal level and, consequently, effective magnetic viscosity $\nu \approx \chi_{dc}/\log(\tau_2/\tau_1)$ is the preferred parameter for gauging the net influence of soil magnetic dispersion.¹³

Equation (90) also indicates that transition time t_V scales with coil radius in approximate accordance with a standard quasi-static scaling relation (e.g. Frischknecht, 1987)

$$t'_V \approx t_V \left(\frac{a'}{a} \right)^2, \quad (91)$$

where t'_V denotes viscous transition time for scaled coil radius a' . Figure 24 displays t_V as a function of coincident coil radius a , with low-frequency conductivity σ_{dc} as a parameter. Trendlines are fit over the range $a = 0.1 - 1.0$ m. Deviation (reduction) from standard squared dependence on a'/a increases as the ratio a/ρ increases with decreasing coil radius. As previously noted, however, the influence is subtle.

The corresponding scaling relation for conductivity ($\sigma = \sigma_a \approx \sigma_{dc}$) is

$$t'_V = t_V \left(\frac{\sigma'_{dc}}{\sigma_{dc}} \right). \quad (92)$$

3.3.7 Non-Magnetic, Dispersive Conductive Soil:

Finally, Lee (1981) and El-Kaliouby, et al. (1995, 1997) have investigated the influence of frequency-dependent electrical conductivity on the TDEM response of a surface-deployed coincident-coil system. Assuming a non-magnetic soil, we have as per Equations (35) and (64)

$$1 + r_{TE} = 1 + \frac{\lambda - u_1}{\lambda + u_1} \quad (93)$$

¹³ In practice, magnetic viscosity is estimated as $\nu \approx \Delta\chi/\log(f_H/f_L)$, with $\Delta\chi = \chi_{LF} - \chi_{HF}$ denoting the differential susceptibility measured between measurement frequencies f_L and f_H . In particular, for measurement frequencies spanning a decade ($f_H/f_L = 10$), $\nu \approx \Delta\chi$. Owing to normalization by χ_{LF} , related parameter $\chi_{FD} = \Delta\chi/\chi_{LF} \times 100$ provides improved discrimination of intrinsic dispersion, related to grain-size distribution of soil magnetic content, but fails to reflect the net extent of effective magnetic viscosity (see also Sections 3.4 and 4.5.1).

with $u_1 = [\lambda^2 + i2\pi f\mu_0\sigma(f)]^{1/2}$. Substituting Equation (93) in Equation (63) and ignoring the impulsive primary response associated with termination of the source current at $t = 0$, yields the step response due to soil

$$v(t) = \mu_0\pi a^2 I \int_0^\infty \int_{-\infty}^\infty \frac{\lambda - u_1}{\lambda + u_1} [J_1(\lambda a)]^2 d\lambda e^{i2\pi ft} df. \quad (94)$$

Lee (1981) evaluates the integral with respect to λ , obtaining a power series solution that is subsequently integrated with respect to complex frequency $f = R e^{i\psi}/2\pi$ by way of appropriate contour integration.

Assuming a Cole-Cole model for electrical conductivity dispersion (Cole and Cole, 1941; Pelton, et al., 1978)

$$\sigma = \sigma_{dc} \left[1 + m \left(\frac{[i2\pi f\tau_\sigma]^c}{1 + [1 - m][i2\pi f\tau_\sigma]^c} \right) \right], \quad (95)$$

the resulting asymptotic integral solution is

$$v(t) = v_6(t) = -\mu_0 a I \int_0^\infty e^{-Rt \sin \psi} \Sigma(R) dR, \quad (96)$$

where

$$\Sigma(R) = \sum_{n=0}^{\infty} \left(\frac{4 \cos \alpha_n [a F(R)]^{2n+3} (2n+2)!}{(2n+5)!(n+1)!n!} - \frac{2 \cos \beta_n [a F(R)]^{2n+2} 2^{4n+2} n! n!}{\pi (2n+4)!(2n)!} \right), \quad (97)$$

R is the contour integration variable and angle $\psi = \pi/4$ defines the branch cut geometry. In addition, we have

$$F(R) = \left[\mu_0 \sigma_{dc} R \left(\frac{1 + 2\delta + \gamma^2}{1 + 2(1-m)\delta + (1-m)^2\gamma^2} \right)^{1/2} \right]^{1/2},$$

$$\alpha_n = Rt \sin(\pi/2 + \psi) + \psi + (2n+3)(\pi/2 + \psi + \phi)/2,$$

$$\beta_n = Rt \sin(\pi/2 + \psi) + \psi + (2n+2)(\pi/2 + \psi + \phi)/2,$$

with

$$\gamma = (\tau_\sigma R)^c,$$

$$\delta = \gamma \cos [(\pi/2 + \psi) c],$$

$$\eta = \gamma \sin [(\pi/2 + \psi) c],$$

$$\phi = \tan^{-1} \left[\frac{\eta}{1 + \delta} \right] - \tan^{-1} \left[\frac{(1-m)\eta}{1 + (1-m)\delta} \right].$$

With the change of integration variable $r = Rt \sin \psi$, the response is readily evaluated numerically employing a Gauss-Laguerre quadrature formulation (El-Kaliouby,

et al., 1995). Results presented by Lee (1981) for specific Cole-Cole parameters, were confirmed independently by Raiche (1983) by way of an alternative computational method. As a check on our numerical evaluation of Equation (96) the same results were reproduced prior to investigating response characteristics on the scale of hand-held sensors. In general, the response predicted by Equation (96) is characterized by a late-time polarity reversal and diminished decay rate. Specific characteristics depend on the nature and degree of electrical polarization and associated dispersion.

Frequency dependence of the electrical conductivity as specified by Equation (95) depends on the static value σ_{dc} , the corresponding high-frequency value σ_∞ (or chargeability $m = (\sigma_\infty - \sigma_{dc})/\sigma_\infty$), the Cole-Cole distribution parameter c and reference time-constant τ_σ as illustrated in Figure 25.

In particular, for $c = 1.0$, Equation (95) yields the related Debye-like dispersion relation

$$\sigma(f) = \sigma_\infty - \frac{\sigma_\infty - \sigma_{dc}}{1 + (1 - m) i 2\pi f \tau_\sigma} \quad (98)$$

and the accompanying transient decay of induced electrical polarization is purely exponential. For an arbitrary time constant distribution $\mathcal{T}_\sigma(\tau)$, with $\int_0^\infty \mathcal{T}_\sigma(\tau) d\tau = 1$, we obtain the general relation.

$$\sigma(f) = \sigma_\infty - (\sigma_\infty - \sigma_{dc}) \int_0^\infty \frac{\mathcal{T}_\sigma(\tau)}{1 + (1 - m) i 2\pi f \tau} d\tau. \quad (99)$$

A $1/\tau$ -scaled, logarithmic time-constant distribution having form

$$\mathcal{T}_\sigma(\tau) = \frac{\mathcal{T}_\sigma(\ln \tau)}{\tau} = \frac{1}{2\pi\tau} \frac{\sin [(1 - c) \pi]}{\cosh [c \ln(\tau/\tau_\sigma)] - \cos [(1 - c) \pi]} \quad (100)$$

yields the Cole-Cole dispersion relation of Equation (95). Figure 25 displays predicted normalized frequency dependence for $\sigma_{dc} = .01$ mS/m, $m = 0.3$, $\tau_\sigma = 0.0001$ s and for the Cole-Cole distribution parameter c ranging between 0.01 and 1.0.

The late-time response predicted by Equation (96) for a non-magnetic, electrically polarizable soil is depicted in Figure 26 (together with previous models) for three values of static conductivity. Note that predicted polarity reversal occurs between 0.1 and 1.0 μ s and that corresponding later-time decay rates are substantially reduced compared with the $t^{-5/2}$ dependence observed for a non-dispersive soil. As Lee (1981) noted for $t/\sigma\mu_0 a^2 > 10$, the corresponding late-time response is well approximated by retaining only the initial ($n = 0$) term of the asymptotic series of Equation (97). For parameters in Figure 26, the deviation between single-term and multi-term approximations is minimal for $t \geq 1.0$ μ s.

For the specific case $\sigma_{dc} = 0.01$ S/m, Figure 27 provides some indication of the influence of individual Cole-Cole parameters on the predicted response. For all but

the most rapidly acting polarization processes ($\tau_\sigma > 10^{-8}$ s), polarity reversal and related decay rate reduction occur later as the associated time-constant τ_σ increases (Figure 27a). Increasing chargeability m has, in general, the opposite effect (Figure 27b), leading to earlier polarity reversal. Dependence on the Cole-Cole distribution parameter c is more complicated. For specific parameter values identified in Figure 27c, polarity reversal occurs at minimum time for $c \approx 0.2$ and increases for both lesser and greater values. The general nature and relative influence of Cole-Cole parameters on polarity reversal time t_R is illustrated in Figure 28 for representative parameter ranges and reference values as per Figure 27.

The corresponding rate of increase in related decay rates, following peak negative-valued response is also significant. Related variation with Cole-Cole parameter values is displayed in Figure 29. In general, it is observed that polarization parameters have considerable and complicated influence over the transition from polarity reversal to late-time $t^{-5/2}$ dependence. In particular, for specific parameter values considered, Figure 29 suggests that sustained response (low decay rate) immediately following polarity reversal is associated with increasing τ_σ , moderate m and increasing c . It is also observed, however, that these characteristics do not generally lead to an early phase reversal.

Finally, it is important to appreciate that response characteristics are also dependent on coil radius and conductivity, with polarity reversal occurring later as the product of coil radius and conductivity increases. Figure 30 displays polarity reversal time t_R as a function of coincident coil radius a , with low-frequency conductivity σ_{dc} as a parameter. Lower curves are for $c = 0.5$ and upper curves for $c = 0$ with remaining parameters as per the reference model in Figure 27. Results imply a generalized scaling relation

$$t'_R = t_R \left(\frac{a'}{a} \right)^{2(1-c)}, \quad (101)$$

where, t'_R denotes the reversal time for scaled coil radius a' . Note that for an infinitely broad time constant distribution ($c = 0$), Equation (101) reduces to the standard quasi-static relation $t'_R = t_R(a'/a)^2$ with squared dimensional dependence (e.g. Frischknecht, 1987) as Equation (96) reverts to Equations (66-69) for a non-polarizable soil with low-frequency conductivity $\sigma = 2\sigma_{dc}/(2 - m)$ (Lee, 1981). The corresponding scaling relation for conductivity follows as

$$t'_R = t_R \left(\frac{\sigma'_{dc}}{\sigma_{dc}} \right)^{1-c}. \quad (102)$$

The principal finding, however, is that induced electrical polarization produces a signal polarity reversal and related decay rate reduction within the typical measurement range for metal detectors and related small-scale TDEM sensors. Moreover, it is

evident on the basis of theory-predicted results in foregoing Figures 21, 26 and 27 that specific soil electromagnetic parameters can potentially combine to yield an effective response that is dominated by electrical polarization despite limited magnetic dispersion.

3.4 Summary:

Metal detectors, both frequency (FDEM) and time-domain (TDEM) varieties are significantly influenced by soil electromagnetic properties and predominantly by soil magnetic characteristics. In general, while FDEM systems are principally affected by the absolute levels of soil magnetic susceptibility and electrical conductivity, TDEM systems are more strongly influenced by related dispersion and associated viscosity.

In particular, where soils incorporate a substantial magnetic component having viscous susceptibility, the late-time TDEM response is generally enhanced with t^{-1} decay rate, compared with $t^{-5/2}$ for a non-magnetic or non-viscous magnetic soil.

With few exceptions, the model of soil magnetic dispersion described by Equations (74) and (87), and leading to Equations (88) and (89) (t^{-1} response), appears to be generally supported by available data. In particular, recent multi-frequency measurements of soil magnetic susceptibility (West and Bailey, 2005; Preetz and Igel, 2005; and see Section 4.5.1) are largely consistent with the following approximate relations (for $1/2\pi\tau_2 \ll f \ll 1/2\pi\tau_1$, $\tau_1 \ll t \ll \tau_2$)

$$\frac{\chi_{dc}}{\log(\tau_2/\tau_1)} = -\frac{\partial\chi'(f)}{\partial\log f} = \frac{2}{\pi} \frac{\chi''(f)}{\log e} = -\frac{1}{H_0} \frac{\partial M(t)}{\partial\log t} = \nu \quad (103)$$

(Mullins and Tite, 1973; Dabas, et al., 1992), where the right-most expression defines magnetic viscosity ν as the rate of change of time-dependent magnetization $M(t)$ normalized by the primary source field $H_0(t)$.

General validity of foregoing relations and well-established empirical limits on χ_{FD} reflect natural grain-size variation and imply a correspondingly broad time-constant distribution ($\log(\tau_2/\tau_1) > 10$). It is also observed that the magnitude of soil magnetic viscosity depends on both the extent of underlying dispersion (grain-size/time-constant distribution) and the absolute susceptibility (composition and concentration) of related soil magnetic content (i.e. $\nu \approx \chi_{dc}/\log(\tau_2/\tau_1)$).

Significantly, it is vastly more common to encounter a highly magnetic soil with low viscosity, than a highly viscous soil with low susceptibility. The explanation is that substantial viscosity ($\chi_{FD} > 2\%$) is largely attributable to a significant fine-grained superparamagnetic fraction that generally carries a correspondingly higher intrinsic magnetic susceptibility (Maher, 1988; Forster, et al., 1994; Dearing, et al., 1996). In contrast, a soil incorporating a substantial concentration of stable single-domain or

multi-domain magnetic material can possess a considerable magnetic susceptibility with limited or negligible viscosity.

In theory, only finite magnetic dispersion is required to produce the sustained and characteristic t^{-1} response. However, where magnetic dispersion is limited ($\chi_{FD} < 2\%$), related significance is increasingly dependent on the level of associated susceptibility (concentration of related viscous magnetic constant) to support or effectively amplify the related signature. Where viscous magnetic content is limited and related susceptibility is low, there is increasing potential for the related signature to be superceded by the background $t^{-5/2}$ conductive response (i.e. t_V , given by Equation (90) exceeds the effective measurement time). Clearly, in the limiting case of a non-dispersive magnetic susceptibility, no amount of associated magnetic content yields t^{-1} dependence and whatever level of susceptibility only produces an effective enhancement of electrical conductivity and related response as per Equations (85-86).

Finally, foregoing findings demonstrate that appreciable dispersion of soil electrical conductivity can also produce anomalous and sustained response characteristics within the typical measurement range of hand-held TDEM systems. In particular, significant electrical chargeability yields a characteristic signal polarity reversal and time-dependent decay rate reduction. Numerical modelling on the basis of Equations (96-97) predicts $t^{-3/2} - t^{-5/2}$ dependence (Figure 29). Most significantly, results suggest that for soils with sufficient chargeability, related induced polarization could potentially dominate the TDEM response for soils having non-dispersive or limited magnetic susceptibility.

In general additional work is required to characterize the practical extent and significance of low-frequency electrical dispersion in soils. However, limited available data (e.g. Ogilvy and Kuzmina, 1972; Mehran and Arulanandan, 1977; Iliceto, et al., 1982; Olhoeft, 1985, 1987) suggest that soil electrical chargeability is rarely sufficient to exceed the influence of even moderate magnetic viscosity (see further related discussion in Section 5.0).

In general, the remainder of the current report is devoted to a brief review of relevant theory and methods for measurement and characterization of low-frequency soil electromagnetic properties.

4.0 MEASUREMENT OF SOIL EM PROPERTIES:

As per foregoing discussion of metal detectors and the basic principles of induction electromagnetic measurement systems, it is often useful and instructive to model electromagnetic characteristics of the soil in terms of an equivalent electric circuit. As we move from field sensors to the laboratory, a circuit theory perspective is less an analogy and more a reality. In general, laboratory measurement of low-frequency soil electromagnetic properties employs a range of sample holders or fixtures that are effectively large-scale equivalents of fundamental circuit components, including resistors, capacitors and inductors. The sample soil simply replaces the equivalent resistive, dielectric or magnetic material within the component's interior. The fixture is subsequently driven by a controlled and calibrated source signal (voltage/current) with simultaneous detection of one or more response signals. Finally, appropriate signal conditioning and processing is applied to source and response signals to derive required signal attributes and to compensate for fixture and measurement system response characteristics prior to display and/or storage of measured data.

Again, measurements can be acquired in either time or frequency domain and a considerable range of laboratory instrumentation has been reported. Due to the relative instrumental complexities of time-domain measurements, laboratory characterization of soil electromagnetic parameters is largely carried out by applying a continuous sinusoidal source signal over a range of discrete frequencies. Typically, the relative gain and/or phase of a resulting response signal is quantified with reference to the source signal to yield a vector measurement of the sample's complex impedance or other related parameters. In some cases, sample related deviation of fixture's resonant frequency or related phase characteristics are detected to yield equivalent effective impedance parameters.

Although consideration is also given to appropriate technologies for field measurement of soil electromagnetic properties, the current study has largely focused on laboratory characterization. In addition to assessing the performance of selected special-purpose instrumentation, our primary approach has been to investigate the use of standard off-the-shelf impedance analyzers, multi-frequency LCR meters and similar widely available technologies for measurement of both electrical and magnetic soil properties. In following sections, relevant measurement theory is developed in connection with the simplest of sample fixture configurations to demonstrate the practical characterization of soil electromagnetic properties by measurement of related lumped circuit impedance parameters. We begin by defining the frequency-dependent complex impedance.

4.1 Complex Impedance-Admittance:

In general, the complex impedance of an arbitrary two-terminal network is defined as

$$Z(f) = \tilde{R} + i\tilde{X}, \quad (104)$$

where $\tilde{R}(f)$ denotes the equivalent resistance and

$$\tilde{X}(f) = 2\pi f\tilde{L} - \frac{1}{2\pi f\tilde{C}} \quad (105)$$

represents the equivalent reactance, comprising inductive and capacitive contributions associated with equivalent inductance \tilde{L} and capacitance \tilde{C} , respectively. Alternatively, as indicated in Figure 31, the complex impedance may be written in polar form

$$Z(f) = |Z(f)| e^{i\theta(f)}, \quad (106)$$

with associated frequency-dependent magnitude

$$|Z(f)| = (\tilde{R}^2 + \tilde{X}^2)^{1/2} \quad (107)$$

and corresponding phase angle

$$\theta(f) = \tan^{-1} \left(\frac{\tilde{X}}{\tilde{R}} \right) \quad (108)$$

relative to the resistive axis in the complex impedance plane. Note also that while capacitive reactance leads the resistance by 90 degrees, inductive reactance lags by 90 degrees.

The ratio of resistive to reactive components of the complex impedance

$$D = \tan \delta = \frac{\tilde{R}}{\tilde{X}} \quad (109)$$

is referred to as the dissipation factor or loss tangent $\tan \delta$, where δ is the complement of the phase angle θ . The reciprocal quantity $Q = 1/D$ is termed the quality factor. Finally, in connection with the combination of impedances in parallel (Figure 31), it is advantageous to make use of the inverse impedance or the admittance

$$Y(f) = \frac{1}{Z(f)} = \frac{1}{\tilde{R} + i\tilde{X}} = \frac{\tilde{R} - i\tilde{X}}{\tilde{R}^2 + \tilde{X}^2} = \tilde{G} + i\tilde{B}, \quad (110)$$

where $\tilde{G}(f) = 1/\tilde{R}$ denotes the equivalent conductance and

$$\tilde{B}(f) = 2\pi f\tilde{C} - \frac{1}{2\pi f\tilde{L}} \quad (111)$$

represents the equivalent susceptance, comprising capacitive and inductive contributions associated with parallel equivalent capacitance \tilde{C} and inductance \tilde{L} , respectively. Note that, in general, measured impedance parameters are frequency dependent and typically impure. Consequently, as for basic material parameters, we refer to these measured quantities as equivalent or effective parameters. Figure 32 illustrates basic phase relations for pure and combined circuit elements.

4.2 Electrical Parameters - Theory:

In practice, electrical and magnetic properties of a given soil sample are measured independently using appropriate fixture configurations to selectively enhance the respective response. In particular, while soil magnetic properties are investigated by applying a primary magnetic field, soil electrical parameters are commonly measured in response to a primary electric field.

Expanding on the treatment by von Hippel (1965), we consider a time-varying source potential

$$V = V_0 e^{i2\pi ft}, \quad (112)$$

applied to the terminals of a parallel-plate sample fixture as pictured in Figure 33a. Prior to placing soil in the fixture, the applied potential produces a charging current

$$I = \frac{dQ}{dt} = C_0 \frac{dV}{dt} = i2\pi f \gamma_c \epsilon_0 V, \quad (113)$$

where $Q = C_0 V$ denotes the charge developed on a given plate electrode and $C_0 = \gamma_c \epsilon_0$ is the geometric capacitance of the air-filled sample fixture, with ϵ_0 representing the electrical permittivity of free-space and $\gamma_c = A/\ell$ a geometrical constant given by the ratio of cross-sectional area (A) to separation (ℓ) between electrodes. It follows from Equation (113) that the charging current leads the applied potential by $\pi/2$ radians or 90 degrees (Figure 32). Finally, neglecting fringing effects at edges, the associated electric field within the fixture volume is

$$E = -\nabla V = V/\ell = \frac{q}{\epsilon_0}, \quad (114)$$

where $q = Q/A$ denotes the time dependent surface charge density on a given plate electrode.

Now, for a sample filled soil-box, the effective capacitance, $C = (\epsilon/\epsilon_0) C_0 = \epsilon \gamma_c$, is enhanced by the relative electrical permittivity $\epsilon_r = \epsilon/\epsilon_0$, where ϵ represents the intrinsic soil permittivity.¹⁴ Thus, from Equation (113), we obtain the following

¹⁴ Note the corresponding dielectric constant is the special case defined as $\kappa = \epsilon'(0)/\epsilon_0$, where $\epsilon'(0)$ denotes the static real electrical permittivity and $\epsilon_0 = 8.85 \times 10^{-12}$ F/m denotes the electrical permittivity of free space.

expression for what is effectively the displacement current associated with bound-charge polarization processes within the sample soil

$$I_\epsilon = i2\pi f\epsilon\gamma_c V = J_\epsilon A, \quad (115)$$

where

$$J_\epsilon = \epsilon \frac{dE}{dt} \quad (116)$$

is the associated displacement current density. In addition, there is a free-charge conduction current predicted by Ohm's law

$$I_\sigma = \frac{V}{R} = \frac{V}{\rho\ell/A} = \frac{\gamma_c}{\rho} V = \gamma_c \sigma V, \quad (117)$$

where $R = \rho\ell/A$ denotes the effective electrical resistance, ρ is the electrical resistivity and $\sigma = 1/\rho$ is the corresponding electrical conductivity. In contrast with the displacement current, the conduction current and associated conduction current density

$$J_\sigma = \frac{I}{A} = \sigma E, \quad (118)$$

within the sample volume, are in-phase with the source potential (Figure 32).

Finally, combining Equations (115) and (117) we obtain the net circuit relation

$$I = I_\sigma + I_\epsilon = \gamma_c (\sigma + i2\pi f\epsilon) V \quad (119)$$

and from Equations (116) and (118) the corresponding field relation

$$J = J_\sigma + J_\epsilon = (\sigma + i2\pi f\epsilon) E. \quad (120)$$

Now, as previously described, it is generally observed that soil electrical properties display significant frequency dependence and, consequently, σ and ϵ must be complex-valued parameters

$$\sigma = \sigma' + i\sigma'' \quad \epsilon = \epsilon' - i\epsilon''. \quad (121 - 122)$$

Therefore, we have

$$\begin{aligned} \sigma + i2\pi f\epsilon &= (\sigma' + i\sigma'') + i2\pi f(\epsilon' - i\epsilon'') \\ &= (\sigma' + 2\pi f\epsilon'') + i2\pi f\left(\epsilon' + \frac{\sigma''}{2\pi f}\right) \end{aligned}$$

and, as a result, Equations (119) and (120) become

$$I = \gamma_c (\tilde{\sigma} + i2\pi f\tilde{\epsilon}) V, \quad (123)$$

$$J = (\tilde{\sigma} + i2\pi f\tilde{\epsilon}) E, \quad (124)$$

where

$$\tilde{\sigma} = \sigma' + 2\pi f\epsilon'' \quad \tilde{\epsilon} = \epsilon' + \frac{\sigma''}{2\pi f} \quad (125 - 126)$$

denote real-valued composite effective parameters (as per Section 2.0 Equations 13-14). In particular, while complex conductivity and complex permittivity are associated with free and bound charge processes, respectively, real-valued effective conductivity and effective permittivity are similarly associated with loss (power dissipation) and polarization (energy storage) processes. For example, it is observed that viscous rotational displacement current associated with polarization of dipolar molecules contributes in-phase with the Ohmic loss current associated with mobile ion transport.

Similarly, the effective polarization of the mobile charge distribution associated with interfacial polarization processes is in-phase and indistinguishable from the dielectric polarization of bound atomic and molecular charge. It is only possible to separate and quantify related contributions to composite effective parameters based on the relative phase of associated currents.

In practice, it is also important to appreciate that in addition to reflecting material parameters representative of the sample soil, related in-phase and quadrature signal components also include parasitic contributions associated with fixture hardware and cabling (Haruta, 2000). The influence of higher order electromagnetic fields is assumed to be negligible. For example, magnetic fields associated with time varying current density and related induced eddy currents are assumed to have no appreciable influence even for strongly magnetic and/or conductive soils.

Recognizing Equation (123) as a combination of parallel currents, we measure in-phase and quadrature components of the net current I with gain-phase reference to source potential V to yield the corresponding frequency-dependent complex admittance $Y(f) = I/V$ over a range of discrete source frequencies between 100 Hz and 100 kHz.

For the present case of a sample-filled soil-box, Equation (123) yields

$$Y(f) = \frac{I}{V} = \tilde{G} + i\tilde{B} = \gamma_c (\tilde{\sigma} + i2\pi f\tilde{\epsilon}), \quad (127)$$

and, therefore, assuming that the effective susceptance of the parallel-plate fixture is purely capacitive, $B = i2\pi f\tilde{C}$, we have¹⁵

$$\tilde{\sigma} = \sigma' + 2\pi f\epsilon'' = \frac{\tilde{G}}{\gamma_c} = \frac{1}{\gamma_c \tilde{R}} = \frac{1}{\tilde{\rho}} \quad (128)$$

¹⁵ Note that the equivalent parallel capacitance \tilde{C}_p is related to the equivalent series capacitance \tilde{C}_s by $\tilde{C}_p = \tilde{C}_s(1 + D^2)^{-1}$, where $D = \tilde{R}/\tilde{X} = \tilde{G}/\tilde{B}$ denotes the dissipation factor.

$$\tilde{\epsilon} = \epsilon' + \frac{\sigma''}{2\pi f} = \frac{\tilde{C}}{\gamma_c}. \quad (129)$$

where $\tilde{\rho} = 1/\tilde{\sigma}$ defines the corresponding effective electrical resistivity.

Again, it is emphasized that measured complex impedance spectra can also reflect superimposed response signatures associated with fixture hardware and cabling. Electrode polarization phenomena are also potentially significant sources of error. Methods to reduce and compensate for these parasitic responses, including four-terminal vs. two-terminal measurement configurations, are discussed further in Section 4.4. For now, we turn our attention to the measurement of soil magnetic properties.

4.3 Magnetic Parameters - Theory:

In direct analogy with the previous section, we consider the same time-varying source potential

$$V = V_0 e^{i2\pi ft}, \quad (130)$$

in this case, applied to the terminals of a solenoidal sample fixture as depicted in Figure 33b. Here, in accordance with Faraday's induction law $V = L_0(dI/dt)$, the applied potential produces a magnetizing current

$$I = \frac{1}{L_0} \int V dt = \frac{V}{i2\pi f \gamma_\mu \mu_0}, \quad (131)$$

where $L_0 = \gamma_\mu \mu_0$ denotes the inductance of the air-cored solenoid, γ_μ is a coil specific geometric constant and $\mu_0 = 4\pi \times 10^{-7}$ H/m is the magnetic permeability of free-space. In particular, $\gamma_\mu = N^2 A/\ell$, where A denotes the cross-sectional area of the solenoid, ℓ is its length and N is the number of turns. Finally, note that in contrast with the case of the parallel-plate fixture, Equation (131) indicates that the drive current lags the applied potential by $\pi/2$ radians or 90 degrees (Figure 32).

Now, upon introducing a coaxial sample core into the fixture, the effective inductance, $L = (\mu/\mu_0) L_0 = \mu \gamma_\mu$, is enhanced by the relative magnetic permeability $\mu_r = \mu/\mu_0$ and assuming an associated frequency-dependent, complex-valued soil magnetic permeability

$$\mu = \mu' - i\mu'', \quad (132)$$

we obtain the general relation

$$I_\mu = \frac{V}{i2\pi f \gamma_\mu} \left(\frac{1}{\mu' - i\mu''} \right) = \frac{V}{2\pi f \gamma_\mu (\mu'' + i\mu')} \quad (133)$$

for the net current, within the sample-cored solenoid. By way of appropriate instrumentation, the in-phase and quadrature components of the net current I are detected

and measured with gain-phase reference to the source potential V to yield the corresponding frequency-dependent complex impedance

$$Z(f) = \frac{V}{I} = \tilde{R} + i\tilde{X} = 2\pi f\gamma_\mu (\mu'' + i\mu') \quad (134)$$

over a range of discrete source frequencies. Assuming the reactive impedance of the solenoid fixture to be purely inductive, $\tilde{X} = 2\pi f\tilde{L}$, soil magnetic parameters are related to measured equivalent impedance parameters according to the following expressions

$$\mu' = \frac{\tilde{L}}{\gamma_\mu} = \mu_0(\chi' + 1) \quad (135)$$

$$\mu'' = \frac{\tilde{R}}{2\pi f\gamma_\mu} = \mu_0\chi'', \quad (136)$$

where χ' and χ'' denote corresponding in-phase and quadrature components of the associated complex, frequency-dependent magnetic susceptibility $\chi(f) = \chi'(f) - i\chi''(f)$. Consequently, complex magnetic susceptibility components follow directly from the difference between related impedance parameters measured before and after insertion of the sample core as

$$\chi' = \frac{\Delta L}{\gamma_\mu\mu_0} = \frac{\Delta L}{L_0} \quad (137)$$

$$\chi'' = \frac{\Delta R}{2\pi f\gamma_\mu\mu_0} = \frac{\Delta R}{2\pi fL_0} \quad (138)$$

where $\Delta L = L - L_0$, $\Delta R = R - R_0$ and R_0 denotes the resistance of the air-cored solenoid.

Note that a magnetic loss current associated with the quadrature permeability (susceptibility) and related viscosity is phase shifted by 180 degrees and effectively reduces the apparent resistive loss current $I_c = V/R_c$ in the solenoid's windings. In addition, there is a potentially significant back current associated with the development of inductive eddy currents within an electrically conductive sample core. Finally, although higher order electromagnetic fields are generated within the sample soil in connection with time-variation of related secondary fields, related influence on the measured response is presumed to be negligible.

Finally, it is noted that an alternative approach is to design a solenoid having specified open-coil resonant frequency $f_0^* = 1/2\pi(L_0C_0)^{1/2}$ (where C_0 represents the coil's equivalent distributed capacitance) and to similarly derive the permeability (susceptibility) by measuring the deviation $\Delta f^* = f^* - f_0^*$, where $f^* = 1/2\pi(LC_0)^{1/2}$ denotes the resulting resonant frequency on insertion of the sample core. In practice, the LC oscillator circuit is rather more complicated, however improved accuracy and precision

make resonant frequency methods the standard approach for dedicated susceptibility meters and we shall return to these methods in connection with description of commercially available susceptibility instruments. First, we turn our attention to the practical measurement of soil electrical conductivity.

4.4 Electrical Parameters - Measurement:

As discussed in previous sections (see Section 2.0 and including footnote 1), it is assumed that the metal detector response is adequately described under a quasistatic assumption that displacement currents associated with electrical permittivity $\tilde{\epsilon}$ are negligible compared with conduction currents associated with conductivity $\tilde{\sigma}$. Consequently, the following discussion is limited to measurement of the electrical conductivity and the corresponding reciprocal quantity, electrical resistivity $\tilde{\rho}$.

As a point of departure, methods investigated for laboratory and field measurement of electrical conductivity may be viewed as generalizations and extensions of ASTM Standards G57-06 and G187-05 (ASTM, 2005, 2006).

4.4.1 Laboratory Methods and Procedures:

Laboratory measurement of direct current soil electrical conductivity is carried out routinely in connection with a wide range of agricultural and engineering applications. Although specifications vary considerably, the sample fixture is generally referred to as a soil box and roughly approximates the parallel plate capacitor model discussed in Section 4.2. In particular, we have adopted a standard format (Figure 34) with geometry designed such that electrical resistance measured in four-electrode configuration yields soil electrical resistivity directly in Ohm-cm units¹⁶. The corresponding design constraint is $\gamma_c = A/\ell_V = 1.0$, where A denotes the area of end-plate electrodes and $\ell_V = x_1$ is the separation between interior potential electrodes. Resulting resistivity (conductivity) follows as $\rho = 1/\sigma = \gamma_c R = R$.

Alternatively, the interior potential electrodes can be removed, leading to standard two-electrode resistivity $\rho = 1/\sigma = \gamma_c R = (A/\ell)R$ as per Equation (128), where $\ell = x_1 + 2x_2$ is the full length between end-plate electrodes. Concurrently, however, it is important to appreciate that the current soil box design is inconsistent with the assumption $\gamma_c \gg 1.0$ for an ideal parallel plate capacitor and, consequently, Equation (127) for the associated electrical permittivity is invalid. In particular, it can be demonstrated that for small γ_c , the basic relation $C = \gamma_c \epsilon$ no longer holds and, rather, the effective capacitance approaches a constant value as fixture length increases. As noted above, however, our present interest is limited to the electrical conductivity and there is no similar limitation on the relation $R = \rho/\gamma_c = 1/\gamma_c \sigma$.

¹⁶ Soil box fixtures employed for investigations reported here are commercially available from MC Miller Inc. (www.mcmiller.com). Similar purpose-built fixtures are available from other suppliers

The primary advantage of the present soil box design is the inclusion of interior potential electrodes to permit four-electrode measurements to minimize the influence of electrode polarization effects at end-plate electrodes as illustrated in Figure 35. Notice that while a simple two-electrode Impedance (or Admittance) measurement given by the vector ratio of source voltage V_s and source current I_s , neglects the influence of the polarization field E_p within the sample, the corresponding four-electrode measurement samples the net effective field $\tilde{E} = E_s - E_p$ via related voltage drop V across interior potential electrodes. Finally, it is important to emphasize the distinction between “four-terminal” and “four-electrode” measurements. In particular, it is noted that both two-electrode and four-electrode measurements, as previously described, are acquired in four-terminal configuration, with signal current and signal voltage detected separately in parallel circuits.

Unfortunately, existing standards for soil electrical resistivity characterization typically call for measurement of static or “low-frequency” resistivity ρ_{dc} and, consequently, commercially produced electrical resistivity meters invariably employ a single low-frequency or commutated DC voltage source with no capability for multi-frequency measurements. For this reason, laboratory measurements of frequency-dependent electrical resistivity (conductivity) have generally employed impedance, LCR or gain-phase analyzers developed for electronic test and measurement applications.

In general, multi-frequency impedance analyzers and LCR meters are configured for four-terminal measurement. Figure 36 displays a generic four-terminal impedance analyzer as configured for both two-electrode and four-electrode soil box impedance measurements. Unfortunately, experimentation and related investigation reveals that, in practice, the design of common impedance analyzers and LCR meters is not conducive to accurate impedance measurements in the desired four-electrode configuration. On the contrary, LCR meters are engineered primarily for testing and quality control on two-lead electronic components and, consequently, as commonly configured¹⁷, the four-terminal measurement circuit assumes only minimal contact impedance $Z_H = Z_{hc} + Z_{hp}$ between H_c (high current) and H_p (high potential) terminals and, similarly, $Z_L = Z_{lc} + Z_{lp}$ between L_c (low current) and L_p (low potential) terminals (Haruta, 2000).

¹⁷ The standard design is an autobalancing bridge circuit and is considerably more complicated in detail than portrayed in Figures (37-38). The source signal generated by a precision oscillator is applied at current terminal H_C . Resulting vector potential drop across the sample volume is sensed at the H_P terminal with reference to a common shield conductor maintained at virtual ground by a feedback controlled balance oscillator with sensing at the L_P terminal. Test current returning via the shield conductor is gauged by monitoring current through a calibrated range resistance at the L_C terminal (see Haruta, 2000 for details).

The corresponding two-electrode soil-box configuration is depicted in Figure 37. In contrast, as illustrated in Figure 38, the four-electrode soil-box measurement configuration implies $Z_H \gg Z_{hc} + Z_{hp}$ and $Z_L \gg Z_{lc} + Z_{lp}$, with $Z_H \approx Z_L$ on the same order of magnitude as the sample impedance Z_S . Unfortunately, the foregoing condition strongly restricts the function of common four-terminal impedance analyzers and LCR meters for four electrode resistivity (conductivity) measurement (particularly for low-moisture (resistive) soil condition).

In view of the foregoing limitation on LCR meters and required portability for field characterization of soil electrical characteristics, we have simultaneously investigated an alternative approach employing a stand-alone signal generator and digital multi-meters (DMMs). We shall refer to related measurements as GVI (generator-voltage-current) measurements. In effect, related four-terminal measurement configurations, as illustrated in Figure 39, are identical to those for the integrated impedance analyzer with the advantage that voltage and current measurement circuits are entirely independent. An isolation amplifier is added at the voltmeter input to avoid related circuit interaction, particularly at high frequencies.

Relative performance characteristics of investigated measurement configurations are illustrated in Figure 40 for untreated Vancouver tap water and for both 75 ml and 250 ml soil-box fixtures. Note that, in general, all investigated methods yield results in good agreement with water conductivity as monitored via a YSI Model 34 conductivity meter. The observed shift between 75 ml and 250 ml fixtures is attributable to a related shift in tap water conductivity. Given the uniform single-phase nature of water, no substantial electrophysical or electrochemical polarization processes are anticipated within the sample volume and, consequently, it is assumed that observed frequency dependence is attributable to a combination of fixture, cabling and instrument effects. Finally, it is noted that a conductivity of approximately $\sigma \approx 2.5$ mS/m ($\rho \approx 400$ Ohm-m) is representative of moderately resistive soils for which parasitic signatures, including electrode polarization effects, are generally more pronounced.

We first consider results for two-electrode measurement configurations. In particular, as anticipated, two-electrode LCR measurements confirm a roughly frequency-independent resistivity for water samples, with the exception of a minor apparent reduction at the upper band limit of 100 kHz. In contrast, corresponding two-electrode GVI measurements display a pronounced decrease in apparent electrical resistivity for frequencies approaching and exceeding 10 kHz. Experimentation confirms, however, that observed effects are related to input impedance characteristics of the voltmeter (DVM) and are largely eliminated by isolating the DVM from the measurement circuit. Isolation is accomplished by insertion of a unity-gain instrumentation amplifier at the voltmeter input as indicated in Figure 39. Although resulting measurements confirm improved response characteristics, there remains a minor apparent increase in measured resistivity at high frequencies attributed to underestimation of the test

current. As required, calibrated compensation adjustments can be applied to correct for related minor roll-off of the current meter’s frequency response.

As regards four-electrode results, it is observed that similar high frequency effects are encountered for GVI measurements. However, again, isolation of the DVM from impedance characteristics of the potential measurement circuit (including sample impedance), largely eliminates related measurement error. More significantly, four-electrode LCR measurements illustrate the severely restricted function of these instruments in four-electrode configuration. In particular, it is noted that the HP4192A impedance analyzer yields adequate sample characterization only over a limited frequency range between approximately 100 Hz and 4 kHz. Measurement error is unacceptable for both lower and higher frequencies.

Foregoing results for untreated Vancouver tap water illustrate both the limitations of standard LCR meters and the viability of the considerably lower cost GVI approach. Although the latter method yields only scalar measurement of apparent electrical parameters (versus phase-sensitive vector impedance/admittance provided by LCR meters), the advantage of four-electrode measurement capability is significant. It is notable that only minor, if any, electrode polarization effects are observed for tap water samples and this is likely attributable to a relatively high ion mobility in proximity to electrodes. There is some suggestion of a minor polarization effect in the case of the 75 ml fixture where it is observed that four-electrode measurements yield a marginally lower resistivity than corresponding two-electrode measurements. However, the opposite deviation is observed in the case of the 250 ml fixture, suggesting that minor offsets between 2-electrode and 4-electrode measurements are of questionable significance. In contrast, as we shall see, electrode polarization effects can be clear and considerable for a soil-filled fixture and, particularly at lower soil moisture levels.

For example, Figure 41 compares the previous result for Vancouver tap water with a local loam soil having similar conductivity, but also displaying substantial frequency dispersion. The gravimetric moisture content $w = M_w/M_s$ is approximately 15%, where M_w and M_s denote mass of water and mass of the lab-dry solid fraction, respectively. In contrast with results for Vancouver tap water samples, measurements on the loam soil display clear evidence of both intrinsic dispersion and electrode polarization. In particular, two-electrode resistivity measurements clearly exceed corresponding four-electrode measurements, particularly at lower frequencies, and imply an apparently higher level of overall frequency dispersion. In general, these features are the typical signatures of electrode polarization.

As discussed in Section 3.3.7, a common measure of soil electrical polarization and related dispersion is the electrical chargeability defined by

$$m = \frac{\rho_{dc} - \rho_\infty}{\rho_{dc}} = \frac{\sigma_\infty - \sigma_{dc}}{\sigma_\infty}, \quad (139)$$

where ρ_{dc} and σ_{dc} denote low-frequency or static electrical parameters and ρ_{∞} and σ_{∞} represent corresponding high-frequency values. For example, for the loam soil in Figure 41, Equation (137) yields a chargeability of roughly $m = 0.16$ for 4-electrode GVI measurements compared with approximately $m = 0.20$ for 2-electrode LCR data.

Frequency dependent resistivity/conductivity for three DRDC reference soils are displayed in Figures 42-44 on the same scale as Figures 40 and 41. In view of evident limitations, four-electrode LCR measurements are not considered. Results for the DRDC Australia-A soil in Figure 42 illustrate that in general, as conductivity increases, the absolute level of electrode polarization effects diminish. Thus, given the direct relation between moisture and conductivity for a given soil, it follows that electrode polarization phenomena are observed to increase as moisture content decreases for a particular soil (and potentially above some threshold moisture level).

The Australia-A soil also displays relatively limited absolute dispersion. However, due to normalization by absolute conductivity/resistivity, it is clear that electrical chargeability can remain significant. In particular, although only subtle dispersion is observable on the present scale, chargeabilities in the range $m = 0.11 - 0.17$ are comparable to those for the loam soil in Figure 41 with comparatively evident frequency dependence.

The DRDC Cambodia-1 soil in Figure 43 is considerably more resistive for a given moisture content than the previous Australia-A soil. Moreover, consistent with prior observations, electrode polarization effects are more substantial and increase considerably with increasing resistivity as moisture decreases. In addition, comparison of results for Australia-A and Cambodia-1 soils for a consistent moisture level of $w = 15\%$ illustrates that the extent of electrode polarization is influenced considerably by soil resistivity and related characteristics (ionic content, texture, clay content, etc.) as well as by moisture content.

Results for the Cambodia-1 soil again demonstrate that greater absolute dispersion does not translate directly to higher chargeability. Although absolute dispersion is substantially greater than observed for the Australia-A soil, corresponding chargeabilities for four-terminal GVI measurements are considerably lower.

Finally, results for the DRDC (UNMAC) Bosnia soil (Figure 44) reveal the relatively conductive nature of the soil and further reinforce previously observed relations between electrical resistivity, moisture level, electrode polarization, absolute dispersion and chargeability. In particular, it is noted that for a moisture level of approximately 16%, there is practically no visible indication of electrode polarization on the present scale and no significant chargeability. It is also notable for the Bosnia soil and, as a general rule, that degraded measurement accuracy for GVI measurements at high-frequency is less apparent with increasing soil conductivity. In fact, as predictable on

the basis of related prior discussion, the functionality of LCR and impedance analyzers in four-electrode configuration is also much improved for conductive soil samples.

Dependent on actual fixture volume and the relative scale of soil heterogeneity, it may be advisable (depending on bulk soil texture) to exclude coarser-grained fractions from measurement. In general, as reported in Cross (2000), the nature of soil electrical properties is largely determined by finer-grained soil fractions due to comparatively enormous surface area and related moisture and pH-dependent ionic exchange capacity/mobility. Consequently, for predominantly fine-textured soils, the influence of coarser-grained gravel components is ordinarily minimal. In connection with testing of DRDC reference soils, as reported above, minor gravel fractions were excluded via dry sieving at #3 (6.73 mm) mesh (consistent with subsequent magnetic analysis - Section 4.5.1).

Because soil electrical conductivity and related frequency variation are strongly dependent on moisture level, soil samples should be well sealed and related laboratory characterization should be carried out as soon after sampling as possible. In addition to assessing as-received electrical characteristics, the range and variation of moisture dependent electrical characteristics can be established by subsequently saturating the sample with distilled (deionized) water and acquiring a series of measurements as soil moisture is reduced, initially via air drying and ultimately via incremental oven treatment. Note, where samples are allowed to dry within the measurement fixture, due consideration should be given to potential influence of differential moisture loss from the open surface of the contained sample. The advantage, however, is that soil fabric remains constant. Alternatively, samples can be removed from the fixture between successive measurements to ensure uniform drying. Whatever the method, related procedure should be described and sample moisture level should be determined and recorded in connection with all associated measurements.

Where samples are allowed to air-dry within the sample fixture, an additional consideration is the potential influence of increasing sample-electrode contact impedances due to sample contraction and related physical separation between electrodes and sample soil. While related influence at current electrodes is relatively insignificant and can be overcome by adding a small amount of distilled water at the electrode-sample contact, corresponding effects (particularly significant capacitive impedance) at potential electrodes are relatively difficult to address and represent a limiting source of measurement error at low moisture levels.

A final procedural consideration is the way in which sample soil is placed into the soil box or other fixture and related porosity/permeability influence on measured soil electrical properties. As regards measurement under as-sampled moisture condition, it is generally recommended that sample soil be gradually transferred to the fixture with application of limited shaking, mild mechanical shocks (i.e. lightly impacting fixture on bench top) and limited direct pressure to achieve moderate and uniform compaction.

In particular, sample soil should *not* be compacted in layers and, in general, stratification should be avoided. Where as-sampled conditions are not of particular interest and, generally, in connection with characterization of moisture-dependent electrical properties, sample soil should be transferred to the fixture in lab-saturated (soil paste) condition for optimum uniformity of fabric. Despite optimum procedure, however, it should be appreciated that lab-measured soil electrical properties can differ substantially from in situ characteristics and, wherever possible, in situ measurement is preferred. In contrast, soil magnetic properties (excluding remanent magnetization) depend primarily on soil mineralogy and temperature and are largely unaffected by soil fabric and/or related moisture level/distribution. Consequently, as discussed in Section 4.5, lab-measured soil magnetic susceptibility is adequately corrected for relative compaction via comparatively straight forward density normalization (assuming reasonable constraints on in situ bulk density).

4.4.2 Laboratory Instrumentation:

Sample Fixture:

There is clearly considerable latitude on specifying an appropriate sample fixture. However, as described in the previous section, it is recommended that the fixture be designed to facilitate four-electrode measurements for purpose of avoiding the influence of electrode polarization. In addition, it is noted that potential electrodes should be sufficiently removed from current electrodes to avoid the region of polarized charge accumulation and should be separated by a sufficient interval to ensure a sizable potential gradient. As a rule of thumb, the ratio of end-plate electrode area A to related separation ℓ should satisfy $A/\ell < 1.0$ and should not exceed $A/\ell = 10$.

Good quality connectors should be employed to minimize related contact impedances and electrodes should be fabricated from brass, stainless steel or other corrosion resistant materials. It is noted that non-polarizable electrodes (e.g. copper/copper sulphate) could also be considered to avoid possible polarization effects at interior potential electrodes. Although it is anticipated that related influence is minimal, this assumption has not been investigated or confirmed. Again, Figure 34 provides approximate specification for soil-box fixtures employed here. Additional guidance is provided in ASTM G57-06 and G187-05.

Impedance Analyzers and Multi-Frequency LCR Meters:

There is a wide range of commercially available impedance analyzers and multi-frequency LCR meters. Figure 45 pictures two precision LCR meters utilized for the current study. For purpose of measuring frequency-dependent soil electrical conductivity/resistivity as described in the previous section, we recommend the following general specifications.

First, the frequency range should extend from 10 Hz to 100 kHz, with discrete test frequencies of 100 Hz, 1 kHz, 10 kHz as a minimum requirement. Specified test signal level should be $\geq 1.0 V_{RMS}$ and preferably $\geq 5.0 V_{RMS}$ into 50Ω . Typically, the source voltage level is regulated and selectable, with corresponding test current dependent on sample load. Some instruments also permit current regulation with compliance to a maximum specified source voltage. In general, high quality, precision instruments are capable of accurate impedance measurements at test current levels as low as $1.0 \mu A$. Recommended measurement ranges are Conductance - $G (|Y|, \theta)$: $\leq 1.0 \mu S$ to $\geq 100.0 mS$ (parallel circuit mode) and Resistance - $R (|Z|, \theta)$: $\leq 10.0 \Omega$ to $\geq 1.0 M\Omega$ (series circuit mode). As regards measurement accuracy, we recommend a basic accuracy of 1%. However, actual performance is a function of load impedance and instrument-specific characteristics as functions of frequency should be reviewed. Display resolution should be at least 4.5 digits and multi-fold measurement averaging capability is a significant asset.

Finally, as a practical matter, a particularly significant performance parameter is the effective input impedance, which must be sufficiently high to avoid loading effects in connection with highly resistive (dry) soils. As a minimum requirement, we recommend $Z_0 \geq 10 M\Omega$. As previously discussed, however, a major limitation of investigated LCR meters is poor performance in four-electrode configuration (for resistive soils) due to effectively high contact resistances between potential-current electrode pairs. On the basis of limited product research and related inquiries, it is our impression that the vast majority of multi-frequency LCR meters and impedance analyzers are based on the same or similar auto-balancing bridge designs and, consequently, it is presumed that similar restrictions apply. Specific design characteristics and related performance specifications should be confirmed with the instrument manufacturer.

GVI Instrumentation:

Basic instrumentation/apparatus for GVI measurements reported here is displayed in Figure 46. The selection of commercially available signal generators and digital multimeters (DMM) is yet greater than for impedance analyzers and LCR meters. However, there is also far greater latitude in related performance characteristics and, consequently, greater care is required in selecting appropriate instrumentation.

Signal Generator: In practice, given relatively modest requirements on frequency range, nominally 10 Hz - 100 kHz, and noting that signal stability effects are eliminated by the ratiometric nature of GVI measurements, the primary requirement on the signal generator is that it supply a sufficient signal level. In particular, we recommend $\geq 10.0 V_{pp}$ into 50Ω as a minimum specification. Actual test signal level and related test current are dependent on sample load.

Voltage/Current Meters: Compared with modest requirements on signal source characteristics, constraints on DMM performance for voltage and current measurement

are substantially more restrictive and it is generally recommended that a matched pair of instruments be employed. It is also recommended that DMMs be battery powered to avoid ground loop currents and optimum isolation.

Meters should read true RMS voltage/current over a minimum frequency range of 10 Hz to 100 kHz and with a response time of ≤ 1.0 s. Note that the foregoing bandwidth requirement is particularly demanding for current and only higher performing meters will meet this specification¹⁸. Recommended measurement ranges are Voltage - V : ≤ 0.1 mV to ≥ 10.0 V and Current - I : ≤ 0.1 μ A to ≥ 10.0 mA, with minimum 4.5 digit (12-14 bit) resolution.

Again, as for impedance instrumentation, sufficiently high input impedance is key to avoiding loading effects, particularly at higher frequencies. Assuming a high impedance isolation amplifier is employed at front-end of volt meter (as pre previous description), an adequate input impedance specification is ≥ 10 $M\Omega$ / ≤ 100 pF. Alternatively, in absence of external isolation, an minimum input impedance of ≥ 100 $M\Omega$ / ≤ 100 pF is recommended.

Isolation Amplifier: In general, the isolation amplifier is a unity-gain instrumentation amplifier having high input impedance (>100 $M\Omega$, ≤ 20 pF), broad band-width (DC-100 kHz), linear phase characteristics and high common-mode rejection (>100 dB, ≤ 1 kHz).

4.4.3 Field Methods and Procedures:

Four-Electrode Resistivity:

In principal, methods described in Section 4.4.1 can be also be employed for in situ measurement of soil electrical conductivity/resistivity using a quadrapole electrode array as per Figure 47. In fact, the scale and very near-surface focus of landmine detection are uniquely conducive to the objective.

Again, within a uniform, continuous and isotropic medium, the electric field \mathbf{E} and the related current density \mathbf{J} are related via Ohm's law

$$\mathbf{J} = \sigma \mathbf{E}, \tag{140}$$

where σ , denotes the electrical conductivity. Furthermore, noting that the electric field is the gradient of a related scalar potential V ,

$$\mathbf{E} = -\nabla V, \tag{141}$$

¹⁸ Although use of an external, current-sampling shunt resistor is generally discouraged, where employed, it is imperative that the resistor have a sufficiently low temperature coefficient (≤ 20 ppm/degree C) and should handle no more than 10% of rated power. It should also be appreciated that related current bandwidth is inevitably reduced (due to stray capacitance effects) in comparison with related voltage specification.

we have

$$\mathbf{J} = -\sigma \nabla V. \quad (142)$$

Assuming conservation of charge and uniform conductivity, the potential field arising for a point (current source) electrode delivering steady-state current I follows as

$$V(r) = \frac{I}{2\pi\sigma} \frac{1}{r}, \quad (143)$$

where r denotes radial distance from the point electrode. As illustrated in the upper panel of Figure 48, resulting equipotential surfaces are hemispheres everywhere orthogonal to radially directed current flow. Now, assuming a second point (current sink) electrode of equal strength and opposite polarity at some finite distance, the combined potential at an arbitrary point P_1 is

$$V = \frac{I}{2\pi\sigma} \left(\frac{1}{r_1} - \frac{1}{r_2} \right), \quad (144)$$

where r_1 and r_2 denote radial distances between respective current electrodes, I_1 and I_2 , and the point P_1 . Again, the resulting current flow pattern and orthogonal equipotentials are illustrated in Figure 48.

Now, consider the linear four-pole electrode array depicted in the lower panel of Figure 48. Note that the configuration comprises two potential electrodes located within the interval between two current electrodes driven by a signal source. In general, the separation between any two electrodes is arbitrary. It follows from foregoing standard development that the potential difference measured between the interior electrodes is

$$\Delta V = \frac{I}{2\pi\sigma} \left[\left(\frac{1}{r_1} - \frac{1}{r_2} \right) - \left(\frac{1}{r_3} - \frac{1}{r_4} \right) \right]. \quad (145)$$

Solving for conductivity, we obtain

$$\sigma = \frac{1}{2\pi} \left(\frac{I}{\Delta V} \right) \left[\left(\frac{1}{r_1} - \frac{1}{r_2} \right) - \left(\frac{1}{r_3} - \frac{1}{r_4} \right) \right] \quad (146)$$

or, alternatively, for the corresponding electrical resistivity

$$\rho = \frac{1}{\sigma} = 2\pi \left(\frac{\Delta V}{I} \right) \left[\left(\frac{1}{r_1} - \frac{1}{r_2} \right) - \left(\frac{1}{r_3} - \frac{1}{r_4} \right) \right]^{-1}. \quad (147)$$

In general, the result in Equation (147) is referred to as the apparent electrical resistivity

$$\rho_a = \gamma R, \quad (148)$$

where $R = \Delta V/I$ is the measured electrical resistance and

$$\gamma = 2\pi \left[\left(\frac{1}{r_1} - \frac{1}{r_2} \right) - \left(\frac{1}{r_3} - \frac{1}{r_4} \right) \right]^{-1} \quad (148)$$

is a geometrical factor accounting for the influence of the particular electrode arrangement. The most common and routinely employed configuration for soils characterization is the Wenner array, having a constant electrode interval a . Substituting $r_1 = r_4 = a$ and $r_2 = r_3 = 2a$ in Equation (148) yields $\gamma = 2\pi a$ and the resulting apparent resistivity $\rho_a = 2\pi a R$. It emphasized that only for a uniform, isotropic ground do we have $\rho = \rho_a$.

As regards the depth of investigation for in situ four-electrode resistivity measurements, initial insight can be obtained by considering the distribution of subsurface current density. In particular, assuming a uniform soil, the horizontally directed current density at arbitrary point P at depth z within the vertical plane of current electrodes C_1 and C_2 (Figure 48) follows from Equations (142) and (144) as

$$\begin{aligned} J_x &= -\sigma \frac{\partial V}{\partial x} \\ &= -\frac{I}{2\pi} \frac{\partial}{\partial x} \left(\frac{1}{r_1} - \frac{1}{r_2} \right), \end{aligned} \quad (150)$$

where $r_1 = (x^2 + z^2)^{1/2}$ and $r_2 = [(\ell - x)^2 + z^2]^{1/2}$, ℓ denoting the separation between current injection electrodes and x represents an arbitrary offset as depicted in Figure 48. Now, on substituting r_1 and r_2 and for point P located at depth z beneath the dipole midpoint ($x = \ell/2$), we obtain

$$J_x(z) = \frac{I}{2\pi} \frac{\ell}{(\ell^2/4 + z^2)^{3/2}}. \quad (151)$$

The predicted x-directed current density for a fixed ℓ -length dipole is displayed in the upper panel of Figure 49 as a function of z/ℓ and with normalization by the corresponding surface current density $J_0 = J_x(0) = 4I/\pi\ell^2$. As anticipated, current density decreases monotonically with increasing depth and is reduced to 30% of maximum surface value at $z/\ell \approx 0.56$. What is more significant, however, is the variation of horizontal current density for fixed depth z as a function of variable dipole length ℓ . This result is also displayed in Figure 49 with normalization by the maximum value, occurring in general for $z/\ell = 1/\sqrt{2} \approx 0.71$. In effect, this result reveals the considerable extent to which the sampling of a specified depth interval is dependent on array aperture and the degree of related resolution. Having said this, however, it is important to appreciate that the foregoing result addresses only source related sensitivity (“illumination”) and ignores the influence of depth-selective sampling characteristics associated with a particular potential electrode arrangements in relation to the source current dipole.

Corresponding sensitivity functions (Fréchet derivatives), reflecting the combined depth sampling characteristics of a given linear four-pole electrode configuration on

a uniform conductive half-space are predicted by the following relation reported by Oldenburg (1978)

$$S(r, z) = s(r_1, z) - s(r_2, z) - s(r_3, z) + s(r_4, z), \quad (152)$$

where

$$s(r_k, z) = \frac{1}{r_k} \frac{(2z/r_k)^2}{[1 + (2z/r_k)^2]^{3/2}}.$$

Computed sensitivities are displayed in the lower panel of Figure 49 for both the Wenner array and an alternative (Schlumberger) configuration, having $r_4 = r_2$, as for the Wenner array, but with potential electrode interval $\ell_V = r_2 - r_1 = r_3 - r_4 \ll \ell$. In particular, Figure 49 depicts the case for $\ell_V/\ell = 0.05$ compared with $\ell_V/\ell = 0.33$ for the Wenner array. It is notable that in addition to a substantially reduced sensitivity level (reflecting relatively limited voltage difference for minimally separated potential electrodes), peak sensitivity is marginally deeper and less well focused. In other words, the Schlumberger array provides marginally lower depth resolution than the Wenner configuration. However, the primary advantage of the Wenner configuration is enhanced sensitivity. Note that maximum sensitivity for the Wenner configuration occurs at approximately $z/\ell = 0.2$, consistent with a commonly accepted investigation depth of roughly $a/2$ (see also Roy and Apparao, 1971; Barker, 1989).

An alternative perspective on the effective depth of investigation considers the corresponding integrated sensitivities given by $\Sigma(r, z) = \int_0^z S(r, x) dx$.¹⁹ Corresponding results are also displayed in the lower panel of Figure 49 as functions of z/ℓ . It is noted that normalized (scaled by associated maximum value) integrated sensitivity for the Wenner configuration only marginally exceeds that for the Schlumberger array for given z/ℓ . More significantly, it is observed that peak sensitivity corresponds with an integrated sensitivity of approximately 30% of maximum, while 70% of maximum is reached only for z approaching 0.5ℓ ($z \approx 1.5a$). Altogether, foregoing results suggest that, in theory, the Wenner configuration provides relatively enhanced sensitivity and an effective investigation range approximately equivalent to electrode interval a .

¹⁹ The resulting integrated sensitivity is given by

$$\Sigma(r, z) = \Sigma(r_1, z) - \Sigma(r_2, z) - \Sigma(r_3, z) + \Sigma(r_4, z),$$

where

$$\Sigma(r, z) = \frac{(z/r_k)^2}{r_k} \left[\frac{\sinh^{-1}(2z/r_k)}{(2/r_k)^3} - \frac{z}{(z/r_k)^2 [(2z/r_k)^2 + 1]^{1/2}} \right].$$

Figure 50 displays corresponding two-dimensional sensitivity distributions for the same two arrays, albeit with a substantially larger $\ell_V/\ell \approx 0.175$ ratio for the Schlumberger array (Dahlin and Zhou, 2004).

In practice, soils are rarely uniform, particularly surface soils, and it is important to appreciate related limitations of foregoing development. Where significant depth dependence or stratification is expected, it is recommended that small-scale vertical electrical soundings (VES) be acquired and that appropriate computer-based inversion methods be applied to yield related characterization of depth-dependent electrical conductivity. Qualitative indication of non-uniformity is obtained by gauging the related extent and sense of measured apparent conductivity/resistivity with incremental increase of electrode interval a . Where significant variation is observed, an alternative to computer-based inversion is to acquire a sequence of small-scale fixed-interval measurements at incremental depth within one or several test pits.

Although only limited testing has been carried out, initial results suggest that small-scale quadrupole measurements employing a standard function generator and matched digital multimeters is a viable approach for in situ characterization of frequency dependent electrical conductivity/resistivity of near-surface soils. Related research and development, however, remains a work in progress.

Preliminary results for two local soils are displayed in Figures 51. In particular, apparent electrical resistivity is displayed for loam and sand soils under generally moist conditions and following one or more minor precipitation events. Measured apparent electrical resistivity for Wenner electrode intervals $a=10, 20$ and 40 cm indicates that depth-dependent resistivity is significantly different for the two soils. As anticipated the sand soil is generally more resistive than the loam soil. Moreover, relatively resistive surface conditions ($a=10-20$ cm) for the sand are consistent with higher porosity/permeability and lower moisture retention capacity, permitting the relatively rapid downward percolation of precipitation. In contrast, the loam soil is substantially more conductive at surface and resistive at depth ($a=40$ cm).

More significantly, and consistent with general expectation, the apparent resistivity of both soils decreases significantly with increasing frequency (low-frequency AC resistivity (10 Hz) is generally in close agreement with commutated DC measurements). Moreover, as anticipated, chargeability (Equation 139) for the loam soil (10 Hz-1 kHz) is roughly twice that for the sand. As for initial laboratory measurements using the same instrumentation, however, abrupt and/or accelerated fall-off at frequencies above approximately 10 kHz is likely attributable to loading effects that have subsequently been addressed by providing enhanced isolation at potential measurement inputs. In addition, irregular high frequency variation (increased apparent resistivity in the range of 5-20 kHz) observed for the sand soil with $a = 0.4$ m may reflect similar instrumental effects.

Unfortunately, due to the preliminary nature of these experiments, actual soil moisture levels and precipitation history were not monitored. In general, further testing is required to: 1. verify the effectiveness of enhanced isolation (as per laboratory measurements); 2. investigate potential influence of limited signal levels for larger electrode intervals; and 3. to assess performance over a wider range of soil conditions, including more conductive soils. It is also planned to investigate the application of basic 1D inversion for frequency/depth-dependent resistivity/conductivity structure.

FDEM Conductivity:

Alternatively, field measurements of electrical conductivity can be acquired via a range of dual-coil frequency domain electromagnetic (FDEM) devices that are primarily designed for engineering and agricultural investigations. A sample of representative instruments is pictured in Figure 52, with related brief description in Section 4.4.4.

In general, FDEM conductivity meters operate in the so-called low induction number (LIN) regime. In particular, with reference to previous related development in Section 3.1, the LIN regime is defined as $\eta \ll 1.0$ and, in practice, instruments are designed to operate within the range $\eta < 0.5$ as outlined in Figure 53, where the quadrature response is approximately a linear function of conductivity. More generally, as emphasized in Section 3.1, the response characteristics of a given dual-coil configuration are a complicated function of coil orientation and frequency (e.g. Tabbagh, 1986). However, commercially available systems are typically based on a fixed-offset coplanar coil system that is operable in either horizontal coplanar (HC or “vertical dipole”) or vertical coplanar (VC or “horizontal dipole”) via 90 degree axial rotation.

As per Equation (29) in Section 3.1, the induction number is given by

$$\eta = \alpha s = \frac{s}{d_s} = (\pi f \mu \sigma)^{1/2} s, \quad (29)$$

where the so-called response parameter α is the real part of the low-frequency (quasi-static) propagation constant $\gamma \approx (i2\pi f \mu \sigma)^{1/2}$ (see Chapter 2, Equation 12) and effectively the reciprocal of the corresponding skin depth $d_s = (\pi f \mu \sigma)^{-1/2}$. s denotes the separation between transmitter and receiver coils.

Under the LIN assumption $s \ll d_s$ for coplanar coils, the quadrature component of the secondary to primary magnetic field ratio H_s/H_p (see Footnote 8 - Equation 37.5) at the receiver coil can be approximated (McNeill, 1980, Kaufman and Keller, 1983) as

$$\left(\frac{H_s}{H_p} \right)_Q \approx \frac{\pi f \mu \sigma s^2}{2}, \quad (153)$$

with result that an appropriately designed FDEM instrument is capable of reading electrical conductivity directly via appropriate calibration and scaling.

That is,

$$\sigma = \gamma_Q \left(\frac{H_s}{H_p} \right)_Q, \quad (154)$$

where γ_Q denotes an instrument-specific scaling factor.

In complete analogy with sensitivity functions described for quadrapole electrode arrays, corresponding relations have been derived (McNeill, 1980; Kaufman and Keller, 1983) for the s -weighted depth sensitivity of horizontal (HC) and vertical (VC) coplanar systems. Results are respectively

$$S_{HC-Q}(Z) = \frac{4Z}{(4Z^2 + 1)^{3/2}} \quad (155)$$

and

$$S_{VC-Q}(Z) = 2 - \frac{4Z}{(4Z^2 + 1)^{1/2}} \quad (156)$$

where $Z = z/s$. Foregoing results, depicted graphically in Figure 54, illustrate that while the horizontal coplanar (“vertical dipole”) coil configuration yields depth-focused sampling characteristics similar to those for quadrapole electrical arrays, the vertical coplanar (“horizontal dipole”) configuration has maximum sensitivity at surface, decreasing monotonically with increasing depth. In effect, measured conductivity represents a corresponding depth-weighted average value. In the lower panel of Figure 54 we display corresponding integrated sensitivities $\Sigma(Z) = \int_0^Z S(x) dx$ ²⁰ and it is notable that the vertical coplanar coil arrangement attains 70% of integrated response within approximately $z = 0.75s$ compared with roughly twice that $z = 1.5s$ for the horizontal coplanar configuration.

Given the scale of smaller FDEM instruments ($s \approx 1.0$ m), foregoing results suggest that these devices are not ideally suited for the limited depth of interest in connection with metal detector performance evaluation. Although depth sensitivity characteristics can be selectively focused to some degree by appropriate adjustment of sensor height above grade, the extent of potential measurement bias due to deeper soils should be given due consideration.

As described above for four-electrode electrical conductivity measurements, vertical electromagnetic soundings can be acquired by recording a series of measurements with the instrument raised incrementally above grade. Computer-based inversion methods are applied to resulting measurements to derive an optimized estimate of actual depth-dependent electrical conductivity. Similarly, a rapid semi-quantitative indication of depth-variability is obtained by noting the variation in instrument readings as the

²⁰ Corresponding integrated sensitivities follow from Equations (155) and (156) as

$$\Sigma_{HC-Q}(Z) = 1 - 1/(4Z^2 + 1)^{1/2} \quad \Sigma_{VC-Q}(Z) = 1 + 2Z - (4Z^2 + 1)^{1/2}.$$

device is raised from grade to a height of approximately $1.5s$. For a uniform soil, displayed conductivity decrease monotonically with increasing height in accordance with integrated sensitivity relations in the lower panel of Figure 54. In particular, s -weighted height dependent response above a uniform ground is given by $R(H) = \int_H^\infty S(x) dx$ ²¹, where $H = h/s$ and h is height above grade. Corresponding response characteristics are depicted in Figure 54 (see McNiell and Bosnar, 1999).

A similar semi-quantitative assessment of spatial heterogeneity is obtained by comparing measurements at grade with the instrument in two orthogonal orientations. For a uniform or vertically stratified soil, the two readings are identical and, in general, the degree of departure between the two readings is directly related to the extent of lateral heterogeneity.

Finally, it is our experience that FDEM conductivity meters are not particularly accurate or stable in an absolute sense, with related error due principally to imperfect nulling of the the primary field and related thermal drift. Consequently, where instruments of this variety are to be employed, the device should be operated in surface sensitive configuration (i.e. appropriate coil orientation / sensor height) and manufacturer specified calibration adjustments should be carried out regularly (for optimum accuracy in advance of individual measurements), to control zero drift. In general, while FDEM instruments are clearly advantageous for mapping spatial variability in soil electrical conductivity, it is our experience that four-electrode measurements are preferable for accurate absolute characterization, including for provision of calibration and constraints on FDEM mapping.

4.4.4 Field Instrumentation:

Four-Electrode Resistivity:

Instrumentation requirements for in situ four-electrode conductivity (resistivity) measurement are largely the same as described in Section 4.4.2 for equivalent laboratory measurements. As noted, related research and development remains ongoing. However, it is clear that principal restrictions are limited source/transmitter voltage and the input impedance of potential measurement instrumentation. As a practical matter, even reasonably high-voltage (>30 Vpp) AC waveform generators are a rare commodity and, although there is no shortage of audio frequency amplifiers, amplifiers having an upper band-limit beyond 20 kHz are also relatively scarce. In general, electrode contact resistance is the chief obstacle, with considerable source voltage required to establish a sufficient test current level (nominally > 0.1 mA). Similarly, while it is not unusual for voltmeters (and, particularly, “electrometers”) to provide a DC input resistance in excess of 100 M Ω (and as high as 100 G Ω), it is rare for AC

²¹ Resulting response functions follow from Equations (155) and (156) as

$$R_{HC-Q}(H) = 1/(4H^2 + 1)^{1/2} \quad R_{VC-Q}(H) = (4H^2 + 1)^{1/2} - 2H.$$

input impedance to exceed $10\text{ M}\Omega$, typically shunted by $<100\text{ pF}$, due to limitations on effective bandwidth (i.e. time constant). For this reason, an isolation amplifier (see Section 4.4.2), having input impedance in excess of $100\text{ M}\Omega$, is a necessity to avoid related loading effects.

As regards the electrode array, it is recommended that copper or stainless electrodes be used with a minimum diameter $>5.0\text{ mm}$ and, as a rule of thumb, electrodes should not be inserted to a depth exceeding approximately $1/5$ of the electrode interval a . Although it may be advantageous to employ porous, non-polarizable electrodes for potential detection, preliminary comparison between stainless and Cu-CuSO_4 electrodes has revealed no indication of significant electrode polarization in tested soils. Finally, it is recommended that the length of all leads be kept to minimum and that coaxial cabling be employed to as great an extent as possible.

Again, as for laboratory measurements, it is also possible to use a precision impedance analyzer or LCR meter to the extent that it is sufficiently portable. However, as discussed in Sections 4.4.1 and 4.4.2, the common auto-balancing bridge design is not designed for four-electrode measurements and related measurement error can be substantial, particularly at high-frequency and for resistive soils. In general, regardless of instrumentation, it is recommended that characterization of frequency dependent soil electrical conductivity be constrained by coincident DC measurements with a integrated and purpose-built resistivity meter.

FDEM Conductivity Meters:

A range of FDEM conductivity meters are commercially available. A sample of common instruments is pictured in Figure 52, together with related instrument design parameters. As noted, the vast majority of commercially produced instruments employ a coplanar coil arrangement. However, we are aware of at least one small-scale instrument (DUALEM-1S: $f=9\text{ kHz}$, $s=1.0\text{ m}$) that combines a perpendicular coil arrangement with vertical coplanar coils, to yield complementary surface sensitive and depth focused sampling characteristics. The Geonics EM38-DD and EM38-MK2 provide similar dual sensitivity characteristics by configuring two separate coplanar instruments in orthogonal orientation about axis (the latter instrument is a recent integrated system with added flexibility of dual coil separations of 1.0 m and 0.5 m). Note (Figure 52) that in addition to single frequency devices, instruments providing multiple measurement frequencies are also available (e.g. Geopex GEM-2 and GSSI EMP-400), allowing assessment of related frequency dependence and associated viscous influence on TDEM sensors. Fortunately, under LIN conditions, depth sensitivities given by Equations (155-156) are not significantly dependent on frequency, so that variable frequency measurements with a given device provides direct indication of electrical dispersion (assuming accurate calibration adjustments and linear response characteristics).

4.5 Magnetic Parameters - Measurement:

Although there are no formalized standards for measurement of soil magnetic properties, laboratory measurement of magnetic susceptibility and related frequency dependence via the Bartington MS2B dual frequency system is a de facto standard. As described in Section 3.3, magnetic viscosity and related frequency dispersion of the magnetic susceptibility have a uniquely significant influence on the performance of pulse induction metal detectors and consequently, development and assessment of instrumentation for characterization of frequency-dependent magnetic parameters has been a principal focus. We begin by describing impedance based measurements as previously developed in Section 4.3 and compare results with corresponding measurements via the Bartington MS2B and the recently available SM-100 multi-frequency system from ZH Instruments. We subsequently provide a brief description of portable systems for in situ susceptibility measurement.

4.5.1 Laboratory Methods and Procedures:

At the outset of work reported herein, characterization of frequency-dependent susceptibility relied primarily on the Bartington MS2B dual frequency system, yielding magnetic susceptibility at 456 Hz and 4.65 kHz. Consequently, in connection with measurement of frequency-dependent electrical conductivity our initial aim was to investigate the practical potential of multi-frequency impedance-based measurements of complex magnetic susceptibility as developed in Section 4.3.

Initially and in analogy with the soil-box sample-fixture described in Section 4.4.1, a simple solenoidal sample fixture was fabricated to permit impedance analysis of soil magnetic parameters. The prototype fixture is displayed in Figure 55 together with pertinent data and a graph, depicting theory-predicted axial magnetic flux density as a function of position along the coil's axis (with reference to coil midpoint). Axial flux density is computed via the following approximate relations

$$B_x(x) \approx \frac{\mu NI}{2\ell} \left(\frac{\ell/2 - x}{[R^2 + (\ell/2 - x)^2]^{1/2}} + \frac{\ell/2 + x}{[R^2 + (\ell/2 + x)^2]^{1/2}} \right); \quad -\frac{\ell}{2} \leq x \leq \frac{\ell}{2}$$

$$B_x(x) \approx \frac{\mu NI}{2\ell} \left(\frac{\ell/2 + x}{[R^2 + (\ell/2 + x)^2]^{1/2}} - \frac{\ell/2 - x}{[R^2 + (\ell/2 - x)^2]^{1/2}} \right); \quad |x| > \frac{\ell}{2} \quad (157)$$

for an ℓ -length solenoid about the x-axis, centered on the origin and comprising N closely spaced turns of radius R (see Purcell, 1963). In particular, peak flux density at the center of the test fixture is approximately

$$B_x(0) \approx \frac{\mu_0 NI}{(4R^2 + \ell^2)^{1/2}}, \quad (158)$$

yielding $B \approx 12 \mu\text{T}$ and corresponding field $H = B/\mu_0 \approx 10 \text{ A/m}$ for a nominal drive current of $I = 10 \text{ mA}$,

A rough estimate of corresponding self inductance follows as

$$L_0 \approx \frac{\pi R^2 N B_x(0)}{I} = \frac{\mu_0 \pi R^2 N^2}{(4R^2 + \ell^2)^{1/2}}, \quad (159)$$

with result $L_0 \approx 110 \mu\text{H}$ for the air-cored fixture. A more accurate approximation (Wheeler, 1982)

$$L_0 \approx \frac{10\pi\mu_0 N^2 R^2}{9R + 10\ell} \quad (160),$$

yields $L_0 = 98 \mu\text{H}$, in reasonably good agreement with a measured inductance of $L_0 \approx 102 \mu\text{H}$.

Complete frequency-dependent complex impedance characteristics of the fixture (measured via a HP 4192A low-frequency impedance analyzer) are displayed in Figure 56. By design, the fixture's effective resistance and inductance are roughly frequency independent over the desired measurement band of 100 Hz to 100 kHz.

As a practical matter it is difficult to achieve a flat response over more than approximately two or three decades. Band limits involve tradeoffs between resistance, inductance and capacitance of coil windings. Although the useful measurement band can extend significantly lower, the transition frequency $f_{RL} = R_0/2\pi L_0$ may be assumed as a conservative lower band-limit. High-frequency response is ultimately restricted by the coil-specific self resonant frequency $f_0^* = 1/2\pi(L_0 C_0)^{1/2}$ (approximately 3 MHz for the present fixture).

As developed in Section 4.3, soil magnetic susceptibility is determined by measuring the deviation in the inductance $\Delta L = L - L_0$ and/or resistance $\Delta R = R - R_0$ of the test fixture on inserting the sample core. As pictured in Figure 55, the soil sample is contained in thin-walled sample tube, having outside diameter only marginally less than the inside diameter of the coil former. As a first approximation, in-phase and quadrature components of the complex soil magnetic susceptibility are given by Equations 137 and 138 as $\chi' = \Delta L/\gamma_\mu \mu_0 = \Delta L/L_0$ and $\chi'' = \Delta R/2\pi f \gamma_\mu \mu_0 = \Delta R/2\pi f L_0$, respectively.

More precise relations, accounting for actual core radius are

$$\chi' = K_f \frac{A_{coil}}{A_{core}} \frac{\Delta L}{L_0} \quad (161)$$

$$\chi'' = K_f \frac{A_{coil}}{A_{core}} \frac{\Delta R}{2\pi f L_0}, \quad (162)$$

where A_{coil} and A_{core} denote respective cross-sectional areas and K_f represents an empirical correction factor accounting for shape-related demagnetization and residual fixture effects (Epstein, 1954). In practice, given $\mu_r \approx 1.0$ for soils and assuming a sufficiently long sample core ($\geq \sim 3\ell$), demagnetization effects are minimal. The residual fixture constant K_f is determined by way of calibration with a chemical compound having known magnetic susceptibility.

Initial calibration of the prototype fixture coil was carried using reagent-grade manganese carbonate (MnCO_3), an antiferromagnetic (parasitic ferromagnetic) compound with well established and non-dispersive mass susceptibility $\chi_\rho = 1.25 \times 10^{-6} \text{ m}^3/\text{kg}$ at 20°C (Weast, 1971). Results are summarized in Figure 57, depicting measured real-valued mass susceptibility $\chi_\rho = \chi'/\rho_b$, where ρ_b denotes bulk mass density, as a function of test frequency between 100 Hz and 100 kHz. Inductance measurements were acquired via a HP4274A precision LCR meter. In general, there is approximate agreement with the tabulated value (Weast, 1971) and also with measurements reported by Fukuma (2000) for two commonly used instruments (Bartington MS2B and AGICO Kappabridge KLY-3). Subsequent independent measurements via DRDC's Bartington MS2B were also consistent ($\chi_\rho = 1.212 \times 10^{-6} \text{ m}^3/\text{kg}$). Accepting the tabulated value, a mean measured mass susceptibility of $\chi_\rho = 1.1834 \times 10^{-6} \text{ m}^3/\text{kg}$ via measured inductance contrast ΔL implies a fixture calibration constant $K_f = 1.053$.

Subsequently, in connection with a parallel investigation of commercially available instruments for measurement of soil magnetic susceptibility (North, 2006), an additional calibration check was undertaken on a paramagnetic Gd_2O_3 (gadolinium oxide) standard supplied by the USACE-ERDC (North, 2005). Again, measured susceptibility was on average in approximate agreement with results of an inter-laboratory calibration effort reported by Sagnotti, et al. (2003). Results are displayed in Figure 58.

While initial calibration results establish the viability of direct inductance susceptibility measurements, substantial deviation is observed about mean susceptibility values. To a significant extent, observed measurement error has been subsequently reduced by improvements to the fixture apparatus and through development of computer-based measurement control software. Details are provided in Section 4.5.2.

Ultimately, the practical limitation of direct inductance measurements is the very considerable dynamic range required to resolve a necessarily small deviation in a relatively large quantity. In particular, it follows directly from Equation 137 that a basic accuracy of 0.01-0.1 % for highest precision impedance measurement devices imposes an effective limit on volume susceptibility resolution on the order of 10^{-4} SI. In practice, an effective resolution approaching 10^{-5} SI can be achieved for real-valued susceptibility via measurement averaging and with real-time computer-based compensation for thermal drift associated with minor temperature-dependent fluctuation of fixture geometry. However, because the quadrature susceptibility is typically an order

of magnitude smaller and because fixture resistance R_0 is dramatically more sensitive to thermal fluctuation, corresponding resolution would be substantially lower and, consequently, related measurement of quadrature susceptibility has not been pursued.

As we shall see in connection with subsequent comparison of susceptibility measurements for a number of DRDC reference soils, the accuracy of special purpose susceptibility meters, employing a resonant circuit approach, is approximately an order of magnitude better.

Resonant frequency susceptibility meters, including the Bartington MS2B and ZH Instruments SM-100 are based on tuned LC oscillator circuits that incorporate the sensor coil as the inductive circuit element. As for direct inductance measurements, magnetic susceptibility is measured via a two-step measurement cycle, comprising an initial null or calibration reading for the air-cored sensor and a subsequent reading with the sample inserted into the sensor core. Rather than measuring the resulting change in complex impedance, however, these instruments detect a corresponding shift in the resonant frequency $\Delta f^* = f^* - f_0^*$, where $f_0^* = 1/2\pi(L_0\tilde{C}_0)^{1/2}$ is the reference, open-coil resonant frequency and $f^* = 1/2\pi(L\tilde{C}_0)^{1/2}$ is the corresponding resonant frequency on insertion of the sample core. Assuming the coil's effective capacitance \tilde{C}_0 (including fixed or adjustable tuning) is constant, the measured shift in resonant frequency yields the corresponding inductance contrast ΔL and related susceptibility estimate $\chi' = \Delta L/\gamma_\mu\mu_0$, where γ_μ denotes the appropriate coil or fixture constant. The advantage is that frequency (counting) measurements are substantially more accurate than complex impedance (voltage) measurements, particularly with limited dynamic range.

Specific circuit details of MS2B and SM-100 instruments have not been described by the manufacturers and, consequently, it is uncertain whether the tuned circuit is driven by a reference oscillator or whether the resonant frequency shift is measured directly, as a deviation from balanced mixed output or via detection of related phase-shift. Precise mode of frequency selection/tuning for dual or multi-frequency measurement capability is also uncertain, but presumably involves manual or relay controlled switching of matched LC circuit components. Interestingly, however, limited measurements of frequency dependent susceptibility presented here and elsewhere, suggest that dual frequency measurement may, ultimately, provide sufficient characterization in practice.

Figures 59, 60 and 61 display measured frequency-dependent magnetic susceptibility for three DRDC reference soils having significant but substantially different magnetic characteristics. In general, there is good agreement between magnetic susceptibility determined via complex impedance analysis and corresponding measurements with commercially available resonant frequency instruments. Results also reveal a range of interesting and potentially significant issues regarding the influence of soil texture and heterogeneity on measured susceptibility and the extent of related error.

To facilitate meaningful comparison of results for a given soil and between soils, mass-specific susceptibility $\chi_\rho = \chi/\rho$ is charted to account for variable sample compaction and related effect of mass density ρ . In general, it is recommended that mass-specific susceptibility be the primary reported quantity. Alternatively, where volume-specific susceptibility is reported, sample density should also be specified. Ideally, $\rho = \rho_b$, where ρ_b denotes dry bulk density. However, in general, for finite moisture content $\rho > \rho_b$ and the influence of soil moisture level is potentially significant.

As discussed in Sections 3.3.4 and 3.3.6, a common measure of frequency dependence of magnetic susceptibility is

$$\chi_{FD} = \frac{\chi_{LF} - \chi_{HF}}{\chi_{LF}} \times 100\%. \quad (163)$$

However, unlike the electrical chargeability defined in Sections 3.3.7 and 4.4.1, χ_{FD} is referred to a specific measurement band, with χ_{LF} and χ_{HF} denoting magnetic susceptibility at measurement frequencies f_L and f_H a decade apart (i.e. $\log(f_H/f_L) = 1$). In particular, χ_{FD} was principally established in connection with the Bartington MS2B system with measurement frequencies $f_L = 465$ Hz and $f_H = 4.65$ kHz. As discussed in Section 3.3.6, a more relevant indicator of magnetic dispersion, as it affects TDEM sensors, is the differential susceptibility $\Delta\chi = \chi_{LF} - \chi_{HF}$, which is effectively equivalent to the magnetic viscosity (see Equation 103 and related conditions in Section 3.4)

$$\nu = -\frac{\partial\chi'(f)}{\partial\log f} = \frac{\chi_{LF} - \chi_{HF}}{\log(f_H/f_L)} = \frac{\Delta\chi}{\log(f_H/f_L)} \quad (164)$$

for $\log(f_H/f_L) = 1$. Indeed, it is the magnetic viscosity that is responsible for the sustained time-domain response that effectively masks the conductive signal and thereby degrades performance of pulse induction metal detectors. Consequently, apparent viscosity as indicated by log spectral slope $\nu = \partial\chi(f)/\partial\log f$ is the ideal practical predictor of soil influence on time-domain sensors.

Where multi-frequency characterization of soil magnetic susceptibility is available, and where log spectral slope is approximately constant (typically the case as discussed in Sections 3.3.6 and 3.4), apparent viscosity is determined directly via log-linear regression as $\nu = \partial\chi'(f)/\partial\log f$. Moreover, assuming measurement bandwidth exceeds a decade, the regression-determined viscosity is equivalent to the differential susceptibility $\nu = \Delta\chi$ for any two measurement frequencies separated by a decade.²² In general, for dual frequency measurements at arbitrary frequencies, the corresponding relation is $\nu = \Delta\chi/\log(f_H/f_L)$. Note that for mass-specific susceptibility spectra displayed in Figures 59-61, related magnetic viscosity is $\nu = \nu_\rho\rho$, where $\nu_\rho = \partial\chi_\rho(f)/\partial\log f$ represents slope-predicted viscosity via the mass susceptibility spectrum.

²² In contrast, it is noted that $\chi_{FD} = (\Delta\chi/\chi_{LF}) \times 100\% = (\nu/\chi_{LF}) \times 100\%$ depends on reference frequency f_L and related susceptibility χ_{LF} .

Results for the DRDC Bosnia soil in Figure 59 indicate that this soil possesses a considerable magnetic susceptibility with significant frequency dependence. A relatively non-magnetic gravel fraction was excluded from measurement via dry separation on a #3 mesh (6.73 mm) sieve. Although the effective sample volume of the solenoidal fixture (approximately 100 cc) for direct inductance measurements could clearly accommodate larger grains, coarse-grained soil fractions were excluded to permit consistent comparison with measurement systems employing a relatively limited sample volume (i.e. 10 cc)²³. Measured mass-specific susceptibility at 1 kHz is in the range $\chi_\rho = 4.0\text{-}4.75 \times 10^{-6} \text{ m}^3/\text{kg}$ (mean sample mass density as indicated).

In general, there is good agreement between measurements. Five repeat susceptibility spectra were measured via the direct inductance apparatus for a single sample. Measurements were acquired using a computer controlled ESI 2150 precision LCR meter at ten discrete frequencies between 100 Hz and 100 kHz. Measured susceptibility at each frequency represents a 20-fold average of 50 ms measurements at a field of approximately 50 A/m. Log-linear regression yields the indicated fit and observed misfit provides an indication of effective measurement precision. As anticipated, measurement error is evidently most significant at the band-limits of 100 Hz and 100 kHz. In general, however, results are in good agreement with measurements acquired via the two commercial instruments and indicates that the log-linear decrease in magnetic susceptibility with increasing frequency extends well beyond the range of standard measurements.

Although susceptibility measurements via MS2B and SM-100 instruments are modestly higher, the deviation is likely attributable to sample heterogeneity and relatively smaller sample volumes. In addition to MS2B measurements at 465 Hz and 4.65 kHz for a standard 10 cc sample volume, corresponding spectra are also displayed for readings at 500 Hz, 1 kHz, 2 kHz, 4kHz and 8 kHz as measured by the SM-100 instrument, using both an instrument-standard 35 mm film-canister sample holder (approximately 30 cc) and a Bartington standard 10 cc pot centered within a purpose-built 35 mm adapter (see Section 4.5.2). In each case, 10 susceptibility spectra were acquired within a consistent source field of 80 A/m.²⁴

²³ Specification of a #3 mesh (6.73 mm) sieve involves a subjective trade-off between representative soil characterization and the need for standardized and comparable measurements. A #4 mesh (4.75 mm) is more commonly specified and defines the textural transition between sand and gravel (United Soil Classification - USC system). However, resulting separation is substantially more restrictive and, in contrast, a 3/8 in (9.5 mm) mesh is seemingly too large in relation to a 10 cc sample volume. Additional investigations and consultation are required to establish appropriate standard practice.

²⁴ Note that the ZH Instruments SM-100 provides for variable measurement fields between 10 and 320 A/m. Reported spectra were measured at 80 A/m to permit consistent comparison between the SM-100 and the single-field (80 A/m) Bartington MS2B.

Initially, for SM-100 spectra with the standard 35 mm sample holder, the approximately 30 cc sample was repeatedly reconstituted from a single 100 ml source sample to assess related influence of sample heterogeneity. Corresponding variation in measured susceptibility (Figure 59) is approximately $\pm 0.25 \times 10^{-6} \text{ m}^3/\text{kg}$. Following these measurements, the final sample as tested was set aside for reference. Subsequently, 10 cc measurements were similarly acquired on samples reconstituted from a roughly 50 ml source sample with expectation of proportionally greater measurement fluctuation. However, despite anticipation that sample heterogeneity would have more significant influence, it is observed that measurement error for 10 cc sample volumes is, in fact, considerably lower. Unfortunately, source samples were not consistent for the two experiments, suggesting that the result may simply reflect lesser heterogeneity in the 10 cc source sample. It is also observed that the SM-100 yields a marginally higher susceptibility than the MS2B. To ensure consistent comparison, subsequent measurements were acquired on sub-samples reconstituted from the same 100 ml source sample, prior to sub-sample archiving.

As expected, results for the DRDC Australia-A soil in Figure 60 display similar and substantially greater susceptibility variation for 10 cc measurements with both SM-100 and MS2B instruments compared with SM-100 measurements for the instrument-standard 35 mm sample holder. Here, direct inductance measurements are also in particularly good agreement with commercial instruments, yielding a measured susceptibility of approximately $\chi_\rho = 13.5 \times 10^{-6} \text{ m}^3/\text{kg}$, roughly consistent with the mean of MS2B and SM-100 measurements. In comparison with the DRDC Bosnia soil, the DRDC Australia soil is highly susceptible but with relatively limited frequency dependence, with $\chi_{FD} = 1.0\text{-}1.8\%$ versus $\chi_{FD} = 10.3\text{-}11.5\%$ for the Bosnia soil. It is notable, however, that respective differential susceptibility (viscosity) values $\Delta\chi = 192\text{-}319 \times 10^{-6}$ and $\Delta\chi = 427\text{-}534 \times 10^{-6}$ are substantially closer, illustrating the combined influence of susceptibility magnitude and the related level of dispersion. With respect to CEN-WS7 (CEN, 2008) guidelines (Figure 62) for magnitude of susceptibility, the predicted influence of the Australia-A soil (on FDEM detectors) is *very severe* while the Bosnia soil is only *moderate*. In contrast, according to related guidelines for differential susceptibility (influence on TDEM detectors), the Australia-A soil has a marginally *severe* to *very severe* influence while the Bosnia soil falls clearly within the *very severe* category.

Results in Figure 61 for the DRDC Cambodia-2 reference soil reveal yet different magnetic characteristics. In general, it is observed that the Cambodia-2 soil possesses a relatively lower mass-specific susceptibility with a mean value less than $\chi_\rho = 2.0 \times 10^{-6} \text{ m}^3/\text{kg}$. However, a substantially higher mass density $\bar{\rho} \approx 1730 \text{ kg}/\text{m}^3$, compared with $\bar{\rho} \approx 985 \text{ kg}/\text{m}^3$ for the DRDC Bosnia soil means that corresponding volume-specific susceptibility $\chi \approx 346 \times 10^{-5}$ is considerably higher than the respective value $\chi \approx 197 \times 10^{-5}$ for the Bosnia soil, although both soils fall within the *moderate* CEN-

WS7 category with respect to influence on FDEM metal detectors. Again, it is instructive to notice that while the associated $\chi_{FD} = 4.9\text{-}6.1\%$ is intermediate between DRDC Bosnia and Australia-A soils, the corresponding viscosity or differential susceptibility $\Delta\chi = 116\text{-}189 \times 10^{-6}$ is lowest. The explanation, as discussed in Section 3.6.6, is that despite a substantially larger underlying frequency dependence than for the Australia-A soil, the associated susceptibility is nearly an order of magnitude lower with net result that effective apparent viscosity is also marginally lower, with related effect on TDEM sensors categorized as *severe* according to CEN-WS7 guidelines.

Again, as expected, variation in mass-specific susceptibility as measured by MS2B and SM-100 instruments for a 10 cc sample volume $\sim \pm 1.0 \times 10^{-6}$ m³/kg is roughly similar and substantially larger than the corresponding fluctuation for SM-100 measurements with the instrument-standard 35 mm (~ 30 cc) sample holder. Measured susceptibility via the direct inductance approach is again in good agreement with commercial instruments. In general, the larger sample volume of the solenoid fixture limits the relative influence of soil heterogeneity and this may account for a marginally lower susceptibility as observed for the DRDC Bosnia. However, given exclusion of coarser-grained soil fractions, there also remains some potential that the assumed fixture constant $K_f = 1.053$, based on initial MnCO₃ calibration, may be marginally low.

Comparing the above level of 10 cc measurement error with a corresponding level of $\sim \pm 10.0 \times 10^{-6}$ m³/kg for the DRDC Australia-A soil, it is tempting to conclude that measurement error associated with sample heterogeneity is directly related to the magnitude of related susceptibility. Certainly, there is a direct influence, just as the influence of underlying dispersion on net magnetic viscosity is modulated by the level of susceptibility. However, it is also clear that the scale of magnetic heterogeneity, associated texture, sorting and related compositional characteristics of the soil can have significant influence.

Related effects have been investigated to limited extent by analyzing the susceptibility characteristics of specific soil textural components. In particular, a direct relation between absolute susceptibility and related frequency dependence was initially noted in connection with measurements on DRDC Cambodia reference soils. Although the effect is notable in Figure 61 for the Cambodia-2 soil, it is more evident for the Cambodia-1 soil in Figure 63, where we also display corresponding results for five replicate measurements on fine and coarse-grained components as separated via a standard #10 (2.0 mm) sieve. As anticipated, it is observed that the fine-grained soil component contributes the bulk of magnetic viscosity, having both a higher absolute susceptibility and related dispersion. The relationship between magnetic characteristics and grain-size is characterized in the lower portion of Figure 63, where density-normalized viscosity or differential susceptibility $\Delta\chi/\rho$ and frequency dependence parameter χ_{FD} are charted as functions of mass-specific susceptibility (4.0 kHz

- SM100 and 4.65 kHz - MS2B).

As anticipated measurements for coarse and fine-grained separates define distinct fields, with the fine-grained fraction yielding a more tightly defined data field than the coarse-grained fraction. Of course, bulk-sample measurements display a complicated but systematic mixing relationship with respect to coarse and fine-grained fields. Unfortunately, however, because the separates were not derived from the same bulk sample, the range of bulk-sample measurements is not bracketed by end-member textural fields as should presumably be expected for consistent samples.

To confirm this, similar experiments were undertaken in connection with characterization of the DRDC Australia-B soil, with all measurements acquired on subsamples from a consistent bulk-soil volume. Results are displayed in Figure 64. Here, as anticipated, bulk-sample measurements are roughly bracketed by coarse and fine-grained end-member fields. Unexpectedly, however, it is the coarse-grained fraction that is the primary carrier of magnetic viscosity for the Australia-B soil.

To further investigate the ultimate source of relatively limited magnetic viscosity for the Australia-B soil and noting that the coarse-grained fraction included soil aggregates and soil-encrusted rock fragments, the coarse grained fraction was subsequently washed via distilled water to remove all fine-grained material. Simultaneously, the fine-grained separate was further separated on a #200-mesh (75 μm) sieve. Resulting measurements on residual fractions and adjusted for limited sample volume are included in Figure 65 to better define end-member characteristics associated with bulk-sample magnetic properties. In general, experimental results in Figures 63-65 illustrate significant variability and complexity in the relationships between soil textural composition, related magnetic signatures and corresponding influence on bulk soil magnetic properties. Again, it is noted that gravel fractions exceeding approximately 6.75 mm (#3 mesh) were excluded from testing and that further consideration must be given to appropriate instrumentation (particularly measurement volume) and procedures to ensure that laboratory measurements are adequately representative of in situ soil magnetic characteristics.

To summarize foregoing assessment of DRDC reference soils and related implications for methodology and instrumentation, we highlight the following findings:

1. Tested DRDC reference soils appear to be characterized by log-linear frequency dependence over at least three decades of frequency between 100 Hz and 100 kHz. Results presented here and by others (see related discussion in Section 3.4) appear to support the general validity of basic relations set out in Equation (103) and reflect the exponential relationship between the scale of magnetic grains at the stable single domain, superparamagnetic transition and related time-constants for viscous magnetization. To the extent that emerging consensus on this issue continues to be confirmed, dual frequency susceptibility measurements may be perfectly adequate for characterization of related magnetic viscosity.

2. Soil viscosity $\nu = \Delta\chi/\log(f_H/f_L)$ ($\nu = \Delta\chi$ for $f_H/f_L = 10$) is the optimum performance indicator for soil influence on TDEM sensors and reflects both the magnitude and frequency dependence of soil magnetic susceptibility. It is important to appreciate, however, that magnetic soil components that are chiefly responsible for net susceptibility and viscosity are not necessarily one and the same.
3. Soil heterogeneity can yield substantial measurement error that increases with decreasing sample volume. Consequently, it is recommended that multiple measurements be acquired and that the mean values be reported in connection with instruments employing smaller measurement volumes (e.g. 10 cc). It is also recommended that further consideration be given to development or adaptation of existing instruments for accommodation of larger volume samples.
4. Influence of soil heterogeneity is complicated by significant complexity in the relationships between soil textural composition, related magnetic signatures and corresponding influence on bulk soil magnetic properties.
5. Despite significant exceptions, frequency dependence of susceptibility is less prone to volume-dependent measurement error than is the magnitude of susceptibility.

4.5.2 Laboratory Instrumentation:

Following sections provide additional information and recommendations regarding previously described instrumentation for multi-frequency laboratory characterization of magnetic susceptibility. A brief description of alternative instruments is also provided.

Direct Inductance - Sample Fixture:

Initial design of a prototype solenoid sample fixture for direct inductance measurement of soil magnetic susceptibility was guided by two primary objectives: a substantially larger sample volume than provided by standard instruments and as broad as possible measurement bandwidth. As previously noted, it is difficult to achieve a flat response over more than approximately two or three decades and, in addition to dimensional characteristics, band limits involve tradeoffs between resistance, inductance and effective capacitance of coil windings. In practice, fixture design is guided by use of appropriate approximations for modelling of coil impedance parameters and related response characteristics. Fixture design should also take advantage of unique performance characteristics of the specific impedance analyzer or LCR meter to be used.

In addition, it should be appreciated that accurate and repeatable complex impedance measurements require frequent compensation adjustments and related immobilization of the the fixture and connecting leads (particularly beyond the extent of ground-referenced shielding). The final rigidly mounted fixture configuration employed here

is illustrated in Figure 66, including expanded view of a special purpose connector/switching block to ensure dependable short and open compensation adjustments.

Finally, while previous results illustrate the advantage of a larger measurement volume in limiting measurement uncertainty associated with sample heterogeneity, a smaller fixture has also been developed for use where relatively limited sample is available. In particular, the small-volume fixture displayed in Figure 67 was designed to accommodate the same 35 mm film-canister sample holder employed for the ZH Instruments SM-100. In addition, a simple adapter has been fabricated to accommodate the standard 10 cc sample vial as displayed in Figure 68 (also for use with ZHI SM-100/105). Accurate and repeatable open and short compensation adjustments are accomplished by removing the socketed coil assembly from the fixture base (open), rotating 120 degrees and reinserting connectors in a shorted configuration.

Although no systematic assessment of the 35 mm fixture has been possible within the scope of the current project, an initial test was carried out on a volume-limited sample of Tiva Canyon Tuff provided by USACE-ERDC (North, 2006). Results are depicted in Figure 69. First, as for DRDC reference soils, 10 replicate spectra are displayed for SM-100 measurements using both the instrument-standard 35 mm sample fixture and for 10 cc samples via a 10cc/35 mm adapter. Equivalent dual-frequency measurements are displayed for the MS2B using the standard 10 cc sample vial and for both 1.0 and 0.1 ranges. In all cases measured samples were reconstituted from the same 75 ml source sample. Note that in contrast with measurements on natural soils, replicate measurements display comparatively little variation due to the relatively homogeneous nature of the powdered tuff.

For comparison, five replicate direct-inductance susceptibility spectra were acquired for a single sample of the Tiva Canyon tuff, using the same computer controlled ESI-2150 precision LCR meter, in this case, with the prototype 35 mm sample fixture. In lieu of prior calibration, resulting measured spectra were subsequently adjusted to approximately match the mean susceptibility measured by MS2B and SM-100 instruments at 1 kHz. In effect, an approximate calibration was obtained for the 35 mm fixture, yielding a fixture constant of $K_f \approx 1.5$. As expected, the calibration constant is substantially greater than unity due to the limited aspect (length/diameter) ratio of the coil. Assuming effective calibration to be accurate, however, it is clear that the frequency dependence of direct inductance spectra are, again, in very good agreement with MS2B and SM-100 measurements.

Specifically, it is observed that the Tiva Canyon tuff is characterized by a susceptibility exceeding $\chi_\rho = 1.0 \times 10^{-5} \text{ m}^3/\text{kg}$ at 1 kHz and an unusually high viscosity, or differential susceptibility, approaching $\Delta\chi = 2500 \times 10^{-6}$, with corresponding χ_{FD} approaching 25 %. Moreover, there is some indication of nonlinearity, (i.e. departure from log-linear relation) particularly at higher frequencies that was not observed in connection with DRDC reference soils. Viscosity and χ_{FD} indicated in Figure 69 are

determined by log-linear regression over the frequency range 200 Hz - 20 kHz. Similar results have been obtained by ZH Instruments (2006), using the recently available SM-105, a higher-frequency equivalent of the SM-100 with measurement frequencies extending from 8 kHz to 128 kHz.

The Tiva Canyon tuff, also referred to as Yucca Mountain tuff, is a well characterized and documented volcanic material, incorporating a relatively narrow grain-size distribution of titanomagnetite in the pseudo-single-domain/superparamagnetic range (Worm and Jackson, 1999). Both single-domain and superparamagnetic reference standards have been prepared via selective sampling of the outcrop (Jackson, et al., 2004; Carter-Stiglitz, et al., 2006). It is our understanding (North, 2006) that tested material is a powdered and homogenized mixture of numerous samples and, thus, presumably has a broader grain-size distribution than previously referenced magnetic standards. However, in general, it is clear that the frequency extent of log-linear frequency dependence decreases as the magnetic grain-size distribution narrows and χ_{FD} increases. It is notable that the measured value of $\chi_{FD} \approx 25$ for the Yucca Mountain tuff is considerably higher than the commonly accepted upper limit of $\chi_{FD} \approx 15$ for natural soils (see related discussion in Chapter 3). Finally, while the Tiva Canyon tuff is certainly a useful reference material, it should be appreciated (consistent with theory) that precise magnetic characteristics are significantly dependent on temperature (e.g. Worm and Jackson, 1999).

Impedance Analyzers and Multi-Frequency LCR Meters:

As noted, direct inductance measurement of soil magnetic susceptibility is ultimately limited by the dynamic range and accuracy of inductance measurements. Consequently, required performance specifications are generally more restrictive than for electrical conductivity measurements. In particular, we recommend that the instrument provide a measurement frequency range of 100 Hz - 100 kHz, with minimum of four discrete test frequencies spanning the range (e.g. 100 Hz, 1 kHz, 10 kHz, 50-100 kHz). The instrument should be capable of providing a test current level of at least 10 mA_{RMS} and preferably 100 mA_{RMS} for specified open-coil fixture impedance. Although it is desirable that the test current level be regulated with sufficient compliance to maintain the specified source current, it is more often the case that only the signal voltage level (≥ 1.0 V_{RMS}) is controlled with resulting test current dependent on load impedance. In general, it is recommended that the source signal level (voltage/current) be adjusted to yield a moderate low-field intensity of approximately 50-100 A/m.

In contrast with the necessity of high (≥ 10.0 M Ω) input impedance for measurement of soil electrical conductivity, the instrument's output impedance characteristics are more significant for accurate measurement of inductance and should match as nearly as possible the fixture's low-frequency impedance. Note for some instruments, output

impedance varies with range and this is potentially problematic for broadband measurements due to related variation in accuracy characteristics of the instrument. To assess specific performance potential of a given instrument, however, it is important to consult specified accuracy formulae or tabulated accuracy data as a function of fixture inductance and measurement frequency. In general, the instrument should have a basic accuracy of $\leq 0.1\%$ and a display resolution of at least 5.5 digits. In practice, specific instrument design is typically tuned to yield optimum performance for either capacitance measurements or inductance measurements rather than middle-ground characteristics across the reactance spectrum.

Finally, it is our experience that computer controlled data acquisition, with automated signal averaging and drift correction, is essential for successful direct induction measurement of soil magnetic susceptibility. However, it should be cautioned that the implied resolution of standardized output data strings can exceed instrument accuracy dependent on range and frequency. Again, consult related accuracy formulas or tabulated characteristics. Ultimately, as previously noted, practical limits on measurement accuracy are in large part determined by the precision and stability of compensation adjustments and related manufacturer-specified procedures should be rigorously implemented.

Bartington MS2B:

The Bartington MS2B susceptibility meter (Bartington, 2005) is depicted in Figure 70. The standard MS2B system comprises a MS2 measurement console and a MS2B dual frequency sensor, with measurement frequencies of 465 Hz and 4.65 kHz. Related field intensity is 80 A/m. The MS2B is a stand-alone instrument with integrated keyboard and display. A serial interface is provided for computer based data storage and analysis. As previously described, the MS2B measures magnetic susceptibility by gauging an associated shift in the selected oscillator frequency. The standard measurement sequence, driven by front panel switches, includes an initial null or “ZERO” reading with the sensor coil open, followed by a “MEASURE” reading with the sample positioned within the sensor coil. For improved accuracy, the manufacturer recommends a subsequent open-coil air “MEASUREMENT” reading χ_A following the sample “MEASUREMENT” reading χ_S to control instrument drift over the measurement interval. The corrected volume susceptibility is $\chi = \chi_S - (\chi_A/2)$.

Measurement precision/resolution is selectable from $\times 1$ and $\times 0.1$ ranges. Corresponding measurement periods are 1.2 s and 12 s, respectively (presumably, the $\times 0.1$ range measurement represents a 10-fold average reading) In both cases, measured volume-specific susceptibility is displayed in units of $\times 10^{-5}$ SI and in the latter case with 0.1×10^{-5} SI accuracy (readings can also be displayed in cgs units). Measurement frequency ($f_L=465$ Hz or $f_H=4.65$ kHz) is similarly controlled via a front panel

switch.²⁵

The diameter of the MS2B sensor core is approximately 36 mm and, as per previous discussion, the standard sample holder is a 10 cc cylindrical vial. However, it is emphasized that non-standard containers can also be used with appropriate adjustment of resulting measurements. The Bartington operation manual provides guidance on the use of non-standard sample holders and related required adjustments, including centering of the platen on which the sample is lowered into the sensor coil. It is also noted that the MS2 can be operated with a larger volume, single-frequency sensor. In particular, the MS2B62 sensor core has interior diameter of approximately 62 mm and accommodates a standard 250 cc cylindrical sample holder. The MS2B62 sensor operates at a nominal frequency of 1.64 kHz with a field intensity of approximately 80 A/m, consistent with the MS2B.

Figure 71 illustrates the results of a simple experiment to investigate the sensitivity characteristics of the MS2B sensor and related significance in connection with use of non-standard sample holders. Initially, as per standard operating procedure, sensor platen height was adjusted to yield maximum reading (0.1 scale) for the 1% Fe₃O₄ calibration standard (it is noted that improved adjustment would likely be obtained by utilizing a more highly susceptible standard). Subsequently, the susceptibility of a standard 10 cc sample pot was measured and recorded with incremental addition of a MnCO₃ standard. In particular, 1.00 g increments were added and leveled with due care to minimize any related compaction of the composite sample. Fortunately, 1.00 g increments of the MnCO₃ standard were approximately equivalent to 1 cc volume increments (i.e. $\rho_b \approx 1$ g/cc). The resulting linear relation between volume specific susceptibility (SI) and approximate sample volume is displayed at the upper right of Figure 71.

To investigate the influence of a non-standard sample vial, the experiment was subsequently repeated utilizing the marginally smaller diameter and taller sample pot pictured at the upper left of Figure 71. Measured physical characteristics of the two vials are displayed for reference. In this case, the MnCO₃ standard was added in 0.50 g increments. The corresponding increase as a function of approximate sample volume is displayed at the lower left of Figure 71, with the standard 10 cc pot response (solid line) overlaid for reference. It is noted that the relation is again linear to an approximate sample volume of roughly 8 cc. Note that for the non-standard sample vial, a sample level of 2.3 cm, the nominal height of the standard 10 cc pot, is equivalent to a sample volume of approximately 8 cc. Consequently, it is apparent that the height

²⁵ Note that a sufficient stabilization period should be permitted following change of measurement frequency (experimentation suggests approximately 1 min). The manufacturer recommends that for dual frequency measurements on multiple samples, all samples should be tested at a given frequency and, subsequently, retested at the second frequency following adequate settling period.

of the Bartington 10 cc sample pot was designed to maintain the sample within an optimum range of the sensor midpoint within which the sensor's volume sensitivity is roughly linear. In addition, it is noted that the slope of the linear portion of the sensitivity curve for the non-standard pot is slightly less than that for the standard 10 cc pot, suggesting that within the linear range, volume sensitivity is slightly lower for the smaller diameter sample vial.

In general, experimental results indicate that for a standard 10 cc sample vial, volume susceptibility for a partially filled sample holder can be corrected by the factor h/h_0 , where h denotes an arbitrary height and $h_0 = 2.3$ cm, or by the equivalent volume factor V/V_0 . In general, a similar approach is applicable for any sample holder within the linear sensitivity region and with symmetry about the sensor axis.²⁶ However, it is emphasized that linear volume sensitivity assumes uniform mass density.

Indeed, within the linear sensitivity limit, the sensor is effectively indifferent to volume or equivalent mass sample increments. For example, with reference to the foregoing experiment; if additional sample increments beyond 8 cc were compacted into the non-standard vial, such that the composite sample level remained below the 2.3 cm limit, corresponding susceptibility readings would increase an amount consistent with effective extension of the linear sensitivity trend. Consequently, for an arbitrary sample holder within the linear sensitivity region and with symmetry about the sensor axis, measured susceptibility is linearly related to sample mass as well as sample volume. In fact, in view of the volume biasing effects of variable compaction, it is generally recommended that raw susceptibility readings be converted to mass-specific values via concurrent measurement of sample mass (density) and that mass-specific susceptibility be the primary reported parameter, together with mass density. Having said this, however, it should also be appreciated that sample mass can be skewed by variable soil moisture content and, consequently, samples should be thoroughly air-dried or oven dried at less than 40° C prior to analysis.²⁷

In general, a non-standard sample vial with length extending beyond the linear sensitivity region (assuming symmetry about the sensor access) can be utilized with appropriate calibration via a known reference standard. The appropriate correction factor is $\gamma = \chi/\chi_0$, where χ is the measured susceptibility of the arbitrary standard-filled sample vial and χ_0 denotes the measured susceptibility of the standard-filled 10 cc pot. It is emphasized that calibration measurements for arbitrary and standard

²⁶ For maximum accuracy with partially full or non-standard sample vials, the MS2B platen height should be adjusted for maximum reading prior to subsequent correction by fractional volume V/V_0 .

²⁷ Note that soil magnetic susceptibility for viscous magnetic soils incorporating significant SD-SP content, is temperature dependent and samples should be allowed to stabilize at laboratory temperature prior to analysis (also to avoid thermal affect on measurement instrumentation).

sample pots must allow for readjustment of the platen level for appropriate vertical centering. Moreover, the maximum height of an arbitrary sample pot is restricted by maximum travel of the platen (± 1.0 cm travel and $h_0=2.3$ cm yields maximum vial height of 4.3 cm or, allowing sufficient play for vertical centering, approximately 4.0 cm).

To further establish the sensitivity characteristics of the MS2B sensor, both axial and transaxial field variation were investigated. First, axial sensitivity was established by incrementally increasing the height of the 1% Fe_3O_4 calibration standard above the platen (sensor midpoint). The diagram at upper right of Figure 72 displays the variation of measured volume susceptibility (SI) with increasing sample height (base of sample pot above platen) in 0.5 cm intervals. Note that when the base of the sample pot is located at the upper housing surface level (approximately 4.2 cm), the measured susceptibility $\chi_v = 13.2 \times 10^{-5}$ SI is approximately 4% of the calibrated value $\chi_v = 346.9 \times 10^{-5}$ SI at the sensor midpoint (platen level).

In effect, the observed reduction in measured susceptibility reflects removal of an incremental sample volume from the sensor's linear sensitivity region as previously discussed. As a practical matter, it is noted that calibration of the sensor's vertical sensitivity permits approximate measurement of samples having volume specific susceptibilities beyond the standard operating range of the instrument. For example, the approximate susceptibility of DRDC magnetite soils was measured by positioning a standard 10 cc sample on a sheet of transparent material placed over the sensor cavity and centered on the sensor's axis. Results obtained by calibrated scaling of the raw measured value were in adequate agreement with previous direct-inductance measurements.

Finally, in connection with Figures 71-72, it was previously noted the slope of the sensitivity curve for the non-standard sample pot was marginally less than that for the standard 10 cc pot. It was anticipated that this deviation might reflect variation of field intensity with radial offset from the sensor axis. To investigate the transaxial sensitivity, a small yet responsive probe was fabricated by fixing approximately 0.3 cc of highly susceptible Fe_2O_3 in the cylindrical reservoir of a 1.0 cc syringe (see Figure 73). Related susceptibility measurements were subsequently acquired with probe (oriented vertically) at six incremental positions across the diameter of the platen as illustrated in Figure 73. The process was subsequently repeated with the platen repositioned 0.5 cm and 1.0 cm above the sensor midpoint. Resulting variation of measured susceptibility is displayed at the lower right of Figure 72. It is observed that in all cases, apparent sensitivity is minimum at the axis and increases marginally with radial offset and more significantly with increasing height above the zero referenced platen. It is notable that measured transaxial sensitivity variation is consistent with the marginally lower volume sensitivity observed for the smaller diameter sample pot in Figure 71.

ZH Instruments SM-100/105:

The ZH Instruments SM-100 susceptibility meter (ZH Instruments, 2007) is pictured in Figure 74. In contrast with the stand-alone Bartington MS2B system, control and display functions of the SM-100 are software-implemented via an integrated RS-232 interface. The software control/display panel is displayed in Figure 75. The SM-100 provides substantially more flexibility than the Bartington system, including multiple test frequencies (500 Hz, 1 kHz, 2 kHz, 4 kHz, 8 kHz) and a range of field intensity levels (10 A/m, 20 A/m, 40 A/m, 80 A/m, 160 A/m and 320 A/m). An otherwise equivalent system, the SM-105, offers an extended frequency range (8 kHz, 16 kHz, 32 kHz, 64 kHz, 128 kHz) and a more restricted range of field intensity levels (10 A/m, 20 A/m, 40 A/m, 80 A/m). Test frequency and field intensity parameters are software selectable via a pull-down menu. In addition, SM-100/105 instruments include an integrated scale with 0.01 g resolution, allowing real-time measurement of mass-specific susceptibility.

Although the SM-100 offers substantially greater flexibility in test field characteristics, the fundamental design and measurement sequence is similar to that described for the MS2B. In particular, like the MS2B, the SM-100 measures magnetic susceptibility by gauging an associated shift in the selected oscillator frequency that results on inserting the soil sample into the sensor cavity. Unlike the MS2B, however, the measurement sequence is computer automated with a combination of display and audible prompts cuing the operator to insert and remove the sample and with automatic drift correction implemented in real-time. The corresponding measurement sequence and related drift correction is diagrammatically illustrated in Figure 75.

As previously discussed, the SM-100/105 employs a standard sample holder (35 mm film canister) having approximately 3 times the volume of the Bartington-standard 10 cc vial and, depending, on the scale and extent of soil heterogeneity, this is potentially advantageous. A simple adapter to accommodate the standard 10 cc sample holder is displayed in Figure 68. In general, although project scope did not permit a parallel investigation of SM-100 sensor characteristics, it is reasonable to presume that the sensor has grossly similar sensitivity characteristics and a corresponding linear (i.e. uniform field) sensitivity region. Indeed, measurements acquired for 10 cc samples via the 10 cc to 35 mm adapter were simply scaled by the relative volume factor V_{35}/V_{10} , with resulting excellent agreement for standards. Again, for maximum accuracy it is necessary that the sample volume for a partially full or non-standard sample holder be approximately centered with respect to the sensor axis and the vertical “plane of symmetry” as illustrated in Figure 76. As indicated, two “weighting plates” are supplied with the instrument, one that centers a full 35 mm sample holder and one that centers a half-full 35 mm sample holder. Note that the 10 cc to 35 mm adapter was designed to center the 10 cc sample pot within the standard 35 mm holder and is, consequently, used with the standard (full holder) “weighting plate”.

Finally, no quantitative assessment has been made of accuracy for the integrated strain-gauge mass scale and all reported susceptibility measurements are based on independent measurements of sample mass via a Mettler PE-3600 (0.01 g) bench scale. However, general comparison with corresponding SM-100 measured mass suggests agreement to 0.05-0.1 g.

Alternative Laboratory Instrumentation:

Mention should also be made of another recently developed and commercially available system, the Magnasat developed by Ultradynamics in Australia (Ultradynamics, 2008, North, 2006) and a prototype system developed by the Geophysics Laboratory at the University of Toronto (West and Bailey, 2005). Both instruments employ a null or balanced coil system and yield frequency-dependent complex susceptibility via phase-sensitive detection of the out-of-balance signal produced on insertion of the soil sample. Similar instruments have been previously described by Strangway (1967), Mullins and Tite (1973) and Dabas, et al. (1992). In contrast with the direct inductance approach, a null or balanced coil apparatus offers enhanced resolution by devoting the full extent of system dynamic range to the out-of-balance signal, rather than detecting a corresponding deviation of similar scale in a primary signal several orders of magnitude larger. A simple proof of concept experiment has demonstrated that similar balanced-coil measurements can be acquired using an appropriate dual-coil sample fixture and an off-the-shelf gain-phase analyzer.

There is also a range of single frequency magnetic susceptibility bridges available that could be used in combination to assess frequency dependence of soil magnetic susceptibility. However, where such an approach is taken, instruments should accommodate the same sample holder and due consideration should be given to appropriate and precise inter-calibration. In addition, measurement field intensities should be roughly consistent.

Finally, recent development of special purpose soil magnetic viscosity meters should be noted. In contrast with foregoing frequency-domain instrumentation, viscosity meters are time-domain devices and measure viscosity directly by exposing the sample to a sustained primary magnetic field, subsequently terminating the primary field and gauging the rate of decay of the transient secondary field associated with electromagnetic polarization of the sample. A prototype system has been described by Siegenfeld (2002) and a commercially developed instrument, including a field sensor, is more recently available (Pulsepower Developments, 2008). Measurement windows are in the range 1-100 μ s.

Although direct time-domain measurement of electromagnetic viscosity is clearly of significant interest in connection with assessment of TDEM sensor performance, it is noted that foregoing devices provide no direct indication of absolute magnetic

susceptibility. No testing of these instruments has been undertaken as part of the current study.

4.5.3 Field Methods, Procedures and Instrumentation:

Hand-Held Susceptibility Meter:

Magnetic susceptibility and its frequency variation can be characterized in situ using of a range of special purpose, commercially manufactured instruments. In general, field susceptibility meters are based on the same tuned LC oscillator design and as employed by MS2B and SM-100 laboratory systems. In fact, the Bartington MS2 console can be configured with a handle-mounted MS2D search coil (Figure 77 - left) for single frequency, in situ measurement of soil magnetic susceptibility. A range of hand-held instruments, including the Kappameter KT-6 (Figure 77 - right) are also available.

In place of the cylindrical cavity sensor coil employed for laboratory systems, a planar or low-profile sensor coil comprises the inductive element in the meter's oscillator circuit. The instrument is initially nulled in air and subsequently brought into planar contact with the soil under test for relative measurement of associated susceptibility. Although we are not aware of dual or multi-frequency devices for in situ measurement, instruments are available having a range of operating frequencies so that frequency variation of susceptibility can be established by separate measurements with instruments operating at two or more frequencies.

Unfortunately, due to the variable geometry and limited scale of typical sensor coils (< 10-20 cm), effective measurement volume can differ significantly and is generally restricted to < 5-10 cm. For example, Figure 78 displays the measured depth sensitivity for MS2D and KT-5 (KT-6 equivalent) as reported by Lecoanet, et al. (1999). As a consequence of restricted measurement volume, the effective precision of these instruments is highly sensitive to both soil heterogeneity and surface irregularity. To minimize related influence, the soil surface should be prepared to ensure uniform and continuous sensor contact and measurements should avoid (as possible) anomalous soil heterogeneity to yield readings reflective of mean soil characteristics.

In general, as for in situ electrical conductivity measurements, it is recommended that multiple measurements and appropriate spatial sampling be pursued to characterize mean susceptibility and related spatial variation. Specifically, a series of repeat measurements at each sampling location with the sensor position re-located randomly by a distance comparable to sensor diameter yields useful indication of a representative value and associated deviation. To establish the depth-dependent variation of magnetic susceptibility a sequence of measurements should be acquired at incremental depth within one or several test pits. Finally, Although bulk soil magnetic

susceptibility is typically controlled by magnetic content of the fine-grained soil fraction, the relative susceptibility of larger gravel and cobble-sized grains should also be investigated to assess potential for related magnetic clutter.

In contrast with electrical conductivity measurements, variable soil moisture has only limited diamagnetic influence on soil magnetic properties and, consequently, assessment and monitoring of short-term temporal variation is not ordinarily required.²⁸ In general, temperature dependence is also limited, although potentially significant for highly viscous soils under strong seasonal temperature variation.

FDEM Susceptibility Meters:

Magnetic susceptibility can also be measured via larger dual-coil FDEM devices as previously described for measurement of soil electrical conductivity (see Sections 4.4.4 and Figure 52). Instead of gauging the quadrature response, however, magnetic susceptibility is derived from the in-phase signal component under the same low induction number (LIN) assumption. In particular, as discussed in Section 3.1 and with reference to Equation (29) and Figure 53, it is observed that dependent on coil separation s and for a sufficiently low frequency-conductivity $f\sigma$ product, the induction number η falls within the so-called resistive limit and the in-phase response is almost entirely dependent on magnetic susceptibility and independent of other parameters. In general, for soils having ordinary electrical conductivity ($\sigma \leq 100$ mS/m) and elevated magnetic susceptibility ($\chi \geq 1.0 \times 10^{-3}$), small-scale FDEM devices are typically operating within the resistive limit, particularly at lower operating frequencies, and related magnetic susceptibility is derived directly as

$$\chi = \gamma_I \left(\frac{H_s}{H_p} \right)_I, \quad (165)$$

where γ_I denotes the appropriate instrument-specific scaling factor.²⁹

Again, it should be appreciated that the depth sensitivity of related measurements is strongly dependent on coil orientation and separation and that the effective measurement volume varies accordingly. In analogy with Equations (155) and (156) for the quadrature sensitivity of coplanar coil systems, corresponding expressions for in-phase

²⁸ Note also, experimental investigations by Maier, et al. (2006) appear to confirm that eddy-current effects associated with moisture-dependent soil electrical conductivity have little or no practical influence on the operation of common hand-held susceptibility meters operating at frequencies below 10 kHz.

²⁹ For conductive soils having induction numbers significantly beyond the resistive limit for given instrument parameters, the in-phase response $(H_s/H_p)_I \approx (8/15)(\pi f\mu\sigma s^2)^{3/2}$ is relatively limited and effectively frequency-conductivity $f\sigma$ dominated (see McNeill and Bosnar, 1999).

sensitivity are (McNeill and Bosnar, 1999)

$$S_{HC-I}(Z) = \frac{12Z(8Z^2 - 3)}{(4Z^2 + 1)^{7/2}} \quad (166)$$

and

$$S_{VC-I}(Z) = \frac{12Z}{(4Z^2 + 1)^{5/2}} \quad (167)$$

for horizontal coplanar (HC) and vertical coplanar (VC) systems, respectively. Associated depth sensitivities are depicted in the upper panel of Figure 79, again, as functions of s -normalized depth ($Z = z/s$). Notably, and consistent with Figure 53, the horizontal coplanar sensitivity is negative-valued. More significantly, however, in-phase depth sensitivities for both horizontal and vertical coplanar configurations are well focused, providing considerably better resolution of near-surface conditions than corresponding quadrature conductivity sensitivities in Figure 54. Corresponding integrated sensitivities $\Sigma(Z) = \int_0^Z S(x) dx$ ³⁰ in Figure 79 indicate that 70% of cumulative sensitivity for horizontal coplanar coils is attained for $z < 0.25s$ and for vertical coplanar coils only marginally in excess of $z = 0.5s$. Consequently, compared with sensitivity characteristics for quadrature conductivity measurements (Figure 54), depth of in-phase investigation for standard FDEM instruments is better suited for present purposes.

As described in Section 4.4.3 (in connection with FDEM conductivity measurements and in analogy with quadrupole electrical soundings), vertical electromagnetic soundings can be acquired by recording a series of measurements with the instrument raised incrementally above grade. Computer-based inversion methods are applied to resulting measurements to derive an optimized estimate of actual depth-dependent magnetic susceptibility. Similarly, semi-quantitative assessment of depth-variability is obtained by recording the variation in measured in-phase response as the device is raised from grade to a height of approximately $1.5s$. For a uniform soil, in-phase response should decrease with increasing height in accordance with integrated sensitivity relations in the lower panel of Figure 79. In particular, s -weighted height dependent response above a uniform ground is given by $R(H) = \int_H^\infty S(x) dx$,³¹ where $H = h/s$ and h is height above grade (corresponding response characteristics are also depicted in Figure 79).

Finally, although the in-phase FDEM response (Figure 53) due to induction is effectively frequency independent for soils within the resistive limit, the intrinsic frequency

³⁰ Integrated sensitivities follow from Equations (166) and (167) as

$$\Sigma_{HC-I}(Z) = [(1 - 8Z^2)/(4Z^2 + 1)^{5/2}] - 1 \quad \Sigma_{VC-I}(Z) = -1/(4Z^2 + 1)^{3/2}.$$

³¹ Resulting response functions follow from Equations (166) and (167) as

$$R_{HC-I}(H) = (8H^2 - 1)/(4H^2 + 1)^{5/2} \quad R_{VC-I}(H) = 1/(4H^2 + 1)^{3/2}.$$

dependence of soil electromagnetic properties, particularly the magnetic susceptibility, can have a substantial influence. Consequently, as for FDEM conductivity meters, multi-frequency FDEM susceptibility measurements can potentially provide assessment of magnetic dispersion, associated viscosity and related influence on time-domain (TDEM) sensors as described in Section 3.3.

5.0 SOIL NOISE - SUMMARY AND CONCLUSIONS:

As described in Section 3.0 and with reference to Figure 4, the net response of both frequency-domain (FDEM-CW) and time-domain (TDEM-PI) metal detectors reflects both background and anomalous components, with the anomalous component comprising both *signal* associated with targets of interest (mines) and *noise* or clutter due to localized soil heterogeneity. Moreover, to the extent that compensation circuitry is not provided or is rendered ineffective due to exceptionally strong background response or large-scale gradients, the background component is also effectively noise and potentially imposes a limiting restriction on system performance.

In general, reduced signal to noise ratio implies degraded performance. However, it is important to appreciate that signal to noise ratio is reduced both by decreasing signal and/or increasing noise. In practice, signal levels associated with landmines depend principally on the amount (surface area) of incorporated metal and depth of burial. Composition, shape and orientation of metal components also have influence. Clearly, deeply buried, low-metal mines are the ultimate test of metal detector performance. However, accepting practical limitations on signal, the present study has focused on the origin, nature and extent of soil noise, methods for characterization of associated soil electromagnetic properties and related prediction of metal detector performance.

Background Soil Noise:

Again, there are two basic components of soil noise, background and anomalous. By background noise, we refer to the broad-scale response associated with mean soil electromagnetic properties and, specifically, to background levels that are not effectively cancelled or controlled by compensation circuitry or related adjustments (manual or automated). In general, theoretical analysis and related modelling presented in Chapter 3.0, has confirmed the primary role of soil magnetic characteristics in limiting the performance of both FDEM and TDEM metal detectors. In particular, it is observed that for typical coil geometries and FDEM operating frequencies, the related induction number (Equation 29) satisfies $\eta \ll 1.0$ for the vast majority of natural soils (Figure 9). Moreover, for soils having substantial magnetic susceptibility exceeding $\chi = 1.0 \times 10^{-4} - 1.0 \times 10^{-3}$ SI, the induction number commonly falls within the resistive limit (Figure 10), with related FDEM response dominated by the in-phase component and proportional to magnetic susceptibility. Clearly, where soil magnetic susceptibility is sufficiently high, compensation is ineffective and the background soil noise level exceeds normal signal ranges. Ultimately, with increasing susceptibility, the background response effectively reduces and ultimately saturates available dynamic range, rendering the detector practically inoperable.

As regards practical prediction of related soil influence on FDEM metal detectors, findings reported here generally support guidelines for soil magnetic susceptibility adopted by CEN-WS7 in Table 1 of Figure 62 (CEN, 2006,2008; Billings, et al., 2003). Although the relative influence of electrical conductivity is clearly less significant, there is also a basis in theory for expecting that anomalously high background conductivity levels can too have significant influence, particularly at higher FDEM operating frequencies. Unfortunately, there remains insufficient empirical basis for establishing corresponding gradational guidelines. However, theoretical results in Section 3.1 provide some guidance on significant electrical conductivity levels. For example, on the basis of modelled FDEM response characteristics in Figure 10 (Won and Huang, 2004), the upper diagram in Figure 80 displays the induction number for which the quadrature-phase response is equivalent to the in-phase (resistive limit) response as a function of soil magnetic susceptibility. The corresponding relation between soil magnetic susceptibility and electrical conductivity is depicted in the lower chart with operating frequency as a parameter.³²

It is notable that for the *moderate* susceptibility range ($\chi=50\times 10^{-5}$ - 500×10^{-5} SI) set out in CEN-WS7 (Table 1 of Figure 62), required soil electrical conductivity for equivalent quadrature-phase response ranges from approximately $\sigma=100$ mS/m to roughly $\sigma=10$ S/m, depending on magnetic susceptibility and operating frequency. More significantly, results in Figure 80 confirm that only rare soil environments (e.g. salt-affected soils) with electrical conductivity in excess of $\sigma=1.0$ S/m can have comparable severe influence and that even the most conductive soils are virtually incapable of producing the *very severe* effects of highly magnetic soils ($\chi > 2000\times 10^{-5}$ SI) at metal detector frequencies.

Similarly, as regards background soil influence on TDEM sensors, analysis presented in Section 3.3 demonstrates that soil magnetism is again the primary cause. However, unlike the case for FDEM systems, it is the frequency dispersion of the magnetic susceptibility and equivalent time-domain viscosity that are the key parameters. In particular, as discussed in Sections 3.3 and 3.4, only finite intrinsic dispersion (as indicated by χ_{FD} and commonly associated with the colloidal magnetic soil fraction) is required to trigger a sustained $t^{-3/2}$ viscous response. The precise level of viscosity and related background response (noise), however, depends on the volume concentration and mineral composition of dispersive magnetic material comprising the soil as reflected in the net absolute susceptibility (in general, includes contributions due to non-dispersive as well as dispersive magnetic soil fractions). Again, findings reported here generally support related guidelines established in CEN-WS7. However, interestingly, it is noted that specific viscosity ($\nu = \Delta\chi / \log(f_H/f_L)$) thresholds specified in

³² Note that results in Figure 80 assume $h_N = h/a = 0.6$ and $a = 0.15$ m for equivalent conductivity calculations. It is emphasized that required electrical conductivity for equivalent quadrature-phase response increases with decreasing h_N and with decreasing a .

Table 2 of Figure 62 (established with benefit of related empirical data and together with practical constraints on intrinsic magnetic dispersion) imply related susceptibilities on the order of $\chi = 1.0 \times 10^{-3}$ SI or higher for even *moderate* influence. Clearly, yet higher susceptibilities would be required for soils with limited intrinsic dispersion.

In addition, while findings confirm the uniquely significant influence of magnetic viscosity on TDEM sensor performance, theoretical analysis in Section 3.3 also establishes the potential significance of dispersive soil electrical conductivity. Modelling results summarized in Figures 26 and 27 demonstrate that appreciable dispersion of soil electrical conductivity produces an anomalous and sustained response within the typical measurement range of hand-held TDEM systems. In particular, significant electrical chargeability yields a characteristic polarity reversal and subsequent reduced decay rate with $t^{-3/2} - t^{-5/2}$ dependence. However, while the resulting signature can potentially dominate the TDEM response for weakly magnetic and strongly conductive soils, findings suggest that the natural range of soil electrical conductivity/chargeability is unlikely to yield the *moderate* background response level implied by the related magnetic viscosity threshold ($\nu > 5.0 \times 10^{-5}$ SI) specified in CEN-WS7 (Table 2, Figure 62).³³ Indeed, it is anticipated that only abnormally elevated soil conductivities ($\sigma > 1.0$ S/m) associated with salt-affected soils could yield a similar response and related polarization effects would likely occur at delay times exceeding 100 μ s.

Consequently, the current study generally confirms that background noise levels contemplated by guidelines specified in CEN-WS7, for both FDEM and TDEM metal detectors, are primarily associated with soil magnetic properties. Results do suggest, however, that soil electrical conductivity can have comparable influence at moderate and marginally lower background levels and could potentially constitute a significant source of background soil noise where soil magnetic influence is limited.

Anomalous Soil Noise:

By anomalous soil noise, we refer to localized anomalous response signatures or “clutter” due to small-scale soil heterogeneity or localized contrasts in larger-scale soil

³³ It is notable (and consistent with previous discussion) that viscosity thresholds specified by CEN-WS7 guidelines for TDEM sensors (Table 2, Figure 62) imply very considerable absolute susceptibility levels. For example, with reference to Figure 21, a strongly dispersive magnetic soil ($\ln(\tau_2/\tau_1) = 20$, $\chi_{FD} \approx 10\%$) must also possess a substantial absolute susceptibility ($\chi_{dc} = 0.001$ SI) to yield the threshold viscosity of $\nu = \chi_{dc} / \ln(\tau_2/\tau_1) = 5.0 \times 10^{-5}$ SI for *moderate* effect. Of course, a soil having lesser dispersion (e.g. $\ln(\tau_2/\tau_1) = 100$, $\chi_{FD} \approx 2\%$) requires still higher absolute susceptibility (e.g. $\chi_{dc} = 0.005$ SI) to satisfy the same criterion. Significantly, the same soil would have *severe* influence on an FDEM metal detector according to related CEN-WS7 guidelines (Table 1, Figure 62).

electromagnetic properties that are not effectively controlled by compensation circuitry or related adjustments. In contrast with background soil noise, anomalous noise does not generally restrict dynamic range or otherwise degrade metal detector's function. Rather, anomalous noise is signal-like in character (at levels comparable to weaker signals) and reduces the operator's target recognition and discrimination capacity. In general, while background noise restricts the effective detection limit (probability of detection), anomalous noise increases the false alarm rate. It is also possible for anomalous soil noise to mask lower level signals from underlying targets on a localized spatial scale.

As a practical matter, the influence of anomalous soil noise is primarily significant for low-metal or deeply buried mines for which related signal levels are comparable to soil generated response variation. Unfortunately, expected signal levels and related detection limits are also substantially dependent on the operating characteristics of a given metal detector and, additionally, on background soil properties. Consequently, it is difficult to establish broadly applicable guidelines (e.g. CEN-WS7 provides no related guidance comparable to Tables 1 and 2, Figure 62) for influence of anomalous soil noise as functions of specific soil electromagnetic parameters. Nevertheless, it would appear reasonable to anticipate that a substantially wider range of soil electromagnetic properties (magnetic and electrical) could be significant.

In general, additional studies, both laboratory and field are required to confirm existing guidelines for performance prediction and to further investigate and establish the practical influence of soil electromagnetic parameters. As possible and through whatever agencies or organizations might facilitate or sponsor it, a sustained campaign should be pursued to encourage the measurement, sampling and reporting of soil electromagnetic properties in connection with humanitarian demining operations, particularly where soil conditions are perceived to be problematic. Compilation and analysis of resulting data, together with results of detector-based performance evaluation (as per CEN-WS7 recommendations) would further validate and advance our understanding of soil influence on metal detector performance and could potentially lead to significant technological innovation. We trust that the foregoing review of relevant theory and measurement methodology provides a useful foundation for related future research and development.

REFERENCES CITED

- Agilent Technologies, 2000, *Agilent 4192A LF Impedance Analyzer*, Operation Manual, Agilent Technologies, Kobe, Japan.
- ASTM, 2006, Standard test method for field measurement of soil resistivity using the Wenner four-electrode method, Standard G57-06, ASTM International, Pennsylvania, USA.
- ASTM, 2005, Standard test method for measuring soil resistivity using the two-electrode soil box method, Standard G187-05, ASTM International, Pennsylvania, USA.
- Anderson, W.L., 1979, Numerical integration of related Hankel transforms of orders 0 and 1 by adaptive digital filtering, *Geophysics*, **44**, 7, 1287-1305.
- Anderson, W.L., 1982, Fast Hankel transforms using related and lagged convolutions, *ACM Transactions on Mathematical Software*, **8**, 4, 344-368.
- Barker, R.D., 1989, Depth of investigation of collinear symmetrical four-electrode arrays, *Geophysics*, **54**, 8, 131-137.
- Bartington, 2005, Operation manual for MS2 magnetic susceptibility system, OM0408, Bartington Instruments Ltd., Oxford, UK
<http://www.bartington.com/media/aedd335c/om0408%20MS2%20v46.pdf>
- Billings, S.D., Pasion, L.R. and Oldenburg, D.W., 2003, Characterizing magnetic soils: state of the art and future needs, ITEP Workshop on Reliability Tests for Demining: Berlin, Germany, December 17, 2003.
- Billings, S.D, Pasion, L.R., Oldenburg, D.W. and Foley, J., 2003, The influence of magnetic viscosity on electromagnetic sensors, Proceedings EUDEM2-SCOT-2003, pp. 123-130, Vrije Universiteit Brussel, Brussels, Belgium.
- Billings, S., Guelle, D., and Lewis, A., 2003, Soil influence and ground compensation, Summary of Breakout Session 2, BAM/ITEP Workshop - Reliability Tests for Demining. <http://www.kb.bam.de/ITEP-workshop-03/>
- Borry, F., Guelle, D. and Lewis, A., 2003, Soil characterization for evaluation of metal detector performance, Proceedings EUDEM2-SCOT-2003, pp. 115-122, Vrije Universiteit Brussel, Brussels, Belgium.
- Bruschini, C., 2004, On the low-frequency EMI response of coincident loops over a conductive and permeable soil and corresponding background reduction schemes, *IEEE Transactions on Geoscience and Remote Sensing*, **42**, 8, 1706-1719.
- Bruschini, C., 2002, *A multidisciplinary analysis of frequency domain metal detectors for humanitarian demining*, Ph.D. Dissertation, Vrije Universiteit Brussel, Brussels, Belgium.
- CEN, 2008, CEN Workshop Agreement (CWA): Humanitarian Mine Action - Test and Evaluation - Part 2 - Soil characterisation for metal detector and ground penetrating radar performance, Final Draft, European Committee for Standardization, September 2008,

- http://www.itep.ws/itepnet/pdf/CWA14747Part2_draftv10.pdf
- CEN, 2003, CEN Workshop Agreement (CWA) 14747-1:2003 E: Humanitarian Mine Action - Test and Evaluation - Metal Detectors, European Committee for Standardization, June 2003, http://www.itep.ws/pdf/CWA_metal_detectors.pdf
- Carter-Stiglitz, B.S., Solheid, P.A., Egli, R. and Chen, A.P., 2006, Tiva Canyon Tuff (II): near single-domain reference material available, *IRM Quarterly*, **16**, 1, Institute for Rock Magnetism, University of Minnesota, <http://www.irm.umn.edu/quarterly/irmq16-1.pdf>.
- Chikazumi, S., 1964, *Physics of magnetism*, Wiley, New York.
- Colani, C., 1966, A new type of locating device: I - the instrument, *Archaeometry*, **9**, 3-8.
- Colani, C. and Aitken, M.J., 1966, Utilization of magnetic viscosity effects in soils for archaeological prospection, *Nature*, vol. 212, pp. 1446-1447.
- Cole, K.S., and Cole, R.H., 1941, Dispersion and adsorption in dielectrics, *Journal of Chemical Physics*, **9**, 341.
- Cross, G., 2000, Soil properties and GPR detection of landmines a basis for forecasting and evaluation of GPR performance, Contract Report DRES CR 2000-091, Defence Research Establishment Suffield.
- Dabas, M., Jolivet, A. and Tabbagh, A., 1992, Magnetic susceptibility and viscosity of soils in a weak time varying field, *Geophysical Journal International*, **108**, 101-109.
- Dahlin, T., Zhou, B., 2004, A numerical comparison of 2D resistivity imaging with 10 electrode arrays, *Geophysical Prospecting*, **52**, 379-398.
- Das, Y., 2006, Effects of soil electromagnetic properties on metal detectors, *IEEE Transactions on Geoscience and Remote Sensing*, **44**, 6, 1444-1453.
- Das, Y., 2004, A preliminary investigation of the effects of soil electromagnetic properties on metal detectors, *Proc. SPIE*, vol. 5415, pp. 677-690.
- Das, Y., McFee, J., Russell, K., Cross, G. and Katsube, J., 2003, Soil information requirements for humanitarian demining: the case for a soil properties database, *Proc. SPIE*, vol. 5089, 1146-1157.
- Das, Y., McFee, J. and Cross, G., 2002, Soil properties database for humanitarian demining: a proposed initiative, invited paper presented to the Council of the International Union of Soil Science (IUSS), 17th World Congress of Soil Science, 14-21 August 2002, Bangkok, Thailand.
- Debye, P., 1929, *Polar Molecules*, Dover, New York.
- Dearing, J.A., Dann, R.J.L., Hay, J.A., Loveland, B.A., Maher, B.A. and O'Grady, K., 1996, *Geophysical Journal International*, **124**, 228-240.
- Dunlop, D.J. and Özdemir, Ö., 1997, *Rock magnetism: fundamentals and frontiers*, Cambridge University Press, Cambridge.
- El-Kailouby, H.M., Hussain, S.A., Bayoumi, A.E., El-Diwany, E.A. and Hashish, E.A., 1995, Effect of clayey media parameters on the negative response of a coincident

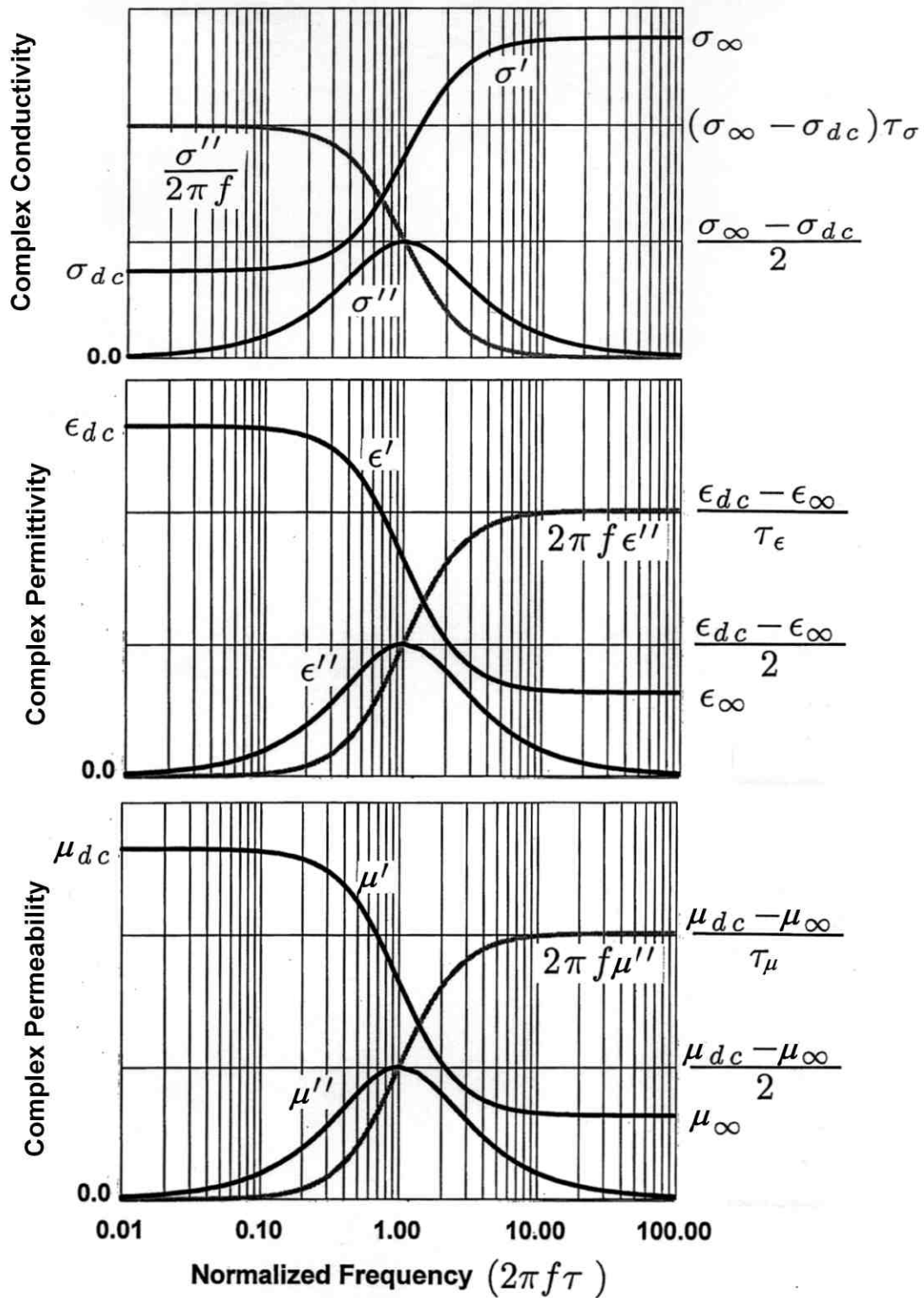
- loop, *Geophysical Prospecting*, **43**, 595-603.
- El-Kailouby, H.M., El-Diwany, E.A., Hussain, S.A., Hashish, E.A. and Bayoumi, 1997, Optimum negative response of a coincident-loop electromagnetic system above a polarizable half-space, *Geophysics*, **62**, 75-79.
- Epstein, D.J., 1954, Dielectric measuring techniques - b. permeability, in *Dielectric materials and applications*, von Hippel, A.R., Editor, John Wiley & Sons, New York, 122-134.
- Forster, T., Evans, M.E. and Heller, F., 1994, The frequency dependence of low field susceptibility in loess sediments, *Geophysical Journal International*, **118**, 636-642.
- Frischknecht, F.C., 1987, Electromagnetic physical scale modeling, in *Electromagnetic methods in applied geophysics*, Volume 1, Society of Exploration Geophysicists, Tulsa.
- Fukuma, K., 2000, www.sci.kumamoto-u.ac.jp/~fukuma/fukumalec/00SS.ppt
- GICHD, 2006, *Guidebook on detection technologies and systems for humanitarian demining*, Geneva International Centre for Humanitarian Demining, Publication No. 46, Geneva.
- Guéguen, Y. and Palciauskas, V., 1994, *Introduction to the physics of rocks*, Princeton University Press, Princeton, New Jersey.
- Guelle, D., 2002, Soil and its influence on metal detector performance, ITEP Workshop on Soil electromagnetic properties and metal detector performance, EC-JRC, Ispra. <http://itep.ws/pdf/proceedings.pdf>.
- Guelle, D., 2002, Soil and its influence on metal detector performance, ITEP Workshop on Soil electromagnetic properties and metal detector performance, EC-JRC, Ispra, 44-49, <http://itep.ws/pdf/proceedings.pdf>.
- Guelle, D., Smith, A., Lewis, A., and Bloodworth, T., 2003, *Metal detector handbook for humanitarian demining*, Office for Official Publications of the European Communities, Luxembourg.
- Grant, F.S. and West G.W., 1965, *Interpretation theory in applied geophysics*, McGraw-Hill, Toronto.
- Haruta, H., 2000, Impedance measurement handbook, Second Edition, Agilent Technologies Co. Ltd., Kobe, Japan.
- Hewlett Packard, 1981b, Vector impedance meter 4800A, operating and service manual, Hewlett Packard Company, Rockaway, New Jersey.
- Huang, H., and Won, I.J., 2000, Conductivity and susceptibility mapping using broadband electromagnetic sensors, *Journal of Environmental and Engineering Geophysics*, **5**, 4, 31-41.
- Ignetik, R., Thio, Y.C., Westfold, K.C., 1985, Transient electromagnetic field above a permeable and conducting half-space, *Geophysical Journal of the Royal Astronomical Society*, **81**, 623-639.
- Iliceto, V., Santarato, G. and Veronese, S., 1982, An approach to the identification

- of fine sediments by induced polarization laboratory measurements, *Geophysical Prospecting*, **30**, 331-347.
- ITEP, 2002, Proceedings, Soil Electromagnetic Characteristics and Metal Detector Performance: International Test and Evaluation Program for Humanitarian Demining (ITEP), European Commission, Joint Research Centre, Ispra, Italy, 12 December, 2002.
- Jackson, M., Solheid, P., Carter-Stiglitz, B., Rosenbaum, J. and Till, J., 2004, Tiva Canyon Tuff (I): superparamagnetic samples available, *IRM Quarterly*, **14**, 3, Institute for Rock Magnetism, University of Minnesota, <http://www.irm.umn.edu/quarterly/irmq14-3.pdf>.
- Johansen, H.K. and Sorensen, K., 1979, Fast Hankel transforms, *Geophysical Prosp.*, **27**, 876-901.
- Kaufman, A.A., and Keller, G.V., 1983, *Frequency and transient soundings*, Elsevier, New York.
- Keller, G.V. and Frischkencht, F.C., 1966, *Electrical methods in geophysical prospecting*, Pergamon Press, New York.
- King, R.W.P., and Smith, G.S., 1981, *Antennas in matter: fundamentals, theory and applications*, MIT Press, Cambridge, MA.
- Krause, J. D., 1984, *Electromagnetics*, 3rd Edition, McGraw-Hill, New York.
- Lecoanet, H., L ev eque, F., and Segura, S., 1999, Magnetic susceptibility in environmental applications: comparison of field probes, *Physics of the Earth and Planetary Interiors*, **115**, 191-204.
- Lee, T., and Lewis, R., 1974, Transient EM response of a large loop on a layered ground, *Geophysical Prospecting*, **24**, 430-444.
- Lee, T., 1981, Transient electromagnetic response of a polarizable ground, *Geophysics*, **46**, 7, 1037-1041.
- Lee, T., 1984, The transient electromagnetic response of a magnetic or superparamagnetic ground, *Geophysics*, **49**, 7, 854-860.
- MacDonald, J., Lockwood, J.R., McFee, J., Altshuler, T., Broach, T., Carin, L., Harmon, R., Rappaport, K., Scott, W., Weaver, R., 2003, *Alternatives for landmine detection*, Rand Corporation, Santa Monica.
- McNeill, J.D., 1980, Electromagnetic terrain conductivity measurement at low induction numbers, Technical Note TN-6, Geonics Ltd., Mississauga, Ontario.
- McNeill, J.D., and Bosnar, M., 1999, Application of "dipole-dipole" electromagnetic systems for geological depth sounding, Technical Note TN-31, Geonics Ltd., Mississauga, Ontario.
- Maher, B.A., 1988, Magnetic properties of some synthetic sub-micron magnetites, *Geophysical Journal International*, **94**, 83-96.
- Maier, G., Scholger, R., and Sch on, J., 2006, The influence of soil moisture on magnetic susceptibility measurements, *Journal of Applied Geophysics*, **59**, 162-175.

- Mehran, M. and Arulanandan, K., 1977, Low frequency conductivity dispersion in clay-water-electrolyte systems, *Clays and Clay Minerals*, **25**, 39-48.
- Mullins, C.E. and Tite, M.S., 1973, Magnetic viscosity, quadrature susceptibility and frequency dependence of susceptibility in single-domain assemblies of magnetite and maghemite, *Journal of Geophysical Research*, **78**, 5, 804-809.
- Nagata, T., 1961, *Rock magnetism*, Revised Edition, Maruzen Company Ltd., Tokyo.
- North, R., 2005, Ryan North, USACE-ERDC, personal communication regarding GdO₂.
- North, R., 2006, Comparison of two new portable magnetic susceptibility measurement systems, *Proceedings SPIE*, vol. 6217.
- North, R., 2006, Ryan North, USACE-ERDC, personal communication regarding Tiva Canyon tuff.
- Ogilvy, A.A., Kuzmina, E.N., 1972, Hydrogeologic and engineering-geologic possibilities for employing the method of induced potentials, *Geophysics*, **37**, 5, 839-861.
- Oldenburg, D.W., 1978, The interpretation of direct current resistivity measurements, *Geophysics*, **43**, 3, 610-625.
- Olhoeft, G.R., 1987, Electrical properties from 10⁻³ to 10⁺⁹ Hz - physics and chemistry, in *Proceedings of 2nd International Symposium on the Physics and Chemistry of Porous Media*, American Institute of Physics, Conference Proceeding 154, AIP, New York.
- Olhoeft, G.R., 1985, Low-frequency electrical properties, *Geophysics*, **50**, 2492-2503.
- Pasion, L.R., Billings, S.D. and Oldenburg, D.W., 2002, Evaluating the effects of magnetic susceptibility in UXO discrimination problems, SAGEEP 2002, Las Vegas.
- Pretz, H. and Igel, J., 2005, Untersuchung der frequenzabhängigen komplexen Suszeptibilität an Bodenproben von Testflächen in Benkovic, Kroatien, Leibniz Institute for Applied Geosciences, www.gga-hannover.de, Hannover, Germany.
- Pulsepower Developments, 2008, Magnetic viscosity meter - MVM1, product data-sheet, Pulsepower Developments (Soil Magnetism Division), Oxford, UK, <http://geophys.com>.
- Purcell, E.M., 1963, *Electricity and magnetism*, McGraw-Hill, New York.
- Raiche, A.P., and Spies, B.R., 1981, Coincident loop transient electromagnetic master curves for interpretation of two-layer earths, *Geophysics*, **46**, 1, 53-64.
- Raiche, A.P., 1983, Negative transient voltage and magnetic field responses for a half-space with a Cole-Cole impedance, *Geophysics*, **48**, 6, 790-791.
- Richter, G., 1937. Über die magnetische nachwirkung am carbonyleisen, *Annalen der Physik*, **29**, 605-635.
- Roy, A., and Apparao, 1971, Depth of investigation in direct current methods, *Geophysics*, **36**, 5, 943-959.
- Sagnotti, L., Rochette, P., Jackson, M., Vadeboin, F., Dinares-Turell, J., Winkler, A., and Mag-Net Science Team, 2003, Inter-laboratory calibration of low-field

- magnetic and anhysteretic susceptibility measurements, *Physics of the Earth and Planetary Interiors*, **138**, 25-38.
- Sears, F.W., and Zemansky, M.W., 1964, *University Physics*, Addison-Wesley, Reading Massachusetts.
- Siegenfeld, A., 2002, Presentation of a transient-transfer measuring instrument for soil and target time response measurement, ITEP Workshop on Soil electromagnetic properties and metal detector performance, EC-JRC, Ispra, 41-43, <http://itep.ws/pdf/proceedings.pdf>.
- Stewart, D.C., Anderson, W.L., Grover, T.P. and Labson, V.F., 1994, Shallow subsurface mapping by electromagnetic sounding in the 300 kHz to 30 MHz range: model studies and prototype system assessment, *Geophysics*, **59**, 8, 1201-1210.
- Strangway, D.W., 1967, Magnetic characteristics of rocks, in *Mining Geophysics*, Volume II, Theory, Society of Exploration Geophysicists, Tulsa.
- Tabbagh, A., 1986, What is the best coil orientation in the Slingram electromagnetic prospecting method?, *Archaeometry*, **28**, 185-196.
- Telford, W.M., Geldart, L.P., and Sheriff, R.E., 1990, *Applied geophysics*, Second Edition, Cambridge University Press.
- Ultradynamics, 2008, MAGNASAT magnetic susceptibility meter, http://www.ultradynamics.com.au/products_magnasat_magnetic_susceptibility_meter_des.htm
- Wagner, K.W., 1913, The theory of incomplete dielectricity, *Annalen der Physik*, **40**, 5, 817-855.
- Ward, S.H. and Hohmann, G.W., 1987, Electromagnetic theory for geophysical applications, in *Electromagnetic Methods in Applied Geophysics*, Volume 1, Society of Exploration Geophysicists, Tulsa.
- Weast, R. C., 1971, *CRC handbook of physics and chemistry*, Magnetic susceptibility of the elements and inorganic compounds, E127-132, 51st Edition, The Chemical Rubber Company, Cleveland, Ohio.
- West, G.F. and Bailey, R.C., 2005, An instrument for measuring complex magnetic susceptibility of soils, Proc. SPIE Vol. 5794, pp. 124-134, 2005
- Wheeler, H.A., 1982, Inductance formulas for circular and square coils, *Proceedings IEEE*, **75**, 2, 256-257.
- Won, I.J., and Huang, H., 2004, Magnetometers and electro-magnetometers, *The Leading Edge*, **23**, 5, 448-451.
- Worm, H.-U. and Jackson, M., 1999, The superparamagnetism of Yucca Mountain tuff, *Journal of Geophysical Research*, **104**, B11, 25,415-25,425.
- Yager, W.A., 1936, The distribution of relaxation times in typical dielectrics, *Physics*, **7**, 434-450.
- ZH Instruments, 2006, Magnetic susceptibility meter SM-100: user's manual, ZH Instruments, Brno, Czech Republic.

ZH Instruments, 2006b, SM-105 portable magnetic susceptibility meter, product leaflet, ZH Instruments, Brno, Czech Republic, www.zhinstruments.com.



**COMPLEX FREQUENCY – DEPENDENT SOIL ELECTROMAGNETIC PROPERTIES
DEBEYE SPECTRA**



PROJECT:	CCMAT Soils	
DRAWN BY:	GMC	DATE: 15 December, 2007

FIGURE:

1

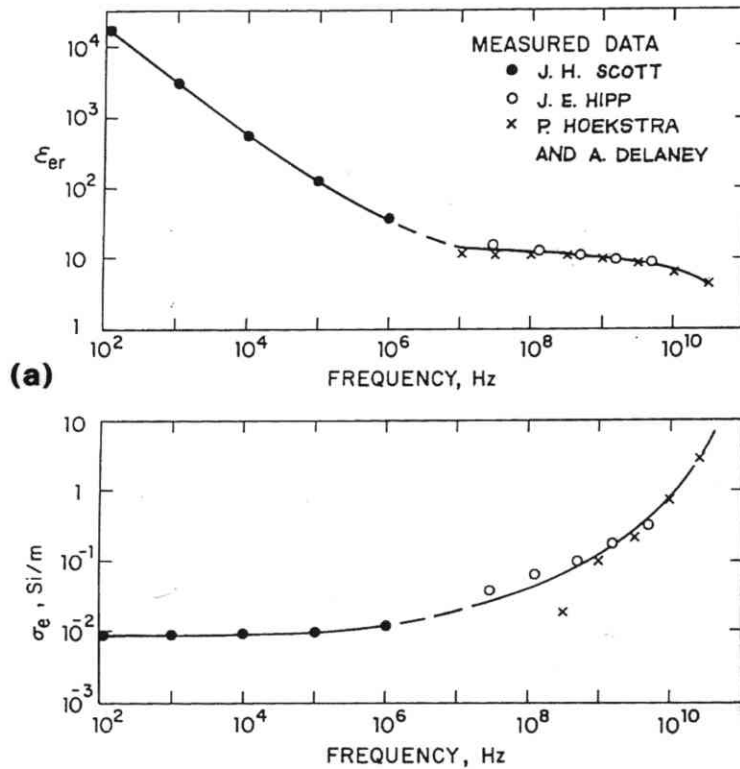
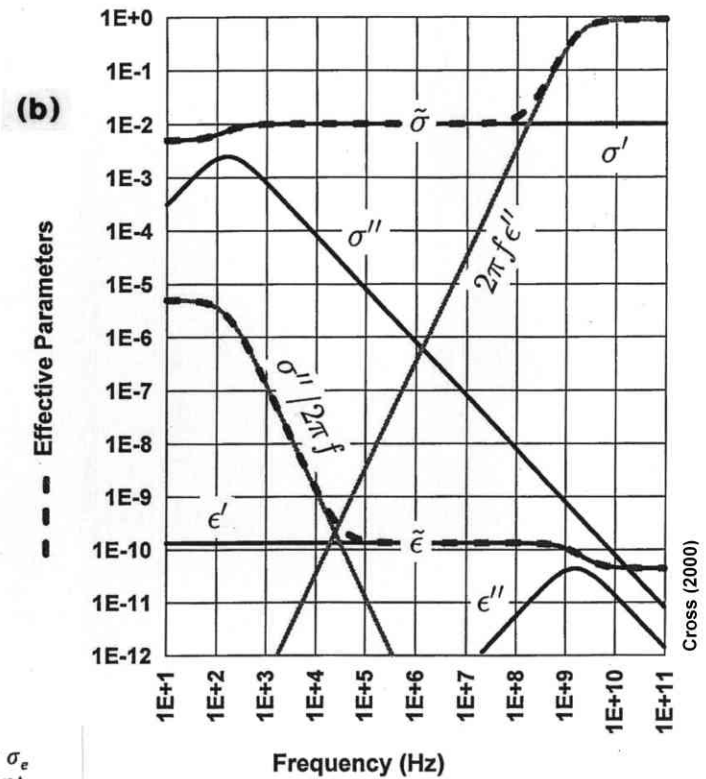
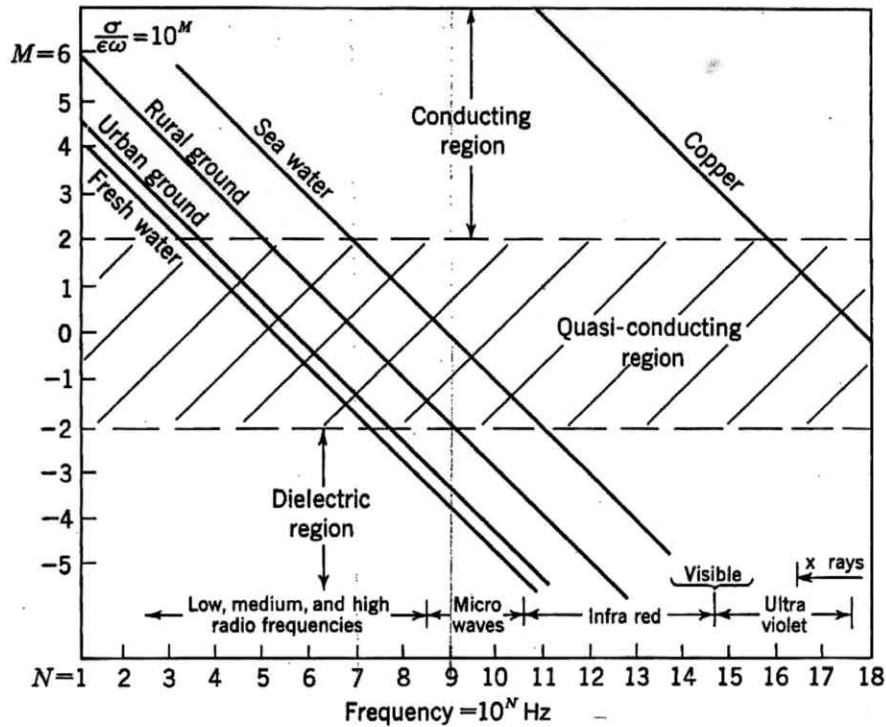
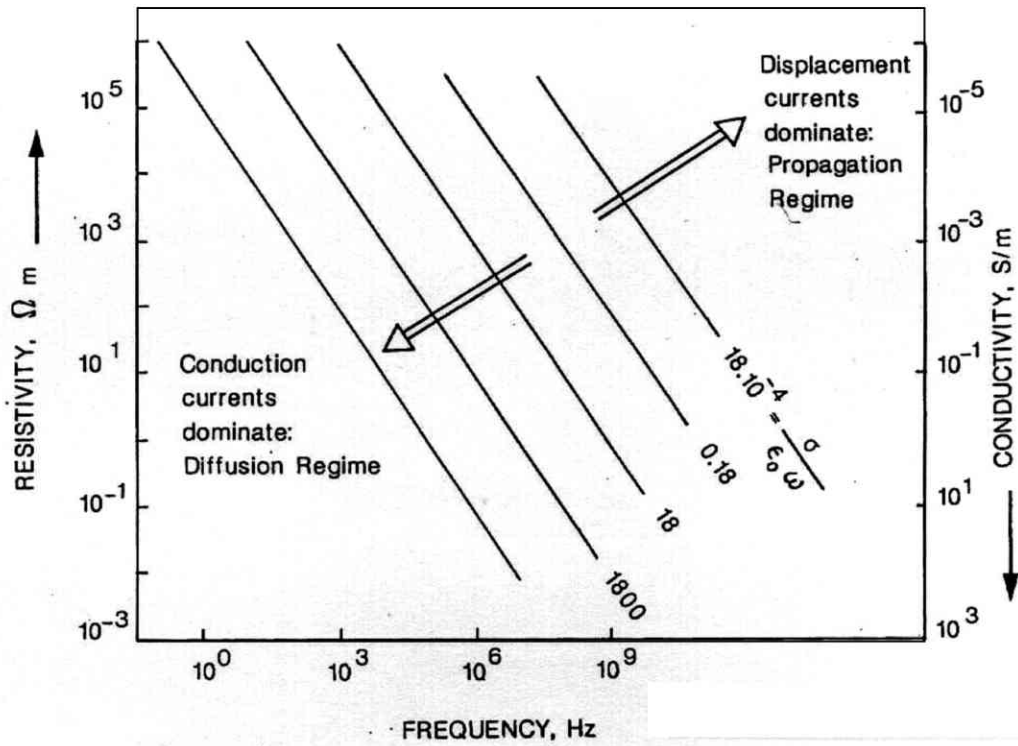


Figure 8.14.2 Relative effective permittivity ϵ_{er} and effective conductivity σ_e as a function of frequency for a typical clay-loam soil with a water content of about 10% by weight. (King and Smith, 1981)





**SOIL ELECTROMAGNETIC PARAMETERS
RESPONSE REGIMES**



PROJECT:

CCMAT Soils

FIGURE:

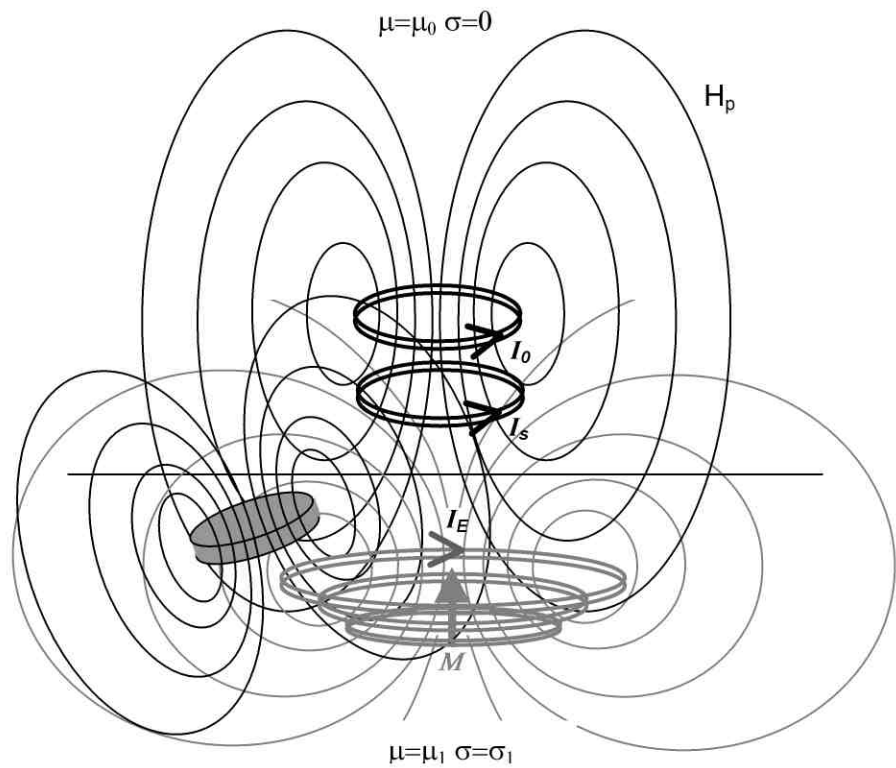
3

DRAWN BY:

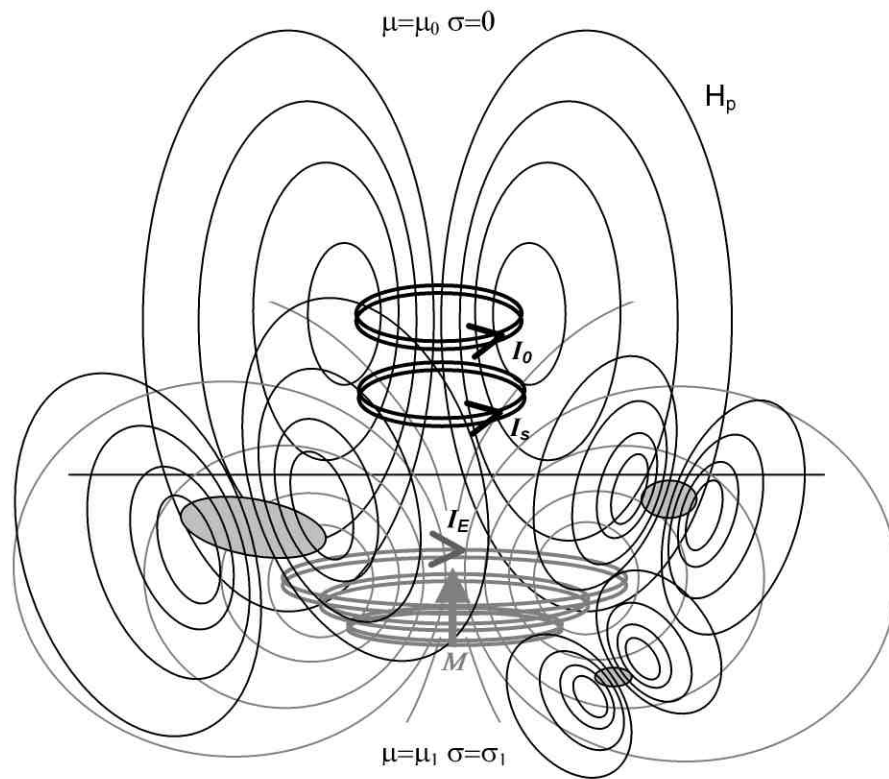
GMC

DATE:

15 December, 2006



Soil Background + Target



Soil Background + Soil Noise



EMI METAL DETECTOR - CONCEPT

FIGURE:

4

PROJECT:

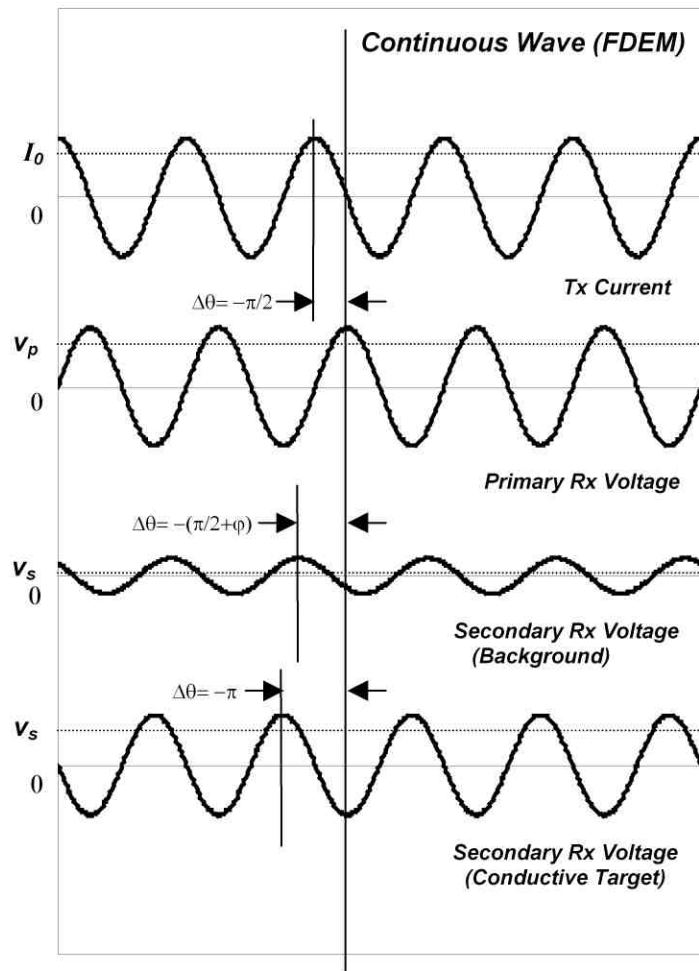
CCMAT Soils

DRAWN BY:

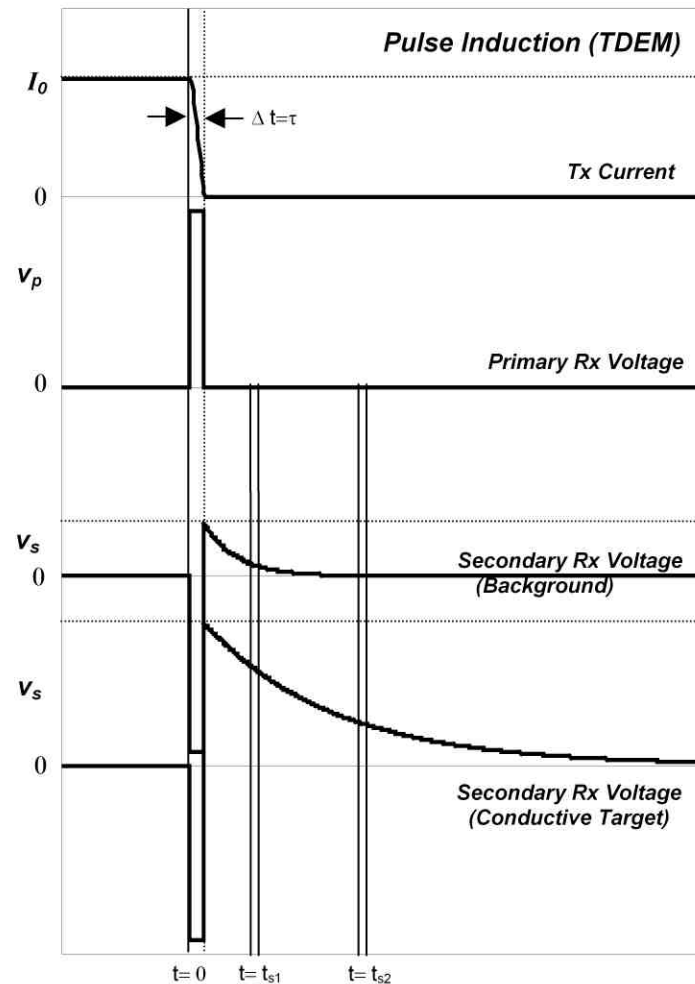
GMC

DATE:

15 December, 2006



Note: phase-shift component ϕ determined by EM properties of host soil.



Note: initial large amplitude transients during termination time τ are limited for display.



**EMI METAL DETECTORS
CONTINUOUS WAVE (FDEM) – PULSE INDUCTION (TDEM)**

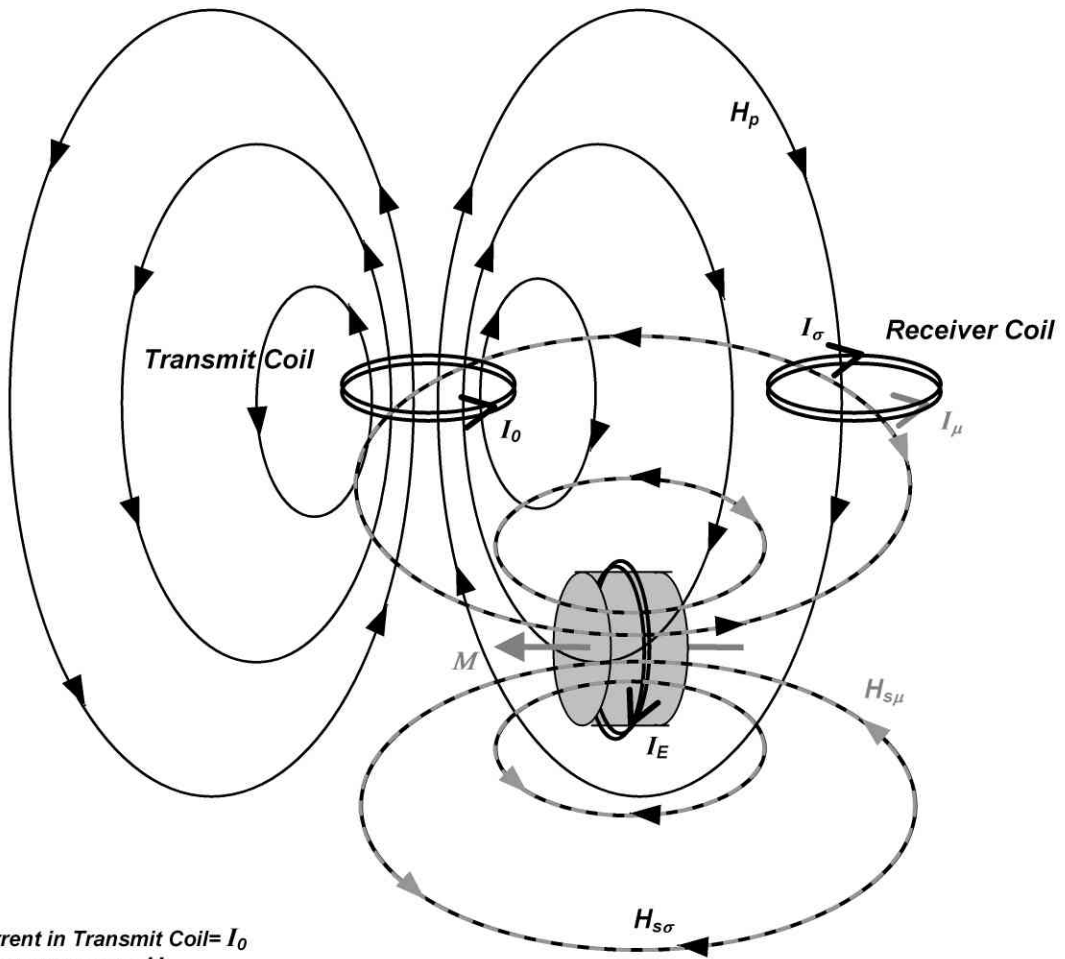
FIGURE:

5

PROJECT: CCMAT Soils

DRAWN BY: GMC

DATE: 15 December, 2006



Source Current in Transmit Coil = I_0
 Primary Magnetic Field = H_p
 Induced Eddy Current in Electrically Conductive Loop = I_E
 Secondary Magnetic Field due to Eddy Current = $H_{s\sigma}$
 Signal Current due to Eddy Current = I_σ
 Induced Magnetization in Magnetically Permeable Core = M
 Secondary Magnetic Field due to Magnetization = $H_{s\mu}$
 Signal Current due to Magnetization = I_μ

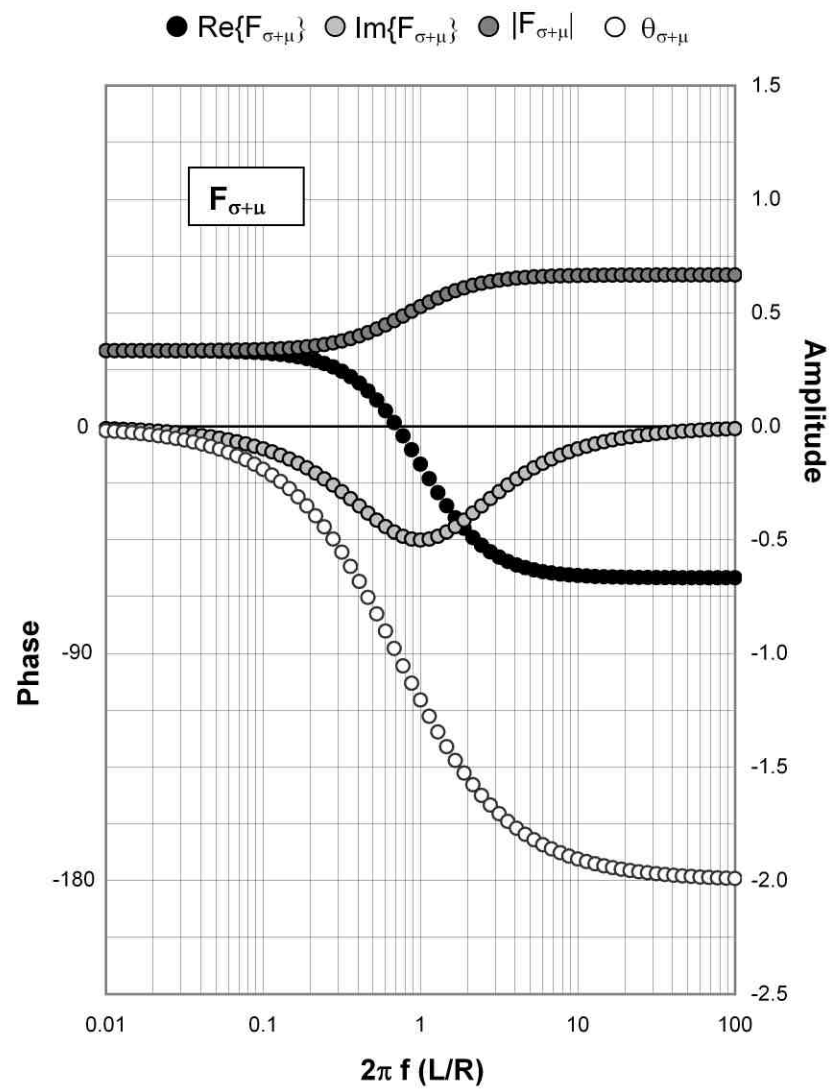
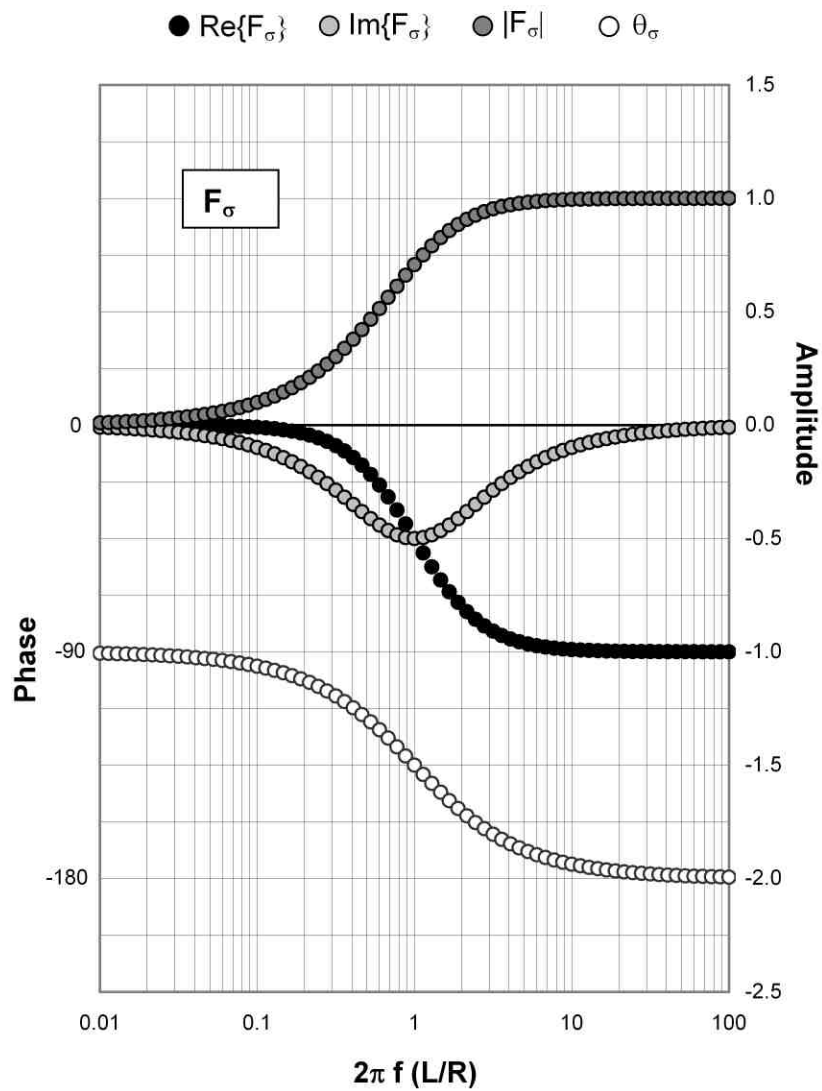
**ELECTROMAGNETIC INDUCTION
 MUTUALLY COUPLED COIL-CORE MODEL**



PROJECT:	CCMAT Soils	
DRAWN BY:	GMC	DATE: 16 December, 2006

FIGURE:

6



**ELECTROMAGNETIC RESPONSE FUNCTIONS
INDUCTION – MAGNETIZATION**

FIGURE:

7

PROJECT:

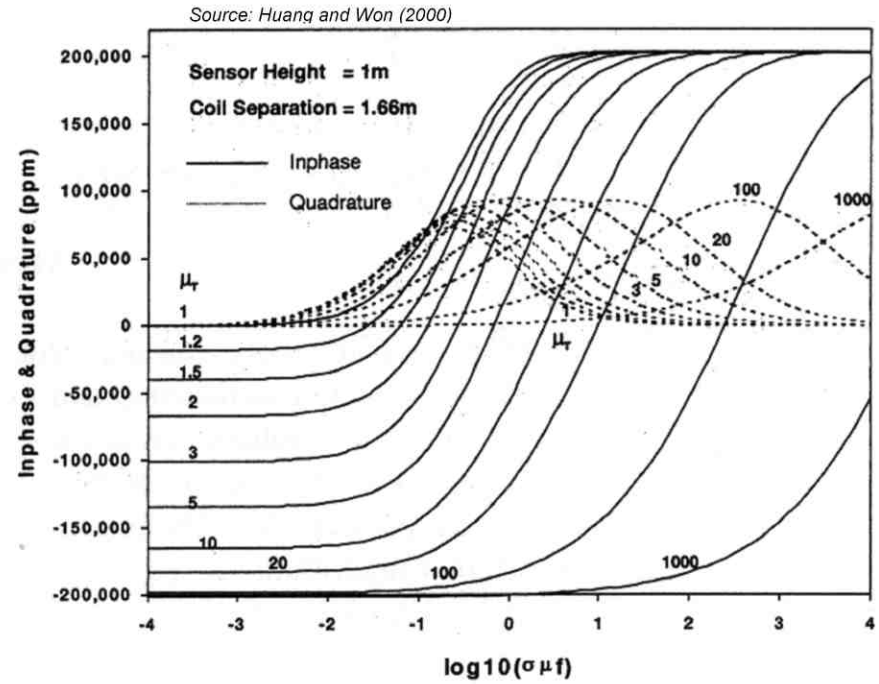
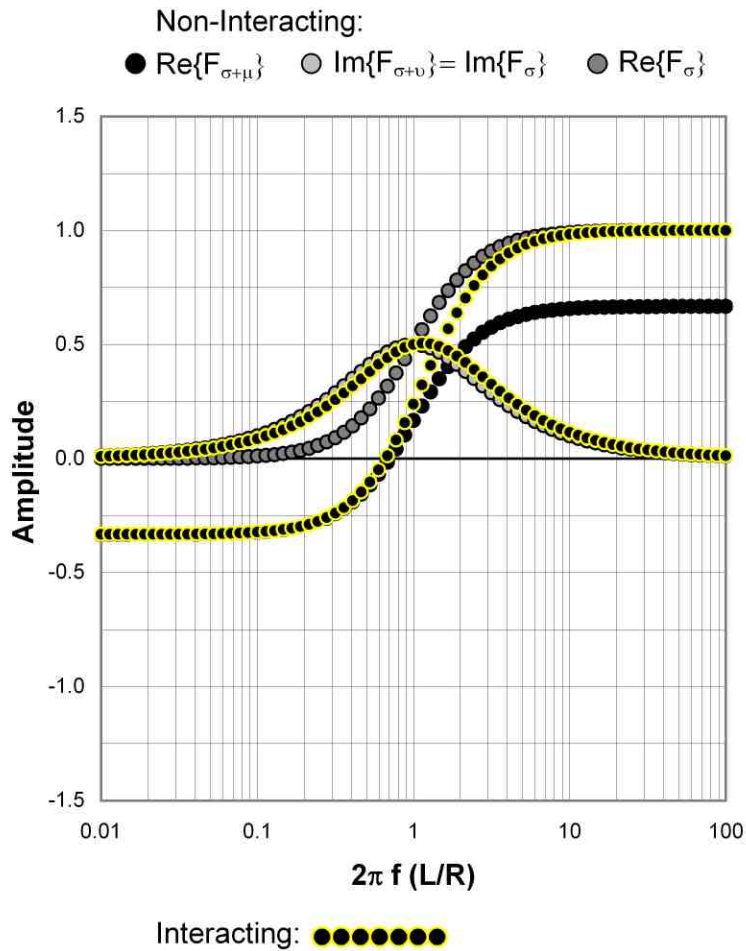
CCMAT Soils

DRAWN BY:

GMC

DATE:

15 December, 2006



**ELECTROMAGNETIC RESPONSE FUNCTIONS
 MODEL – CONDUCTIVE / MAGNETIC HALF-SPACE**

FIGURE:

8

PROJECT:

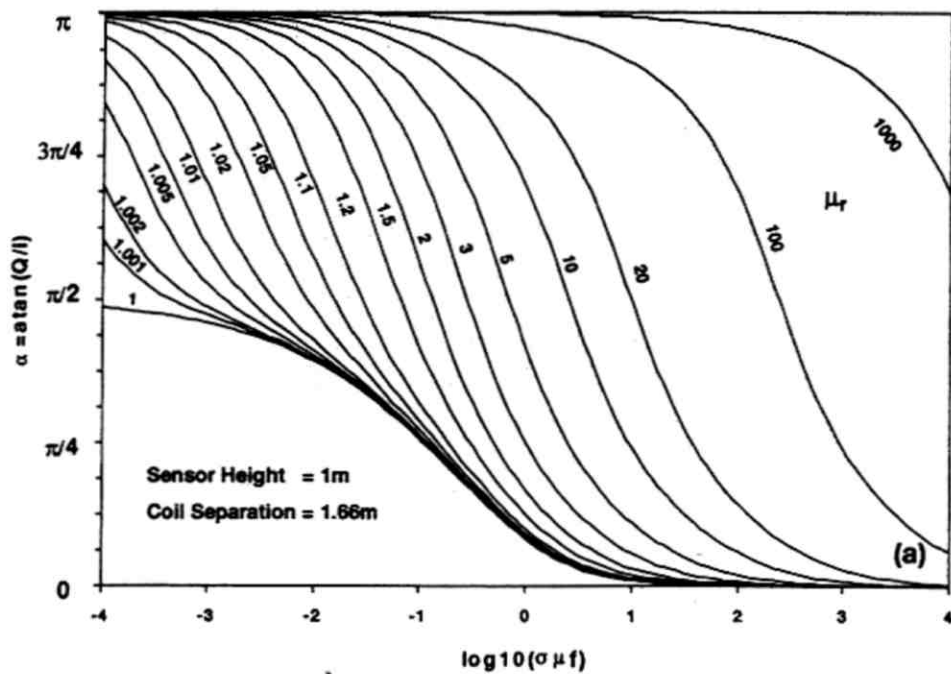
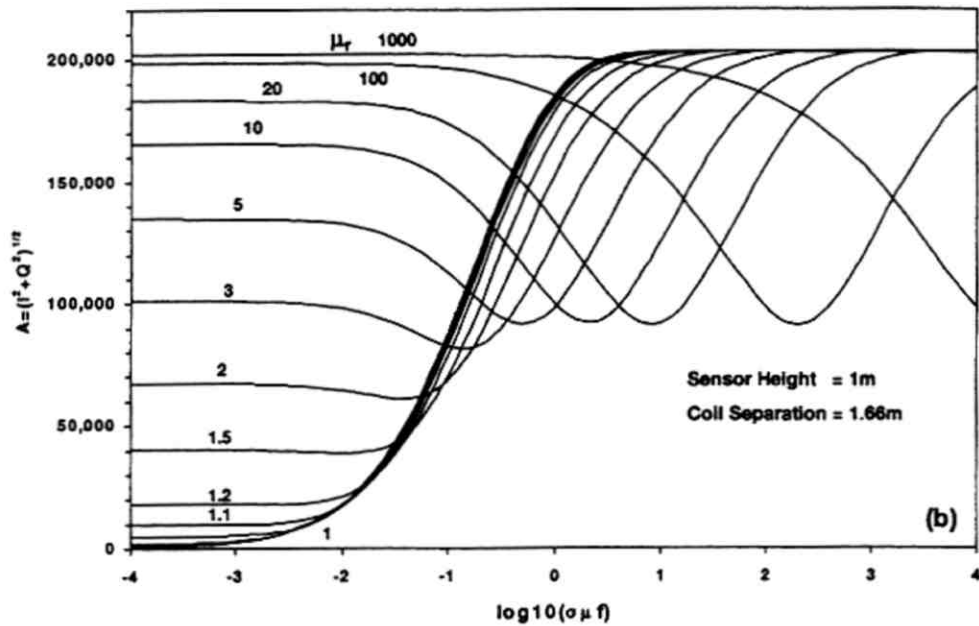
CCMAT Soils

DRAWN BY:

GMC

DATE:

15 December, 2006



Source: Huang and Won (2000)

**THEORETICAL EM RESPONSE – AMPLITUDE / PHASE
VERTICAL MAGNETIC DIPOLE OVER CONDUCTIVE – MAGNETIC HALF-SPACE**

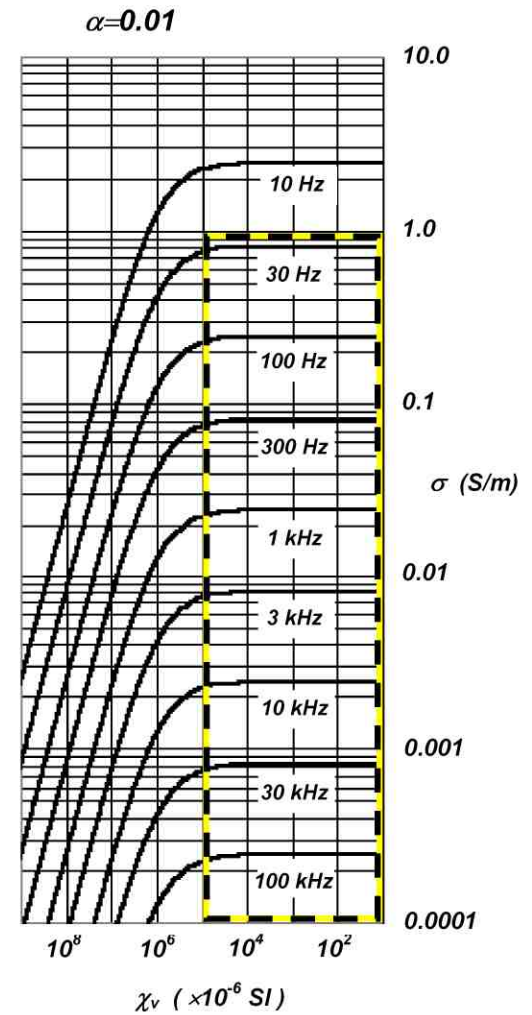
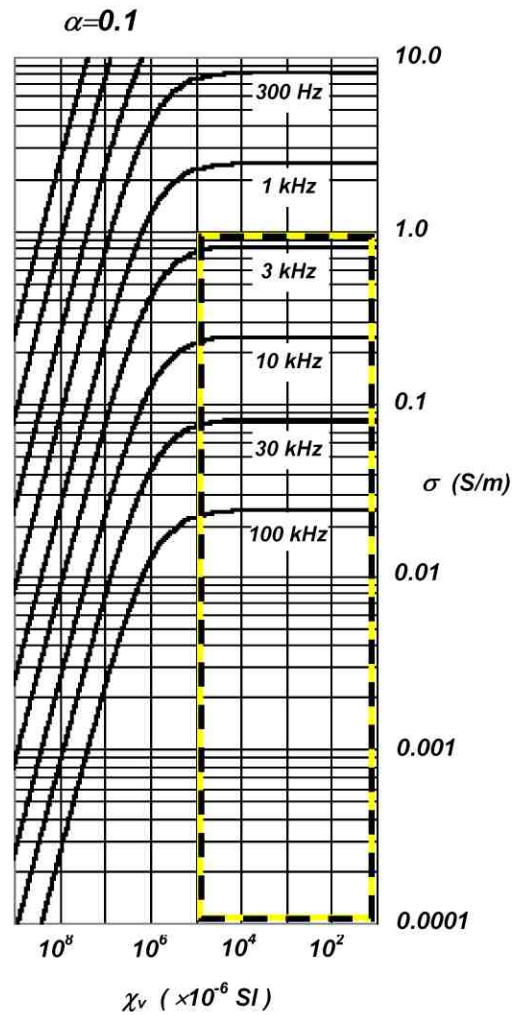
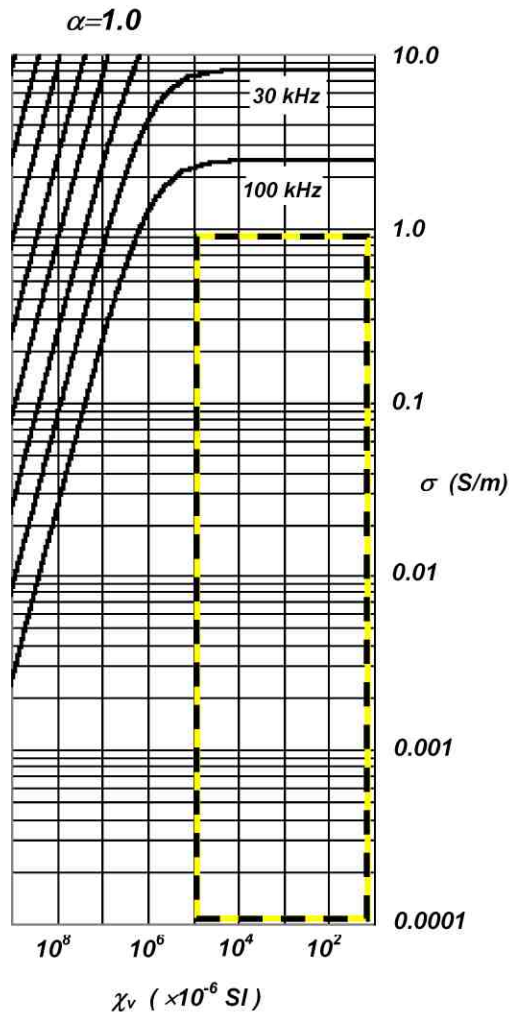


PROJECT: CCMAT Soils

DRAWN BY: GMC DATE: 15 December, 2006

FIGURE:

8.5



Nominal range of natural soil electromagnetic parameters.
 $0.0001 \text{ mS/m} \leq \sigma \leq 1.0 \text{ mS/m}$ $10 \times 10^{-6} \text{ SI} \leq \chi_v \leq 100,000 \times 10^{-6} \text{ SI}$



**INDUCTION NUMBER – SOIL EM PROPERTIES
 FREQUENCY DEPENDENT RESPONSE REGIME**

FIGURE:

9

PROJECT:

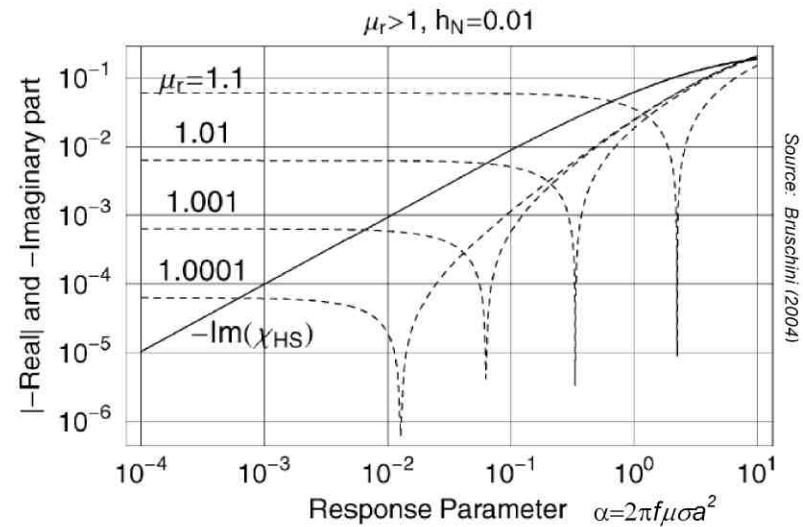
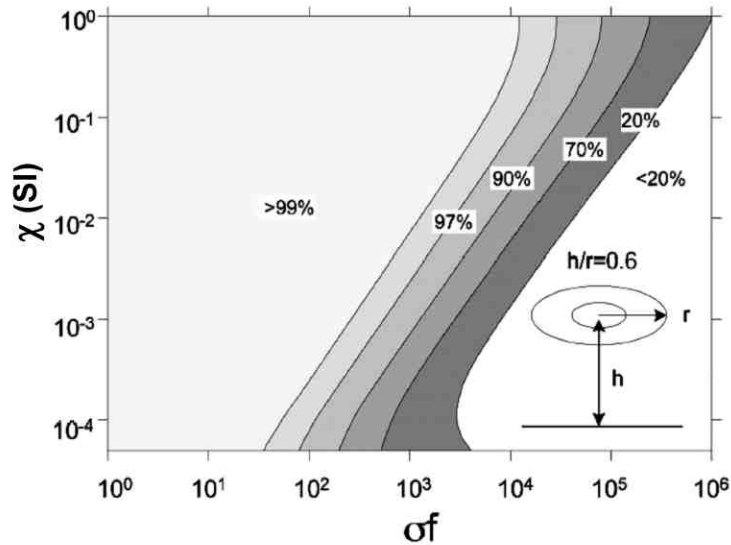
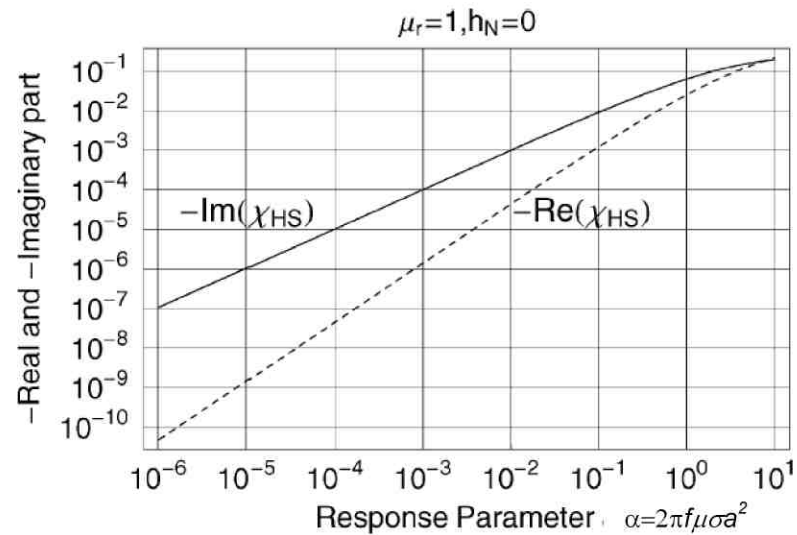
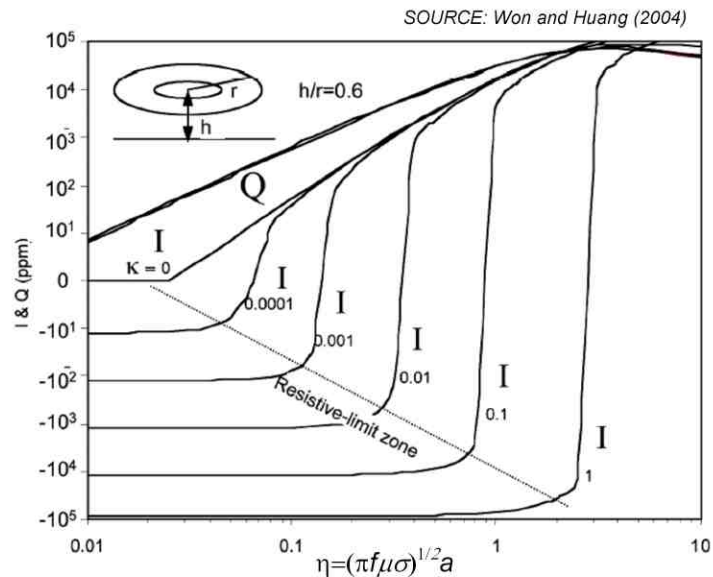
CCMAT Soils

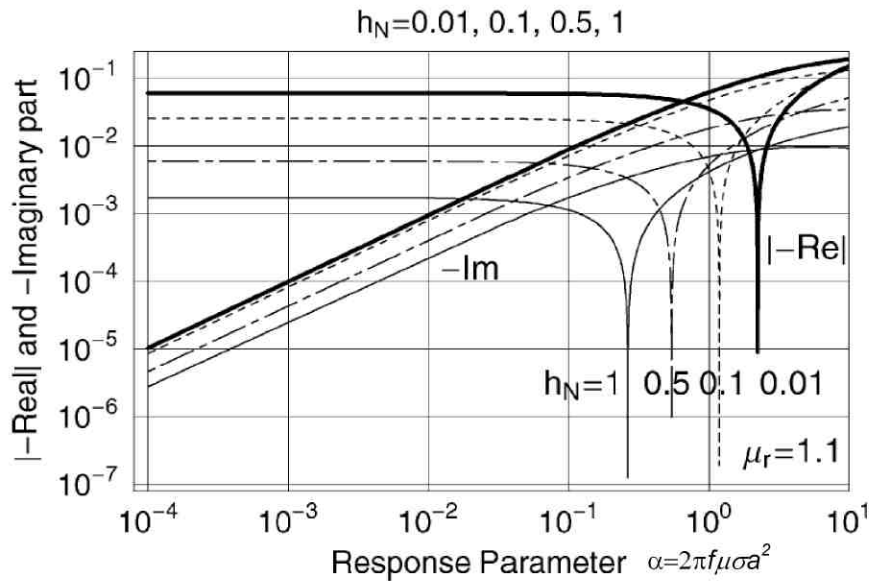
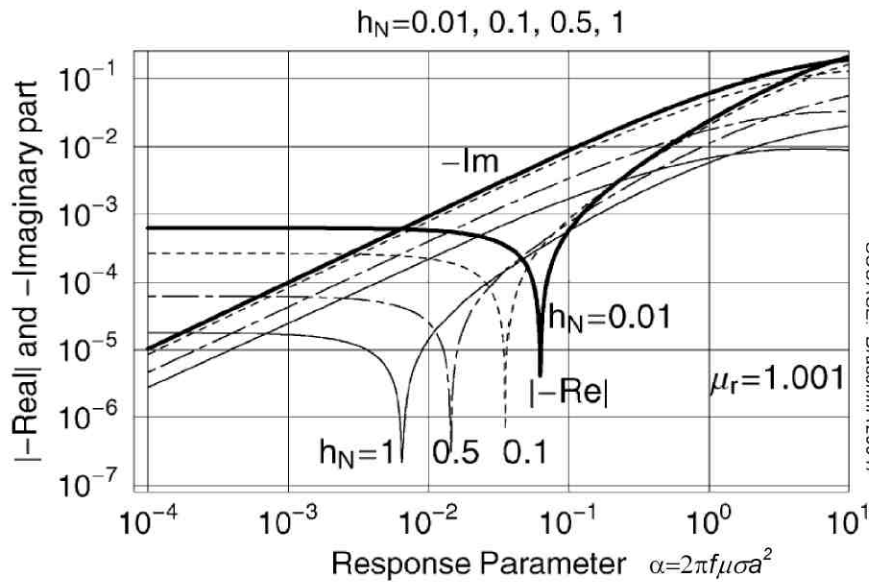
DRAWN BY:

GMC

DATE:

20 February, 2007



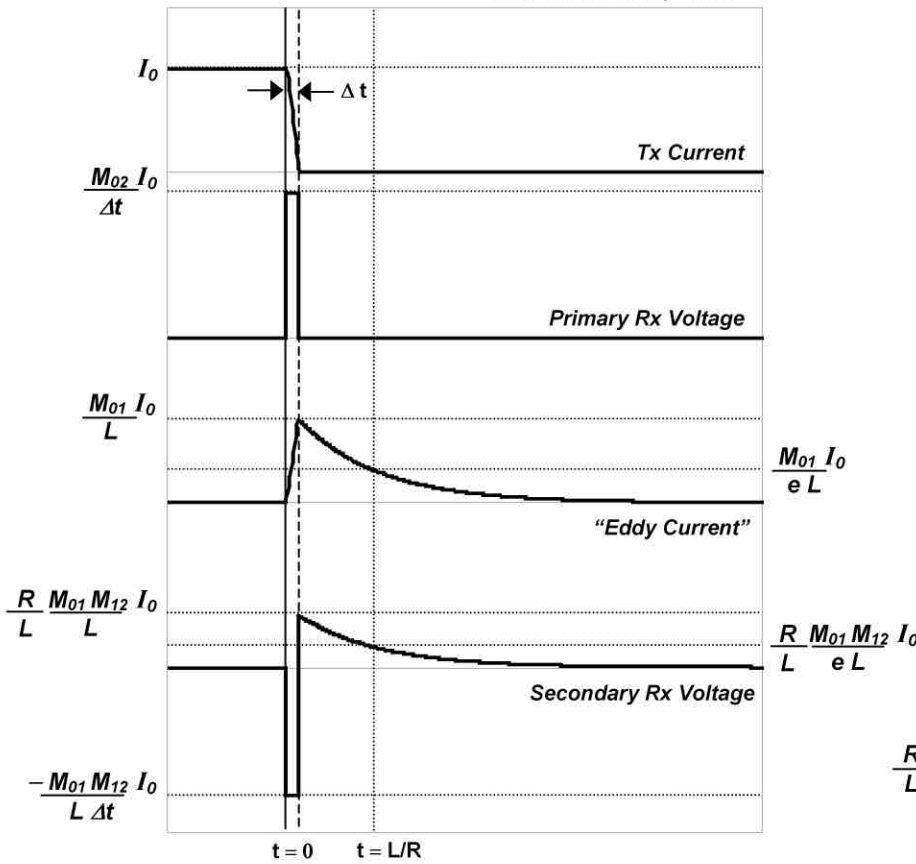


**THEORETICAL FDEM RESPONSE
CONDUCTIVE – MAGNETIC HALF-SPACE / STAND-OFF EFFECT**

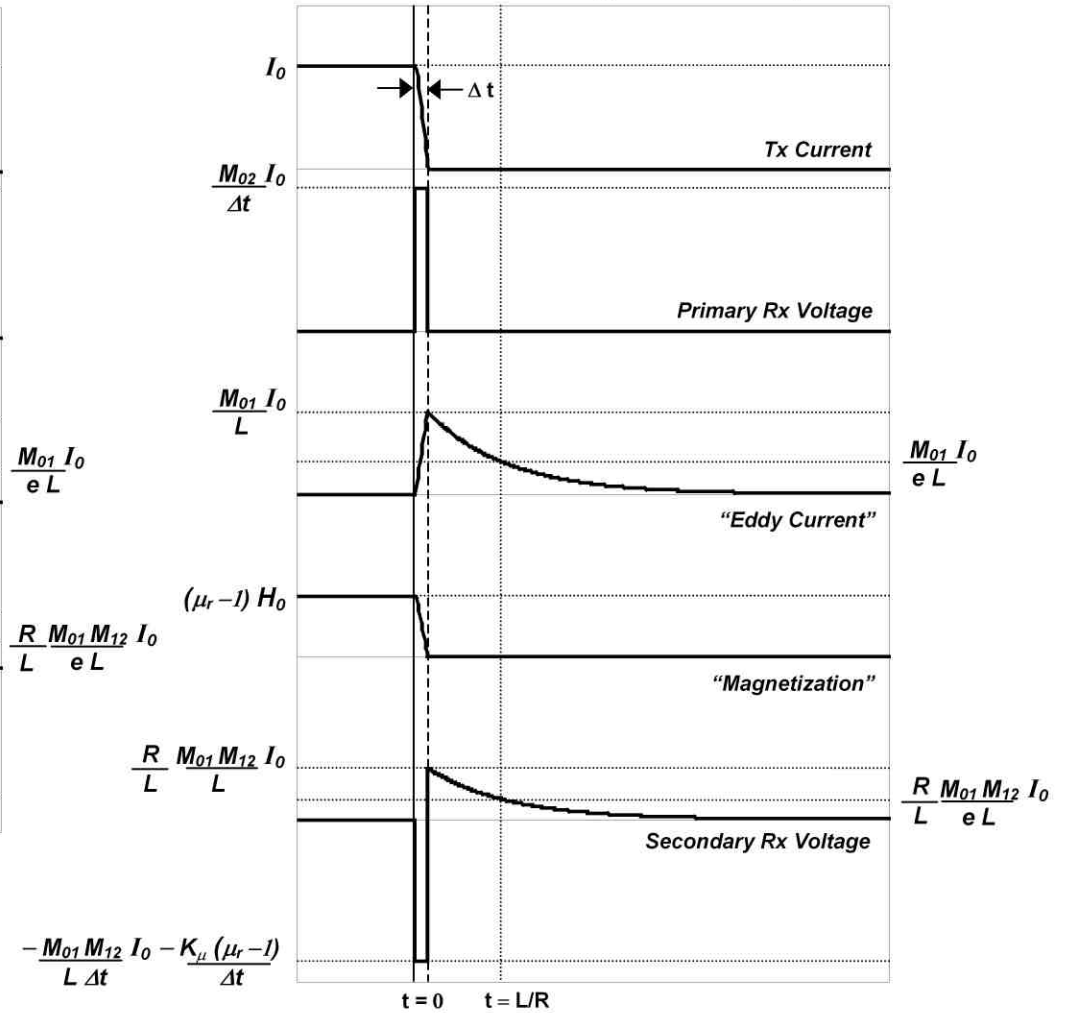


PROJECT:	CCMAT Soils	FIGURE: 11
DRAWN BY:	GMC	
	DATE:	20 February, 2006

Induction Response



Induction-Magnetization Response



$$-\frac{M_{01} M_{12} I_0}{L \Delta t} - K_{\mu} \frac{(\mu_r - 1)}{\Delta t}$$



**TDEM RESPONSE FUNCTIONS
INDUCTION – MAGNETIZATION**

FIGURE:

12

PROJECT:

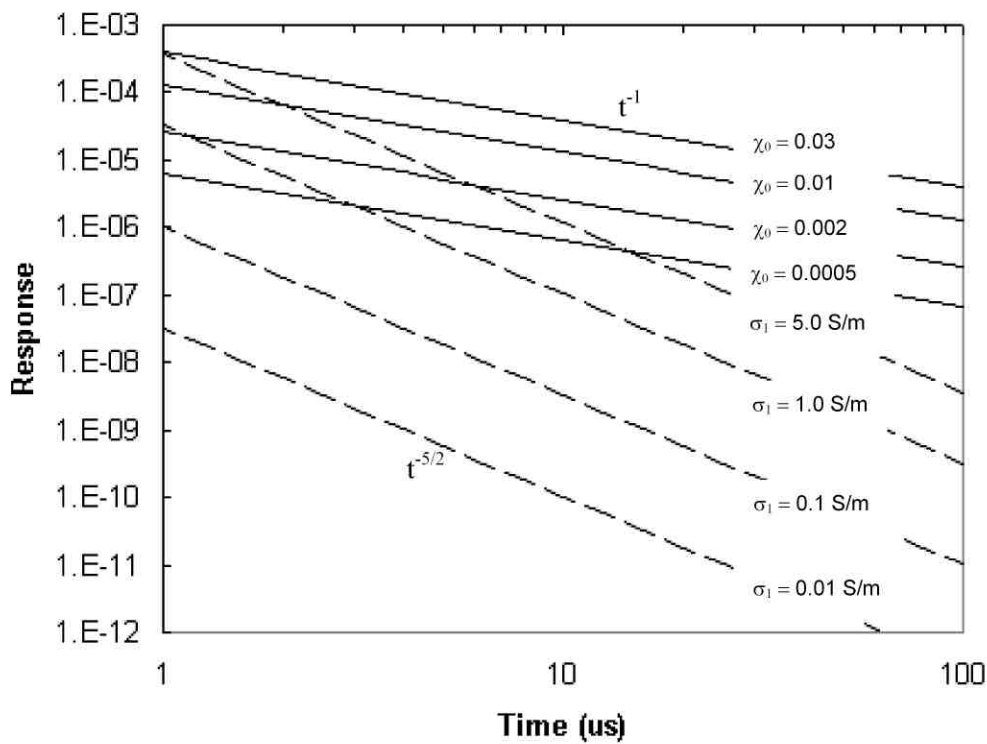
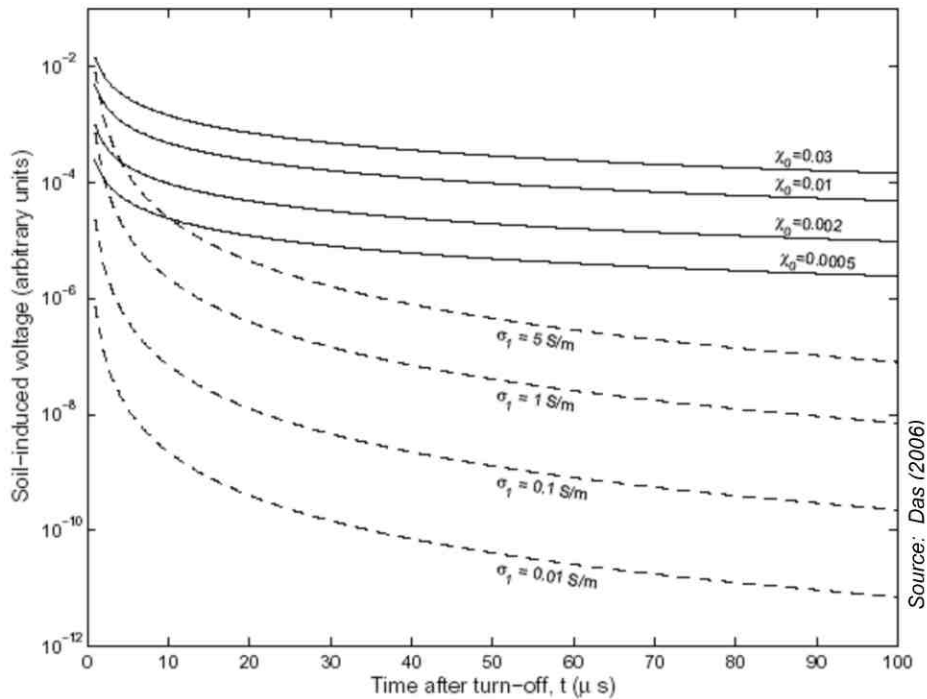
CCMAT Soils

DRAWN BY:

GMC

DATE:

15 December, 2007



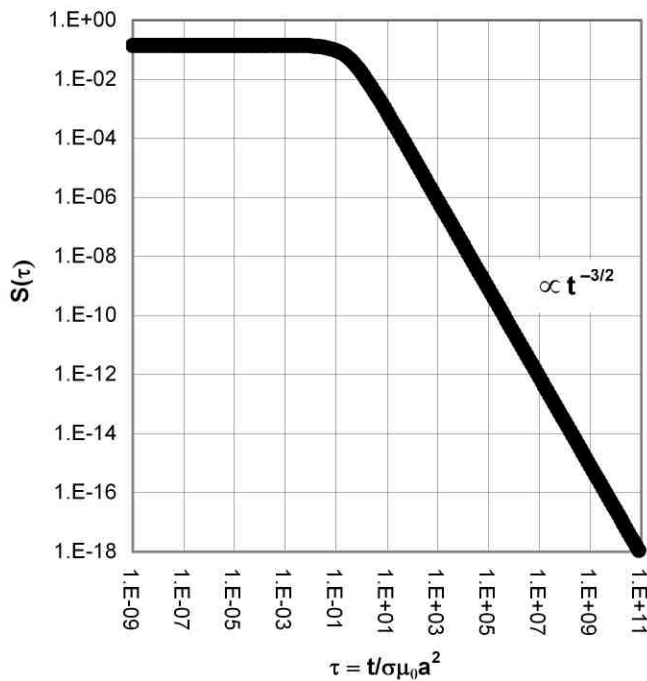
TDEM RECEIVER VOLTAGE RESPONSE
NON-MAGNETIC CONDUCTIVE vs. NON-CONDUCTIVE DISPERSIVE MAGNETIC SOILS



PROJECT: DRDC Soils

DRAWN BY: GMC DATE: 15 February, 2007

FIGURE: 13



1.00E-09	1.41E-01	1.00E-04	1.41E-01	1.00E+01	7.62E-04	1.00E+06	2.47E-11
1.58E-09	1.41E-01	1.58E-04	1.41E-01	1.58E+01	3.87E-04	1.58E+06	1.24E-11
2.51E-09	1.41E-01	2.51E-04	1.41E-01	2.51E+01	2.02E-04	2.51E+06	6.20E-12
3.98E-09	1.41E-01	3.98E-04	1.41E-01	3.98E+01	9.97E-05	3.98E+06	3.11E-12
6.31E-09	1.41E-01	6.31E-04	1.41E-01	6.31E+01	5.05E-05	6.31E+06	1.56E-12
1.00E-08	1.41E-01	1.00E-03	1.41E-01	1.00E+02	2.47E-05	1.00E+07	7.81E-13
1.58E-08	1.41E-01	1.58E-03	1.41E-01	1.58E+02	1.24E-05	1.58E+07	3.91E-13
2.51E-08	1.41E-01	2.51E-03	1.41E-01	2.51E+02	6.20E-06	2.51E+07	1.96E-13
3.98E-08	1.41E-01	3.98E-03	1.41E-01	3.98E+02	3.11E-06	3.98E+07	9.83E-14
6.31E-08	1.41E-01	6.31E-03	1.39E-01	6.31E+02	1.56E-06	6.31E+07	4.93E-14
1.00E-07	1.41E-01	1.00E-02	1.36E-01	1.00E+03	7.81E-07	1.00E+08	2.47E-14
1.58E-07	1.41E-01	1.58E-02	1.31E-01	1.58E+03	3.91E-07	1.58E+08	1.24E-14
2.51E-07	1.41E-01	2.51E-02	1.26E-01	2.51E+03	1.96E-07	2.51E+08	6.20E-15
3.98E-07	1.41E-01	3.98E-02	1.18E-01	3.98E+03	9.83E-08	3.98E+08	3.11E-15
6.31E-07	1.41E-01	6.31E-02	1.06E-01	6.31E+03	4.93E-08	6.31E+08	1.56E-15
1.00E-06	1.41E-01	1.00E-01	9.44E-02	1.00E+04	2.47E-08	1.00E+09	7.81E-16
1.58E-06	1.41E-01	1.58E-01	7.88E-02	1.58E+04	1.24E-08	1.58E+09	3.91E-16
2.51E-06	1.41E-01	2.51E-01	6.16E-02	2.51E+04	6.20E-09	2.51E+09	1.96E-16
3.98E-06	1.41E-01	3.98E-01	4.40E-02	3.98E+04	3.11E-09	3.98E+09	9.83E-17
6.31E-06	1.41E-01	6.31E-01	2.78E-02	6.31E+04	1.56E-09	6.31E+09	4.93E-17
1.00E-05	1.41E-01	1.00E+00	1.68E-02	1.00E+05	7.81E-10	1.00E+10	2.47E-17
1.58E-05	1.41E-01	1.58E+00	9.10E-03	1.58E+05	3.91E-10	1.58E+10	1.24E-17
2.51E-05	1.41E-01	2.51E+00	5.17E-03	2.51E+05	1.96E-10	2.51E+10	6.20E-18
3.98E-05	1.41E-01	3.98E+00	2.79E-03	3.98E+05	9.83E-11	3.98E+10	3.11E-18
6.31E-05	1.41E-01	6.31E+00	1.50E-03	6.31E+05	4.93E-11	6.31E+10	1.56E-18

**S(τ) - RAICHE and SPIES (1981)
COARSE TABULATED DATA**

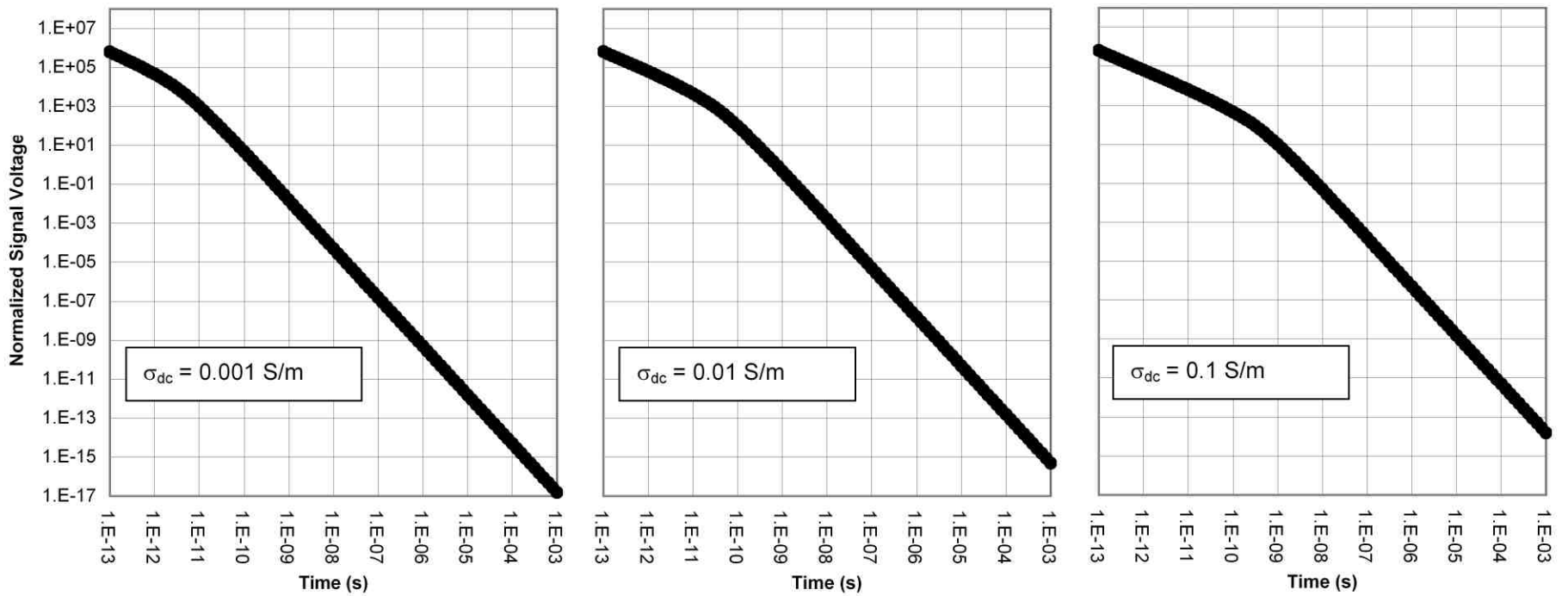


PROJECT: CCMAT Soils

DRAWN BY: GMC DATE: 15 December, 2007

FIGURE:

14



NOTE: Coincident horizontal Tx/Rx ($a = b = 0.1 \text{ m}$) at soil surface.

v1 – non-magnetic, non-dispersive conductive soil



**HORIZONTAL COINCIDENT COIL TDEM RESPONSE
CONDUCTIVE – NON-MAGNETIC SOIL**

FIGURE:

15

PROJECT:

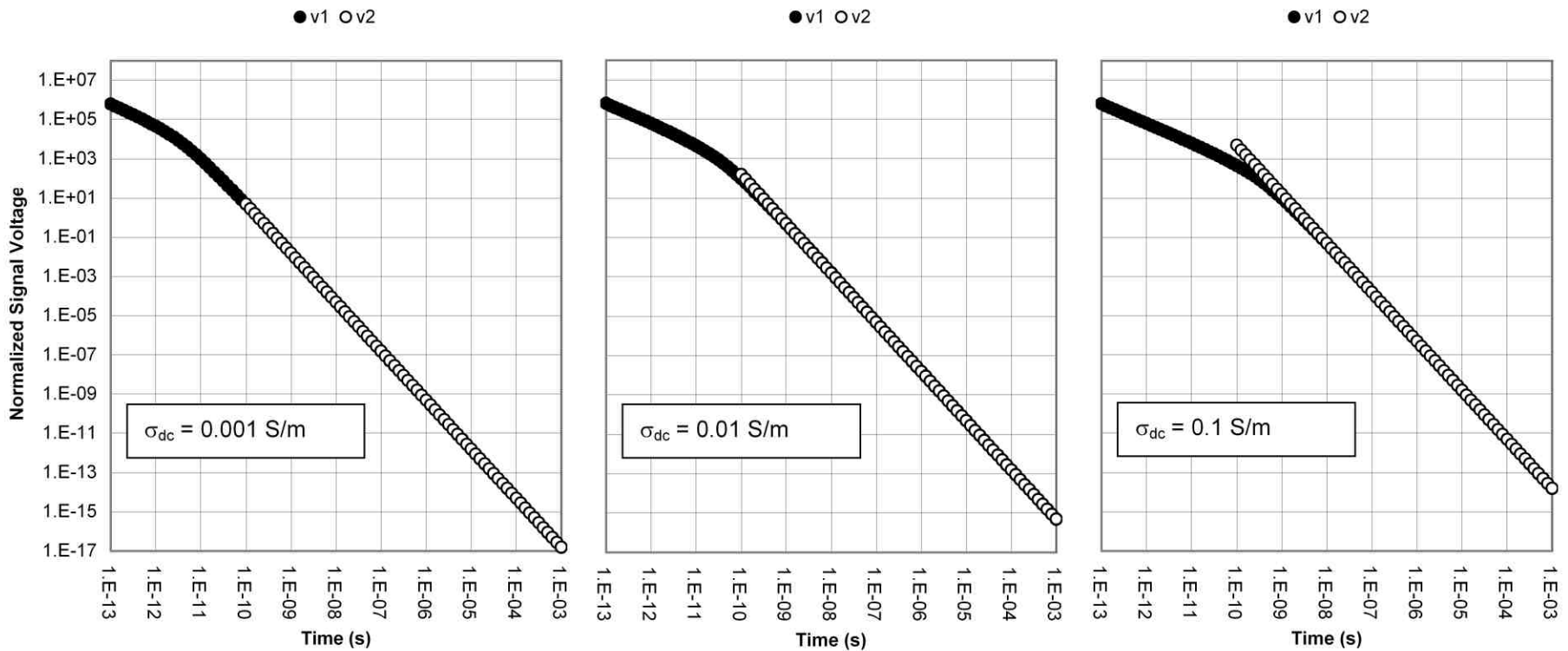
CCMAT Soils

DRAWN BY:

GMC

DATE:

15 May, 2007



NOTE: Coincident horizontal Tx/Rx ($a = b = 0.1 \text{ m}$) at soil surface.

v1 – non-magnetic, non-dispersive conductive soil

v2 – non-magnetic, non-dispersive conductive soil (late time)



**HORIZONTAL COINCIDENT COIL TDEM RESPONSE
CONDUCTIVE – NON-MAGNETIC SOIL (LATE-TIME)**

FIGURE:

16

PROJECT:

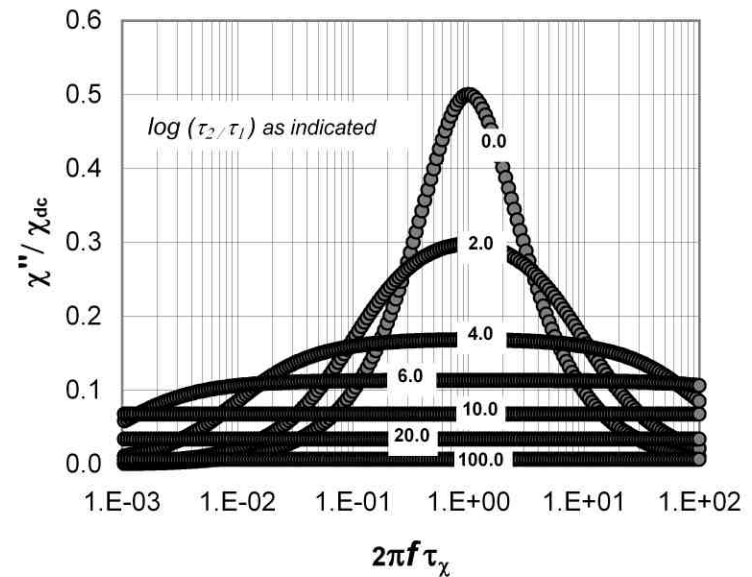
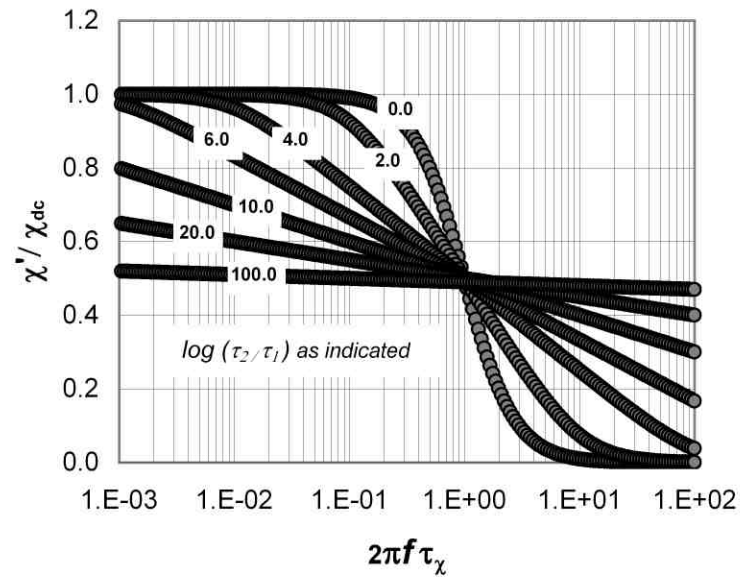
CCMAT Soils

DRAWN BY:

GMC

DATE:

15 May, 2007



**SUSCEPTIBILITY DISPERSION - LOG-UNIFORM MODEL
TIME-CONSTANT BANDWIDTH DEPENDENCE**

FIGURE:

17

PROJECT:

DRDC Soils

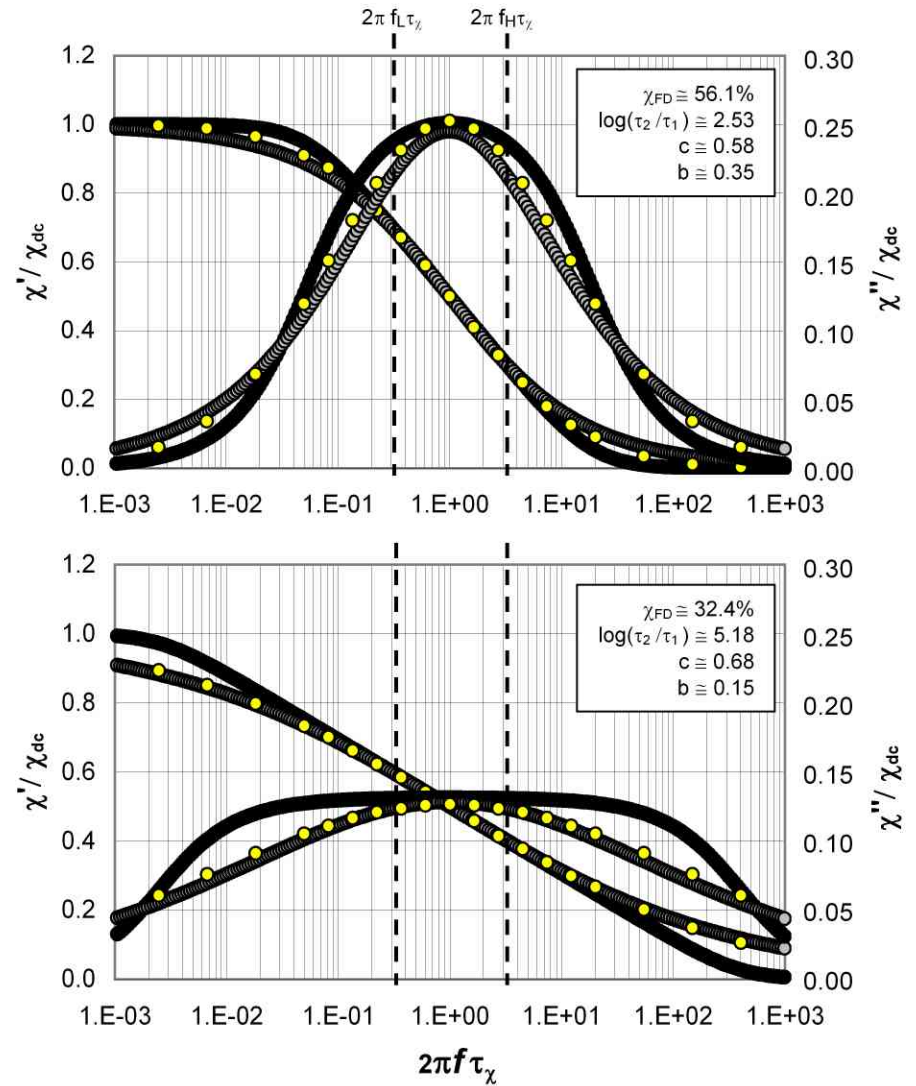
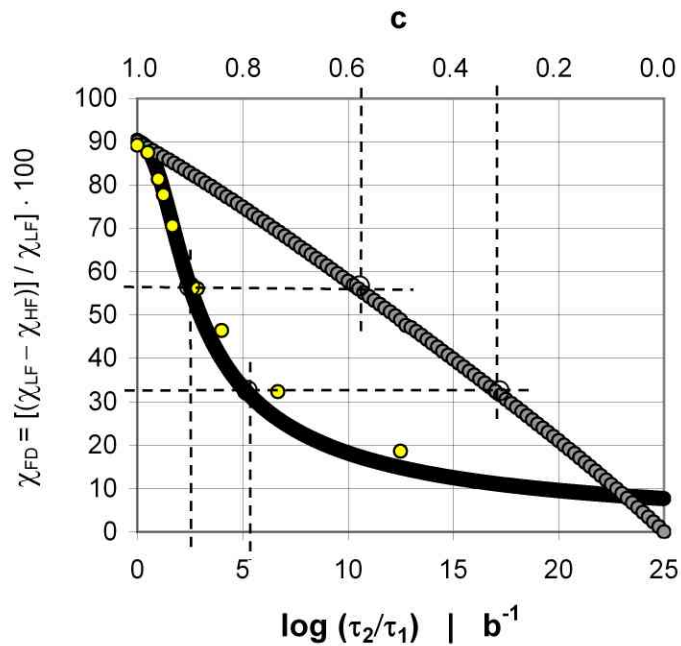
DRAWN BY:

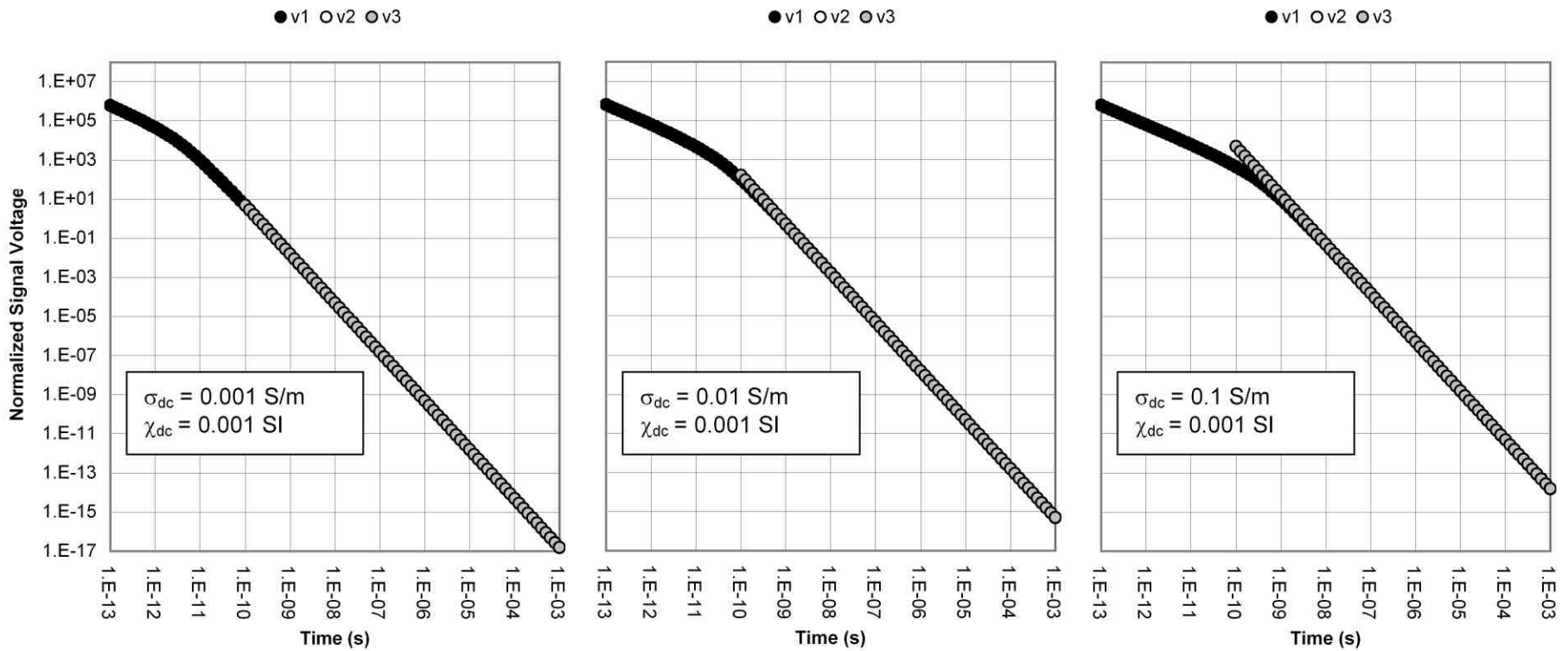
GMC

DATE:

12 December, 2005

- log-uniform Richter $\mathcal{T}_\chi(\ln \tau) = \begin{cases} 0, & \tau < \tau_1; \\ 1/\ln(\tau_2/\tau_1), & \tau_1 \leq \tau \leq \tau_2; \\ 0, & \tau > \tau_2. \end{cases}$
- Cole-Cole $\mathcal{T}_\chi(\ln \tau) = \frac{1}{2\pi} \frac{\sin[(1-c)\pi]}{\cosh[c \ln(\tau/\tau_\chi)] - \cos[(1-c)\pi]}$
- log-normal Wagner $\mathcal{T}_\chi(\ln \tau) = \frac{b}{\sqrt{\pi}\lambda} \exp[-b^2 \ln^2(\tau/\tau_\chi)]$





NOTE: Coincident horizontal Tx/Rx ($a = b = 0.1 \text{ m}$) at soil surface.

v1 – non-magnetic, non-dispersive conductive soil

v2 – non-magnetic, non-dispersive conductive soil (late time)

v3 – non-dispersive magnetic, non-dispersive conductive soil



**HORIZONTAL COINCIDENT COIL TDEM RESPONSE
EFFECT OF NON-DISPERSIVE CONDUCTIVE / MAGNETIC SOIL**

FIGURE:

18

PROJECT:

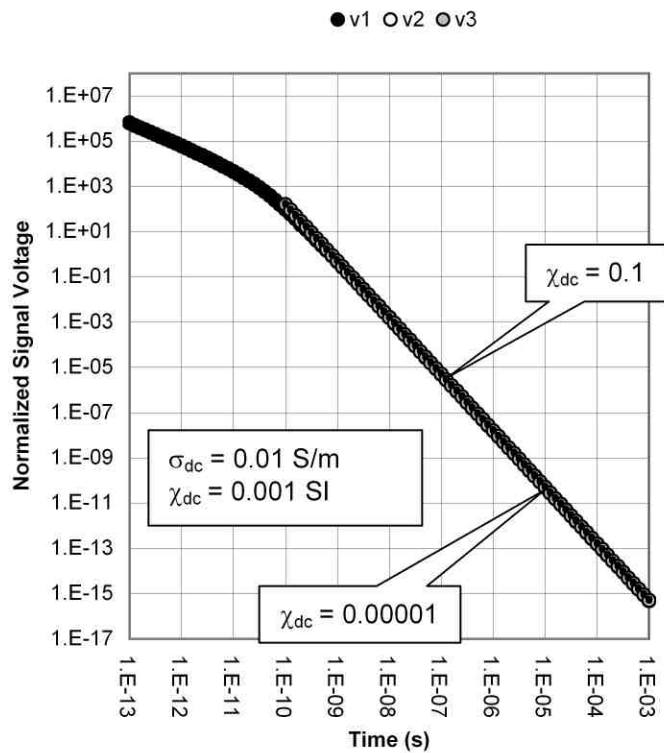
CCMAT Soils

DRAWN BY:

GMC

DATE:

15 May, 2007



NOTE: Coincident horizontal Tx/Rx ($a = b = 0.1 \text{ m}$) at soil surface.

- v1 – non-magnetic, non-dispersive conductive soil
- v2 – non-magnetic, non-dispersive conductive soil (late time)
- v3 – non-dispersive magnetic, non-dispersive conductive soil
- v4 – non-conductive, dispersive magnetic soil



**HORIZONTAL COINCIDENT COIL TDEM RESPONSE
EFFECT OF MAGNETIC SOIL PARAMETERS**

FIGURE:

19

PROJECT:

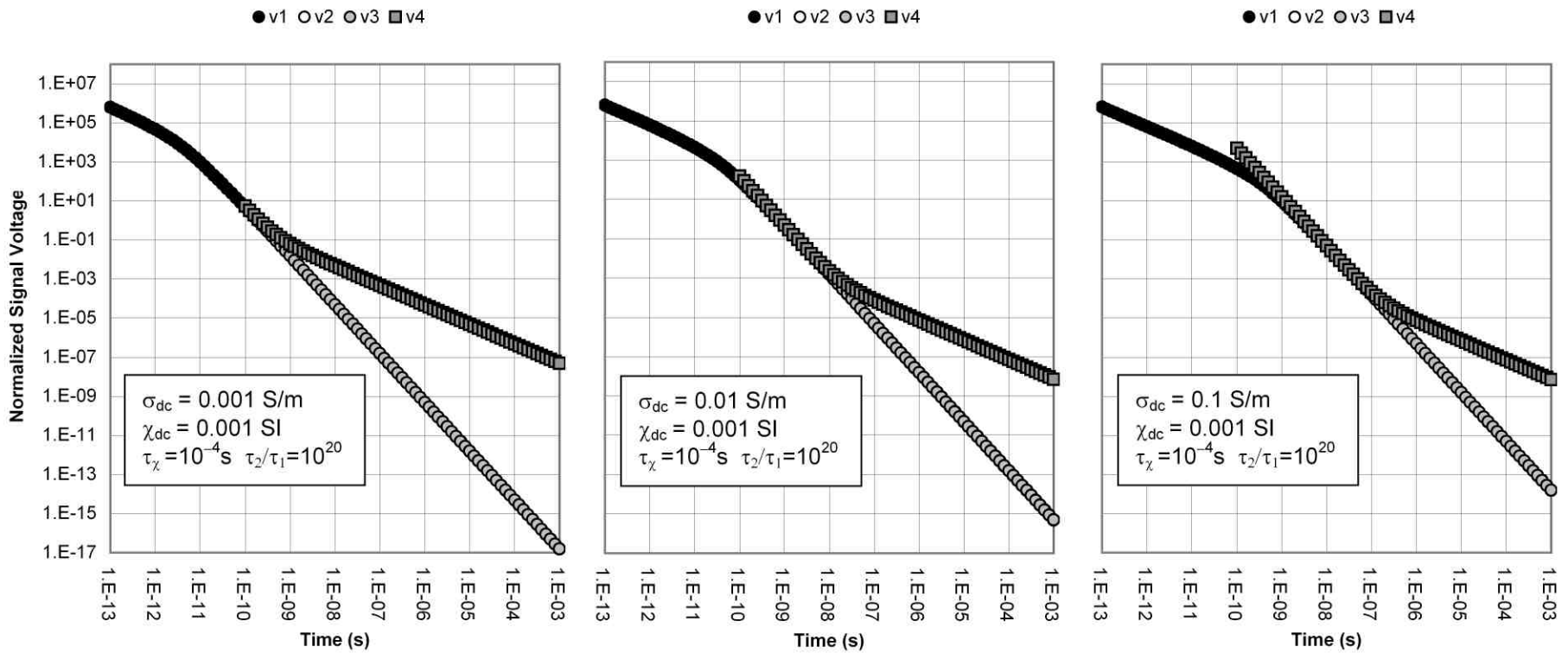
CCMAT Soils

DRAWN BY:

GMC

DATE:

15 May, 2007



NOTE: Coincident horizontal Tx/Rx ($a = b = 0.1$ m) at soil surface.

- v1 – non-magnetic, non-dispersive conductive soil
- v2 – non-magnetic, non-dispersive conductive soil (late time)
- v3 – non-dispersive magnetic, non-dispersive conductive soil
- v4 – non-conductive, dispersive magnetic soil



**HORIZONTAL COINCIDENT COIL TDEM RESPONSE
EFFECT OF DISPERSIVE MAGNETIC SOIL**

FIGURE:

20

PROJECT:

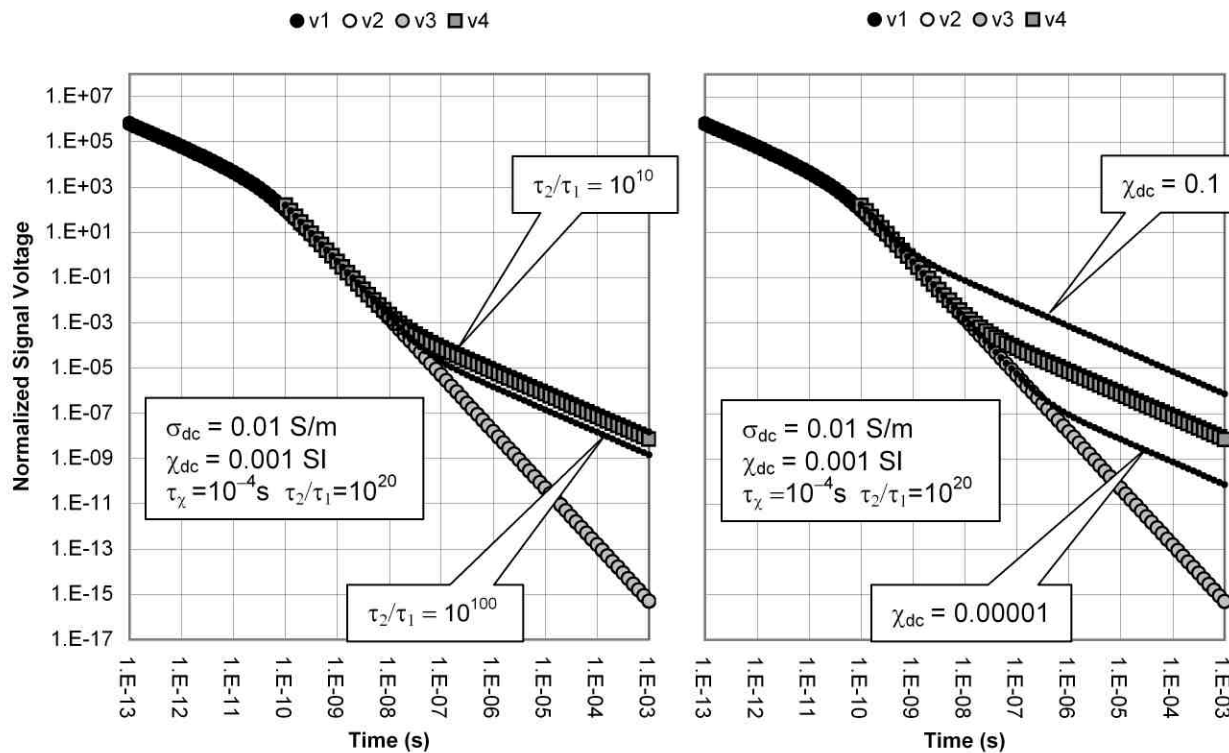
CCMAT Soils

DRAWN BY:

GMC

DATE:

15 May, 2007



NOTE: Coincident horizontal Tx/Rx ($a = b = 0.1 \text{ m}$) at soil surface.

- v1 – non-magnetic, non-dispersive conductive soil
- v2 – non-magnetic, non-dispersive conductive soil (late time)
- v3 – non-dispersive magnetic, non-dispersive conductive soil
- v4 – non-conductive, dispersive magnetic soil



**HORIZONTAL COINCIDENT COIL TDEM RESPONSE
EFFECT OF MAGNETIC SOIL PARAMETERS**

FIGURE:

21

PROJECT:

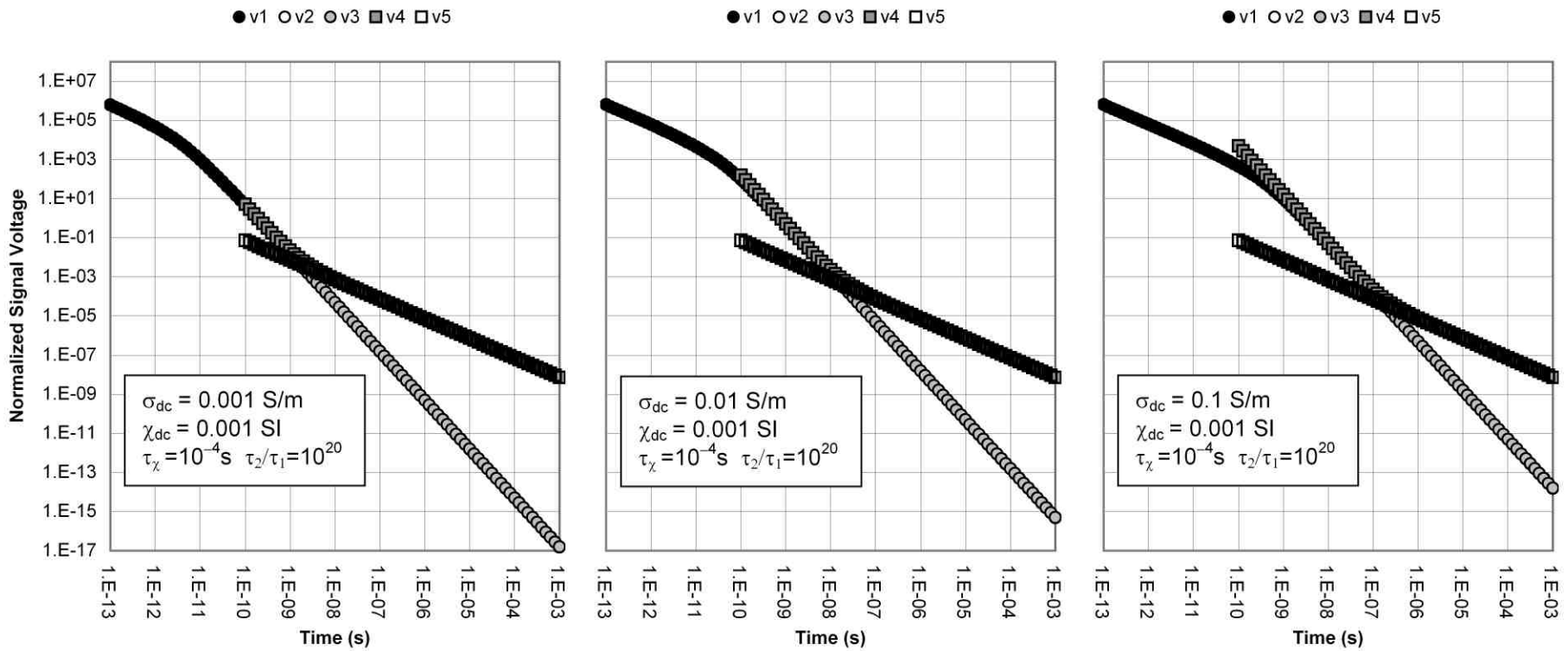
CCMAT Soils

DRAWN BY:

GMC

DATE:

15 May, 2007



NOTE: Coincident horizontal Tx/Rx ($a = b = 0.1 \text{ m}$) at soil surface.

- v1 – non-magnetic, non-dispersive conductive soil
- v2 – non-magnetic, non-dispersive conductive soil (late time)
- v3 – non-dispersive magnetic, non-dispersive conductive soil
- v4 – dispersive magnetic, non-dispersive conductive soil
- v5 – dispersive magnetic, non-dispersive conductive soil (approximation)



**HORIZONTAL COINCIDENT COIL TDEM RESPONSE
EFFECT OF NON DISPERSIVE MAGNETIC SOIL (APPROX)**

FIGURE:

22

PROJECT:

CCMAT Soils

DRAWN BY:

GMC

DATE:

15 May, 2007

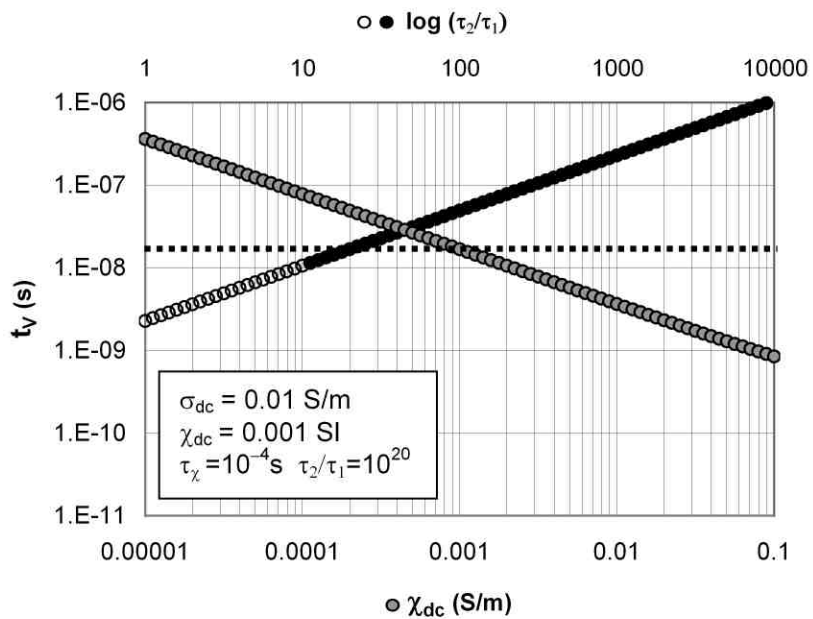


Figure 23.

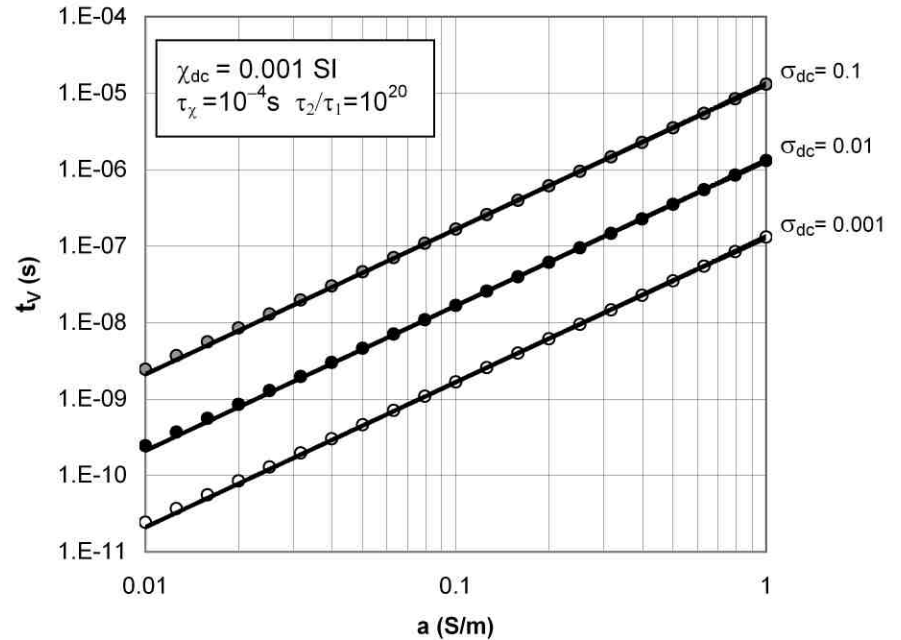


Figure 24.



**HORIZONTAL COINCIDENT COIL TDEM RESPONSE
EFFECT OF NON DISPERSIVE MAGNETIC SOIL (APPROX)**

FIGURE:

23 / 24

PROJECT:

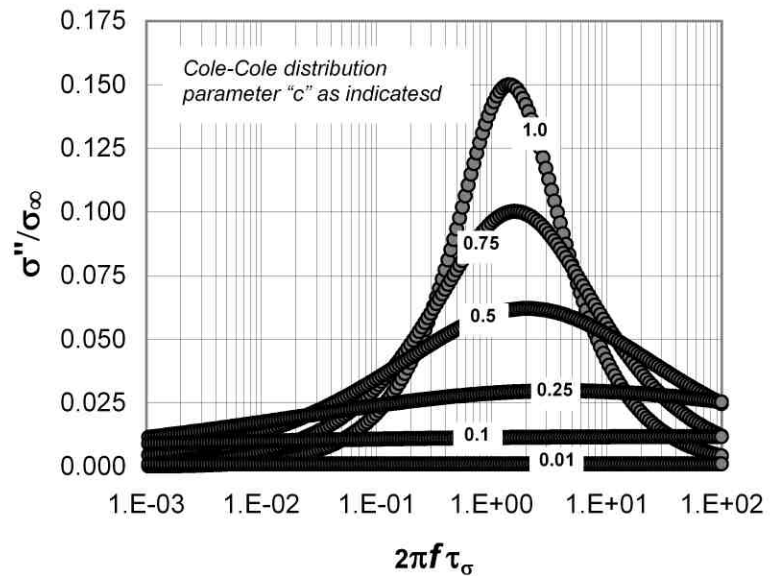
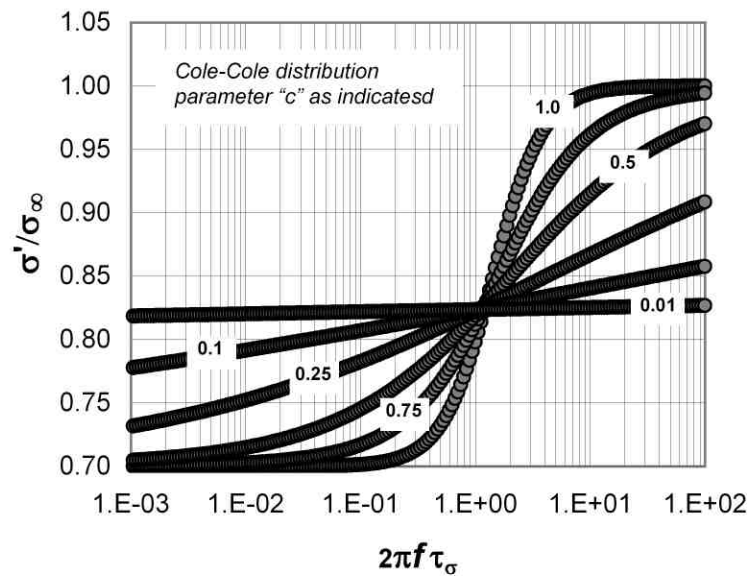
CCMAT Soils

DRAWN BY:

GMC

DATE:

15 May, 2007



**CONDUCTIVITY DISPERSION - COLE - COLE MODEL
DISTRIBUTION PARAMETER DEPENDENCE**

FIGURE:

25

PROJECT:

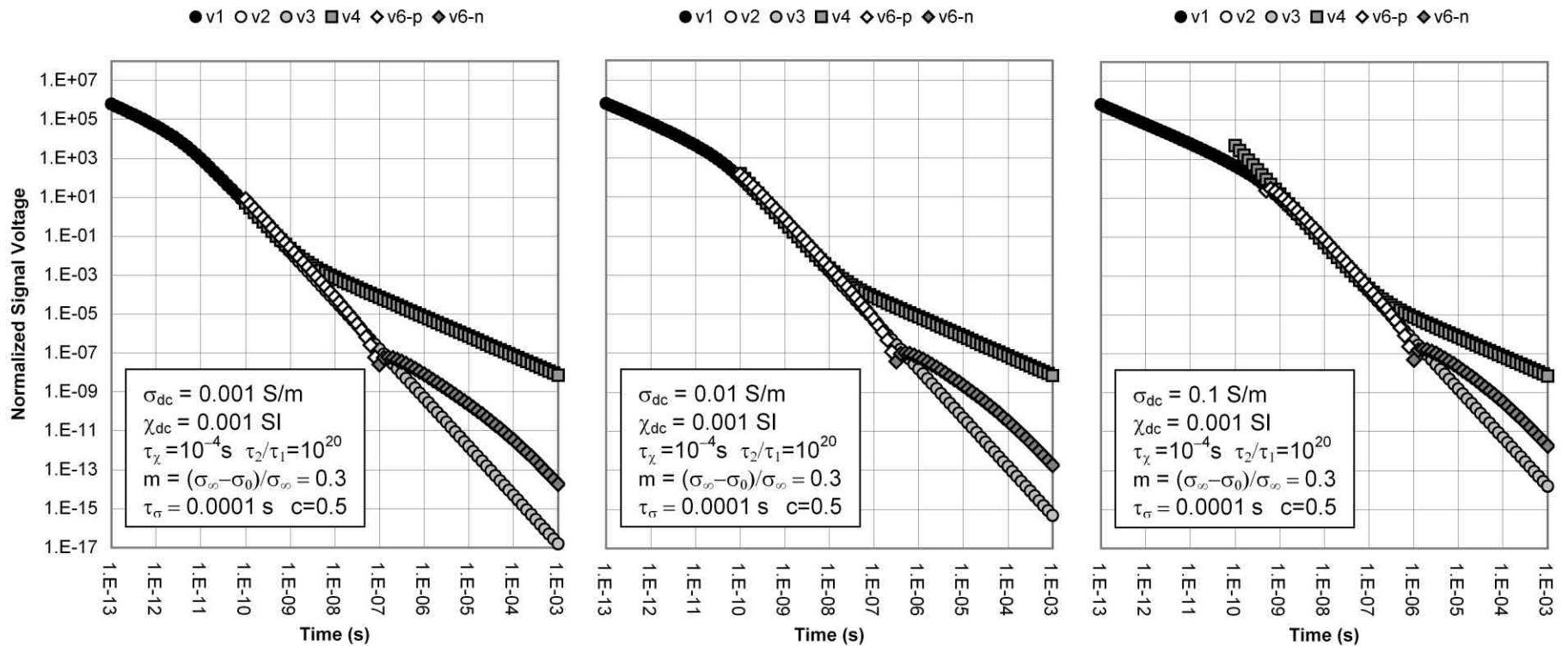
DRDC Soils

DRAWN BY:

GMC

DATE:

12 December, 2005



NOTE: Coincident horizontal Tx/Rx ($a = b = 0.1 \text{ m}$) at soil surface.

- v1 – non-magnetic, non-dispersive conductive soil
- v2 – non-magnetic, non-dispersive conductive soil (late time)
- v3 – non-dispersive magnetic, non-dispersive conductive soil
- v4 – dispersive magnetic, non-dispersive conductive soil
- v6-p – non-magnetic, dispersive conductive soil (positive-polarity – terminated source)
- v6-n – non-magnetic, dispersive conductive soil (negative-polarity – terminated source)



HORIZONTAL COINCIDENT COIL TDEM RESPONSE EFFECT OF DISPERSIVE CONDUCTIVE SOIL

FIGURE:

26

PROJECT:

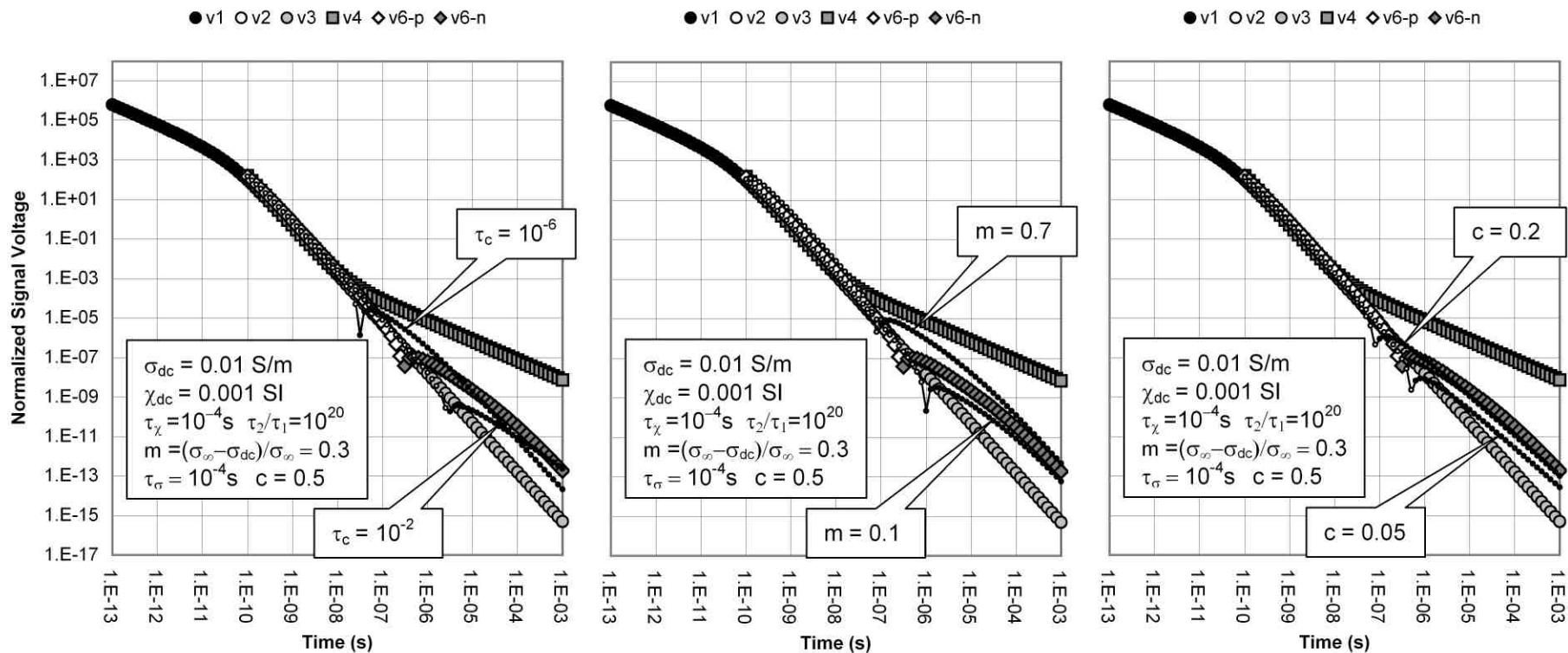
CCMAT Soils

DRAWN BY:

GMC

DATE:

15 May, 2007



NOTE: Coincident horizontal Tx/Rx ($a = b = 0.1 \text{ m}$) at soil surface.

- v1 – non-magnetic, non-dispersive conductive soil
- v2 – non-magnetic, non-dispersive conductive soil (late time)
- v3 – non-dispersive magnetic, non-dispersive conductive soil
- v4 – non-conductive, dispersive magnetic soil
- v6-p – non-magnetic, dispersive conductive soil (positive-polarity – terminated source)
- v6-n – non-magnetic, dispersive conductive soil (negative-polarity – terminated source)



**HORIZONTAL COINCIDENT COIL TDEM RESPONSE
EFFECT OF ELECTRICAL POLARIZATION PARAMETERS**

FIGURE:

27

PROJECT:

CCMAT Soils

DRAWN BY:

GMC

DATE:

15 May, 2007

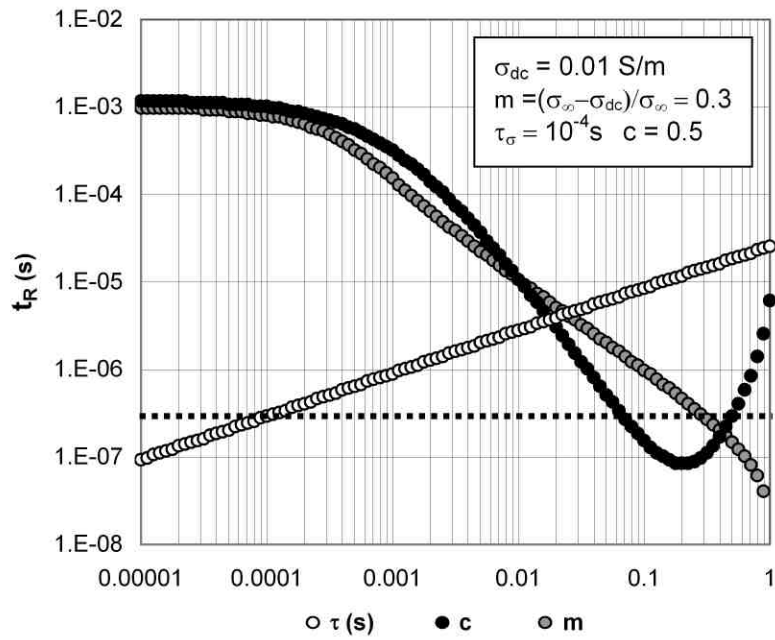


Figure 28.

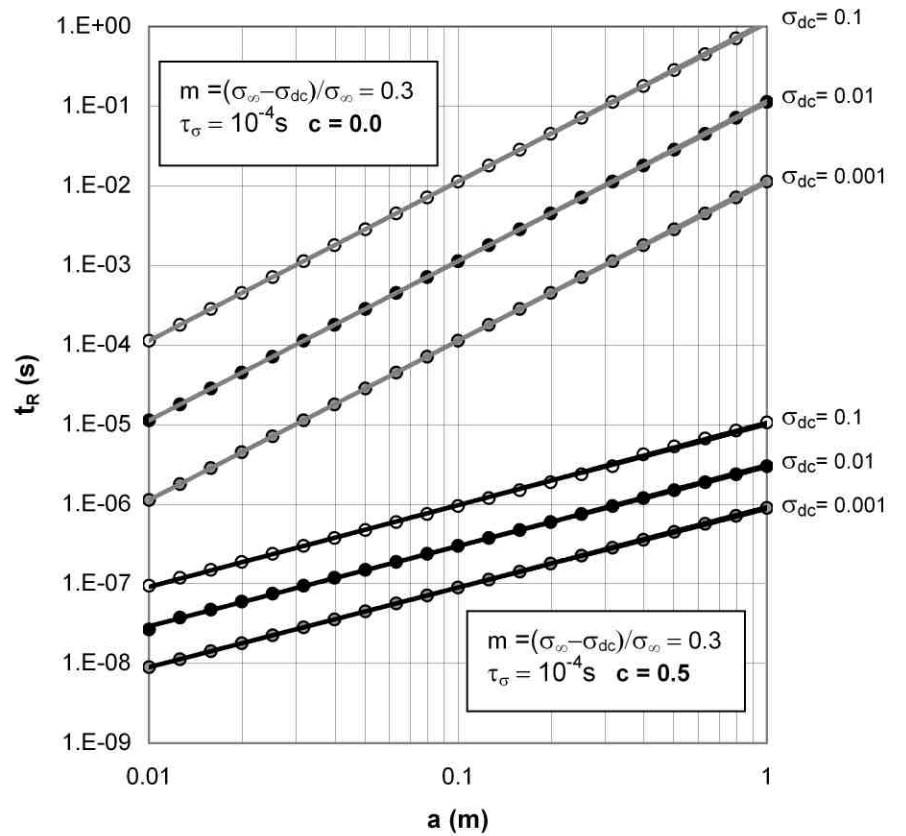


Figure 30.



**HORIZONTAL COINCIDENT COIL TDEM RESPONSE
EFFECT OF NON DISPERSIVE MAGNETIC SOIL (APPROX)**

FIGURE:

28 / 30

PROJECT:

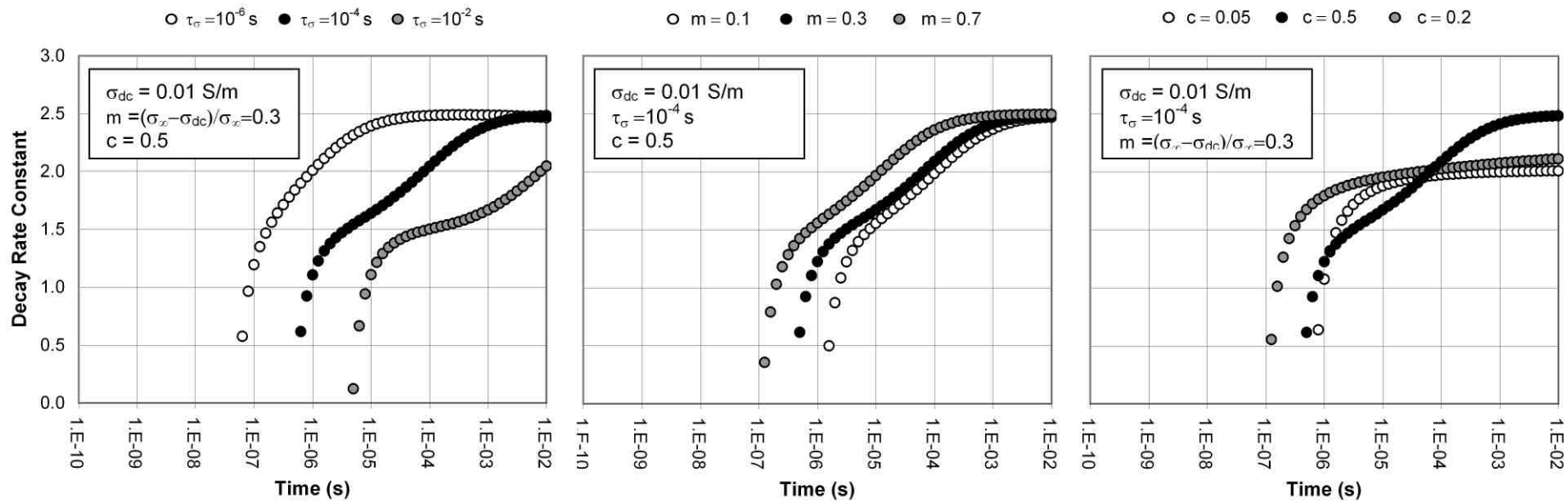
CCMAT Soils

DRAWN BY:

GMC

DATE:

15 May, 2007



NOTE: Coincident horizontal Tx/Rx ($a = b = 0.1 \text{ m}$) at soil surface.

Effective Decay Rate

v6-n – non-magnetic, dispersive conductive soil (negative-polarity – terminated source)



**NEGATIVE-VALUED LATE TIME DECAY RATE
EFFECT OF ELECTRICAL POLARIZATION PARAMETERS**

FIGURE:

29

PROJECT:

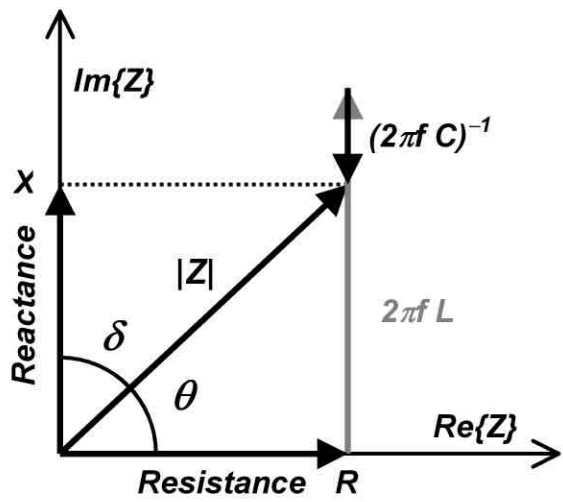
CCMAT Soils

DRAWN BY:

GMC

DATE:

10 December, 2007



Complex Impedance: Z

$Z=V/I$

$Z=R+iX$

$Z=R+i [2\pi f L - (2\pi f C)^{-1}]$

$Z=|Z| \exp(i\theta)$

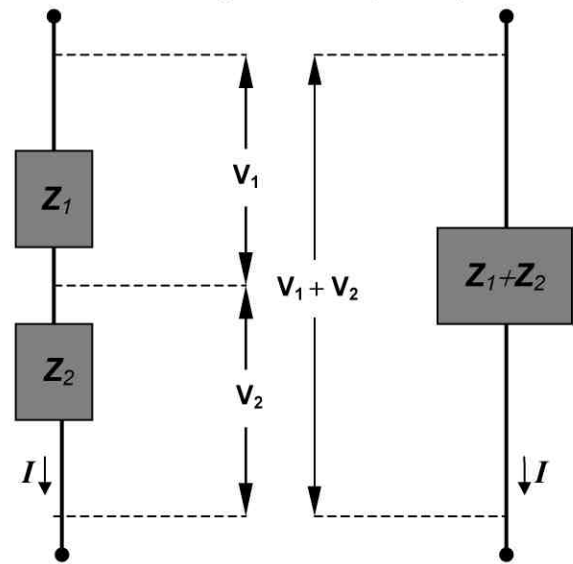
$|Z|=(R^2+X^2)^{1/2}$

$\theta = \tan^{-1}(X/R)$

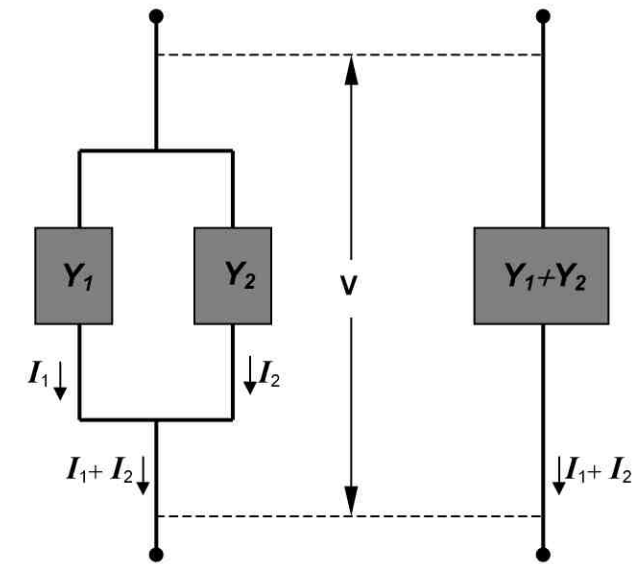
$\delta = \tan^{-1}(R/X)$

Complex Admittance: $Y=Z^{-1}=(R+iX)^{-1}$

Series Impedance ($Z=V/I$)



Parallel Impedance ($Y=I/V$)



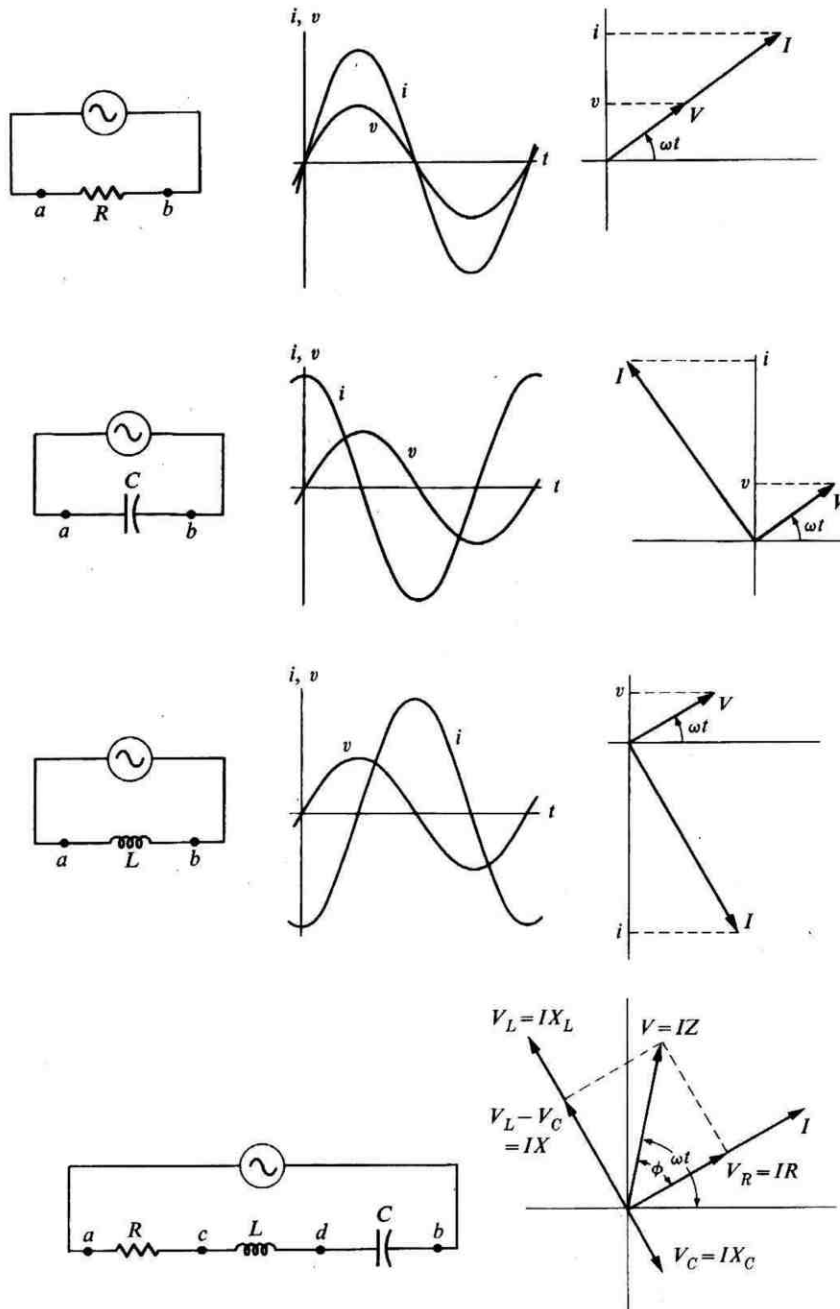
**COMPLEX IMPEDANCE – ADMITTANCE
SERIES – PARALLEL COMBINATION**

FIGURE:
31

PROJECT: DRDC Soils

DRAWN BY: GMC

DATE: 12 December, 2006



Source: Sears and Zemansky, 1964.

COMPLEX IMPEDANCE - THEORY
PURE CIRCUIT ELEMENTS - AMPLITUDE - PHASE CHARACTERISTICS

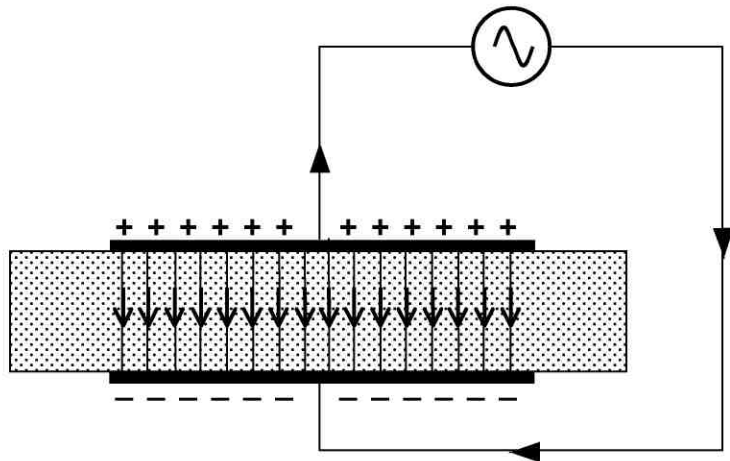


PROJECT: DRDC Soils

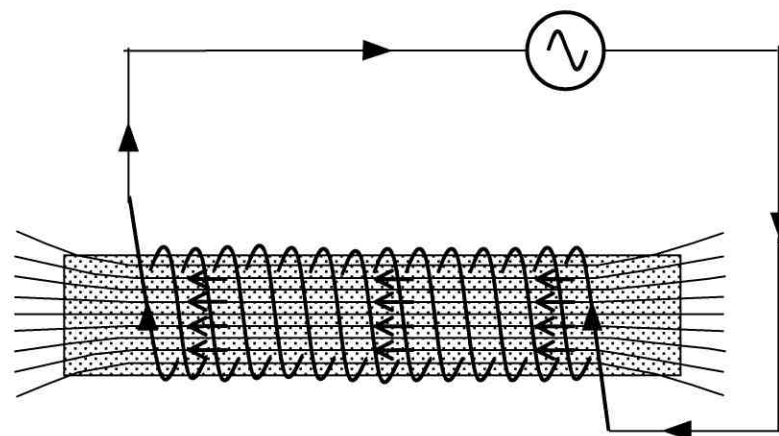
DRAWN BY: GMC DATE: 14 December, 2003

FIGURE:

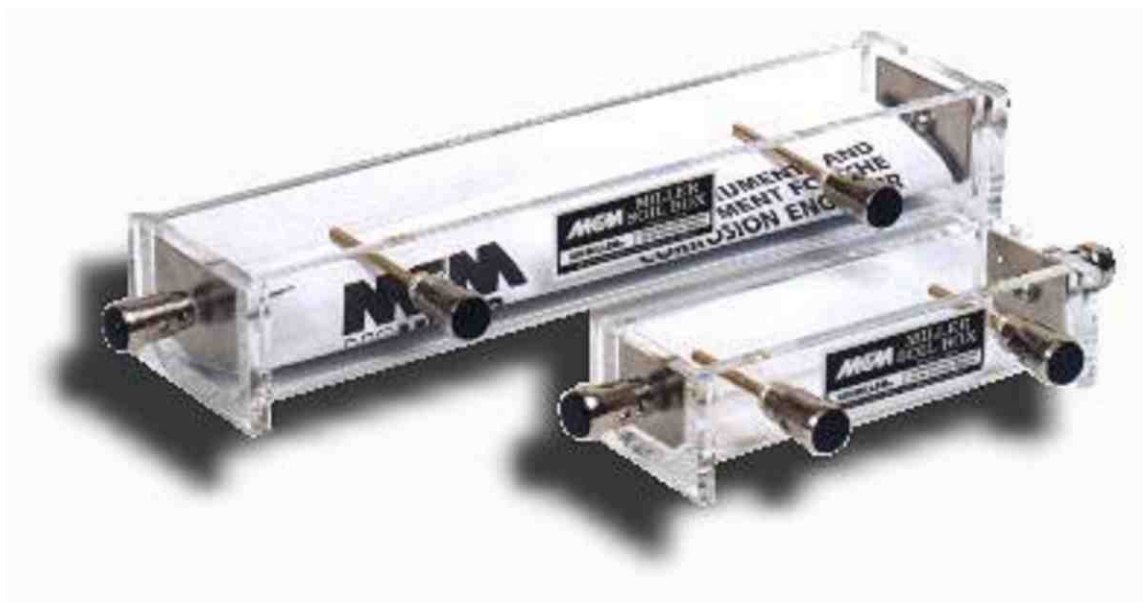
32



(a)



(b)

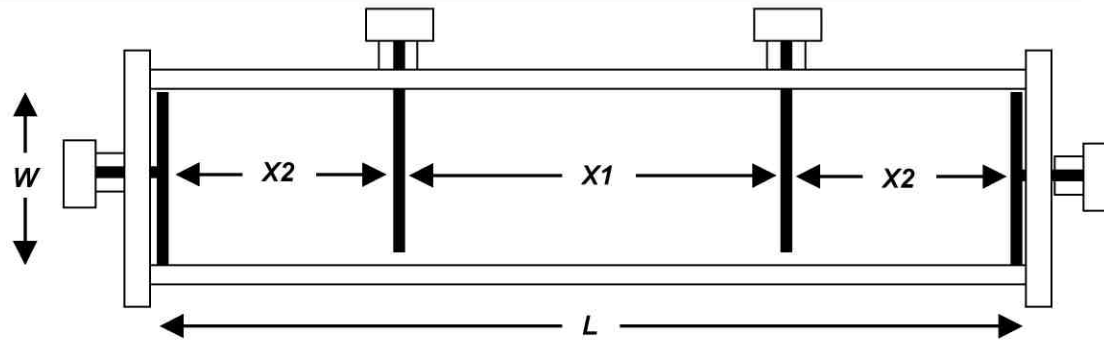


SOIL BOX – PHYSICAL DATA*

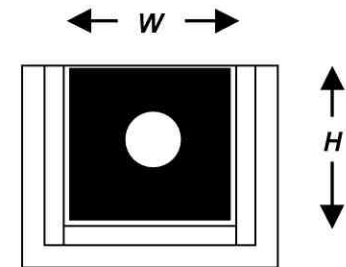
	<u>SMALL</u>	<u>LARGE</u>
Length (L-cm)	11.0	22.0
Width (W-cm)	3.0	3.8
Height (H-cm)	2.4	3.0
X1 (cm)	7.1	12.4
X2 (cm)	1.8	4.6
Mass (g)	130	240
Volume (ml)	75	250

MATERIALS

Body	Lexan
Pin Electrodes	Brass
Plate Electrodes	Stainless Steel



TOP VIEW



END VIEW

* NOTE: Physical data are nominal values - actual data deviate within approximately +/- 0.1 cm



MC MILLER SOIL RESISTIVITY BOX

FIGURE:

34

PROJECT:

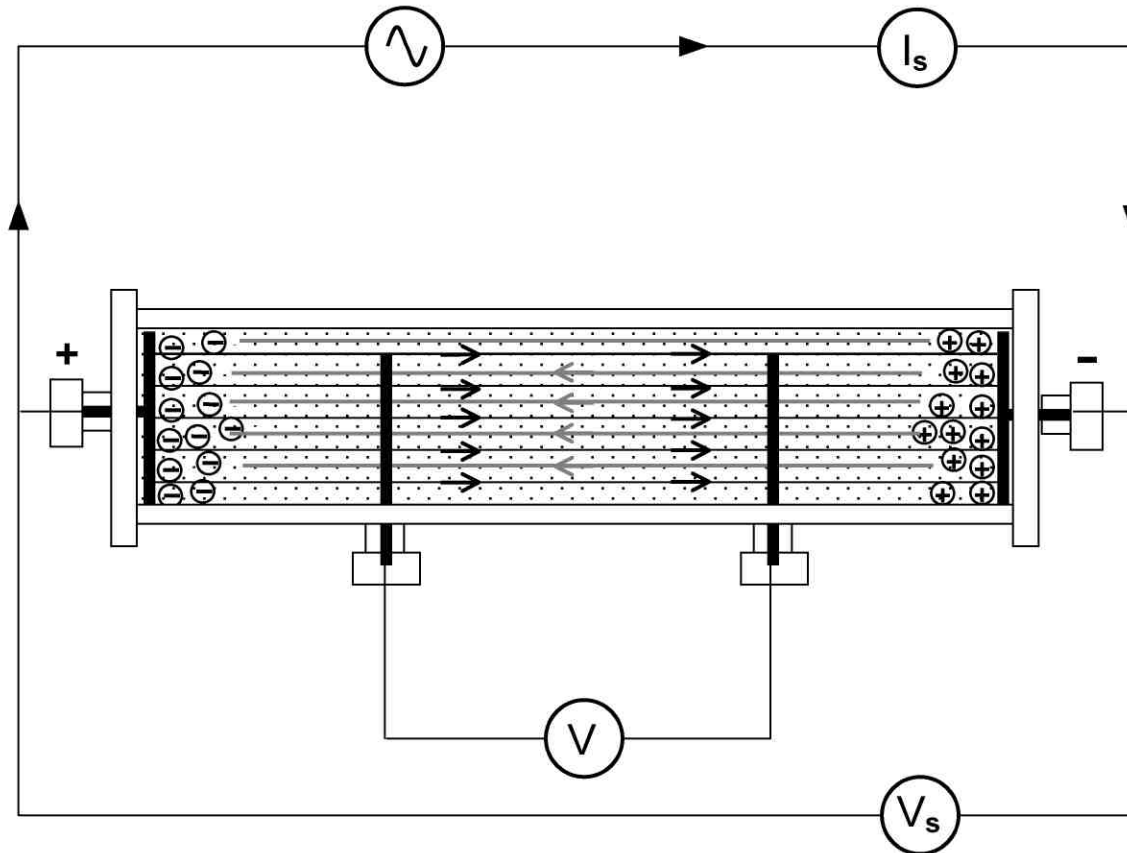
DRDC Soils

DRAWN BY:

GMC

DATE:

14 December, 2003



→ Primary Field
 ← Polarization Field



**FOUR ELECTRODE MEASUREMENT
 ELECTRODE POLARIZATION**

FIGURE:

35

PROJECT:

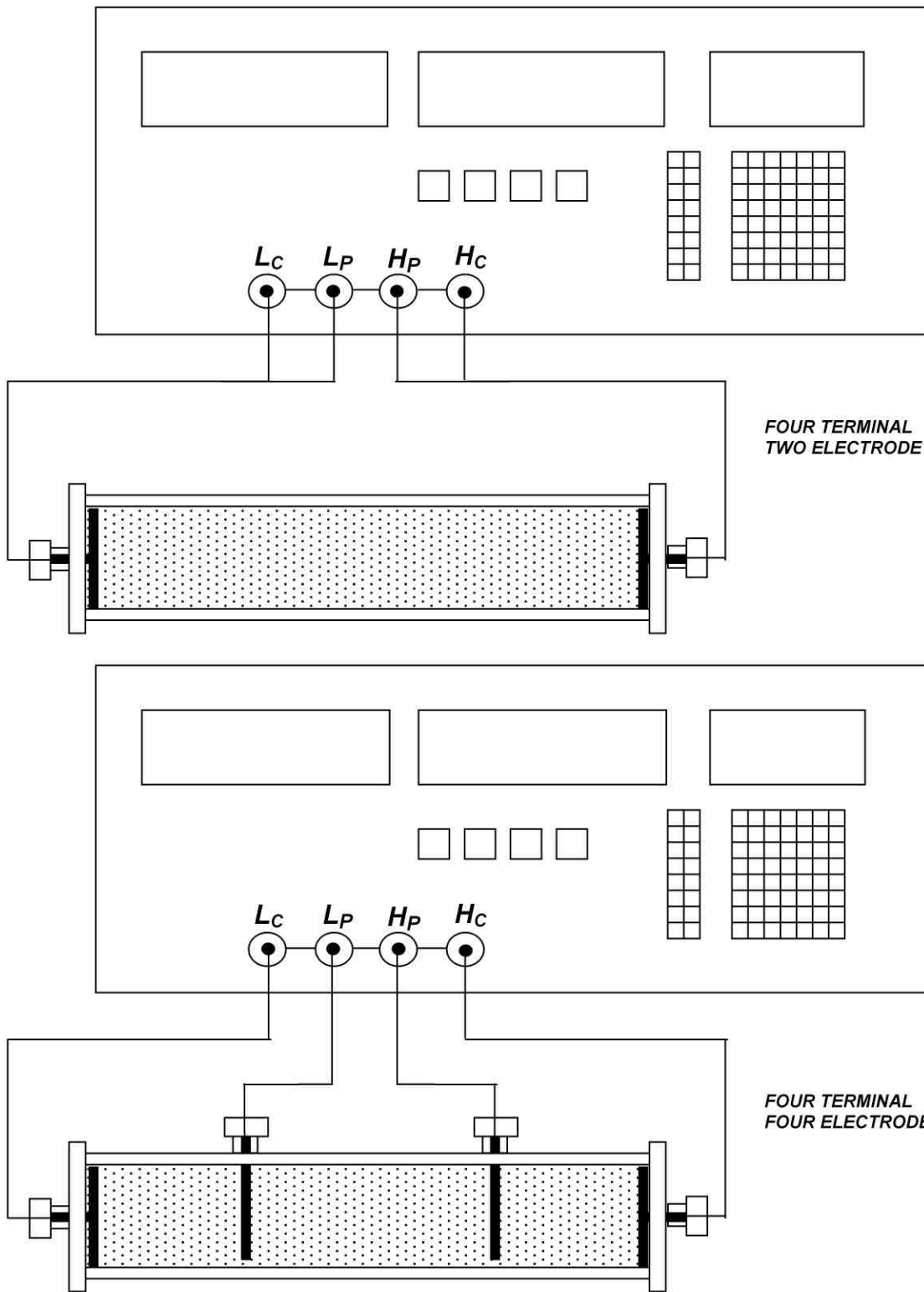
CCMAT Soils

DRAWN BY:

GMC

DATE:

15 May, 2007



**SOIL BOX RESISTIVITY MEASUREMENT CONFIGURATIONS
IMPEDANCE ANALYZER / LCR METER**

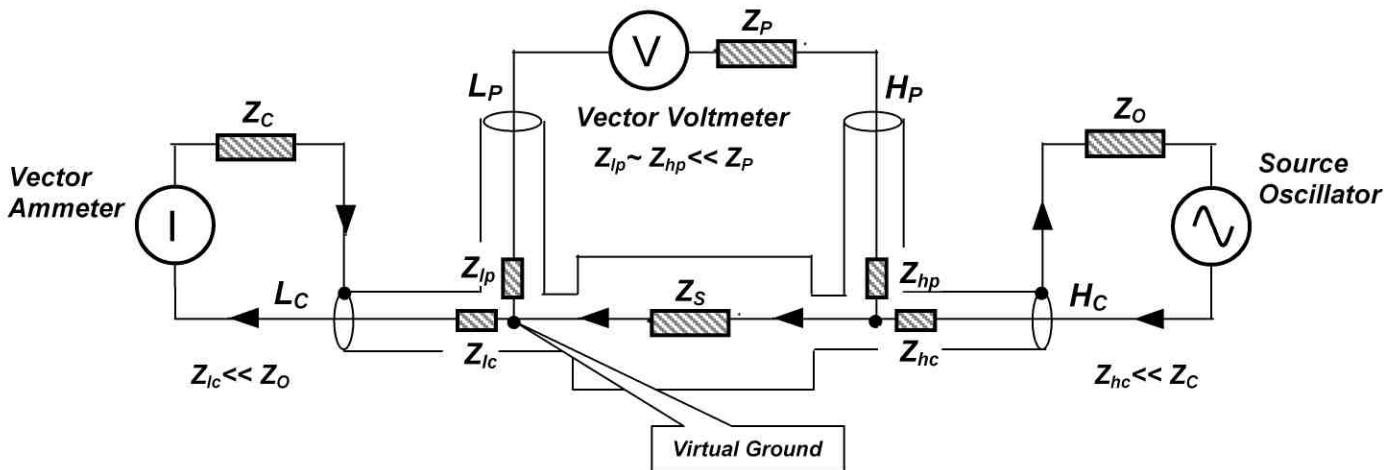
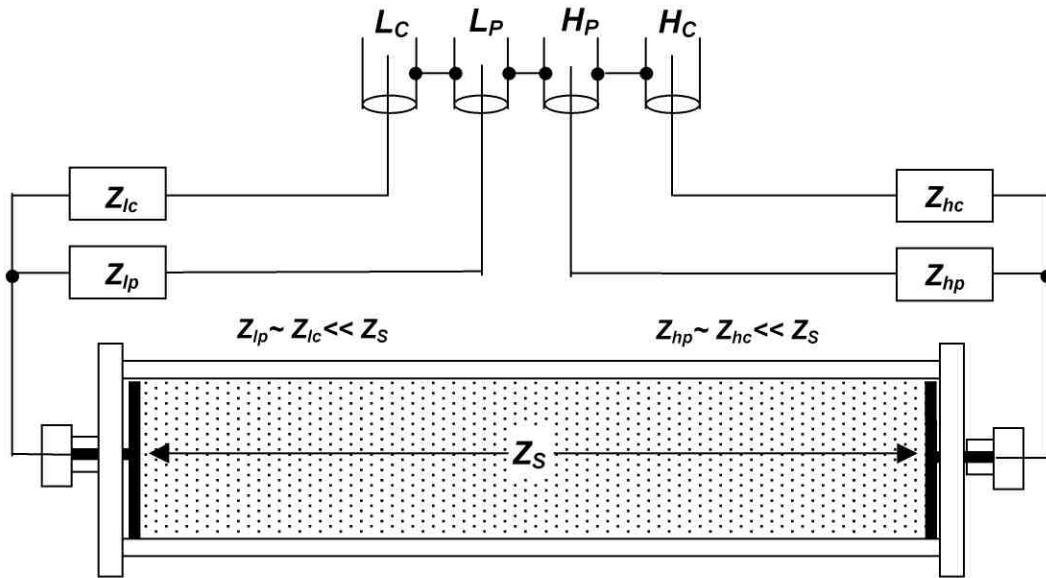


PROJECT: DRDC Soils

DRAWN BY: GMC DATE: 14 December, 2003

FIGURE:

36



Modified after: Agilent Technologies, 2000.

**IMPEDANCE ANALYZER / LCR METER
FOUR ELECTRODE MEASUREMENT**

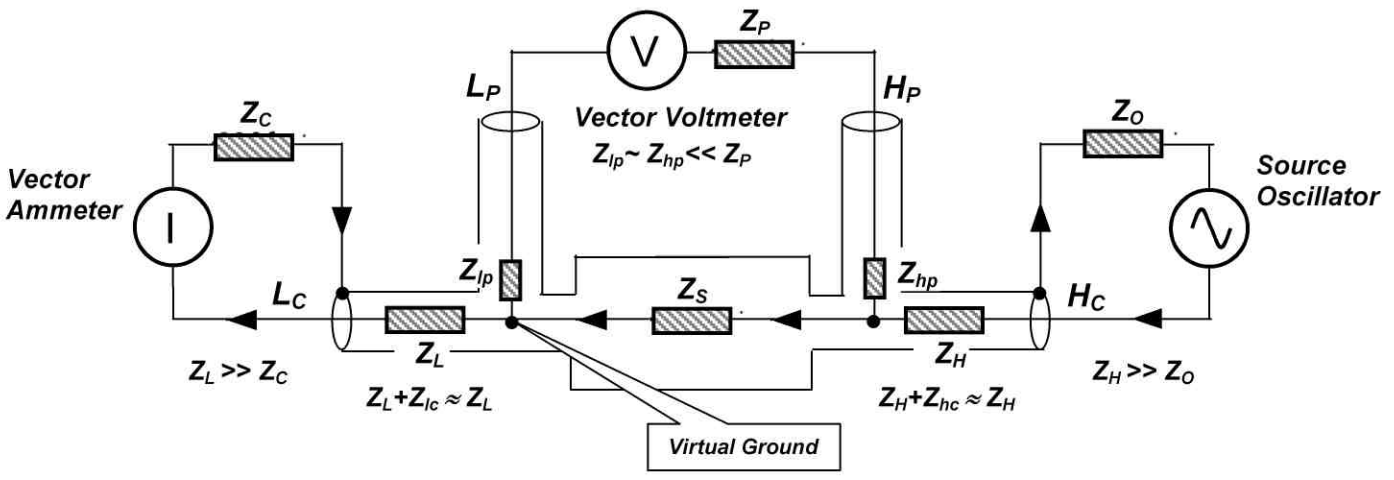
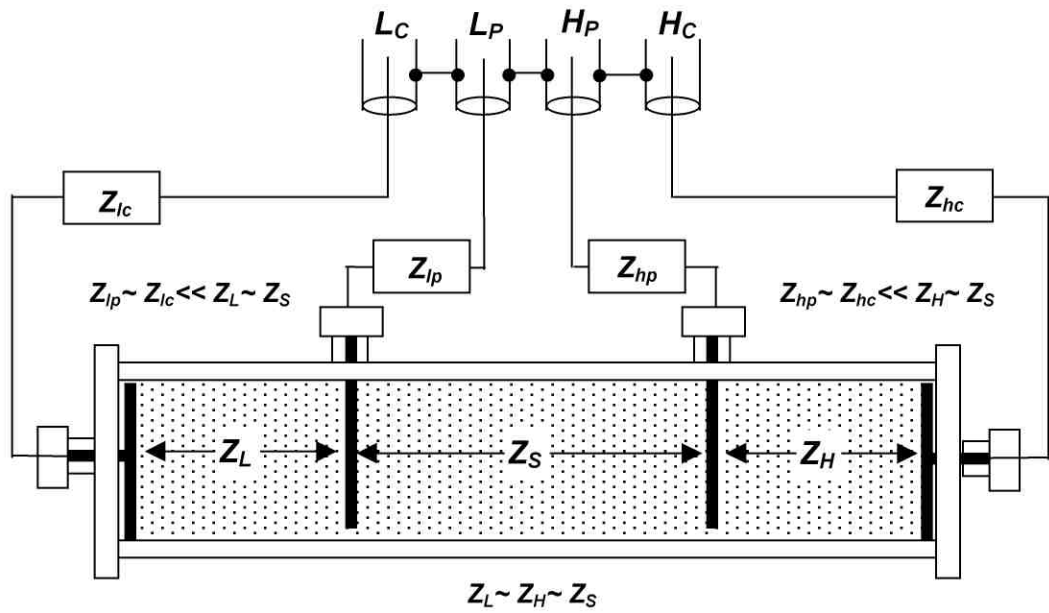


PROJECT: DRDC Soils

DRAWN BY: GMC DATE: 14 December, 2003

FIGURE:

37



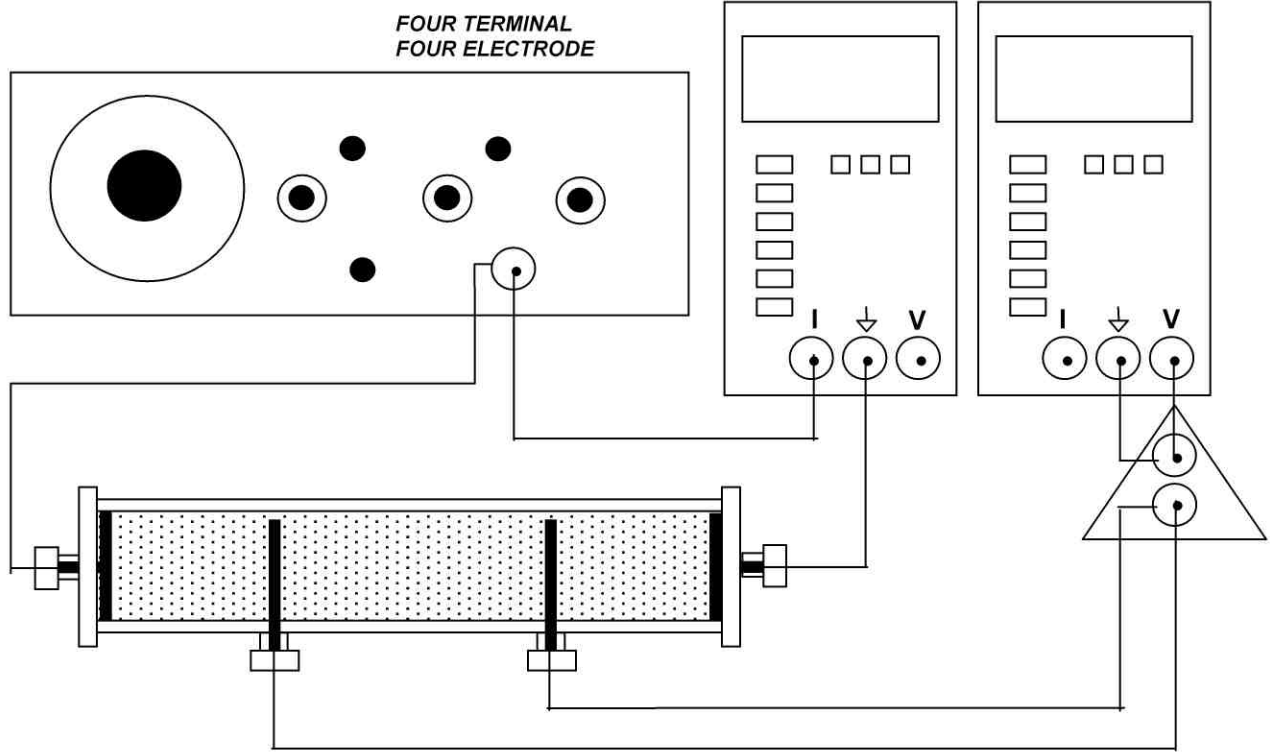
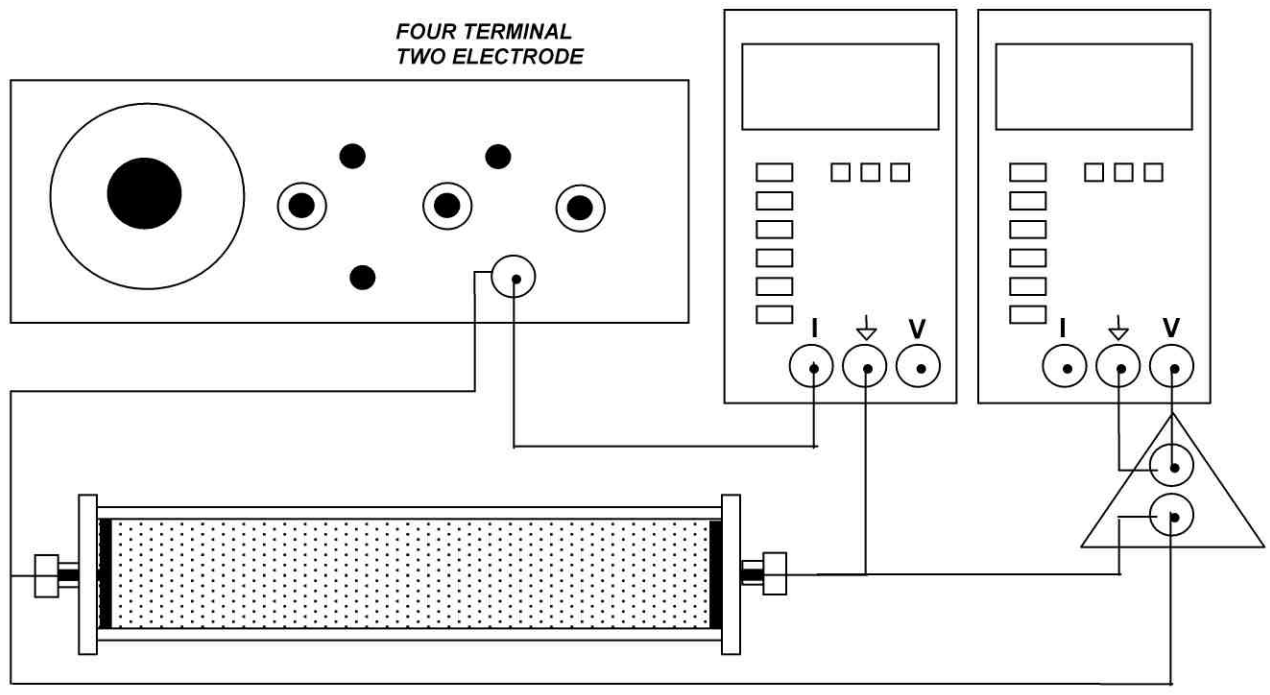
Modified after: Agilent Technologies, 2000.

**IMPEDANCE ANALYZER / LCR METER
FOUR ELECTRODE MEASUREMENT**



PROJECT:	DRDC Soils	
DRAWN BY:	GMC	DATE: 14 December, 2003

FIGURE:
38



**SOIL BOX RESISTIVITY MEASUREMENT CONFIGURATIONS
GENERATOR VOLTAGE CURRENT (GVI) WITH ISOLATION**

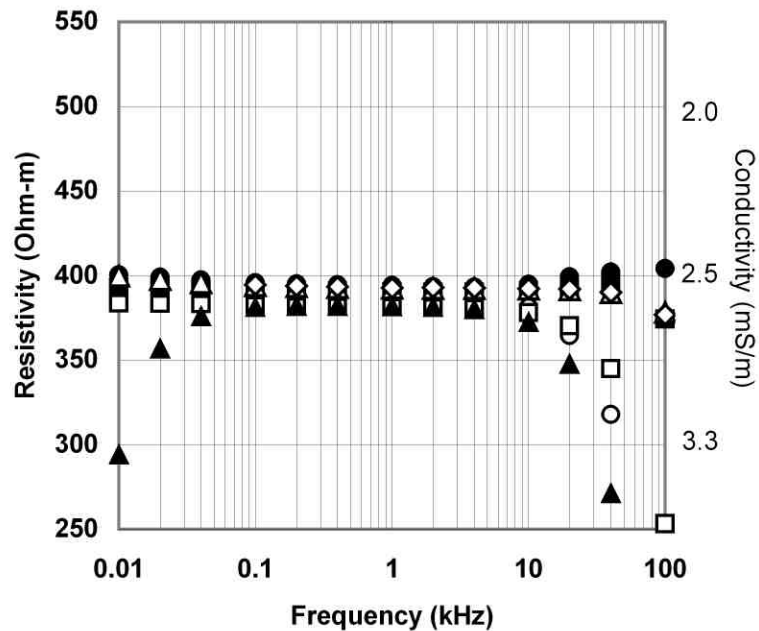


PROJECT:	DRDC Soils	
DRAWN BY:	GMC	DATE:
		14 December, 2003

FIGURE:

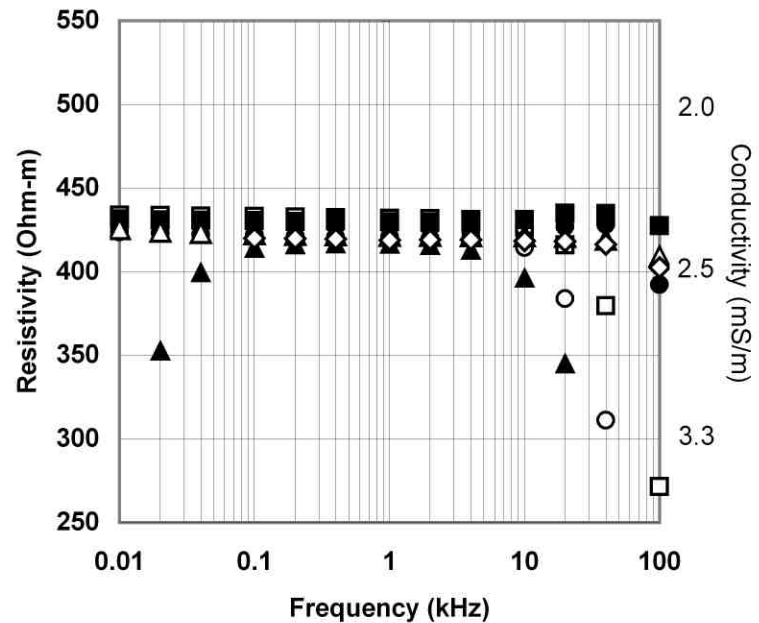
39

- 2-electrode GVI ● 2-electrode GVI - iso
- 4-electrode GVI ■ 4-electrode GVI - iso
- △ 2-electrode HP4192A ▲ 4-electrode HP4192A
- ◇ 2-electrode HP4274A



75 ml Soil Box

- 2-electrode GVI ● 2-electrode GVI - iso
- 4-electrode GVI ■ 4-electrode GVI - iso
- △ 2-electrode HP4192A ▲ 4-electrode HP4192A
- ◇ 2-electrode HP4274A



250 ml Soil Box



**ELECTRICAL RESISTIVITY – VANCOUVER TAP WATER
COMPARISON OF LCR AND GVI METHODS**

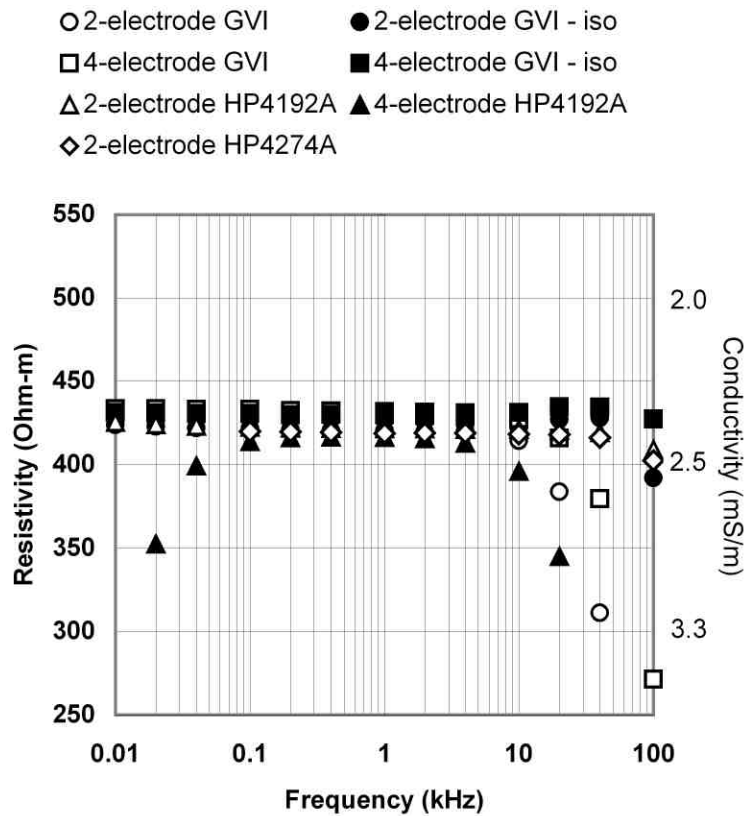
FIGURE:

40

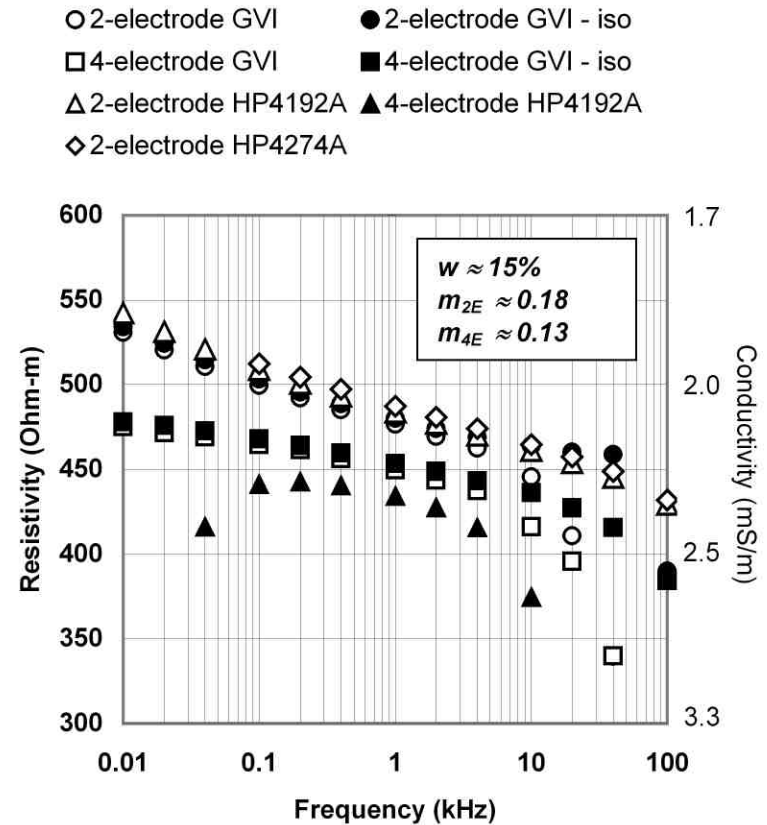
PROJECT: CCMAT Soils

DRAWN BY: GMC

DATE: 15 May, 2007



250 ml Soil Box Vancouver Tap Water



250 ml Soil Box Vancouver Loam Soil

PARAMETERS: w - gravimetric moisture content (referred to "lab-dry" condition).
 m_{2E} - electrical chargeability (2-electrode) HP4192A - 10 Hz, 40 kHz.
 m_{4E} - electrical chargeability (4-electrode) GVI - 10 Hz, 40 kHz.



**ELECTRICAL RESISTIVITY – VANCOUVER LOAM
 COMPARISON OF LCR AND GVI METHODS**

FIGURE:

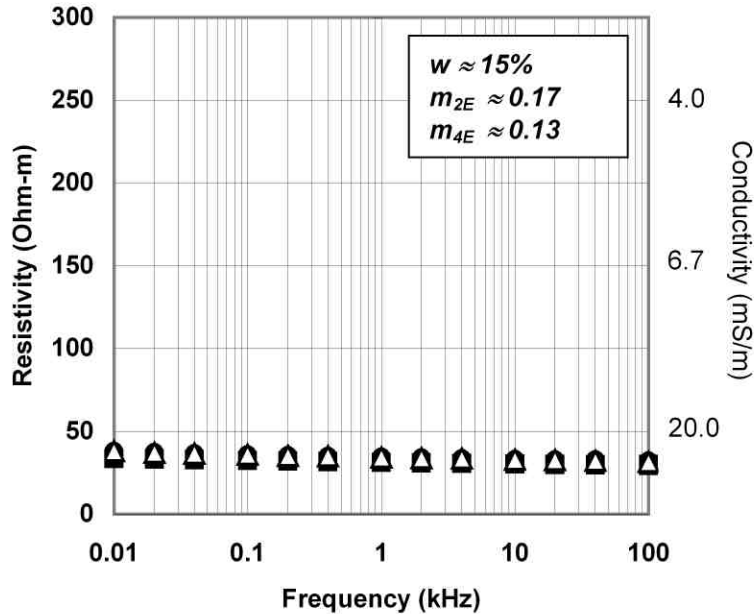
41

PROJECT: CCMAT Soils

DRAWN BY: GMC

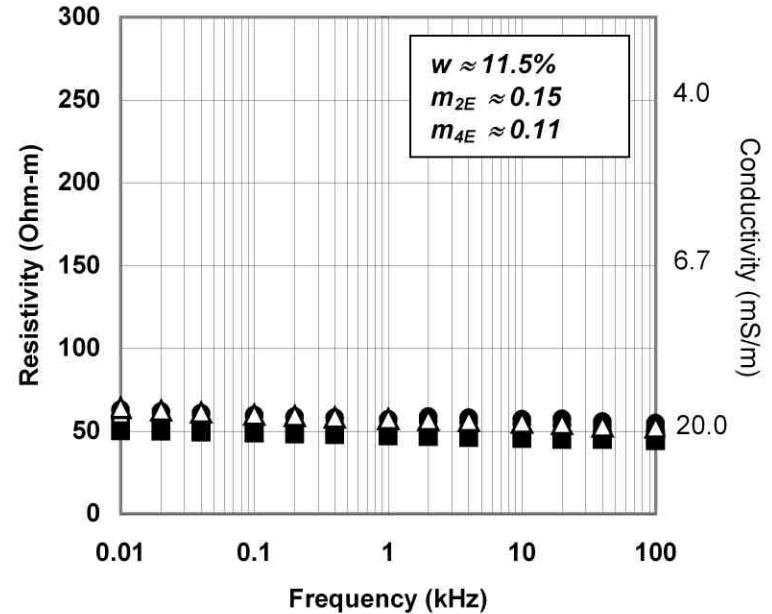
DATE: 15 May, 2007

○ 2-electrode GVI ● 2-electrode GVI - iso
 □ 4-electrode GVI ■ 4-electrode GVI - iso
 △ 2-electrode HP4192A



250 ml Soil Box

○ 2-electrode GVI ● 2-electrode GVI - iso
 □ 4-electrode GVI ■ 4-electrode GVI - iso
 △ 2-electrode HP4192A



250 ml Soil Box

PARAMETERS: w - gravimetric moisture content (referred to "lab-dry" condition).
 m_{2E} - electrical chargeability (2-electrode) HP4192A - 10 Hz, 40 kHz.
 m_{4E} - electrical chargeability (4-electrode) GVI - 10 Hz, 40 kHz.



**ELECTRICAL RESISTIVITY – DRDC AUSTRALIA - A
 COMPARISON OF LCR AND GVI METHODS**

FIGURE:

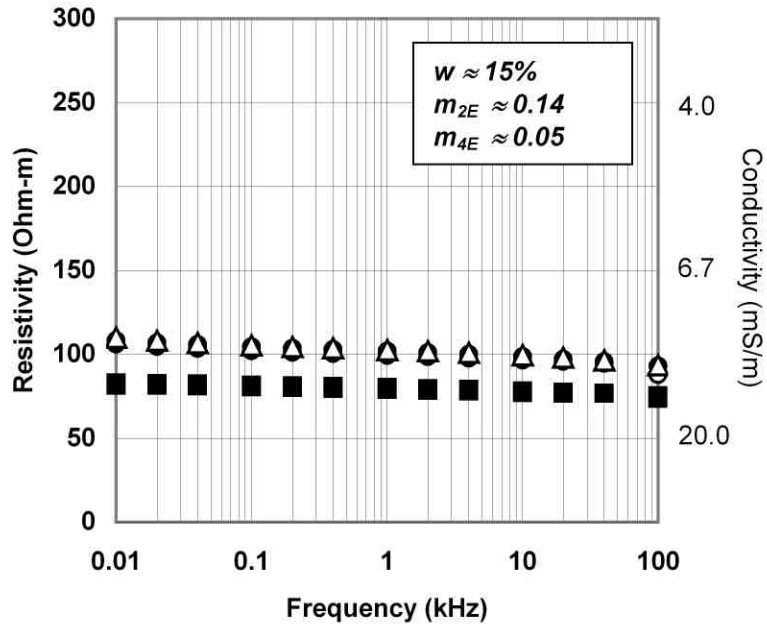
42

PROJECT: CCMAT Soils

DRAWN BY: GMC

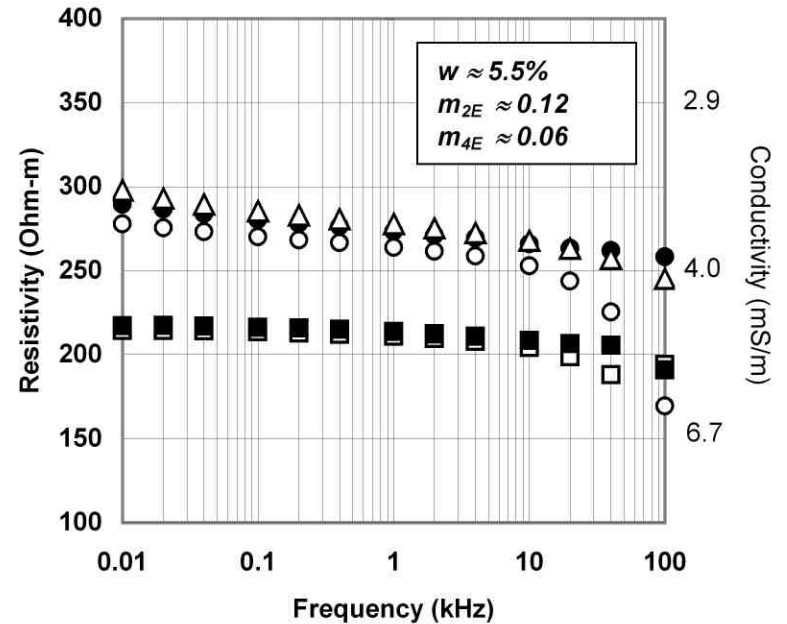
DATE: 15 May, 2007

○ 2-electrode GVI ● 2-electrode GVI - iso
 □ 4-electrode GVI ■ 4-electrode GVI - iso
 △ 2-electrode HP4192A



250 ml Soil Box

○ 2-electrode GVI ● 2-electrode GVI - iso
 □ 4-electrode GVI ■ 4-electrode GVI - iso
 △ 2-electrode HP4192A



250 ml Soil Box

PARAMETERS: *w* - gravimetric moisture content (referred to "lab-dry" condition).
*m*_{2E} - electrical chargeability (2-electrode) HP4192A - 10 Hz, 40 kHz.
*m*_{4E} - electrical chargeability (4-electrode) GVI - 10 Hz, 40 kHz.



**ELECTRICAL RESISTIVITY – DRDC CAMBODIA - 1
 COMPARISON OF LCR AND GVI METHODS**

FIGURE:

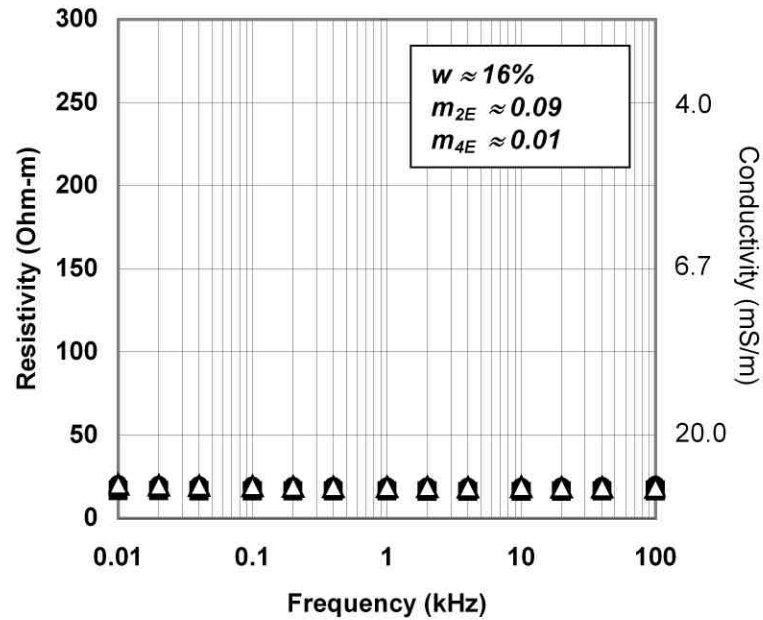
43

PROJECT: CCMAT Soils

DRAWN BY: GMC

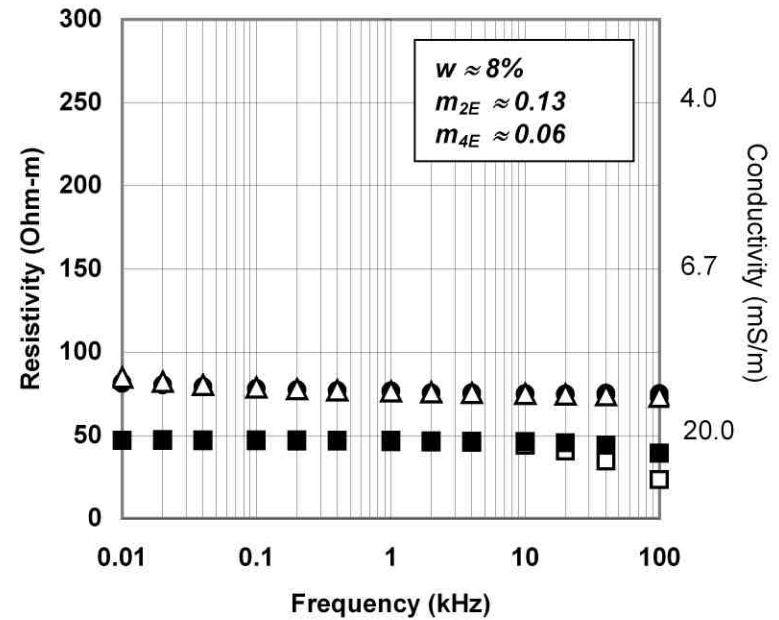
DATE: 15 May, 2007

○ 2-electrode GVI ● 2-electrode GVI - iso
 □ 4-electrode GVI ■ 4-electrode GVI - iso
 △ 2-electrode HP4192A



250 ml Soil Box

○ 2-electrode GVI ● 2-electrode GVI - iso
 □ 4-electrode GVI ■ 4-electrode GVI - iso
 △ 2-electrode HP4192A



250 ml Soil Box

PARAMETERS: w - gravimetric moisture content (referred to "lab-dry" condition).
 m_{2E} - electrical chargeability (2-electrode) HP4192A - 10 Hz, 40 kHz.
 m_{4E} - electrical chargeability (4-electrode) GVI - 10 Hz, 40 kHz.



**ELECTRICAL RESISTIVITY – DRDC (UNMAC) BOSNIA
 COMPARISON OF LCR AND GVI METHODS**

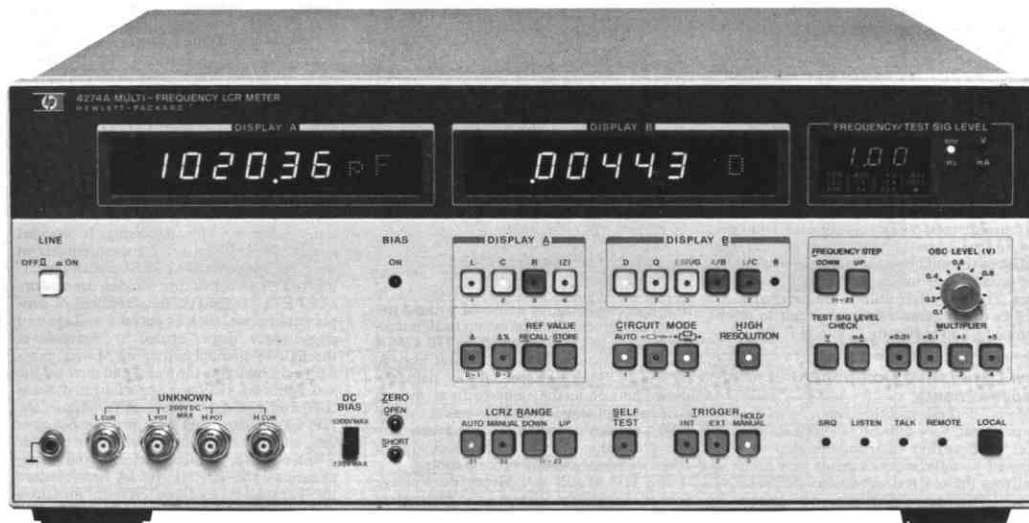
FIGURE:

44

PROJECT: CCMAT Soils

DRAWN BY: GMC

DATE: 15 May, 2007



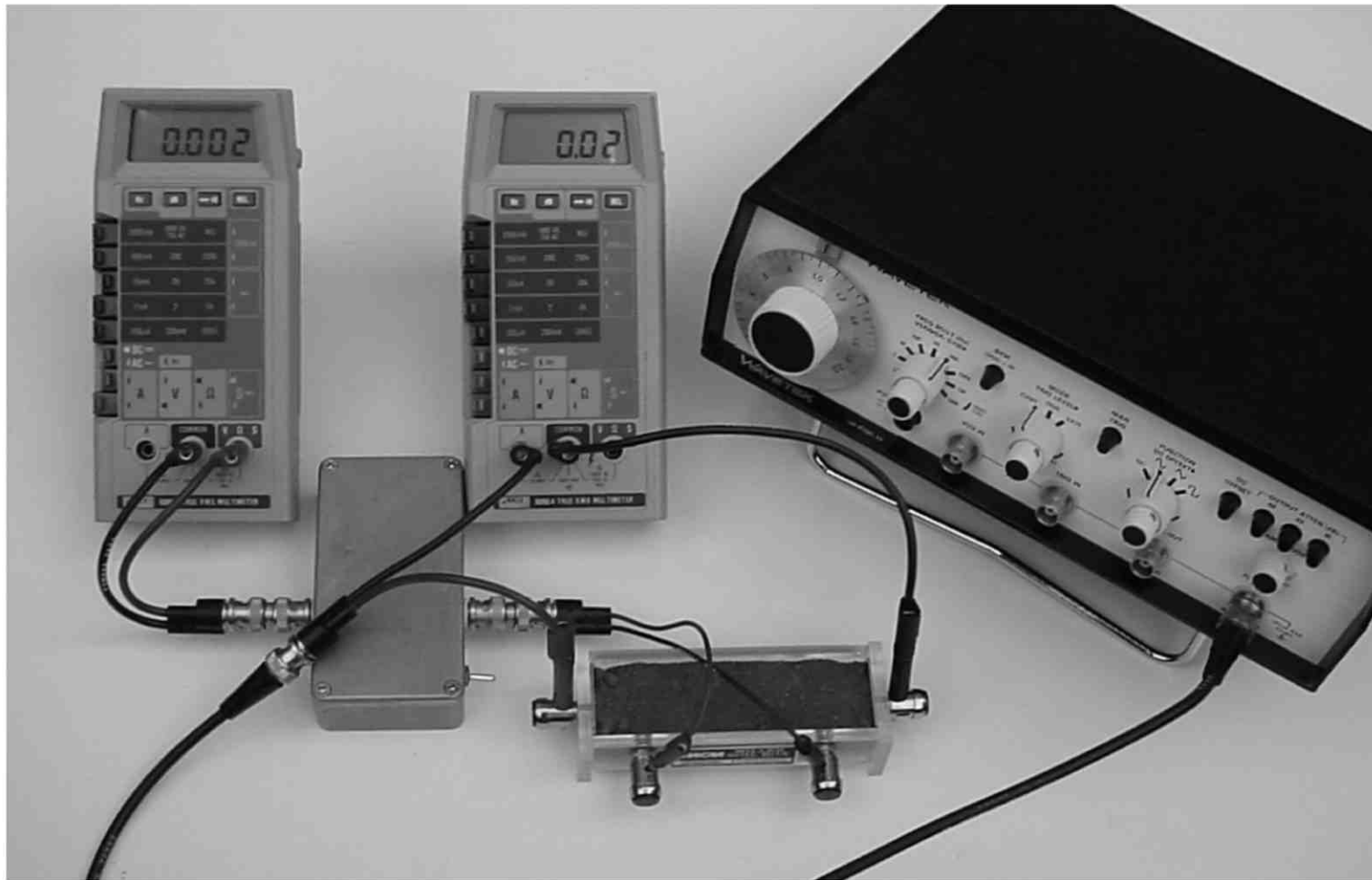
**REPRESENTATIVE PRECISION LCR METERS
HP 4274A – ESI 2150**



PROJECT:	DRDC Soils	
DRAWN BY:	GMC	DATE: 26 March, 2004

FIGURE:

45



**GVI LABORATORY APPARATUS
ELECTRICAL CONDUCTIVITY MEASUREMENT**

FIGURE:

46

PROJECT:

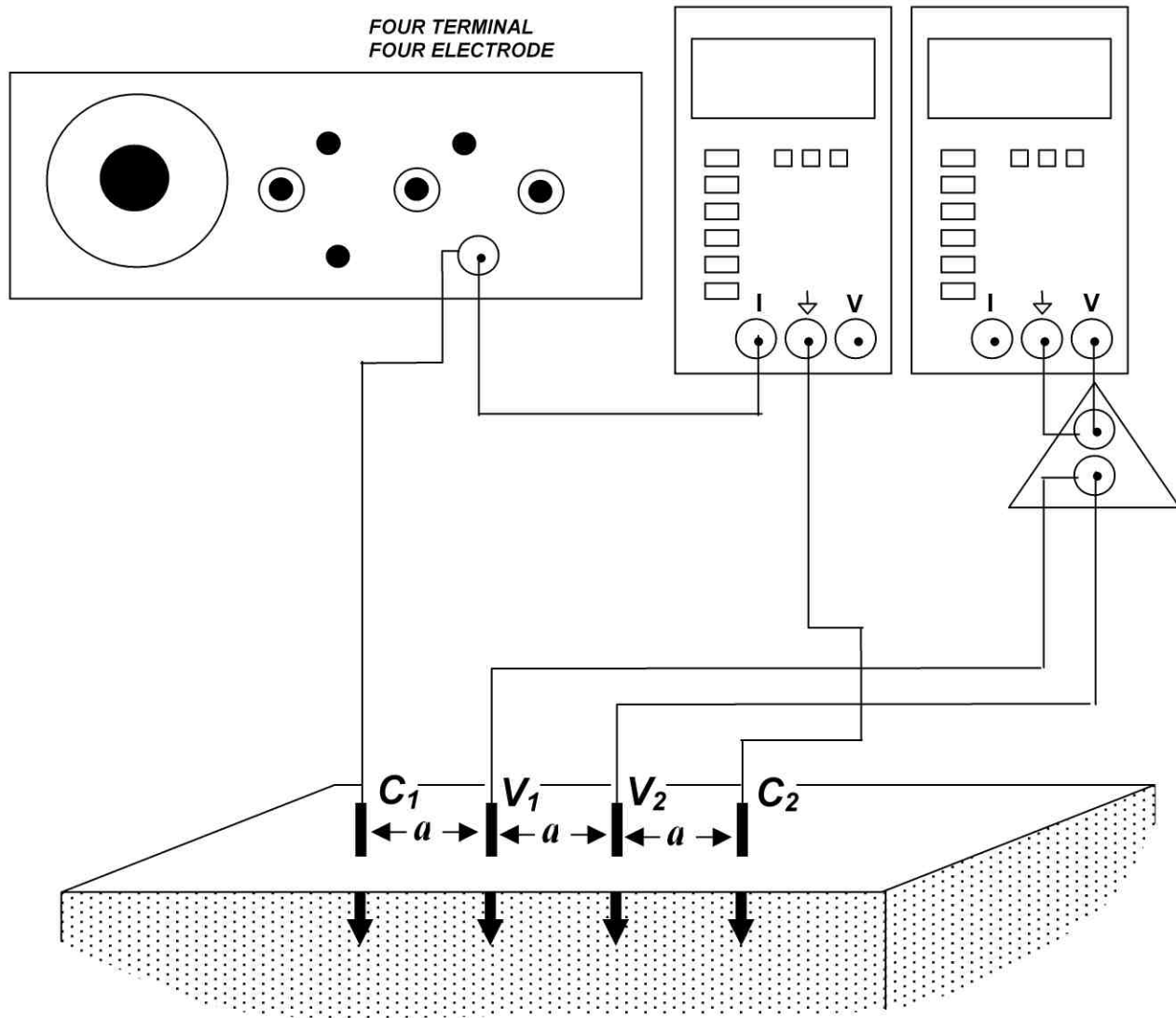
CCMAT Soils

DRAWN BY:

GMC

DATE:

15 February, 2007



**IN SITU ELECTRICAL CONDUCTIVITY MEASUREMENT
GENERATOR VOLTAGE CURRENT (GVI)**



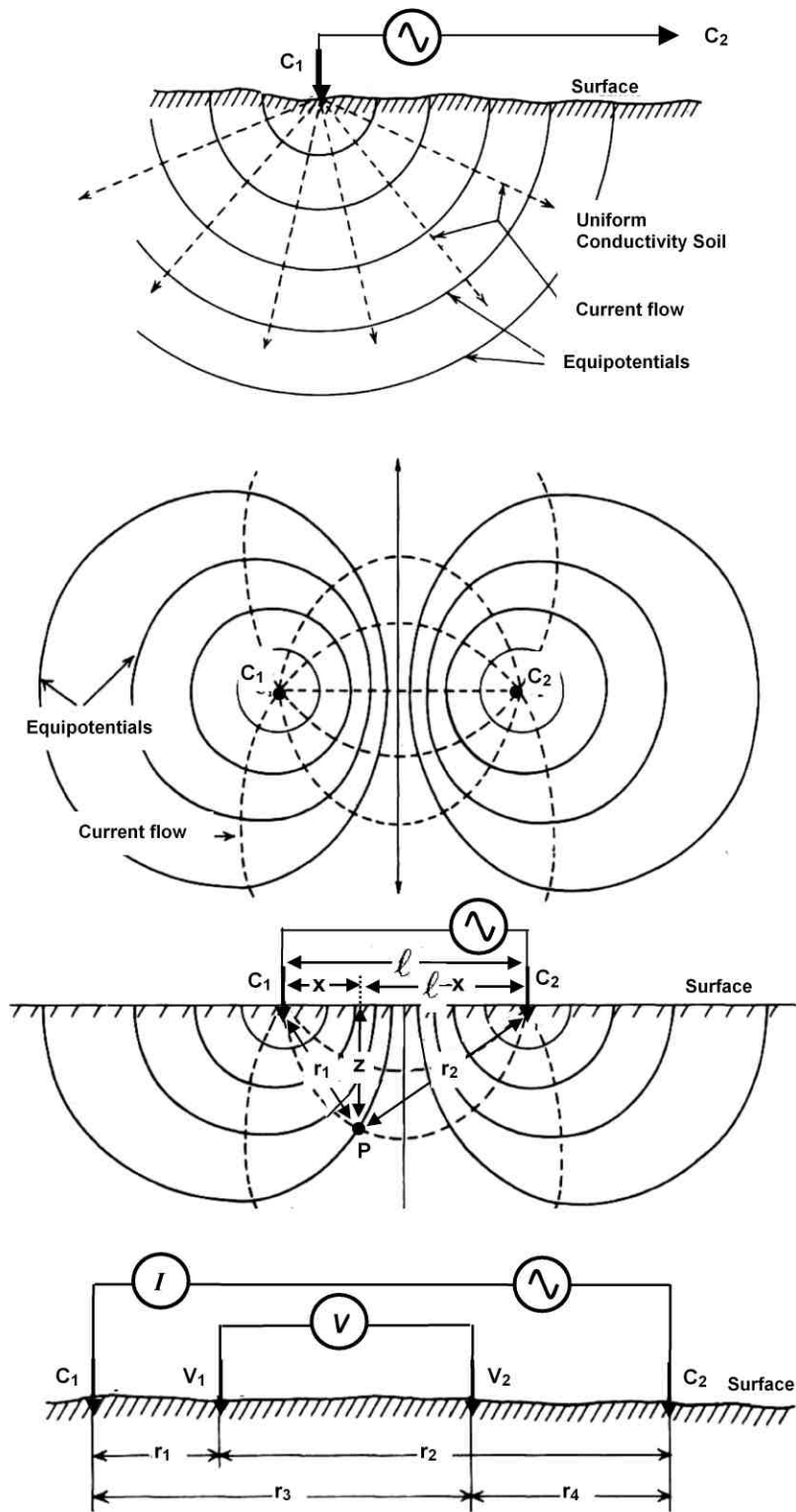
PROJECT:
DRDC Soils

DRAWN BY:
GMC

DATE:
26 March, 2005

FIGURE:

47



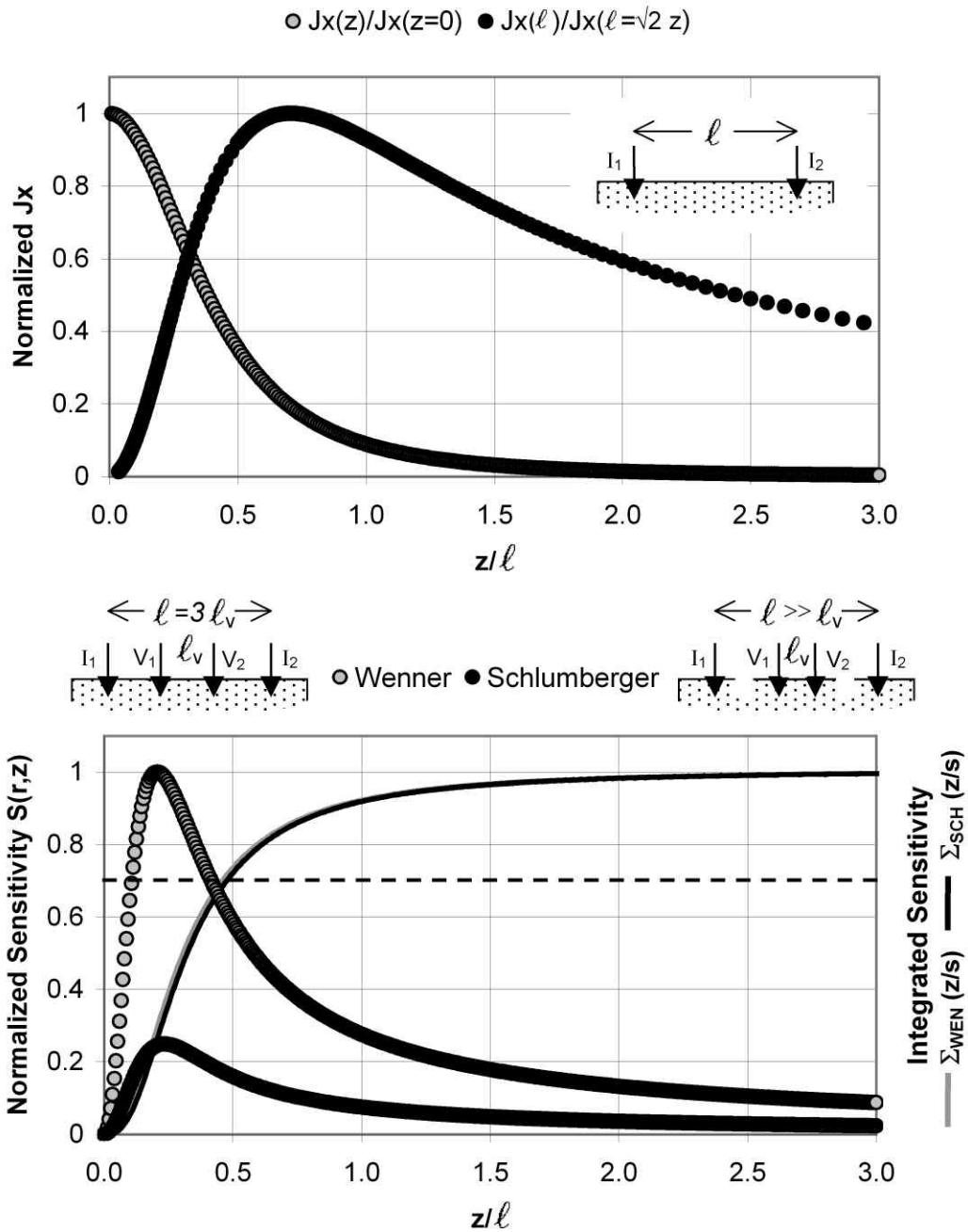
Modified after: Telford, et al., 1990.

**IN SITU ELECTRICAL RESISTIVITY MEASUREMENT
SUBSURFACE POTENTIAL / CURRENT**



PROJECT:	DRDC Soils	
DRAWN BY:	GMC	DATE: 26 March, 2005

FIGURE:
48



**IN SITU ELECTRICAL CONDUCTIVITY MEASUREMENT
1-D QUADRAPOLE SENSITIVITY CHARACTERISTICS**



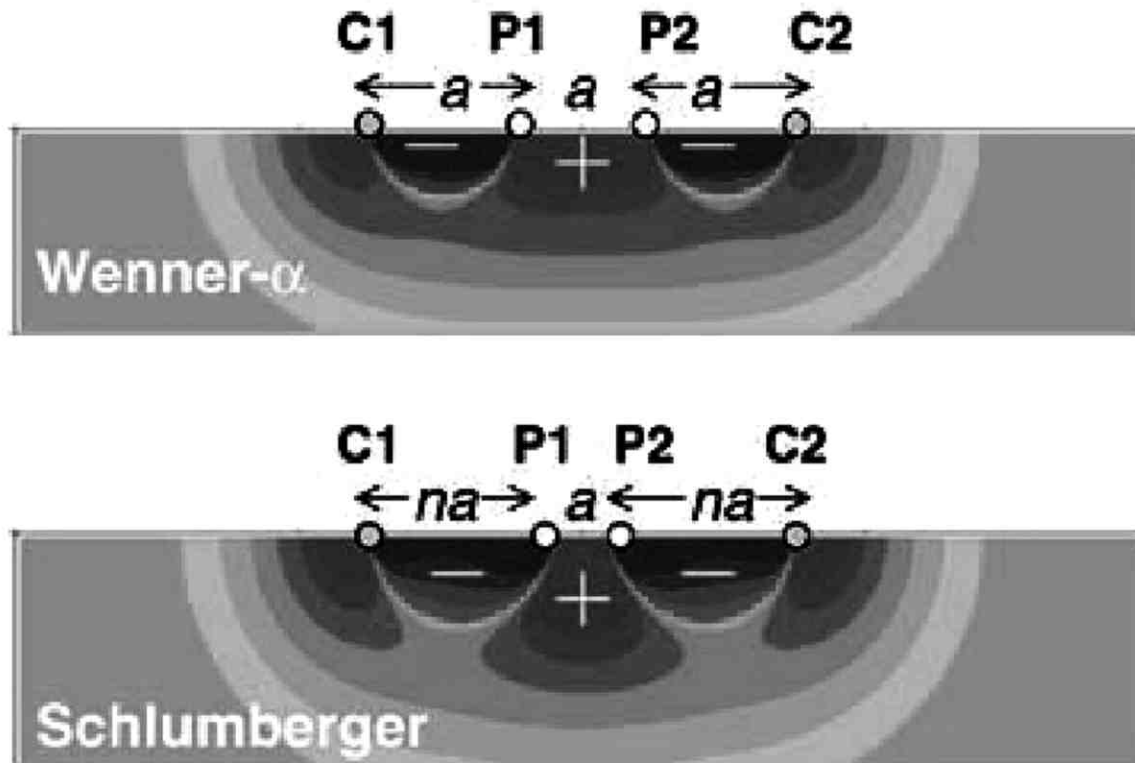
PROJECT:
DRDC Soils

DRAWN BY:
GMC

DATE:
14 February, 2005

FIGURE:

49



SOURCE: Dahlin and Zhou, 2004



**IN SITU ELECTRICAL CONDUCTIVITY MEASUREMENT
2-D QUADRAPOLE SENSITIVITY CHARACTERISTICS**

FIGURE:

50

PROJECT:

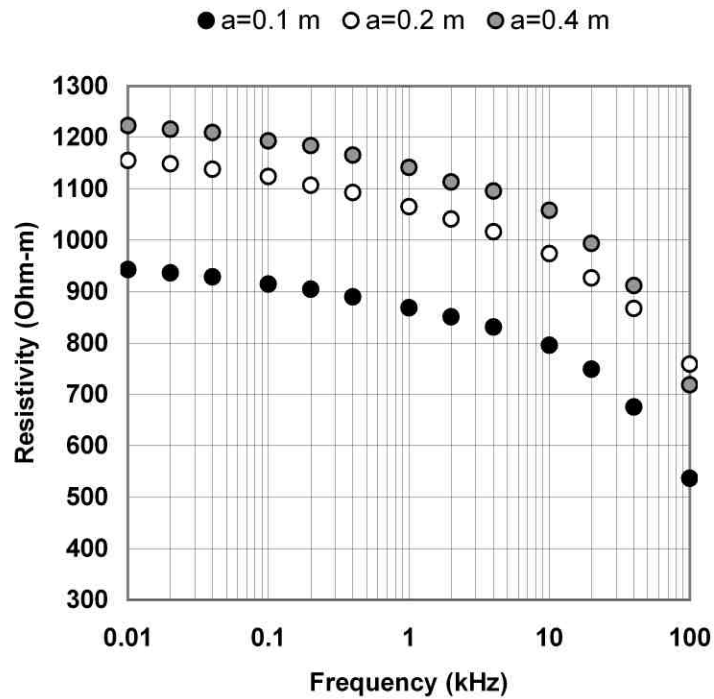
CCMAT Soils

DRAWN BY:

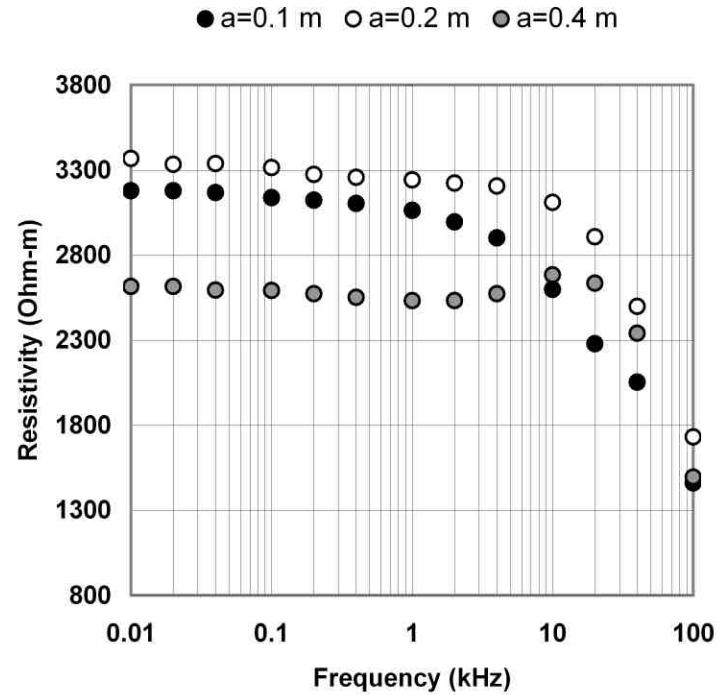
GMC

DATE:

14 February, 2005



Vancouver Loam



Spanish Banks Sand

NOTES: - GVI Apparatus (no isolation amplifier).
 - Wenner Array (a-interval as indicated).



**IN SITU ELECTRICAL RESISTIVITY
 PRELIMINARY – LAOM AND SAND SOILS**

FIGURE:

51

PROJECT: CCMAT Soils

DRAWN BY: GMC

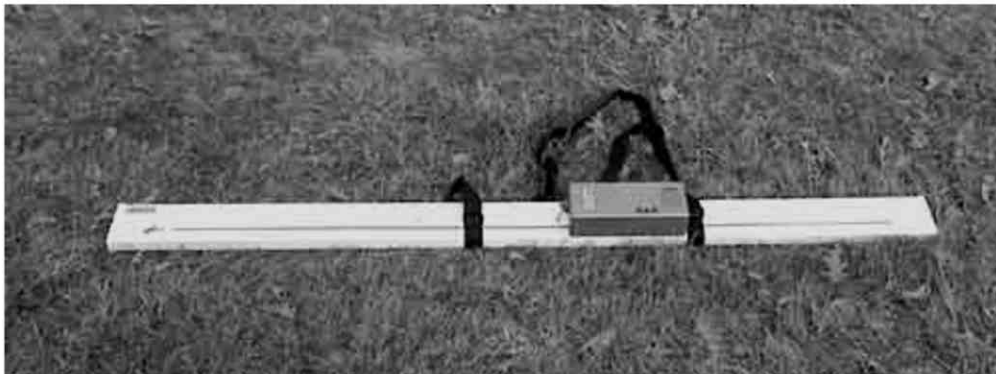
DATE: 18 October, 2006



Geonics EM-38 ($f=14.6$ kHz, $s=1.0$ m)



GSSI EMP-400 ($f=1$ kHz – 16 kHz, $s=1.219$ m)



Geophex GEM-2 ($f=300$ Hz – 48 kHz, $s=1.67$ m)

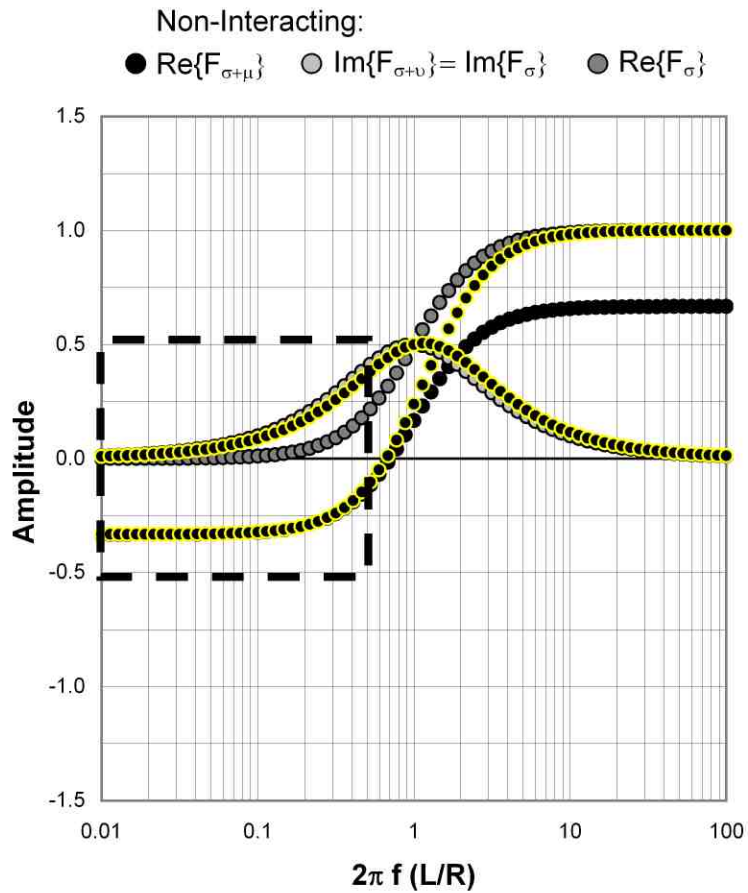
FDEM CONDUCTIVITY/SUSCEPTIBILITY METERS



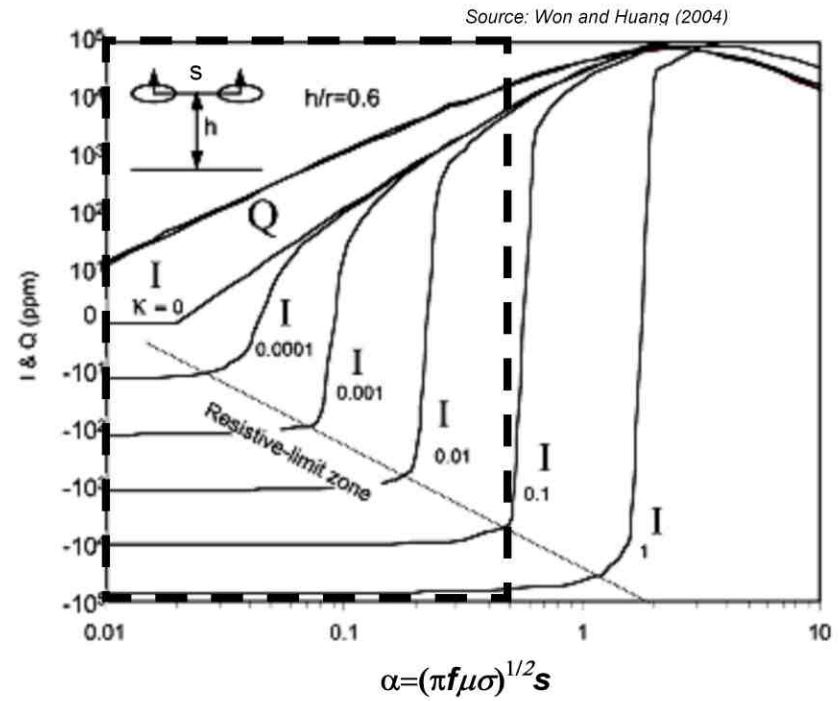
PROJECT:	<i>DRDC Soils</i>	
DRAWN BY:	<i>GMC</i>	DATE: <i>14 December, 2007</i>

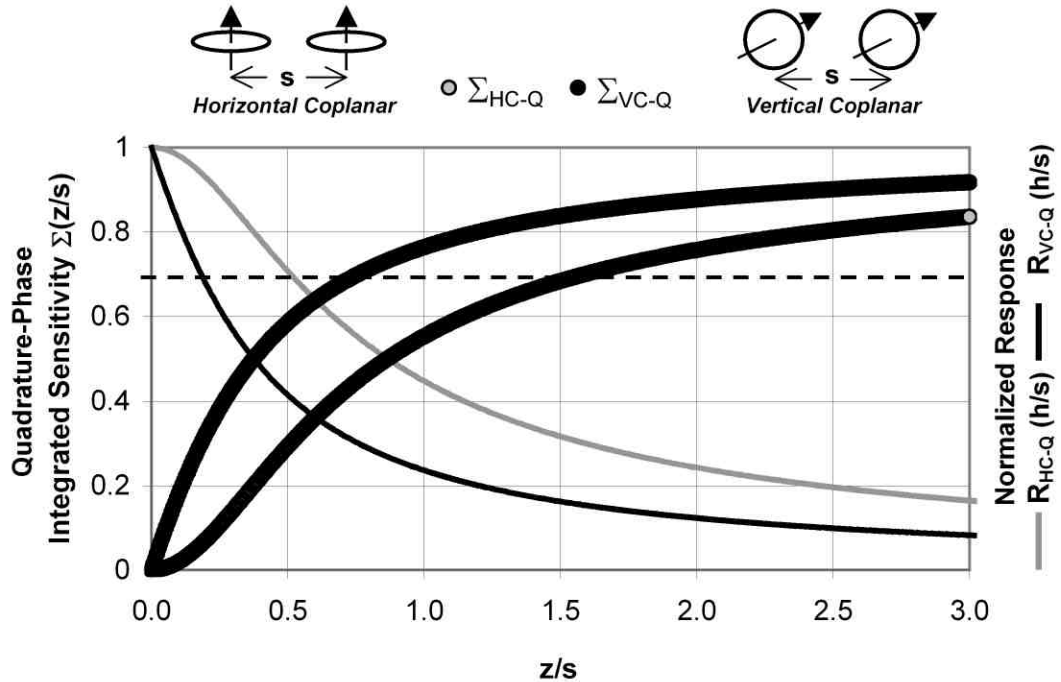
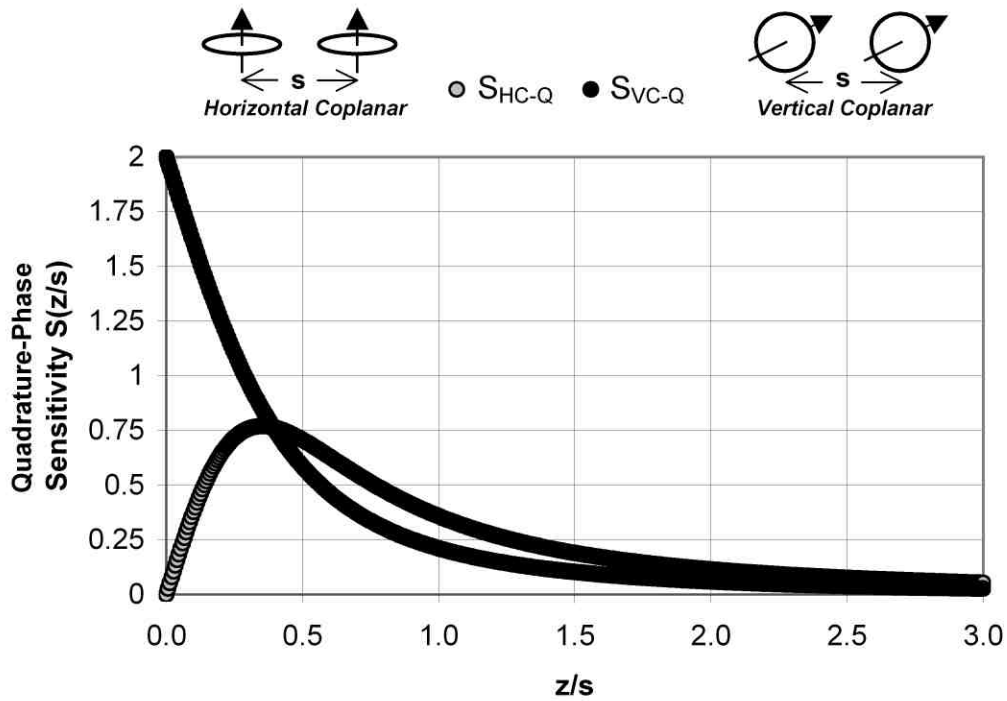
FIGURE:

52



Interacting: ●●●●●●●●





**IN SITU ELECTRICAL CONDUCTIVITY MEASUREMENT
FDEM COPLANAR DEPTH SENSITIVITY CHARACTERISTICS**



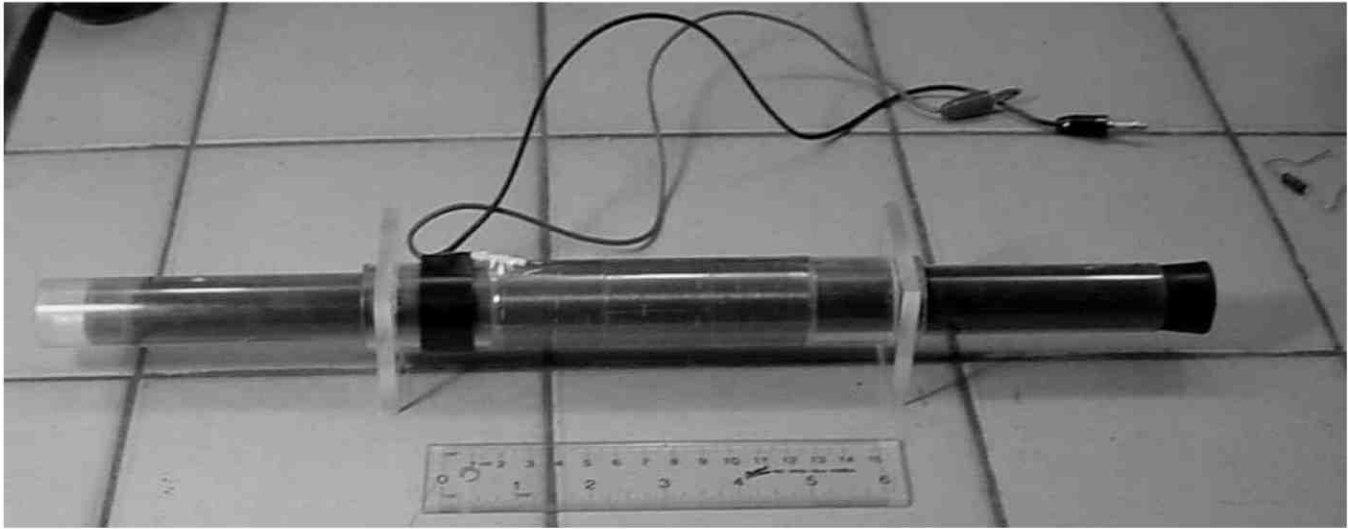
PROJECT: DRDC Soils

DRAWN BY: GMC

DATE: 14 February, 2005

FIGURE:

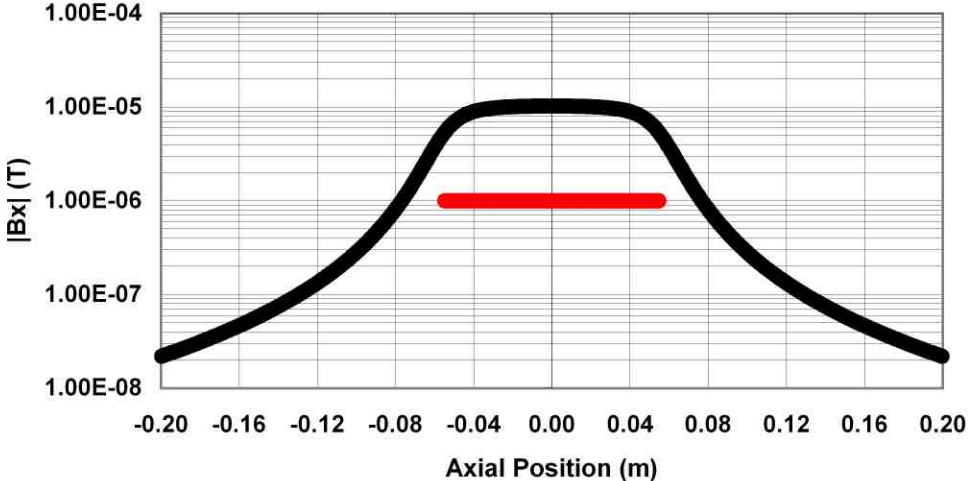
54



PROTOTYPE SOLENOID FIXTURE

Coil Parameters:
 $N=110$
 $R=0.016\text{ m}$
 $l=0.11\text{ m}$

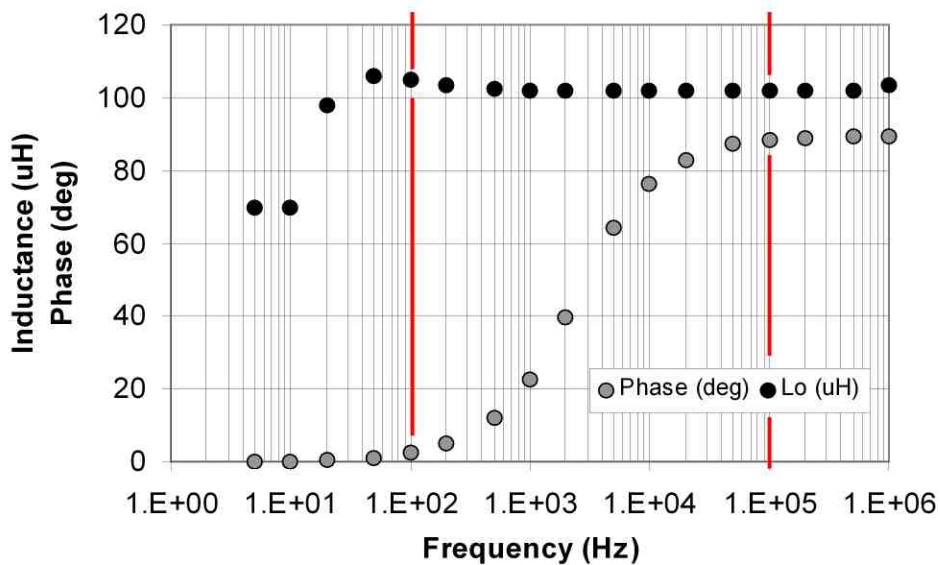
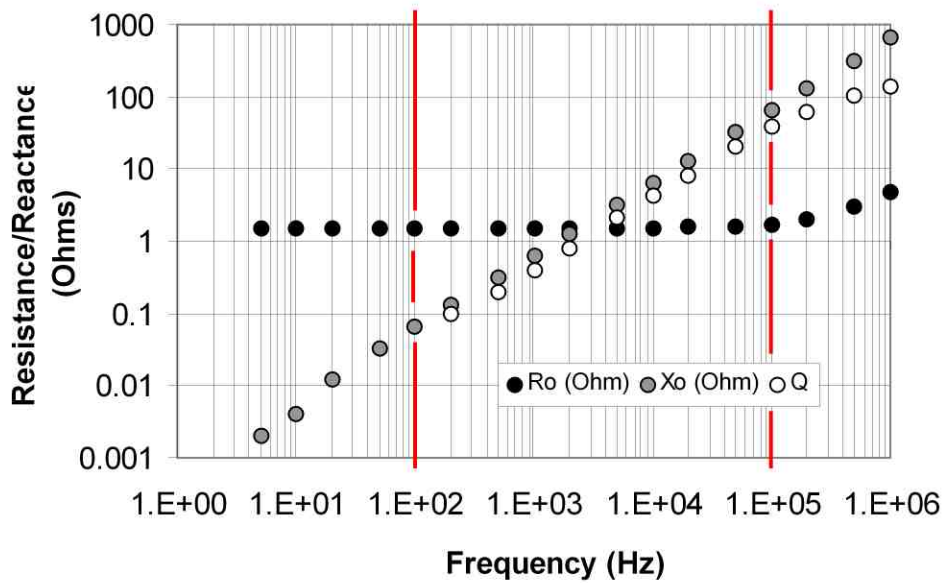
Model Parameters:
 $I_s=8.5\text{ mA}$
 $\mu_r=1.0$



**PROTOTYPE SUSCEPTIBILITY FIXTURE
 AXIAL MAGNETIC FLUX DENSITY**

FIGURE:
 55

PROJECT: CCMAT Soils	DRAWN BY: GMC	DATE: 26 March, 2004
-------------------------	------------------	-------------------------



**PROTOTYPE SOLENOID SUSCEPTIBILITY FIXTURE
COMPLEX IMPEDANCE CHARACTERISTICS**



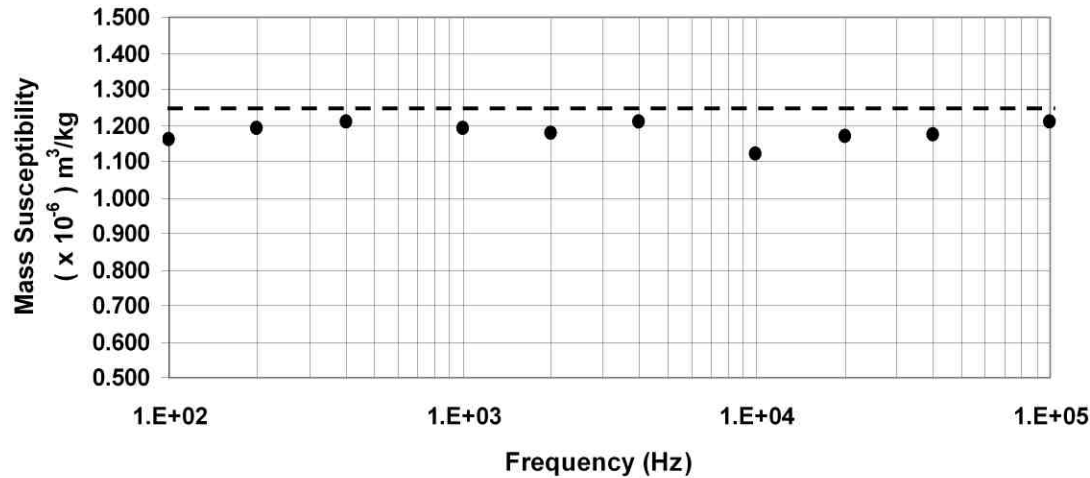
PROJECT:
DRDC Soils

DRAWN BY: *GMC* DATE: *26 March, 2004*

FIGURE:

56

Prototype Single Coil Fixture
 HP4274A Direct Inductance Susceptibility Analysis
 MnCO₃ Standard



NOTES:

1. Dashed line indicates reference value as tabulated CRC Handbook of Chemistry and Physics, 51st Edition (1971).
2. Bartington MS2 and Kappabridge data reported by K. Fukuma, Department of Environmental Sciences, Kumamoto University, Japan.
3. Mean value measured via HP4274A yields fixture calibration constant $K_d=1.053$

CRC Reference

Mass Specific Susceptibility
 $1.2463 \times 10^{-6} \text{ m}^3/\text{kg}$

Fukuma - Bartington MS2

Mass Specific Susceptibility
 $1.1418 \times 10^{-6} \text{ m}^3/\text{kg}$

Fukuma - Kappabridge

Mass Specific Susceptibility
 $1.2472 \times 10^{-6} \text{ m}^3/\text{kg}$

Terrascan - HP4274A

Mass Specific Susceptibility
 Mean (100 Hz – 100 kHz)
 $1.1834 \times 10^{-6} \text{ m}^3/\text{kg}$



**DIRECT-INDUCTANCE SUSCEPTIBILITY MEASUREMENT
 MnCO₃ CALIBRATION STANDARD**

FIGURE:

57

PROJECT:

DRDC Soils

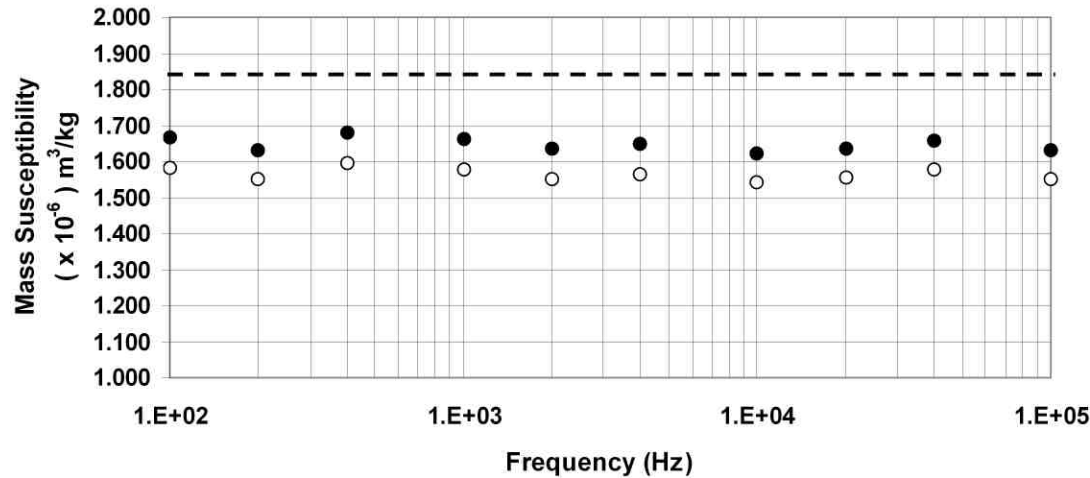
DRAWN BY:

GMC

DATE:

18 September, 2004

Prototype Single Coil Fixture
 HP4274A Direct Inductance Susceptibility Analysis
 Gd₂O₃ Standard



NOTES:

1. Dashed line indicates reference value as tabulated CRC Handbook of Chemistry and Physics, 51st Edition (1971).
2. Bartington MS2 and Kappabridge data reported by L. Sagnotti et al., 2003, Physics of the Earth and Planetary Interiors, 138, 25-38.
3. Mean value measured via HP4274A (○) adjusted (●) via fixture calibration constant $K_d=1.053$ determined for MnCO₃ standard.

CRC Reference

Mass Specific Susceptibility
 $1.8442 \times 10^{-6} \text{ m}^3/\text{kg}$

DRDCS - Bartington MS2

Mass Specific Susceptibility
 $1.5787 \times 10^{-6} \text{ m}^3/\text{kg}$

Sagnotti, et al. - Bartington

Mass Specific Susceptibility
 Mean (Table 2)
 $1.6651 \times 10^{-6} \text{ m}^3/\text{kg}$

Sagnotti et al. - Kappabridge

Mass Specific Susceptibility
 Mean (Table 2)
 $1.7437 \times 10^{-6} \text{ m}^3/\text{kg}$

Terrascan - HP4274A

Mass Specific Susceptibility
 Mean (100 Hz – 100 kHz)
 ○ $1.5648 \times 10^{-6} \text{ m}^3/\text{kg}$
 ● $1.6477 \times 10^{-6} \text{ m}^3/\text{kg}$



**DIRECT-INDUCTANCE SUSCEPTIBILITY MEASUREMENT
 Gd₂O₃ CALIBRATION STANDARD**

FIGURE:

58

PROJECT:

DRDC Soils

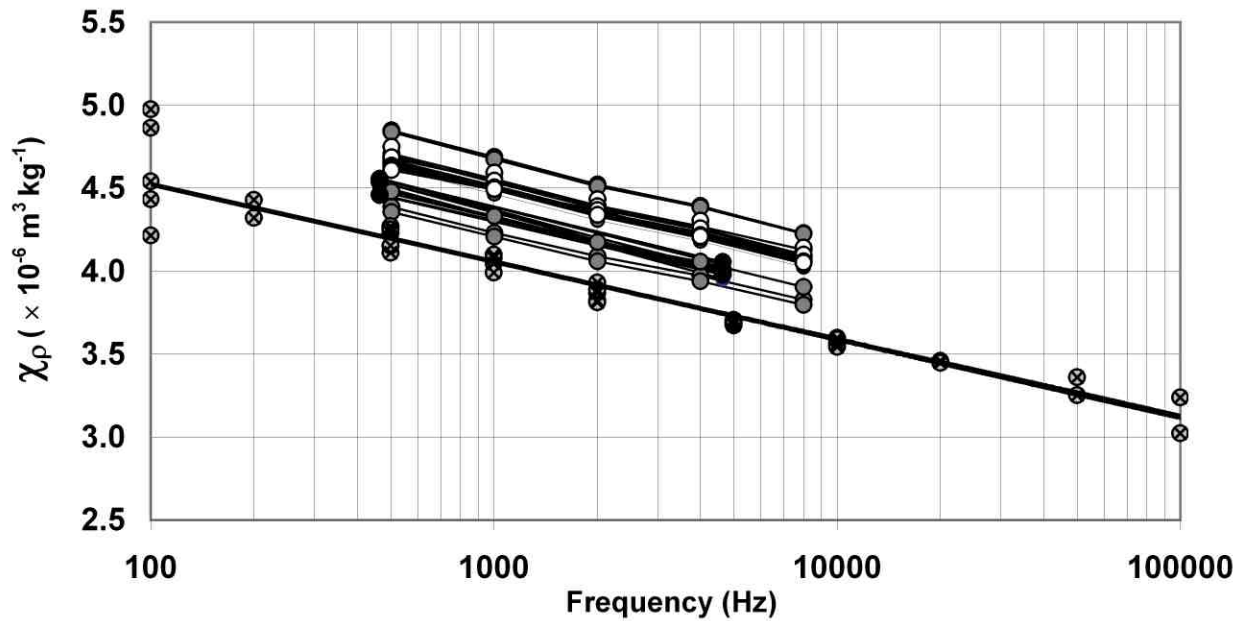
DRAWN BY:

GMC

DATE:

18 February, 2005

- ZHI SM-100 (35 mm) | $\rho \approx 0.99 \text{ g/cm}^3$ | $\Delta\chi = 479 \times 10^{-6}$ | $\chi_{FD} = 10.5 \%$
- ZHI SM-100 (10 cc) | $\rho \approx 1.02 \text{ g/cm}^3$ | $\Delta\chi = 491 \times 10^{-6}$ | $\chi_{FD} = 10.3 \%$
- Bartington MS2B (10 cc) | $\rho \approx 1.02 \text{ g/cm}^3$ | $\Delta\chi = 534 \times 10^{-6}$ | $\chi_{FD} = 11.5 \%$
- ⊗— ESI 2150 LCR | $\rho \approx 0.91 \text{ g/cm}^3$ | $\Delta\chi = 427 \times 10^{-6}$ | $\chi_{FD} = 11.1 \%$
Solenoid fixture



**DRDC BOSNIA REFERENCE SOIL
MASS-SPECIFIC MAGNETIC SUSCEPTIBILITY**

FIGURE:

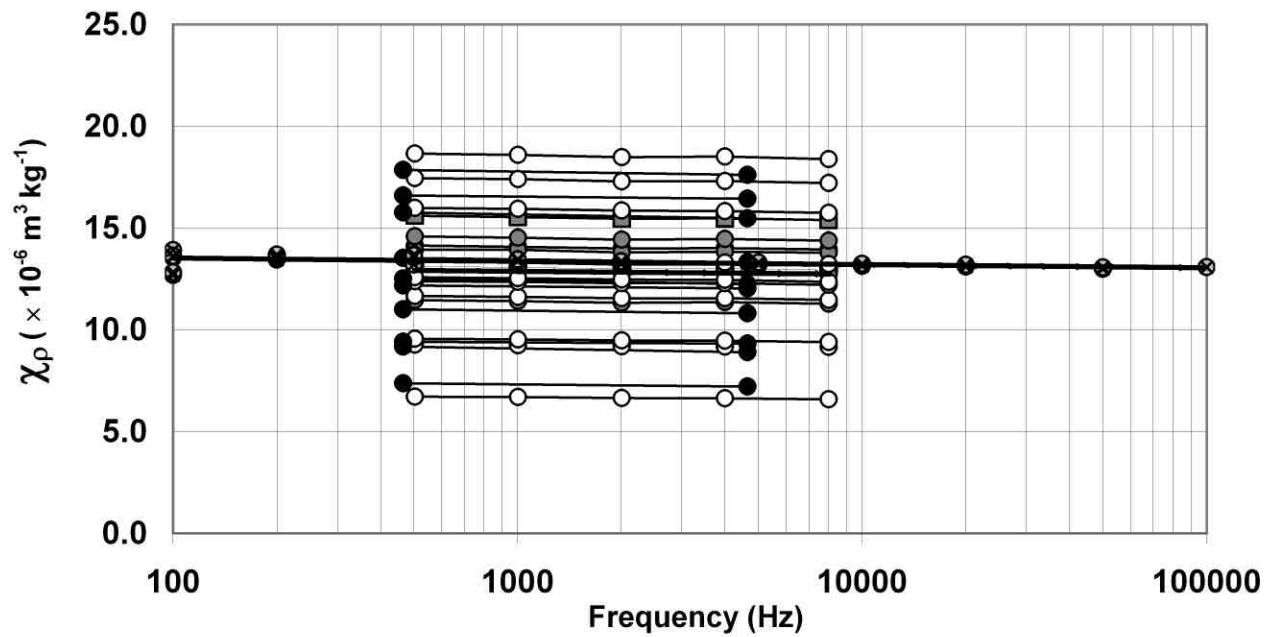
59

PROJECT: CCMAT Soils

DRAWN BY: GMC

DATE: 15 February, 2007

- ZHI SM-100 (35 mm) | $\rho \approx 1.46 \text{ g/cm}^3$ | $\Delta\chi = 210 \times 10^{-6}$ | $\chi_{FD} = 1.1 \%$
- ZHI SM-100 (10 cc) | $\rho \approx 1.53 \text{ g/cm}^3$ | $\Delta\chi = 232 \times 10^{-6}$ | $\chi_{FD} = 1.3 \%$
- Bartington MS2B (10 cc) | $\rho \approx 1.53 \text{ g/cm}^3$ | $\Delta\chi = 319 \times 10^{-6}$ | $\chi_{FD} = 1.8 \%$
- ⊗— ESI 2150 LCR | $\rho \approx 1.70 \text{ g/cm}^3$ | $\Delta\chi = 275 \times 10^{-6}$ | $\chi_{FD} = 1.2 \%$
Solenoid fixture



**DRDC AUSTRALIA - A REFERENCE SOIL
MASS-SPECIFIC MAGNETIC SUSCEPTIBILITY**

FIGURE:

60

PROJECT:

CCMAT Soils

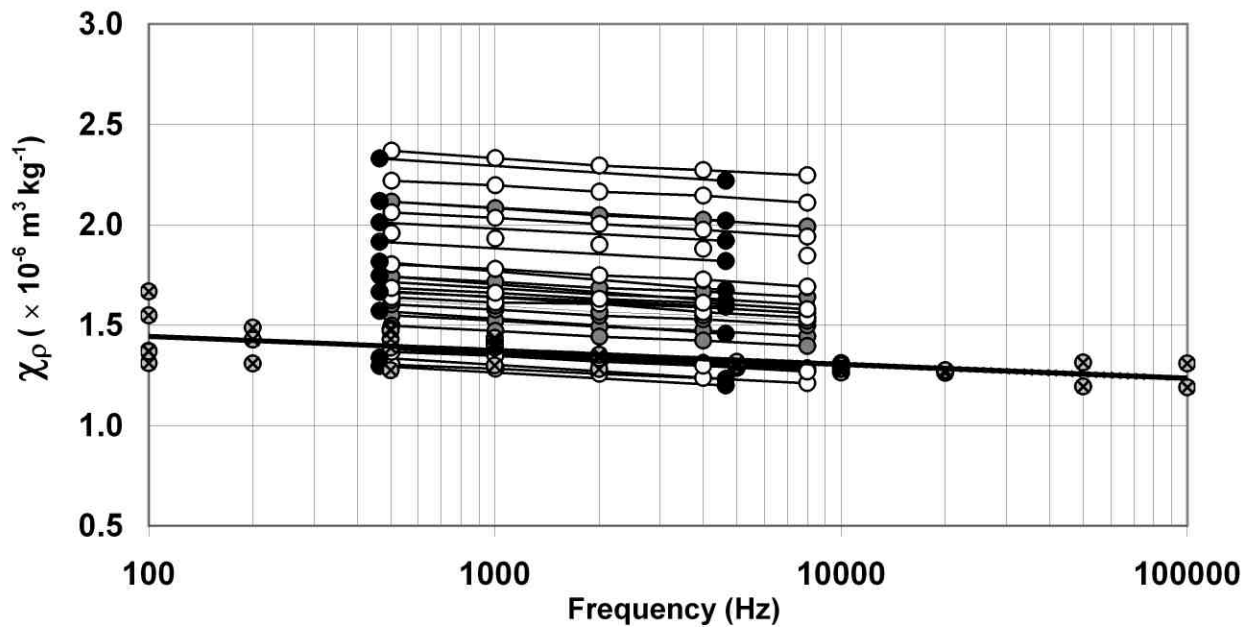
DRAWN BY:

GMC

DATE:

15 February, 2007

- ZHI SM-100 (35 mm) | $\rho \approx 1.67 \text{ g/cm}^3$ | $\Delta\chi = 145 \times 10^{-6}$ | $\chi_{FD} = 5.4 \%$
- ZHI SM-100 (10 cc) | $\rho \approx 1.80 \text{ g/cm}^3$ | $\Delta\chi = 161 \times 10^{-6}$ | $\chi_{FD} = 5.0 \%$
- Bartington MS2B (10 cc) | $\rho \approx 1.80 \text{ g/cm}^3$ | $\Delta\chi = 189 \times 10^{-6}$ | $\chi_{FD} = 6.1 \%$
- ⊗— ESI 2150 LCR | $\rho \approx 1.66 \text{ g/cm}^3$ | $\Delta\chi = 116 \times 10^{-6}$ | $\chi_{FD} = 5.0 \%$
Solenoid fixture



**DRDC CAMBODIA-2 REFERENCE SOIL
MASS-SPECIFIC MAGNETIC SUSCEPTIBILITY**

FIGURE:

61

PROJECT: CCMAT Soils

DRAWN BY: GMC

DATE: 15 February, 2007

Table 1 — Indicative values of magnetic susceptibility that can be expected for soil effects for single frequency continuous wave metal detectors. SOURCE: CWA 14747-1, A3

Soil effect class (Defined in Error! Reference source not found.)	Indicative values of magnetic susceptibility 10^{-5} SI
Neutral	Below 50
Moderate	50 to 500
Severe	500 to 2 000
Very severe	Above 2 000

NOTE These values are indicative only because the effect of a soil on a metal detector depends on the metal detector, and the measured values of susceptibility depend on the measuring instrument.

Table2 — Indicative values of frequency variation magnetic susceptibility that can be expected for soil effects for pulsed induction and most continuous wave metal detectors. SOURCE: Billings, et al. (2003)

Soil effect class (Defined in Error! Reference source not found.)	Indicative values of frequency variation of magnetic susceptibility (458 Hz and 4 580 Hz) 10^{-5} SI
Neutral	Below 5
Moderate	5 to 15
Severe	15 to 25
Very severe	Above 25

NOTE These values are indicative only because the effect of a soil on a metal detector depends on the metal detector, and the measured values of susceptibility depend on the measuring instrument.

Table A.1 — Definition of classes for soil effects on metal detectors

Neutral	A soil has a neutral effect on a metal detector response if it has a no influence on the performance of the metal detector even without ground compensation. For the detector, such a soil is equivalent to air.
Moderate	A soil has a moderate effect on a metal detector response if its influence on the detector performance is noticeable but the metal detector can be used without ground compensation.
Severe	A soil has a severe effect on a metal detector response if it makes the use of ground compensation necessary.
Very severe	A soil has a very severe effect on a metal detector response if the metal detector cannot be used even with ground compensation.



**CEN CWA 14747-2
CLASSIFICATIONS FOR SOIL MAGNETIC EFFECT**

FIGURE:

62

PROJECT:

CCMAT Soils

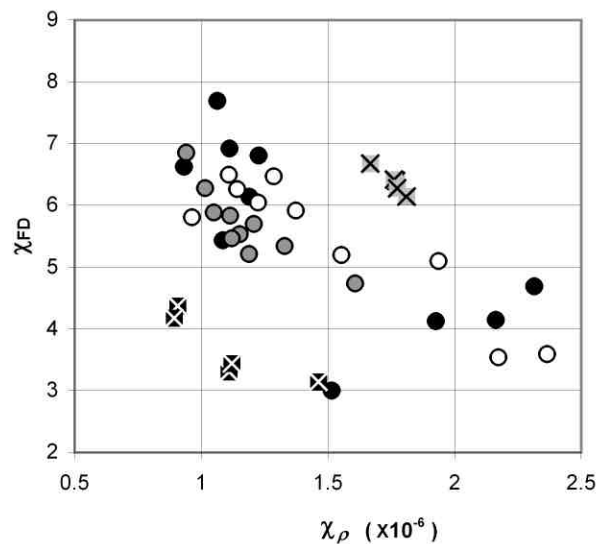
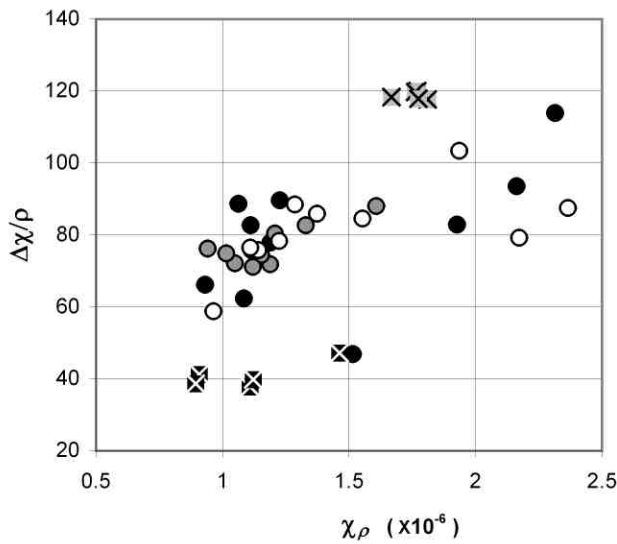
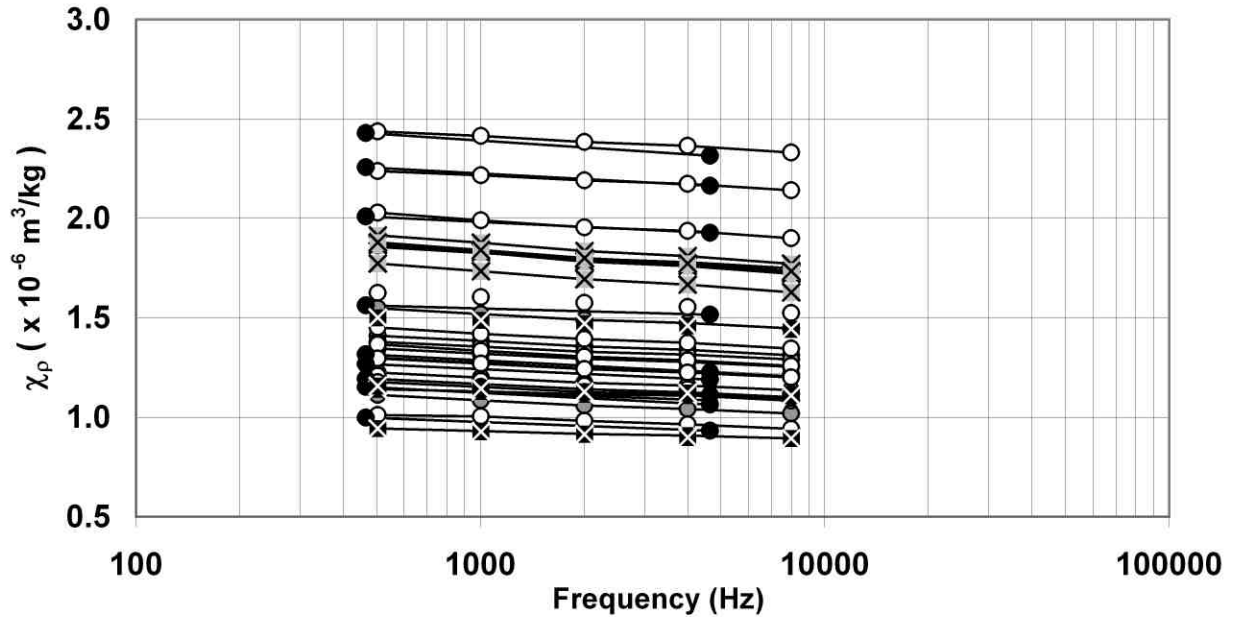
DRAWN BY:

GMC

DATE:

24 October, 2008

- ZHI SM-100 (35 mm, <6.75 mm) | $\rho \approx 1.70 \text{ g/cm}^3$ | $\Delta\chi = 130 \times 10^{-6}$ | $\chi_{FD} = 5.7 \%$
- ZHI SM-100 (10 cc, <6.75 mm) | $\rho \approx 1.81 \text{ g/cm}^3$ | $\Delta\chi = 148 \times 10^{-6}$ | $\chi_{FD} = 5.4 \%$
- Bartington MS2B (10 cc, <6.75 mm) | $\rho \approx 1.81 \text{ g/cm}^3$ | $\Delta\chi = 145 \times 10^{-6}$ | $\chi_{FD} = 5.6 \%$
- X— ZHI SM-100 (35 mm, <2.0 mm) | $\rho \approx 1.46 \text{ g/cm}^3$ | $\Delta\chi = 173 \times 10^{-6}$ | $\chi_{FD} = 6.4 \%$
- X— ZHI SM-100 (35 mm, <6.75 mm, >2.0 mm) | $\rho \approx 1.41 \text{ g/cm}^3$ | $\Delta\chi = 57 \times 10^{-6}$ | $\chi_{FD} = 3.7 \%$



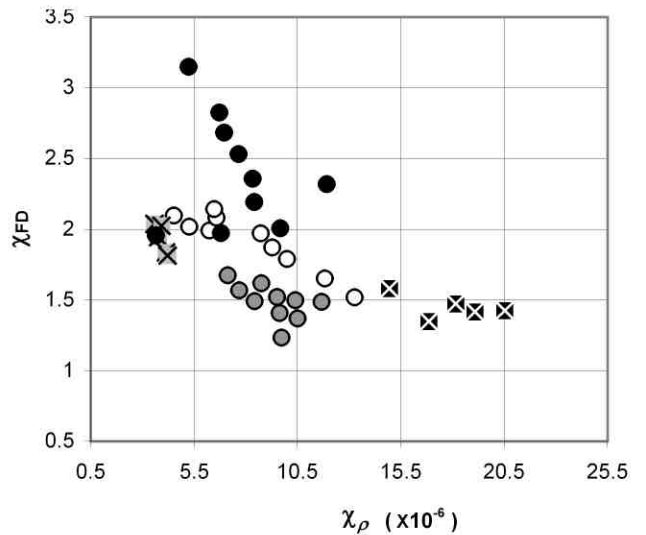
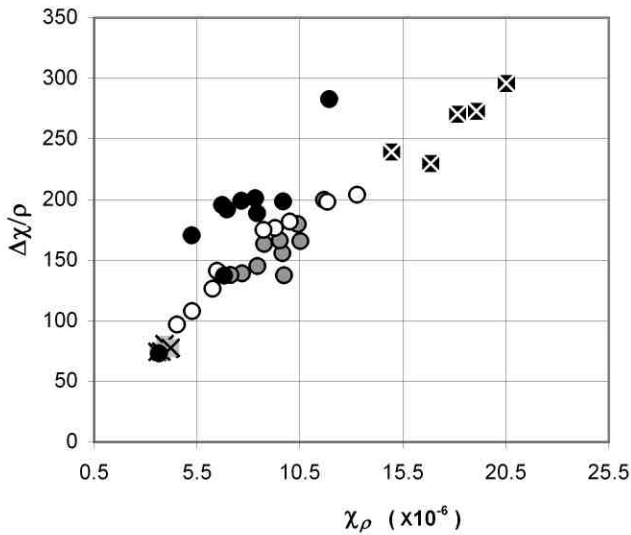
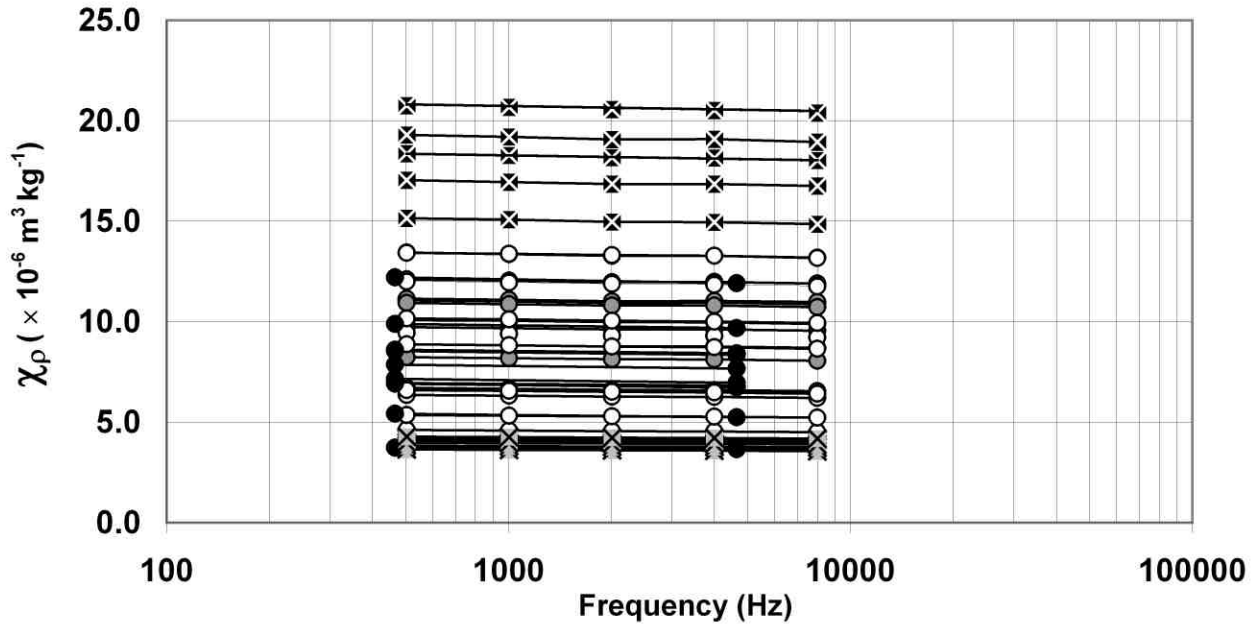
**DRDC CAMBODIA - 1 REFERENCE SOIL
MASS-SPECIFIC MAGNETIC SUSCEPTIBILITY – TEXTURE INFLUENCE**



PROJECT:	CCMAT Soils
DRAWN BY:	GMC
DATE:	6 November, 2008

FIGURE:
63

- ZHI SM-100 (35 mm, <6.75 mm) | $\rho \approx 1.36 \text{ g/cm}^3$ | $\Delta\chi = 216 \times 10^{-6}$ | $\chi_{FD} = 1.5 \%$
- ZHI SM-100 (10 cc, <6.75 mm) | $\rho \approx 1.41 \text{ g/cm}^3$ | $\Delta\chi = 218 \times 10^{-6}$ | $\chi_{FD} = 1.9 \%$
- Bartington MS2B (10 cc, <6.75 mm) | $\rho \approx 1.36 \text{ g/cm}^3$ | $\Delta\chi = 251 \times 10^{-6}$ | $\chi_{FD} = 2.4 \%$
- X— ZHI SM-100 (35 mm, <2.0 mm) | $\rho \approx 1.29 \text{ g/cm}^3$ | $\Delta\chi = 99 \times 10^{-6}$ | $\chi_{FD} = 1.9 \%$
- X— ZHI SM-100 (35 mm, <6.75 mm, >2.0 mm) | $\rho \approx 1.12 \text{ g/cm}^3$ | $\Delta\chi = 291 \times 10^{-6}$ | $\chi_{FD} = 1.5 \%$



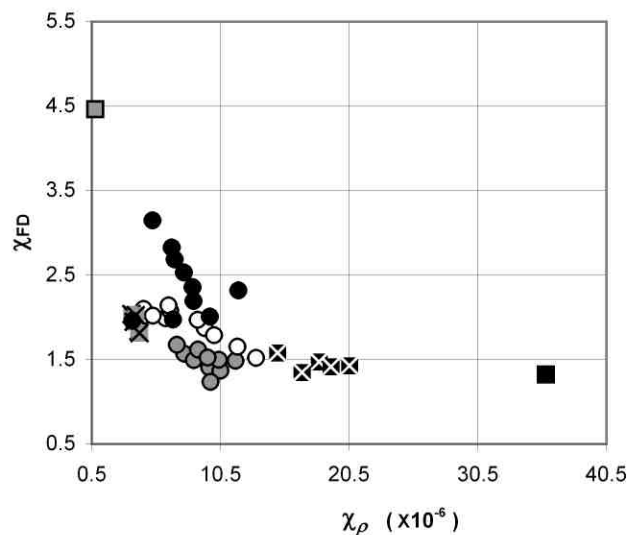
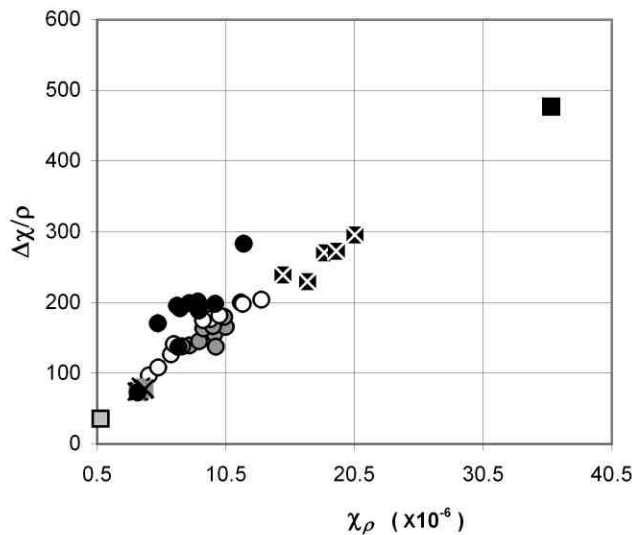
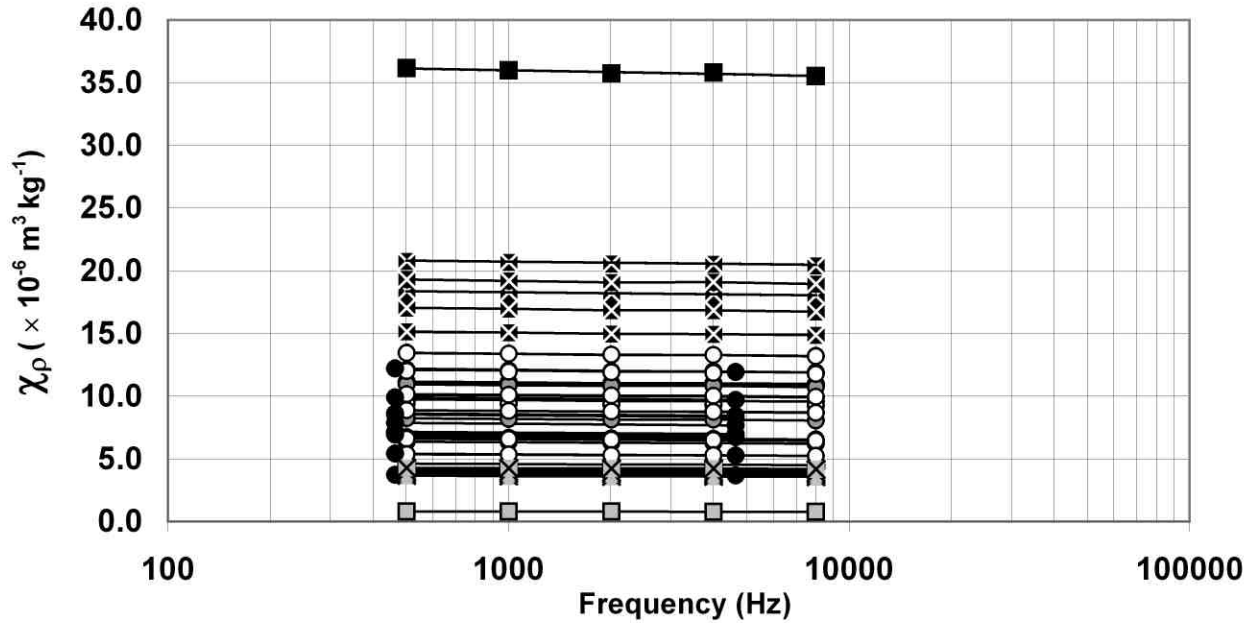
**DRDC AUSTRALIA - B REFERENCE SOIL
MASS-SPECIFIC MAGNETIC SUSCEPTIBILITY – TEXTURE INFLUENCE**



PROJECT:	CCMAT Soils
DRAWN BY:	GMC
DATE:	6 November, 2008

FIGURE:
64

- ZHI SM-100 (35 mm, <6.75 mm) | $\rho \approx 1.36 \text{ g/cm}^3$ | $\Delta\chi = 216 \times 10^{-6}$ | $\chi_{FD} = 1.5 \%$
- X— ZHI SM-100 (35 mm, <2.0 mm) | $\rho \approx 1.29 \text{ g/cm}^3$ | $\Delta\chi = 99 \times 10^{-6}$ | $\chi_{FD} = 1.9 \%$
- X— ZHI SM-100 (35 mm, <6.75 mm, >2.0 mm) | $\rho \approx 1.12 \text{ g/cm}^3$ | $\Delta\chi = 291 \times 10^{-6}$ | $\chi_{FD} = 1.5 \%$
- ZHI SM-100 (10 cc, <0.75 mm) | $\rho \approx 1.00 \text{ g/cm}^3$ | $\Delta\chi = 36 \times 10^{-6}$ | $\chi_{FD} = 4.5 \%$
- ZHI SM-100 (35 mm, <6.75 mm, >2.0 mm) | $\rho \approx 1.67 \text{ g/cm}^3$ | $\Delta\chi = 794 \times 10^{-6}$ | $\chi_{FD} = 1.3 \%$ (washed)

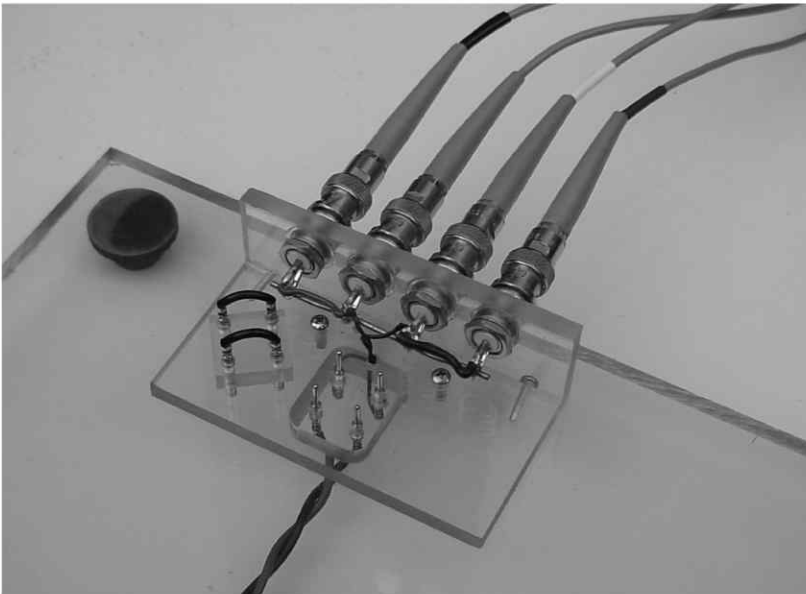
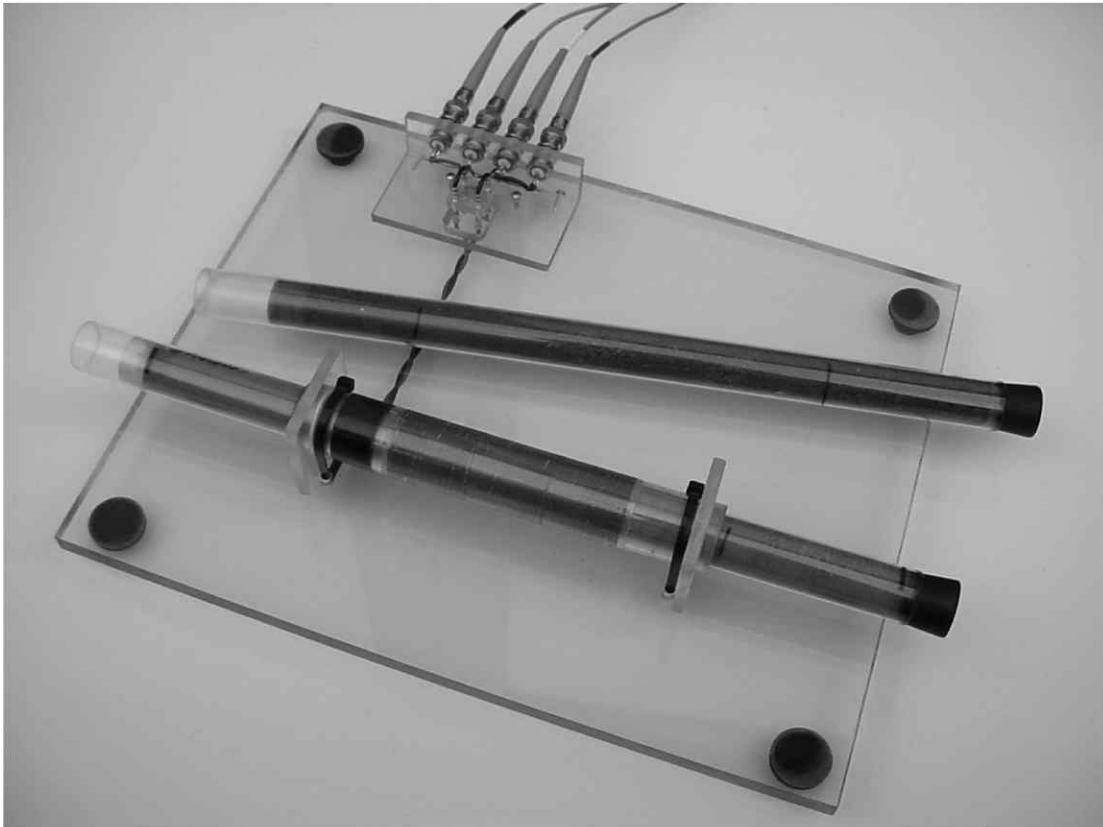


**DRDC AUSTRALIA - B REFERENCE SOIL
MASS-SPECIFIC MAGNETIC SUSCEPTIBILITY – TEXTURE INFLUENCE**



PROJECT: **CCMAT Soils**
 DRAWN BY: **GMC** DATE: **6 November, 2008**

FIGURE:
65



PROTOTYPE SOLENOID SUSCEPTIBILITY FIXTURE

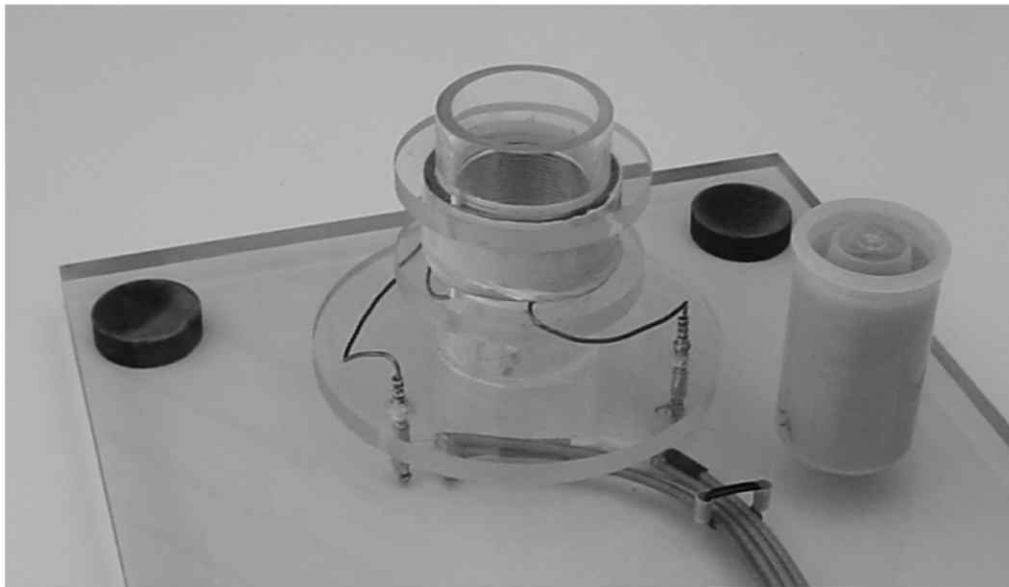
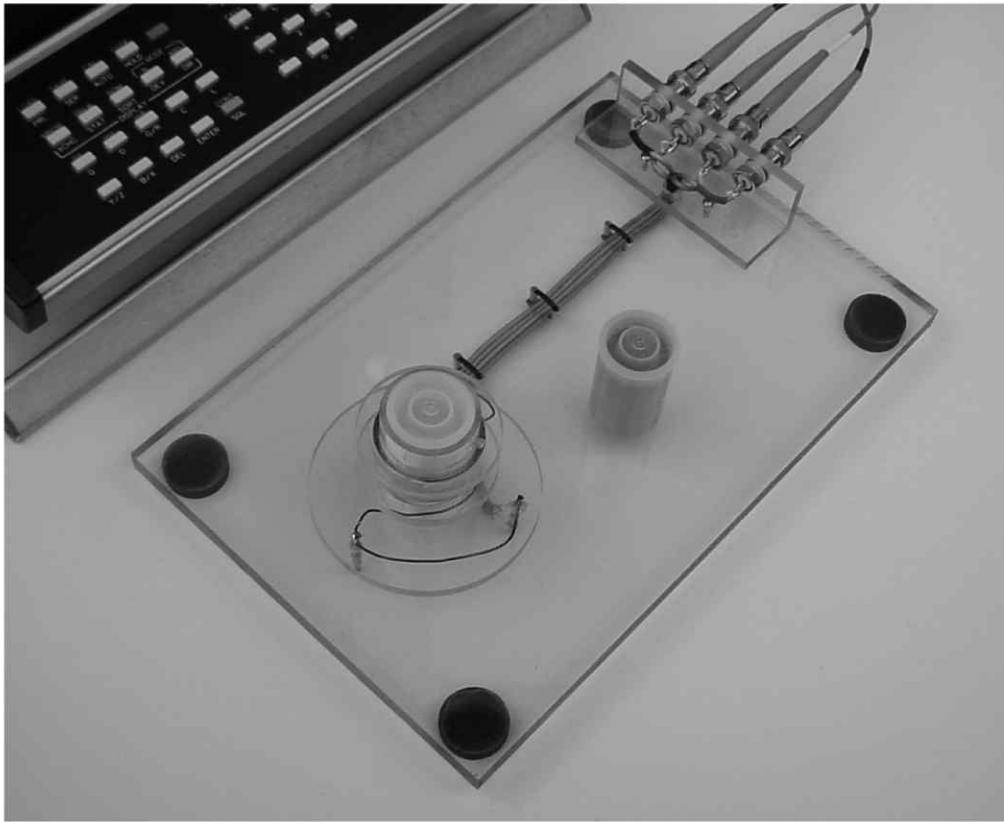


PROJECT: DRDC Soils

DRAWN BY: GMC DATE: 14 December, 2007

FIGURE:

66

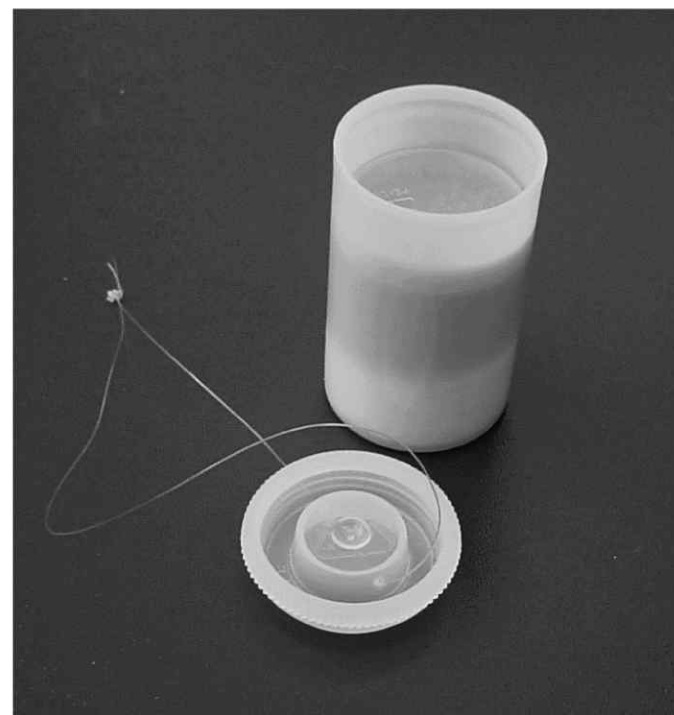
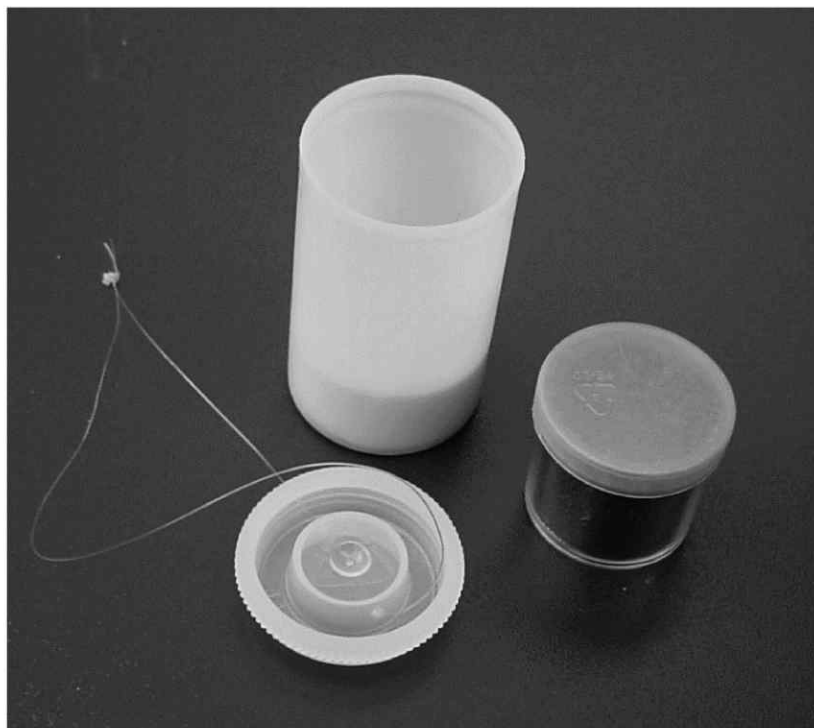


PROTOTYPE 35 mm SUSCEPTIBILITY FIXTURE



PROJECT:	DRDC Soils	
DRAWN BY:	GMC	DATE: 14 December, 2007

FIGURE:
67



NOTES:

1. Bottom 12 mm spacer comprised of dense non-magnetic foam.
2. Standard 10 cc sample vial lid centralizes vial in 35 mm holder.
3. Adapter specific fixture constant required for direct-inductance susceptibility measurements with 10 cc – 35 mm adapter.



10 cc – 35 mm SAMPLE ADAPTER

FIGURE:

68

PROJECT:

CCMAT Soils

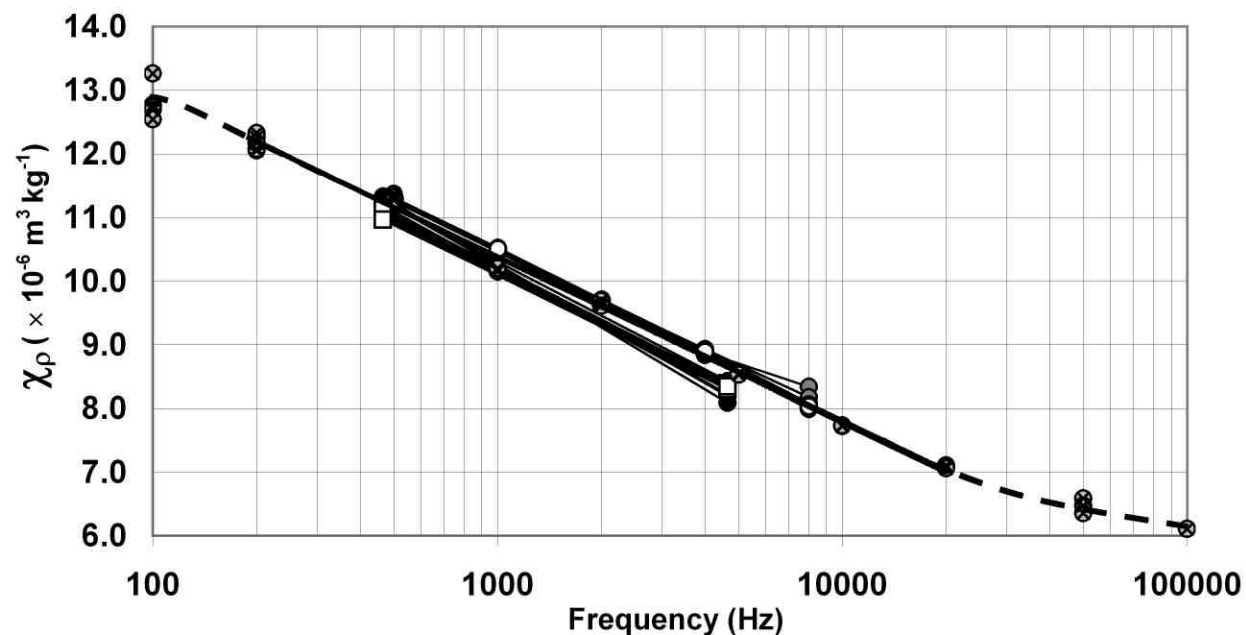
DRAWN BY:

GMC

DATE:

25 September, 2006

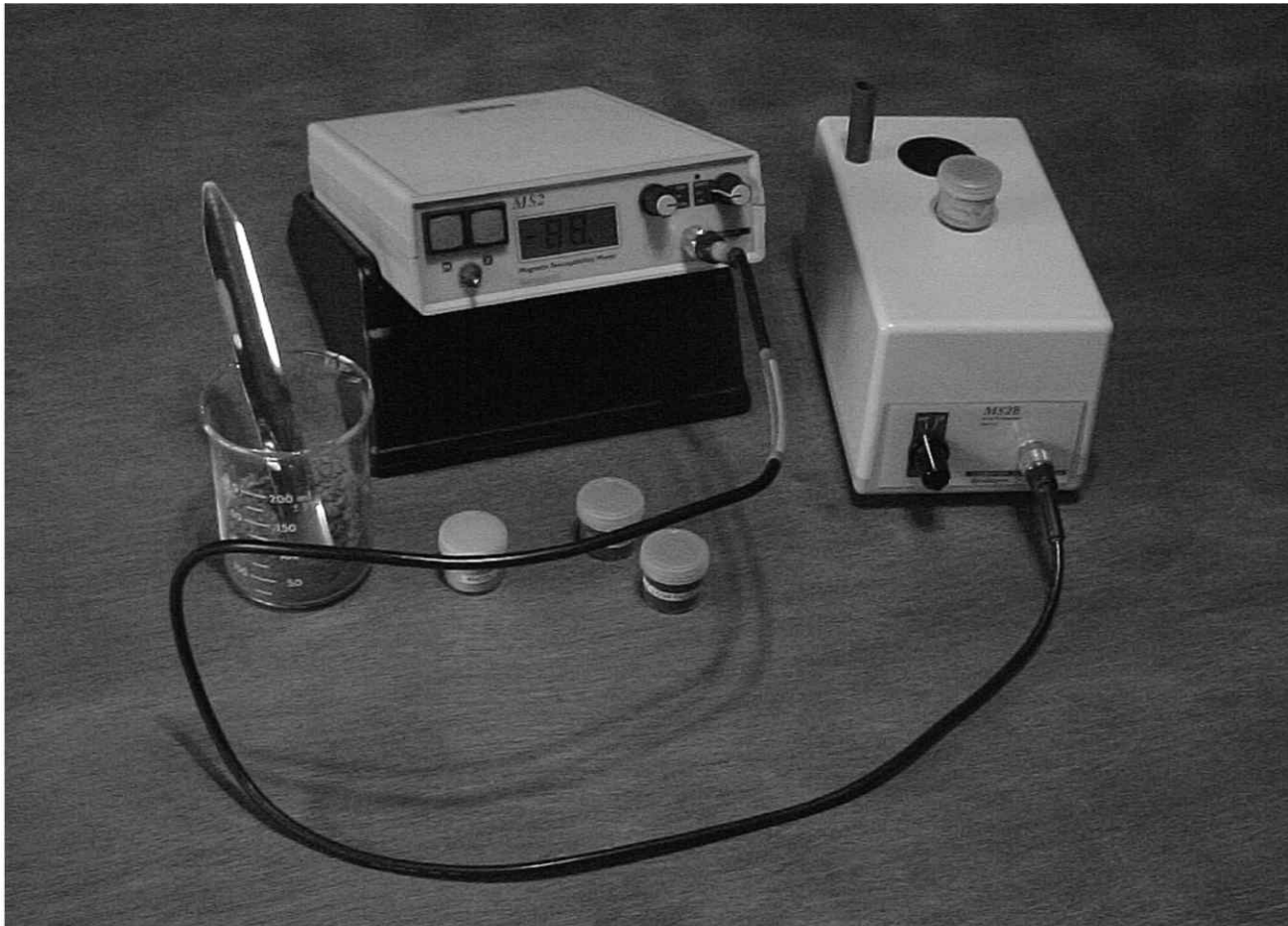
- ZHI SM-100 (35 mm) | $\rho \approx 0.91 \text{ g/cm}^3$ | $\Delta\chi = 2465 \times 10^{-6}$ | $\chi_{FD} = 23.9 \%$
- ZHI SM-100 (10 cc) | $\rho \approx 0.84 \text{ g/cm}^3$ | $\Delta\chi = 2270 \times 10^{-6}$ | $\chi_{FD} = 23.9 \%$
- Bartington MS2B (10 cc – 1.0) | $\rho \approx 0.91 \text{ g/cm}^3$ | $\Delta\chi = 2587 \times 10^{-6}$ | $\chi_{FD} = 25.5 \%$
- Bartington MS2B (10 cc – 0.1) | $\rho \approx 0.92 \text{ g/cm}^3$ | $\Delta\chi = 2468 \times 10^{-6}$ | $\chi_{FD} = 24.3 \%$
- ⊗ ESI 2600 LCR | $\rho \approx 0.92 \text{ g/cm}^3$ | $\Delta\chi = 2378 \times 10^{-6}$ | $\chi_{FD} = 22.9 \%$
35 mm fixture



**USACE-ERDC TIVA CANYON TUFF
MASS-SPECIFIC MAGNETIC SUSCEPTIBILITY**

FIGURE:
69

PROJECT: CCMAT Soils	DRAWN BY: GMC	DATE: 15 February, 2007
--------------------------------	-------------------------	-----------------------------------



**BARTINGTON MS2 – MS2B
DUAL FREQUENCY SOIL SUSCEPTIBILITY METER**

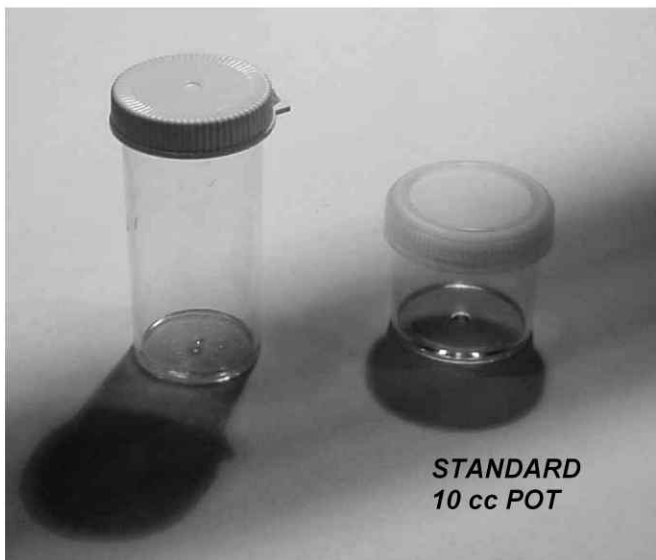
FIGURE:

70

PROJECT: *DRDC Soils*

DRAWN BY: *GMC*

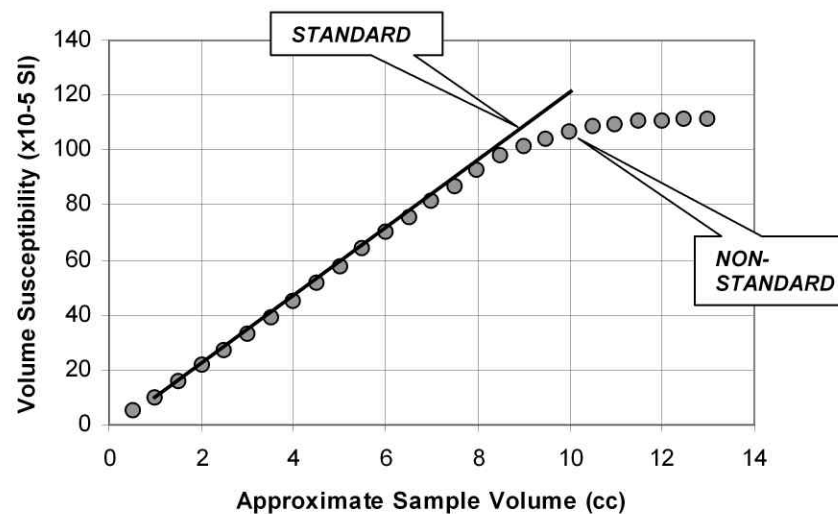
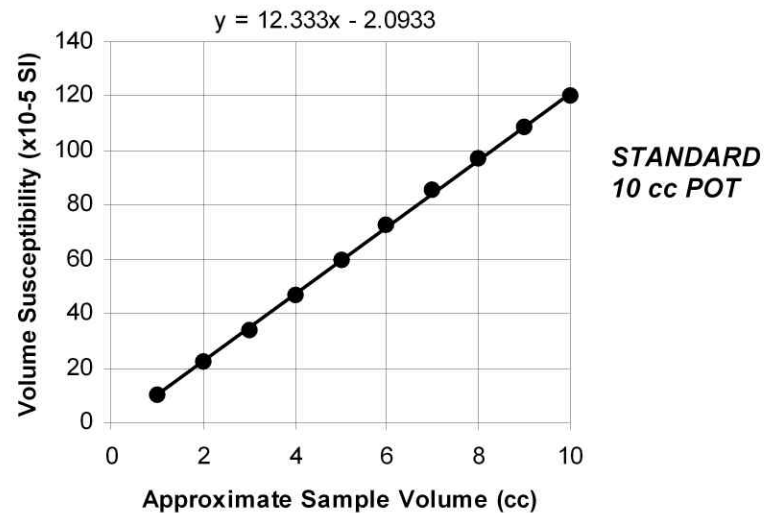
DATE: *20 February, 2007*



NON-STANDARD:
 Height = 4.9 cm
 Diameter = 2.1 cm
 Volume = 16.97 cc

NOTE:
 Volume at 2.3 cm
 Sample level = 7.97 cc

STANDARD 10 cc POT:
 Height = 2.3 cm
 Diameter = 2.4 cm
 Volume = 10.40 cc



**BARTINGTON MS2B SENSOR
 MEASURED SAMPLE VOLUME SENSITIVITY**

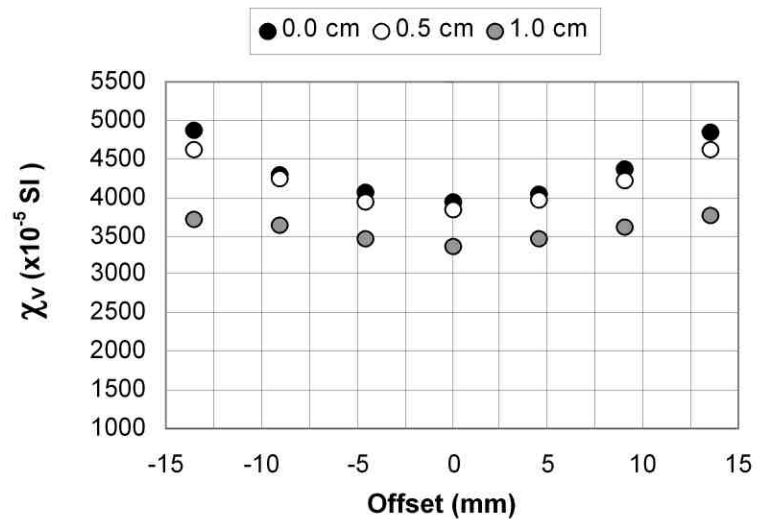
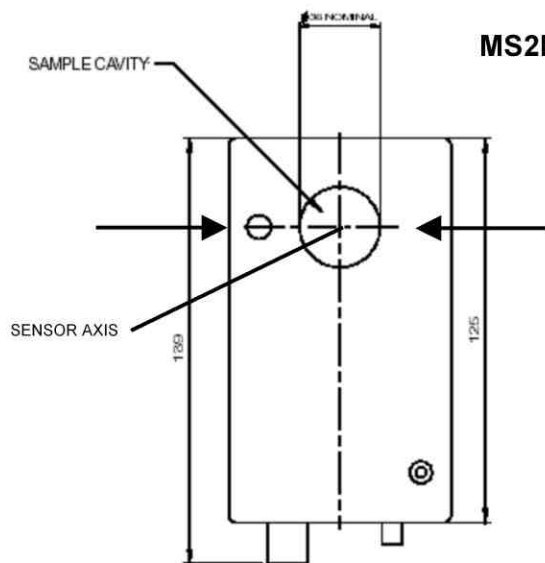
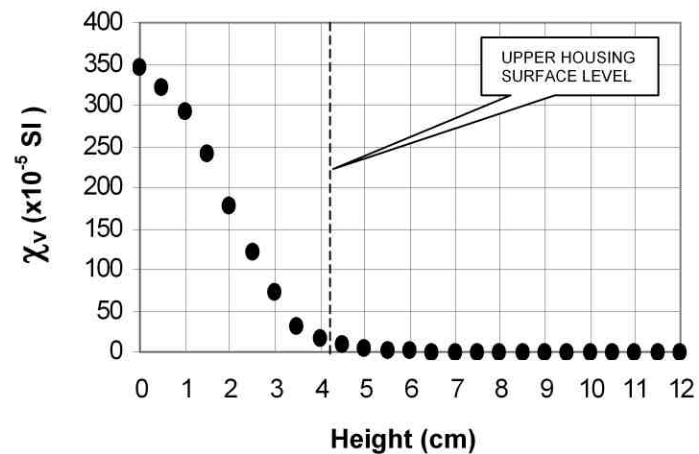
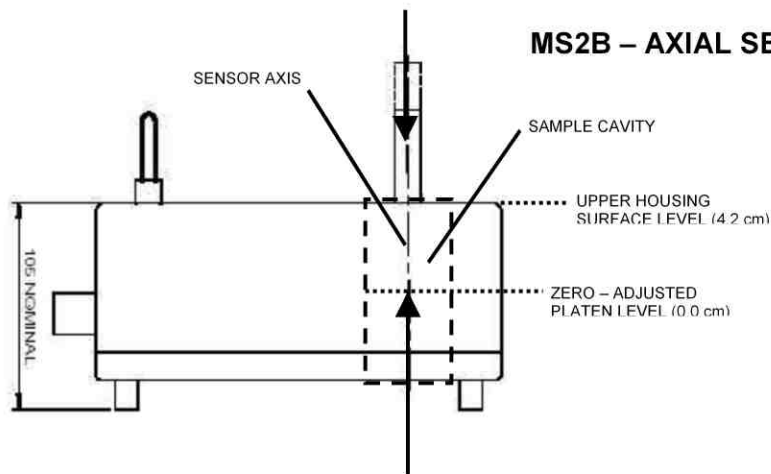
FIGURE:

71

PROJECT: DRDC Soils

DRAWN BY: GMC

DATE: 26 March, 2005



Modified after Bartington Instruments (2005)



**BARTINGTON MS2B SENSOR
MEASURED SENSITIVITY CHARACTERISTICS**

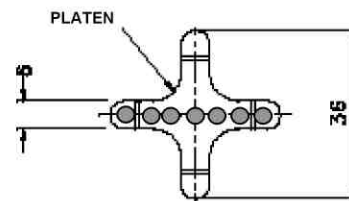
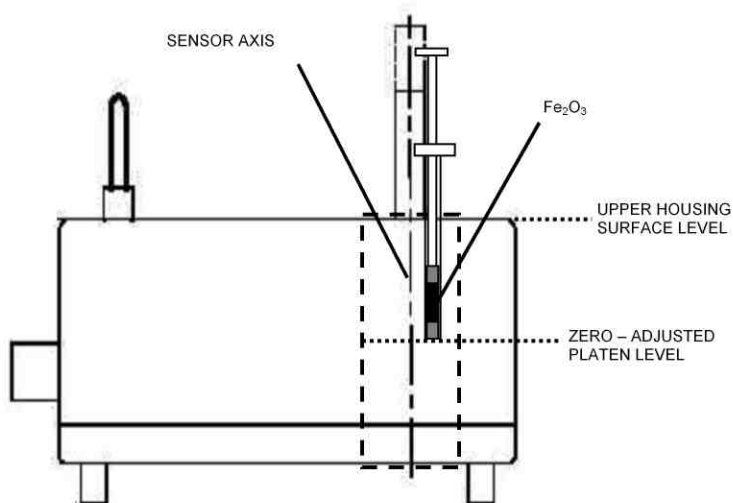
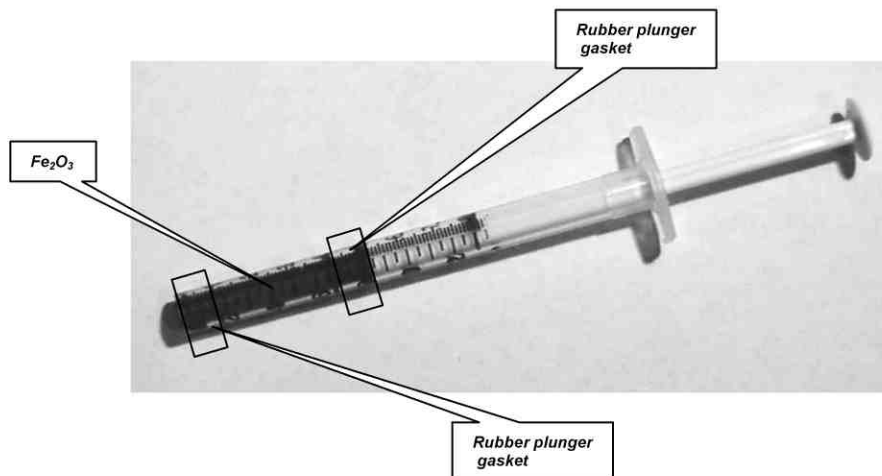
FIGURE:

72

PROJECT: DRDC Soils

DRAWN BY: GMC

DATE: 26 March, 2005



Modified after Bartington Instruments (2005)

BARTINGTON MS2B SENSOR SENSITIVITY PROBE

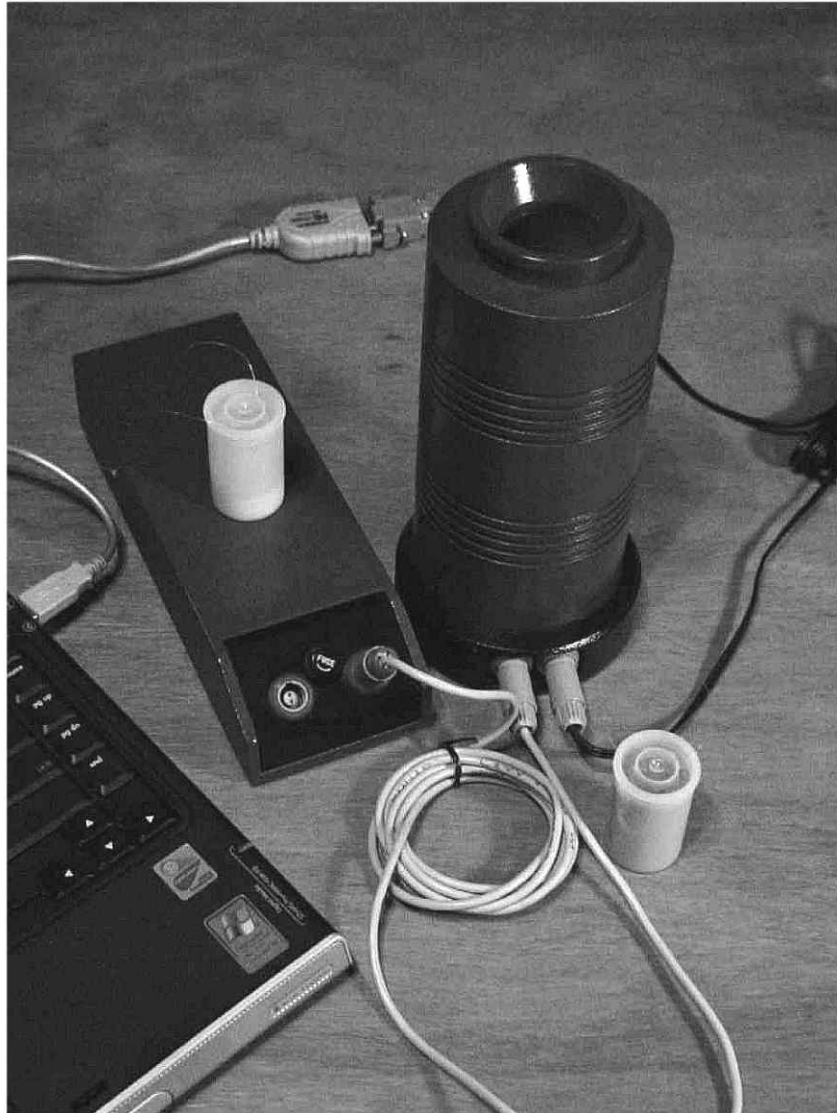


PROJECT:
DRDC Soils

DRAWN BY: *GMC* DATE: *21 March, 2005*

FIGURE:

73



**ZH INSTRUMENTS – SM100
MULTI-FREQUENCY SOIL SUSCEPTIBILITY METER**

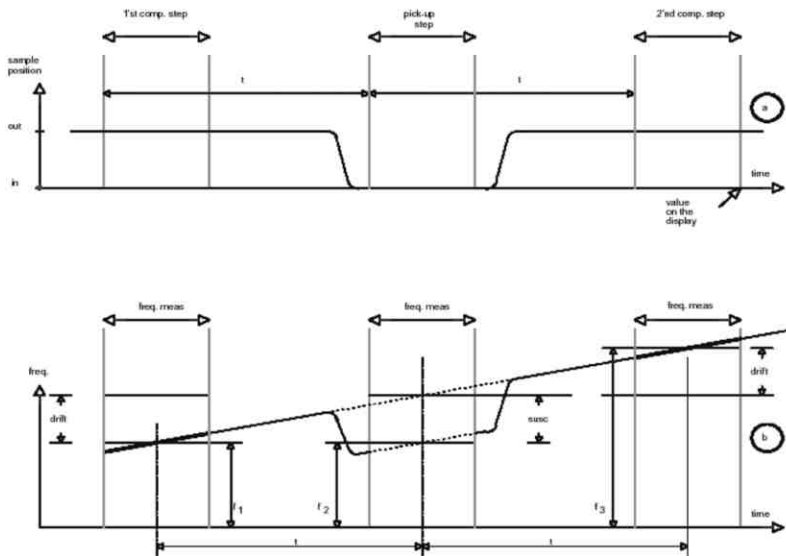
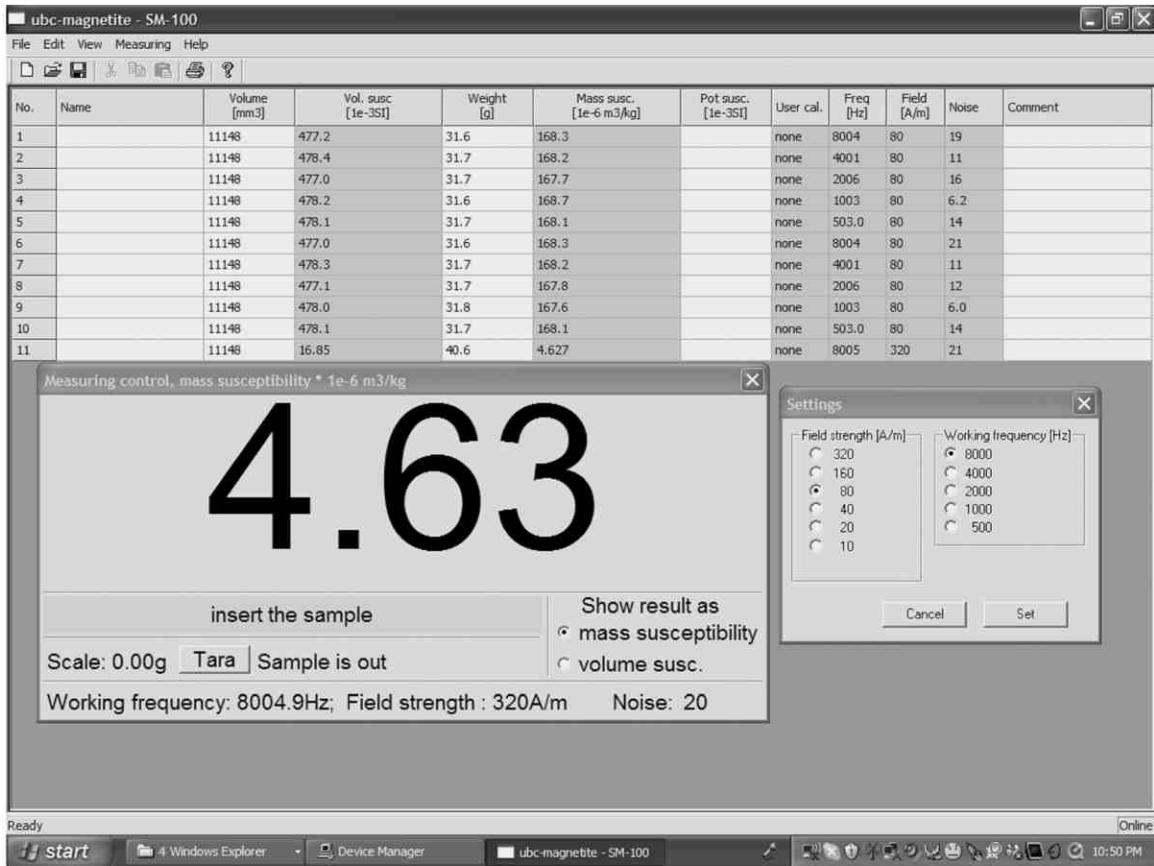


PROJECT:
CCMAT Soils

DRAWN BY: GMC DATE: 20 February, 2007

FIGURE:

74



SOURCE: ZH Instruments (2006)

ZH INSTRUMENTS – SM100 PC INTERFACE APPLICATION – MEASUREMENT SEQUENCE

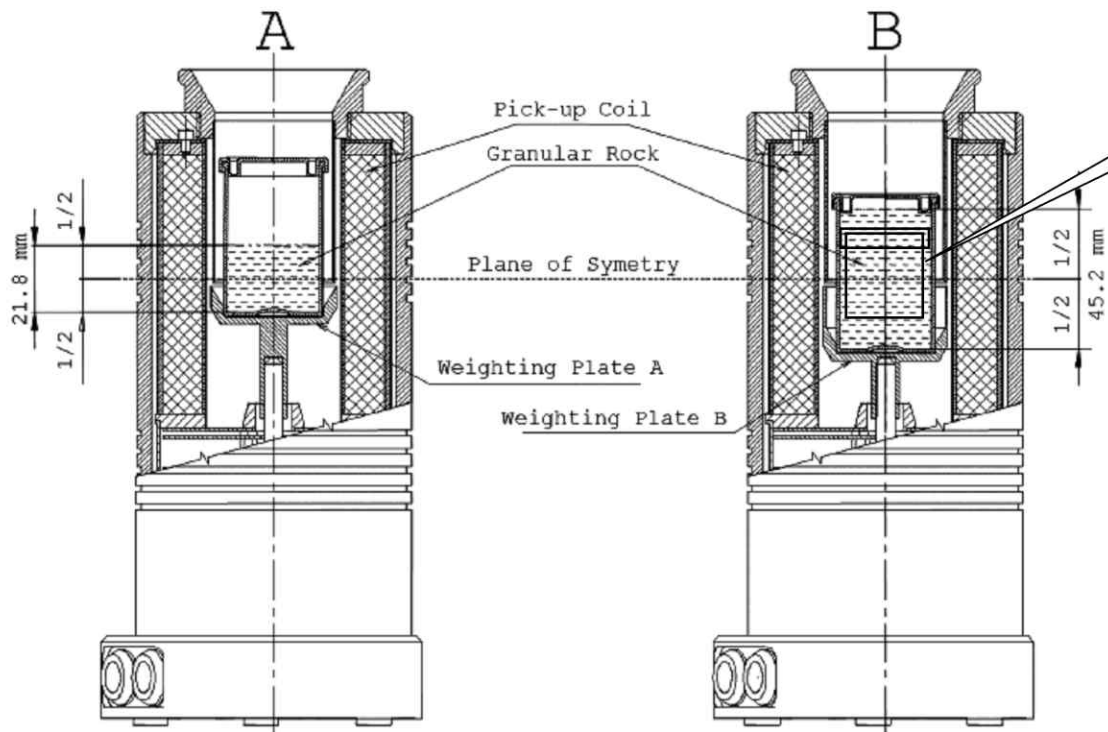


PROJECT: **CCMAT Soils**

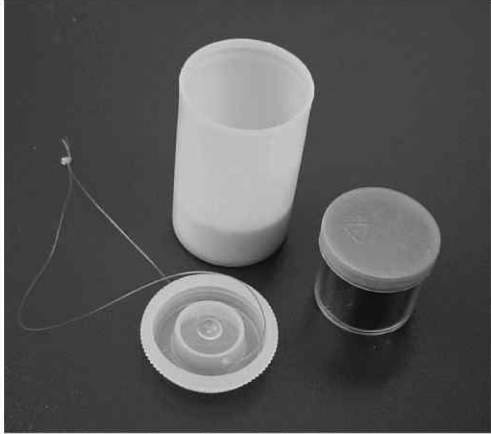
FIGURE:

DRAWN BY: **GMC** DATE: **20 February, 2007**

75



10 cc – 35 mm
Sample adapter



Modified after: ZH Instruments (2006)



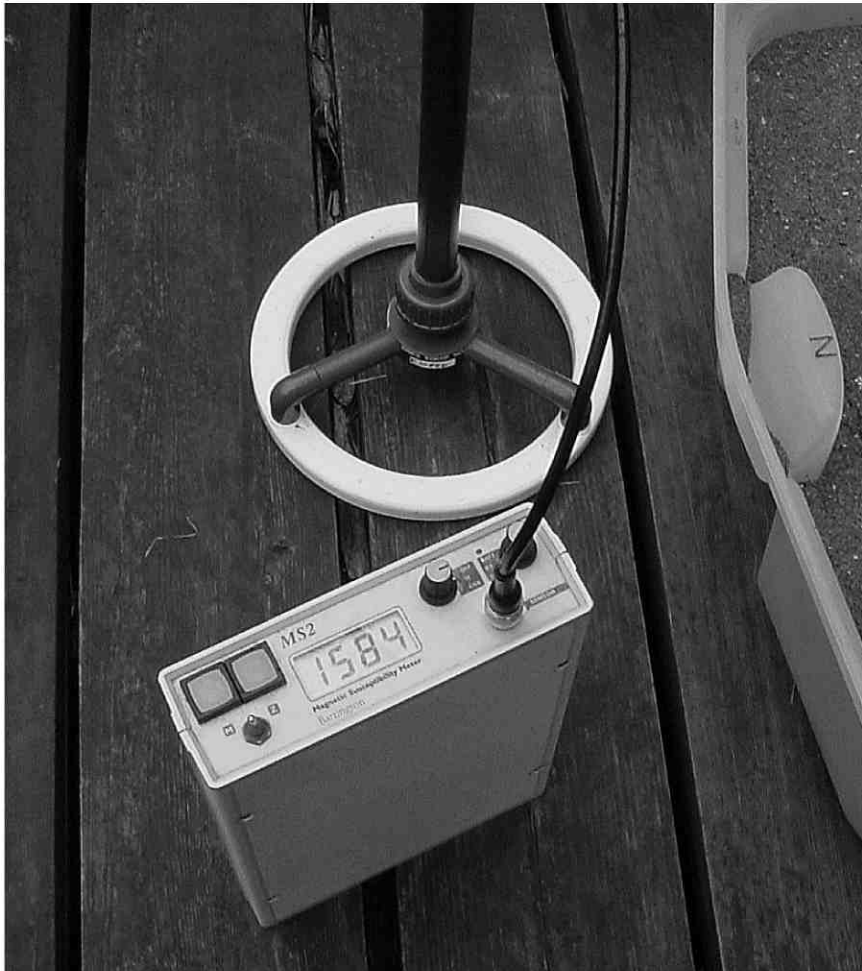
**ZHI SM-100 SENSOR
STANDARD 35 mm SAMPLE HOLDER AND 10 cc ADAPTER**

FIGURE:
76

PROJECT: CCMAT Soils

DRAWN BY: GMC

DATE: 15 February, 2007



Bartington MS2D Field Magnetic Susceptibility System
 Operating Frequency: 0.958 kHz
 Sensitivity: 2×10^{-6} SI



Kappaneter KT-6 Magnetic Susceptibility Meter
 Operating Frequency: 10 kHz
 Sensitivity: 1×10^{-5} SI



Bartington MS2D – Kappaneter KT6
FIELD MAGNETIC SUSCEPTIBILITY MEASUREMENT

FIGURE:

77

PROJECT:

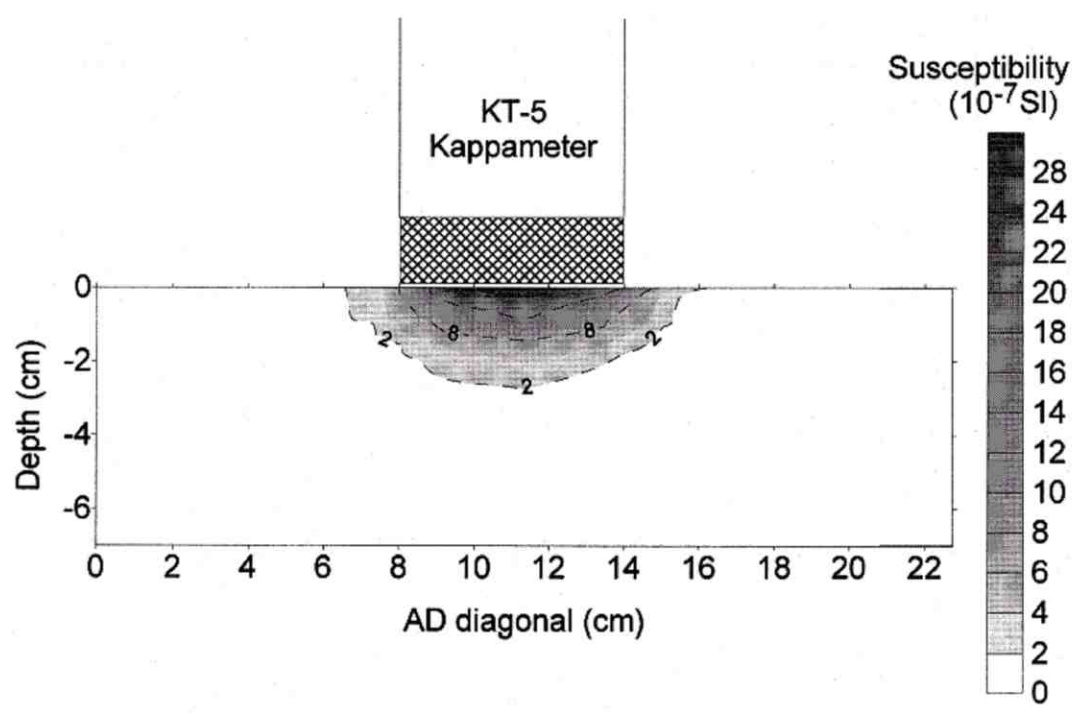
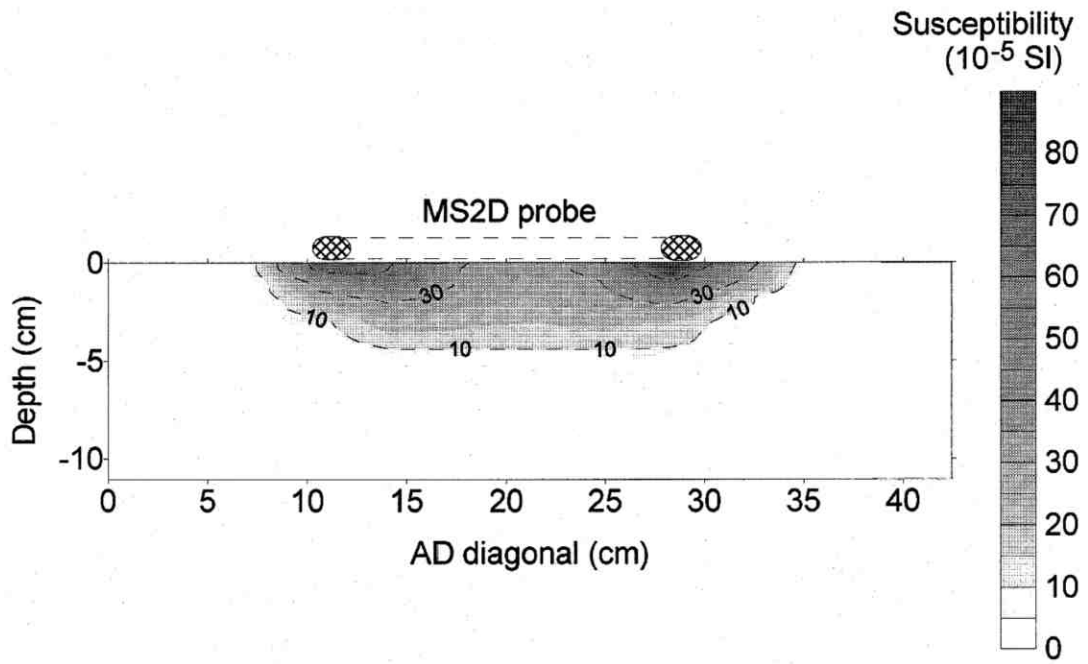
CCMAT Soils

DRAWN BY:

GMC

DATE:

25 September, 2006



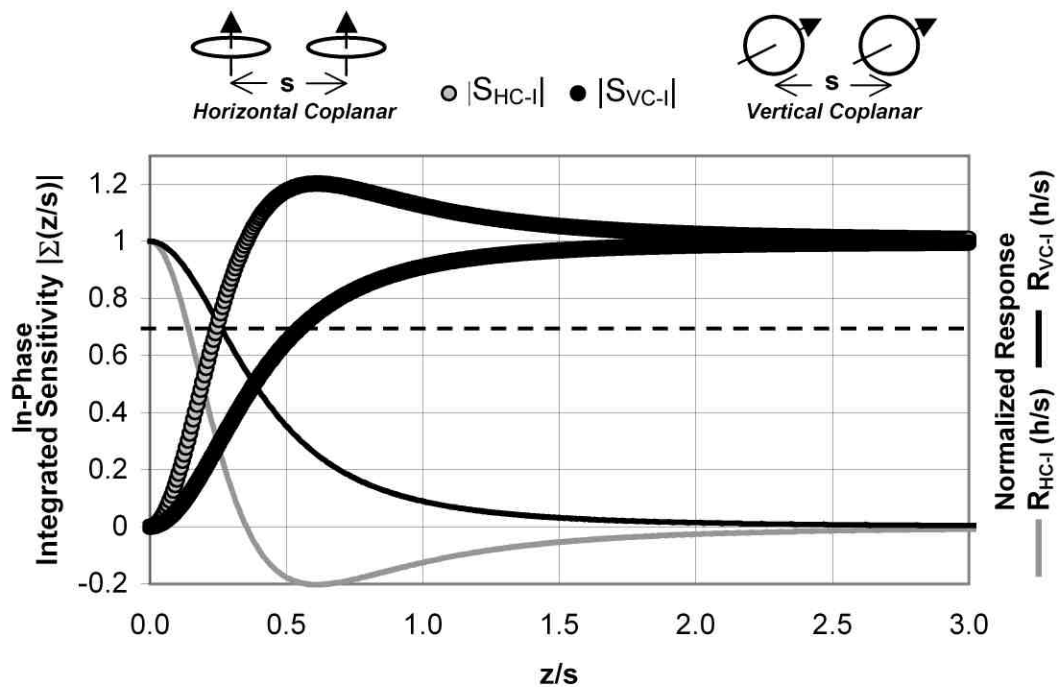
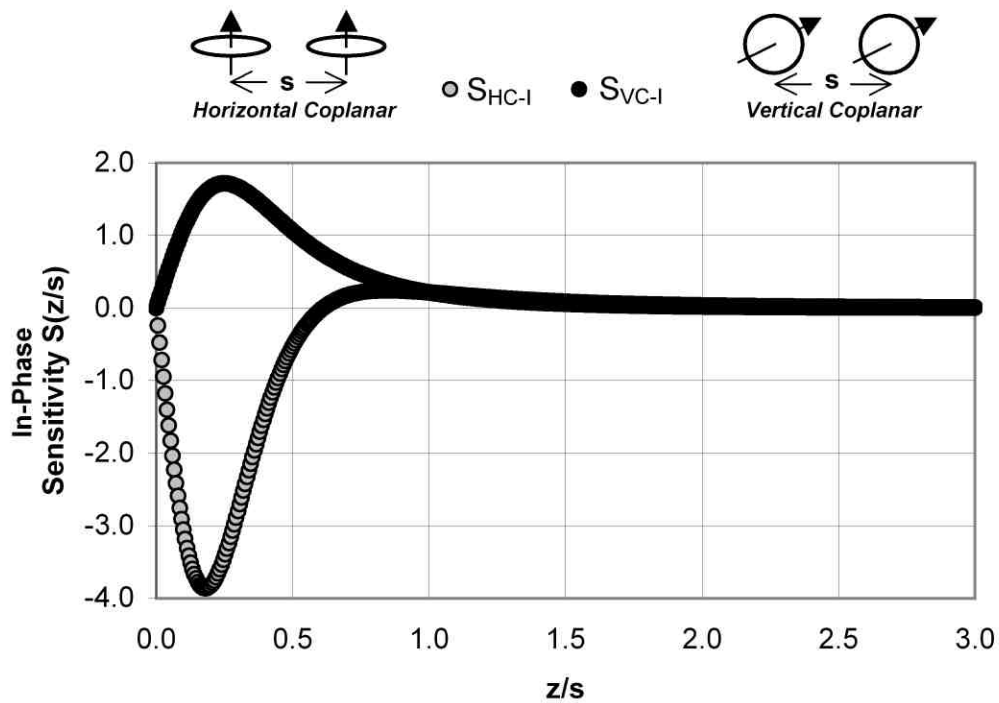
SOURCE: Lecosnet, et al. (1999)

**BARTINGTON MS2D – KAPPAMETER KT6
DEPTH SENSITIVITY DISTRIBUTIONS**



PROJECT:	DRDC Soils	
DRAWN BY:	GMC	DATE: 12 October, 2006

FIGURE:
78



**IN SITU MAGNETIC SUSCEPTIBILITY MEASUREMENT
FDEM COPLANAR DEPTH SENSITIVITY CHARACTERISTICS**



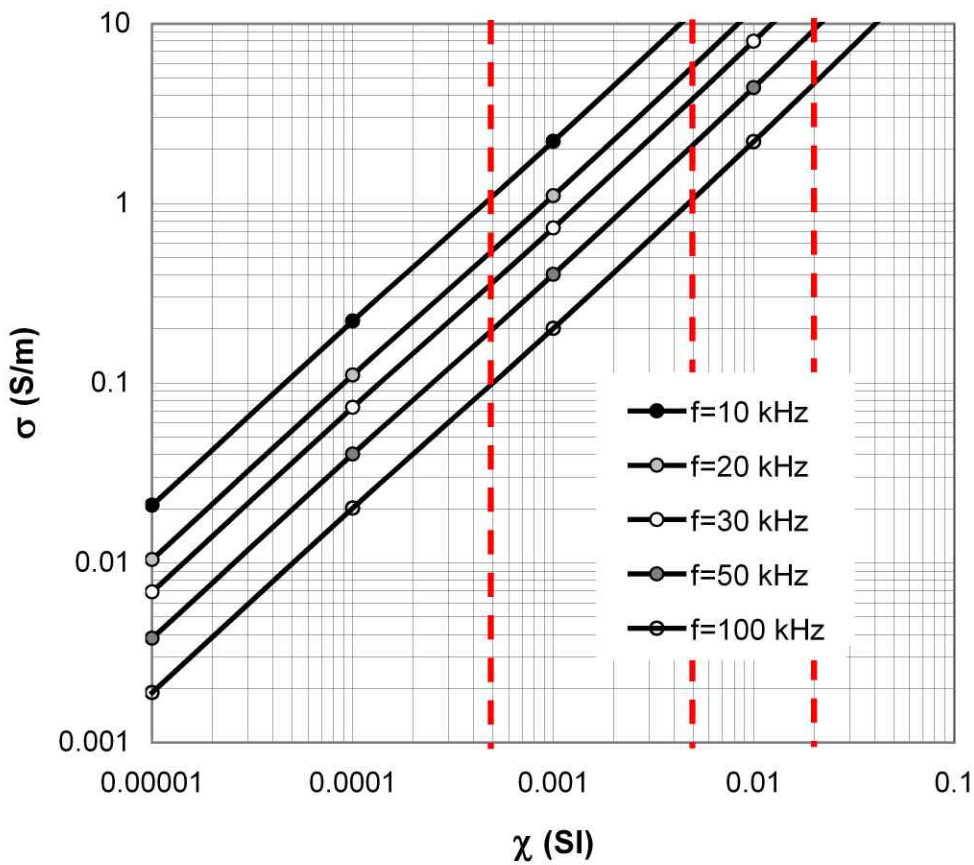
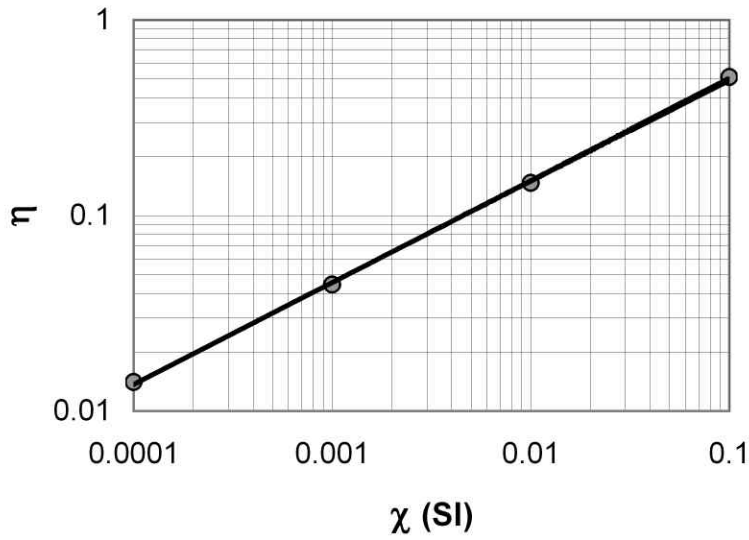
PROJECT: DRDC Soils

DRAWN BY: GMC

DATE: 14 February, 2005

FIGURE:

79



NOTE: Assumes coaxial –coplanar coils with $h_N=h/a=0.6$ and $a=0.15$ m.

--- CEN –WST susceptibility thresholds for soil influence on FDEM metal detectors (see Figure 62).

**THEORETICAL FDEM RESPONSE – BACKGROUND SOIL SENSITIVITY
CONDUCTIVE – MAGNETIC HALF-SPACE**



PROJECT:	CCMAT Soils	
DRAWN BY:	GMC	DATE: 20 February, 2006

FIGURE:
80

UNCLASSIFIED
SECURITY CLASSIFICATION OF FORM
(highest classification of Title, Abstract, Keywords)

DOCUMENT CONTROL DATA		
(Security classification of title, body of abstract and indexing annotation must be entered when the overall document is classified)		
<p>1. ORIGINATOR (the name and address of the organization preparing the document. Organizations for who the document was prepared, e.g. Establishment sponsoring a contractor's report, or tasking agency, are entered in Section 8.)</p> <p>Terrascan Geophysics 4506 West 4th Avenue Vancouver BC V6R 1R3</p>	<p>2. SECURITY CLASSIFICATION (overall security classification of the document, including special warning terms if applicable)</p> <p style="text-align: center; font-size: large;">UNCLASSIFIED</p>	
<p>3. TITLE (the complete document title as indicated on the title page. Its classification should be indicated by the appropriate abbreviation (S, C or U) in parentheses after the title).</p> <p style="text-align: center;">Soil Electromagnetic Properties and Metal Detector Performance: Theory and Measurement</p>		
<p>4. AUTHORS (Last name, first name, middle initial. If military, show rank, e.g. Doe, Maj. John E.)</p> <p>Cross, Guy</p>		
<p>5. DATE OF PUBLICATION (month and year of publication of document)</p> <p>November 2008</p>	<p>6a. NO. OF PAGES (total containing information, include Annexes, Appendices, etc)</p> <p style="text-align: right;">170</p>	<p>6b. NO. OF REFS (total cited in document)</p> <p style="text-align: right;">92</p>
<p>7. DESCRIPTIVE NOTES (the category of the document, e.g. technical report, technical note or memorandum. If appropriate, enter the type of report, e.g. interim, progress, summary, annual or final. Give the inclusive dates when a specific reporting period is covered.)</p> <p>Contract Report</p>		
<p>8. SPONSORING ACTIVITY (the name of the department project office or laboratory sponsoring the research and development. Include the address.)</p> <p>Defence R&D Canada – Suffield, PO Box 4000, Station Main, Medicine Hat, AB T1A 8K6</p>		
<p>9a. PROJECT OR GRANT NO. (If appropriate, the applicable research and development project or grant number under which the document was written. Please specify whether project or grant.)</p>	<p>9b. CONTRACT NO. (If appropriate, the applicable number under which the document was written.)</p> <p style="text-align: center;">W7702-03-R941</p>	
<p>10a. ORIGINATOR'S DOCUMENT NUMBER (the official document number by which the document is identified by the originating activity. This number must be unique to this document.)</p> <p>DRDC Suffield CR 2009-062</p>	<p>10b. OTHER DOCUMENT NOS. (Any other numbers which may be assigned this document either by the originator or by the sponsor.)</p>	
<p>11. DOCUMENT AVAILABILITY (any limitations on further dissemination of the document, other than those imposed by security classification)</p> <p><input checked="" type="checkbox"/> Unlimited distribution <input type="checkbox"/> Distribution limited to defence departments and defence contractors; further distribution only as approved <input type="checkbox"/> Distribution limited to defence departments and Canadian defence contractors; further distribution only as approved <input type="checkbox"/> Distribution limited to government departments and agencies; further distribution only as approved <input type="checkbox"/> Distribution limited to defence departments; further distribution only as approved <input type="checkbox"/> Other (please specify):</p>		
<p>12. DOCUMENT ANNOUNCEMENT (any limitation to the bibliographic announcement of this document. This will normally corresponded to the Document Availability (11). However, where further distribution (beyond the audience specified in 11) is possible, a wider announcement audience may be selected).</p> <p>Unlimited</p>		

UNCLASSIFIED
SECURITY CLASSIFICATION OF FORM

13. ABSTRACT (a brief and factual summary of the document. It may also appear elsewhere in the body of the document itself. It is highly desirable that the abstract of classified documents be unclassified. Each paragraph of the abstract shall begin with an indication of the security classification of the information in the paragraph (unless the document itself is unclassified) represented as (S), (C) or (U). It is not necessary to include here abstracts in both official languages unless the text is bilingual).

Metal detectors are unquestionably the workhorses of humanitarian demining. Although hybrid dual-sensor systems incorporating a ground penetrating radar (GPR) have recently been introduced and are gaining acceptance, a standard electromagnetic induction (EMI) sensor remains the primary mode of detection. Despite ongoing evolution and refinement of metal detector technology, however, the practical performance of both continuous wave (FDEM) and pulse induction (TDEM) systems continues to be restricted by so-called "soil noise" effects. Generally, "problem" or "difficult" soils reduce signal to noise ratio and increase the false-detection rate. At certain locations, the soil effect is so severe as to render a given metal detector practically inoperable. Although soil interference is well established and widely appreciated, the precise origin(s) of related noise has remained elusive as evidenced by the range of common descriptions for problem soils, including "lateritic soil", "mineralized soil", "conducting soil" and "magnetic soil". The absence of clarity and definitive understanding has impeded specification of appropriate methods and procedures for related assessment of soil conditions and for predicting the nature and extent of corresponding influence on a given metal detector technology. To address the foregoing situation, the study reported herein has been part of a broader international effort to define and quantify the effects of soil electromagnetic properties on the operation and performance of metal detectors and allied (GPR) sensors. In particular, the present study is restricted to EMI metal detectors and our aim has been to characterize the nature and extent of influence due to specific soil electromagnetic properties and related frequency dispersion. Our report begins with a brief review of pertinent electromagnetic theory and subsequently explores the basic physics of EMI metal detectors and associated implications for the relative significance of specific soil EM parameters. Particular attention is focused on TDEM sensors and related influence of dispersive soil electromagnetic properties. The balance of the report is devoted to the theory and practice of measuring low-frequency (100 Hz - 100 kHz) soil electromagnetic properties. A range of practical instrumentation and procedures are investigated with reference to three DRDC reference soils.

14. KEYWORDS, DESCRIPTORS or IDENTIFIERS (technically meaningful terms or short phrases that characterize a document and could be helpful in cataloguing the document. They should be selected so that no security classification is required. Identifiers, such as equipment model designation, trade name, military project code name, geographic location may also be included. If possible keywords should be selected from a published thesaurus, e.g. Thesaurus of Engineering and Scientific Terms (TEST) and that thesaurus-identified. If it is not possible to select indexing terms which are Unclassified, the classification of each should be indicated as with the title.)

Electromagnetic Induction, metal detector, land mines, demining, complex magnetic susceptibility soil, conductivity of soil, measurement of soil electromagnetic properties

UNCLASSIFIED
SECURITY CLASSIFICATION OF FORM

Defence R&D Canada

Canada's Leader in Defence
and National Security
Science and Technology

R & D pour la défense Canada

Chef de file au Canada en matière
de science et de technologie pour
la défense et la sécurité nationale



www.drdc-rddc.gc.ca